Synthesis, Design, and Characterization of *N*,*N′*-Tethered *cis*-Indigos

by

Hyejin Hong
B.Sc., University of Victoria, 2014

A Dissertation Submitted in Partial Fulfillment
of the Requirements for the Degree of

DOCTOR OF PHILOSOPHY

in the Department of Chemistry

Supervisory Committee

Synthesis, Design, and Characterization of *N*,*N′*-Tethered *cis*-Indigos

by

Hyejin Hong
B.Sc., University of Victoria, 2014

Supervisory Committee

Dr. Robin G. Hicks, Department of Chemistry
Supervisor

Dr. Peter C. Wan, Department of Chemistry
Departmental Member

Dr. Cornelia Bohne, Department of Chemistry
Departmental Member

Dr. Sara Ellison, Department of Physics and Astronomy
Outside Member

Abstract

Supervisory Committee
Dr. Robin G. Hicks, Department of Chemistry
Supervisor
Dr. Peter C. Wan, Department of Chemistry
Departmental Member
Dr. Cornelia Bohne, Department of Chemistry
Departmental Member
Dr. Sara Ellison, Department of Physics and Astronomy
Outside Member

This dissertation explores the structural modification of indigo into its rare *cis* form by substitution of a short organic bridge between the two indole nitrogen atoms. The synthesized *N*,*N′*-tethered *cis*-indigoids are assessed for their physicochemical properties in order to understand the effect of the organic tether on *cis*-indigoid systems.

Three literature compounds containing “simple” tether structures are synthesized and subjected to complete characterization. Among them, alkyl group based *cis*-indigos, **2.5** and **2.6** exhibit similar absorption wavelengths as the parent indigo while oxalyl-tethered indigo **2.7** shows a large hypsochromic shift due to the strong electron-withdrawing nature of the oxalyl group. The electronics of the tether also affected the HOMO and LUMO energy levels; the oxalyl tether lowered both energy levels in comparison to the alkyl tethers. However, the indigoid co-planarity was strongly affected by the ring size from the tether rather than electronics.

A new tethered *cis*-indigo structure type was discovered in reactions involving quinones. This new tether type consists of a 2,2′-dihydroindigo unit connected to the *cis*-indigo backbone through a central C–C bond of the former. Incorporation of the quinone moiety was observed in **3.2** where the final structure is comprised of two molecules of indigo and one naphthoquinone, while structures of **3.3** and **3.4** contained two indigoid units only. Investigation by CV revealed the strength of the quinone altered the early reaction intermediates. These dimeric *cis*-indigos show a small hypsochromic shift in the absorption compared to the parent indigo and relatively planar *cis*-indigoid backbone. **3.2** demonstrates rich redox behaviours. **3.3** and **3.4** display dynamic behaviours observed by solution VT ^{1}H NMR spectroscopy.

Oxalyl-tethered *cis*-Nindigo **4.6a** and *cis*-indigo monoimine **4.7a** were synthesized and compared with the indigoid counterpart **2.7** to examine the influence of the arylimine groups. Absorption wavelengths of the imine group containing species depended strongly on the electronics of the tether, yet the number of imine groups affected redox potentials. Protonation of **4.6a** (to give H^+oxalyl Nindigo **4.6aH**$^+$) causes a bathochromic shift in the absorption and allows for much easier reduction. The acidity (pK_a) of **4.6aH**$^+$ is estimated between 3.6 – 4.46 in DMSO. A protonated *cis*-Nindigo derivative **4.9aH**$^+$ was obtained via reduction of the oxalyl group and is compared with **4.6aH**$^+$.

Table of Contents

List of Figures

List of Schemes

List of Tables

List of Numbered Compounds

1.1

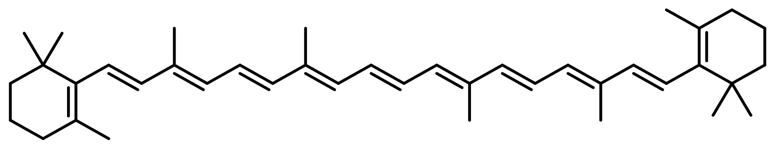

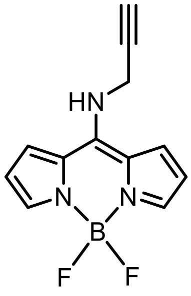

1.2

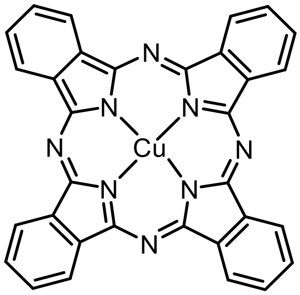

1.3

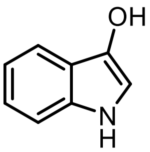

1.4

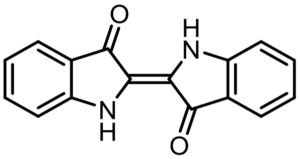

1.5

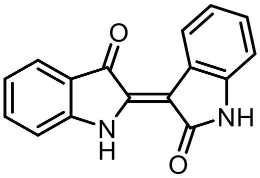

1.6

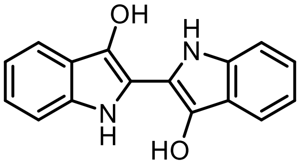

1.7

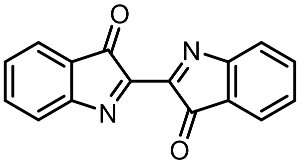

1.8

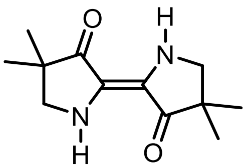

1.9

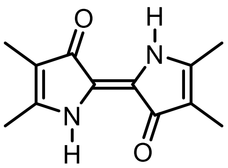

1.10

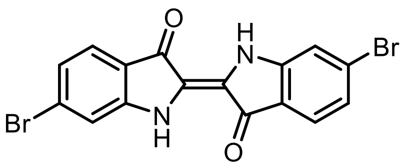

1.11

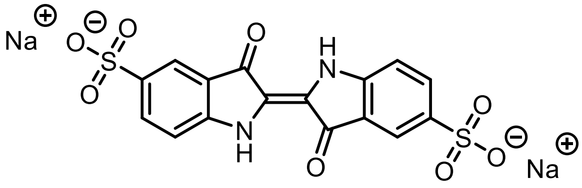

1.12

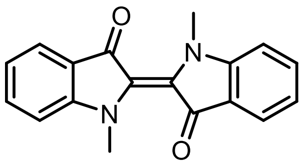

trans-**1.13**

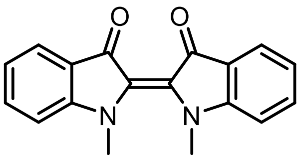

cis-**1.13**

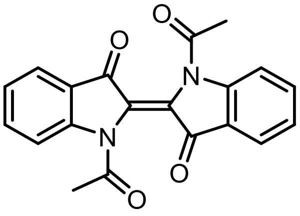

trans-**1.14**

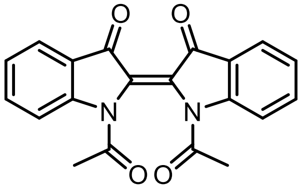

cis-**1.14**

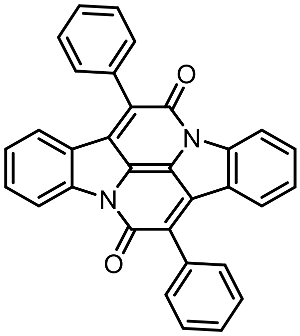

1.15

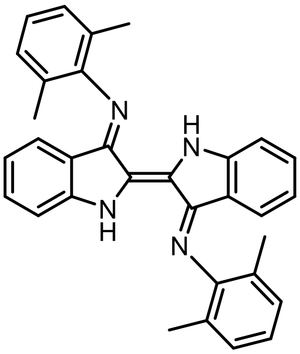

1.16a

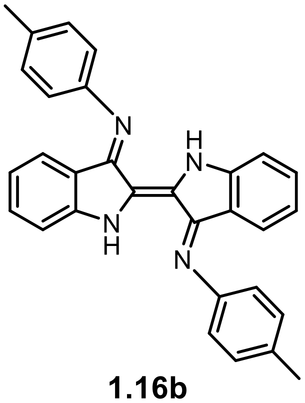

1.16b

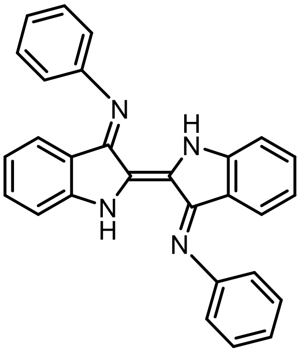

1.16c

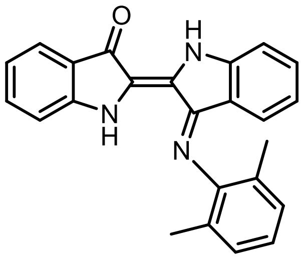

1.17a

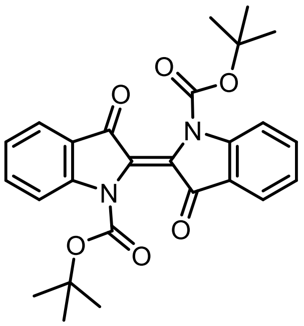

2.1

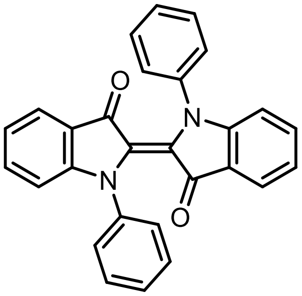

2.2

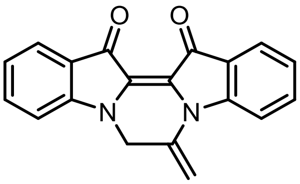

2.3

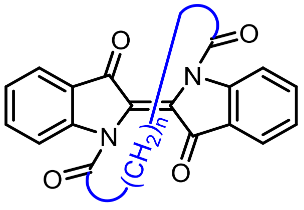

n = 7, 8

2.4

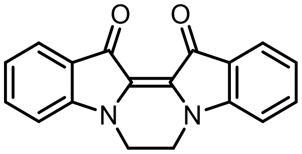

2.5

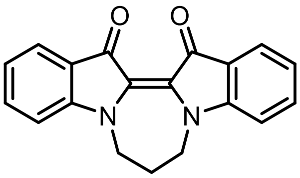

2.6

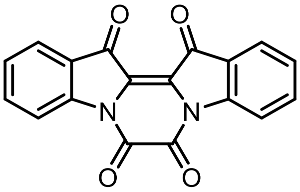

2.7

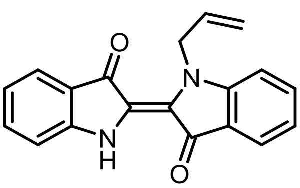

2.8

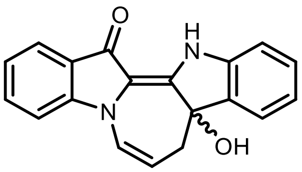

2.9

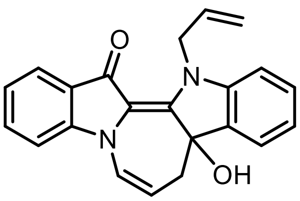

2.10

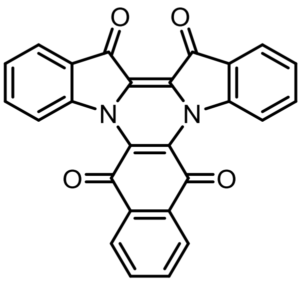

3.1

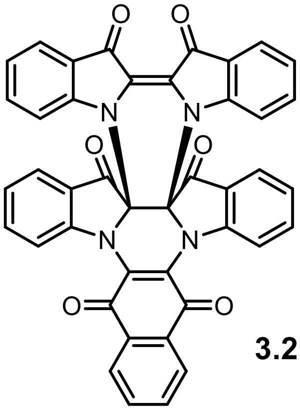

3.2

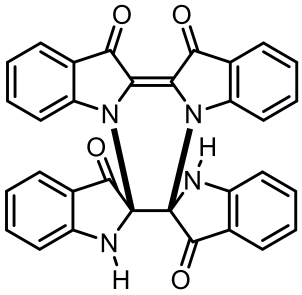

3.3

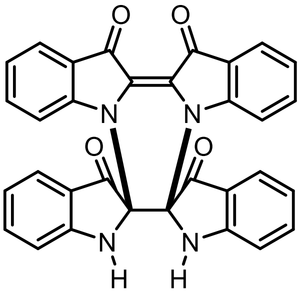

3.4

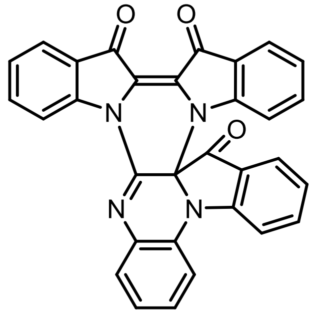

3.5

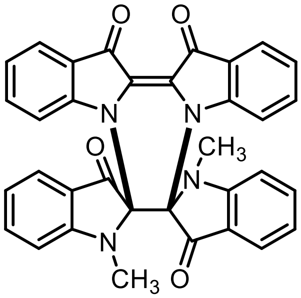

3.6

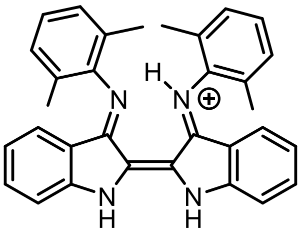

4.1a

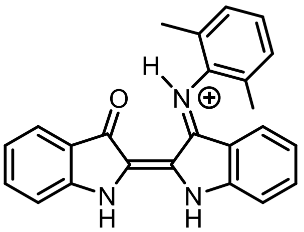

4.2a

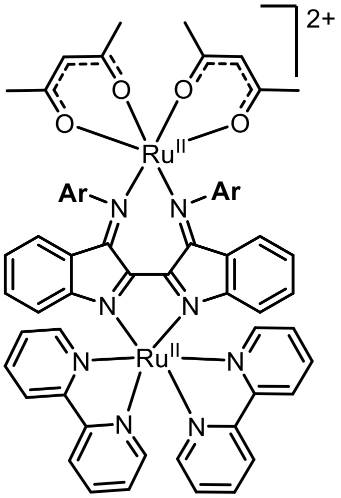

4.3

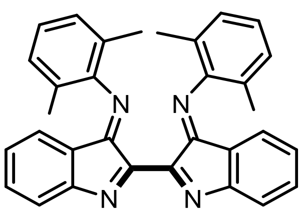

4.4a

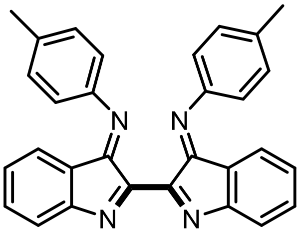

4.4b

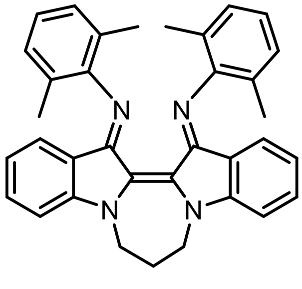

4.5a

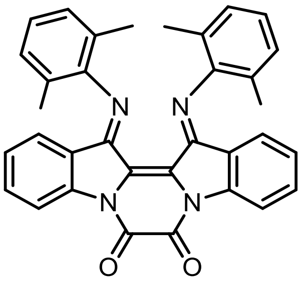

4.6a

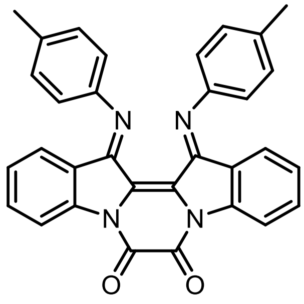

4.6b

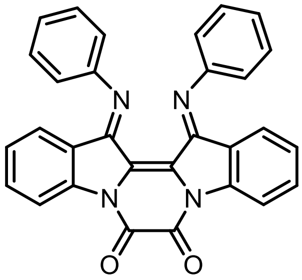

4.6c

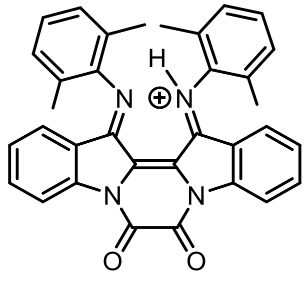

4.6aH^{+}

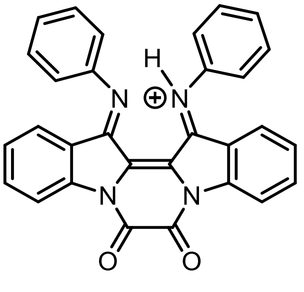

4.6cH^{+}

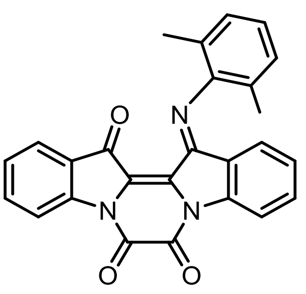

4.7a

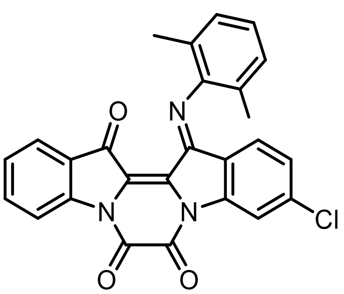

4.7a-Cl

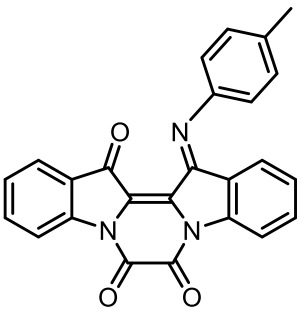

4.7b

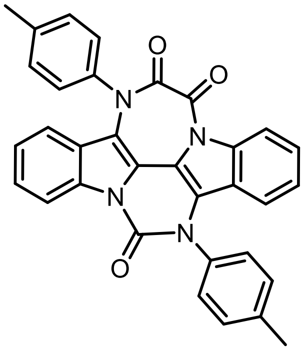

4.8

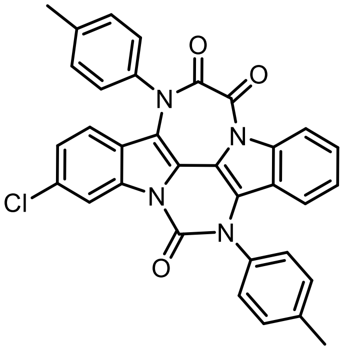

4.8-Cl

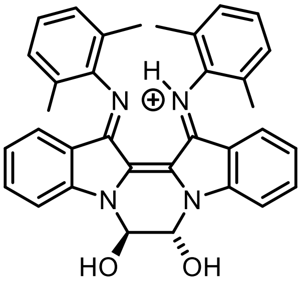

4.9aH$^+$

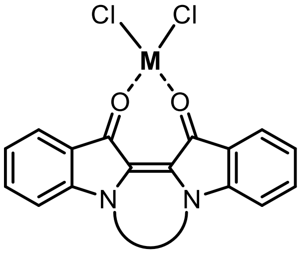

5.1

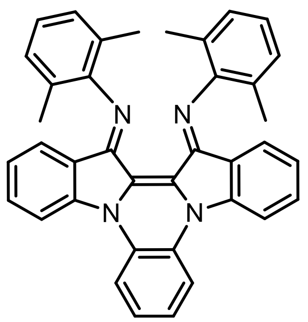

5.2

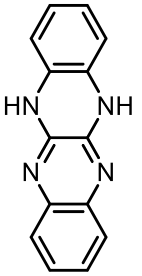

5.3

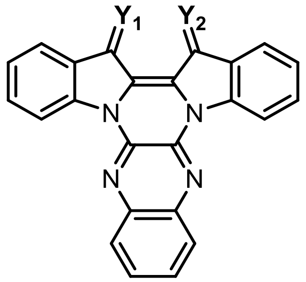

5.4

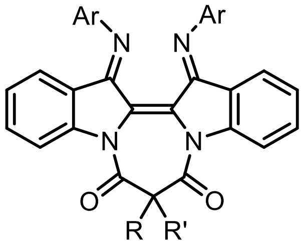

5.5a/b

a: R = R' = H

b: R = H,
R' = CH_3

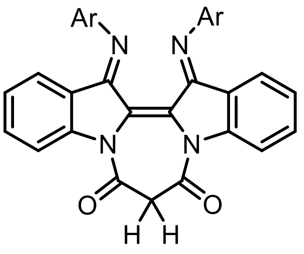

5.5a

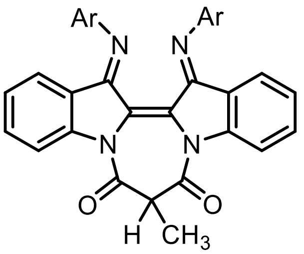

5.5b

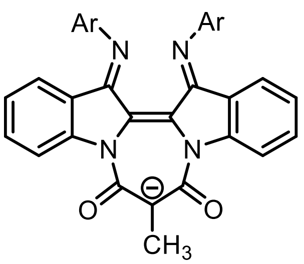

5.5b$^-$

List of Abbreviations

∠	angle
°	degrees
°C	degrees Celsius
1D	one-dimensional
2D	two-dimensional
A	Absorbance
Å	Angstroms
ACN	Acetonitrile
Ar	Aromatic group
BODIPY	boron-dipyrromethene
Br_2NQ	1,2-dibromonaphthoquinone
C=O	carbonyl
ca.	circa (approximately)
CD_2Cl_2	dichloromethane-d_2
$CHCl_3$	chloroform
cm^{-1}	wavenumber
COSY	correlation spectroscopy
CV	cyclic voltammetry
d_1	recycle delay time
DABCO	1,4-diazabicyclo[2.2.2]octane
DCM	dichloromethane
DDQ	2,3-dichloro-5,6-dicyano-1,4-benzoquinone
DFT	density-functional theory
DMF	dimethylformamide
DmP	2,4-dimethylphenyl
DMSO	dimethylsulfoxide
e^-	electron
eq.	equivalence
eV	electron volts
Fc	ferrocene
Fc^+	ferrocenium
HMBC	heteronuclear multiple-bond correlation spectroscopy
HOMO	highest occupied molecular orbital
HPLC	high-performance liquid chromatography
hr	hours
HR-MS	high-resolution-mass spectroscopy
HSQC	heteronuclear single quantum correlation
Hz	Hertz

IR	infrared
K (temp)	Kelvin
LiHMDS	lithium bis(trimethylsilyl)amide
LUMO	lowest unoccupied molecular orbital
m/z	mass-to-charge ratio
mg	milligram
MHz	megahertz
min	minutes
MNova	MestreNova NMR processing software
MO	molecular orbital
mp	melting points
mV	millivolts
NBu_4BF_4	tetrabutylammonium tetrafluoroborate
NBu_4PF_6	tetrabutylammonium hexafluorophosphate
N-H	amine group
nm	nanometer
NMR	nuclear magnetic resonance
NOESY	nuclear Overhauser effect spectroscopy
ns	nanosecond
OFETs	organic field-effect transistor
Ph	phenyl
$\mathrm{p}K_a$	negative log of acid dissociation constant K_a
ppm	parts per million
*p*Tol	4-methylphenyl
R_f	retardation factor
RT	room temperature
s	seconds
S_0	singlet ground state
S_1	first excited singlet state
*t*BOC	*tert*-butoxycarbonyl
t-butyl	*tert*-butyl
THF	tetrahydrofuran
UV	ultra-violet
V	Volts
Vis	visible
Δ	heat
δ	chemical shift (ppm)
Δss	Stokes shift
ε	molar extinction coefficient
λ_{max}	the wavelength of maximum electronic absorption

μA	microampere
Φ_F	fluorescence quantum yield
Φ_{IC}	internal conversion quantum yield
Φ_T	triplet formation quantum yield
$\Phi_{t \rightarrow c}$	*trans*-to-*cis* isomerization quantum yield

Acknowledgements

I would like to firstly thank my supervisor, Dr. Robin Hicks for his guidance over the last seven years. From the beginning as an undergraduate student in the Hicks lab, his insight and patience shaped who I am as a synthetic Chemist. I am truly grateful to have him as my mentor and supervisor. I would like to also thank Dr. Cornelia Bohne for being my committee member and allowing me to use her instrumentation for photophysics studies, and Dr. Peter Wan for valuable discussions about organic chemistry since the beginning of my PhD journey.

I am very fortunate to work with wonderful people in my lab: Dr. Emma Davy introduced me to colour chemistry, which I instantly fell in love with. Dr. Corey Sanz was the person I go to to ask any questions and receive his expertise in solving everything, including X-ray crystals. Dr. Dillon Hofsommer was the CV guru that I was always relying on and helped me obtain beautiful crystal structures. Dr. Geneviève Boice holds the centre of our lab and her knowledge I always looked up to. Shaun MacLean was my lab (soul)mate who has helped me in every possible way, including a TD-DFT figure in this dissertation. I will always cherish our column separation party at 2 am… I also want to acknowledge Nick Richard for teaching me valuable chemistry techniques and Alivia Wang for her hard work. In addition, I would like to thank the Hicks lab undergraduate researchers who contribute to the work in this dissertation: Cassidy Conover and Will Thomas both brought me new perspectives to the research and I truly enjoyed our time together on the project.

I would like to thank Dr. Brian Patrick at the University of British Columbia for collecting X-ray crystallography data since the beginning of my degree. Furthermore, I owe special thanks to the people who helped me finish the research in this difficult time of COVID: Dr. Tyler Trefz for collecting HR-MS data and his magnificent insights on data interpretation, Jessy Oake for performing fluorescence experiments and being an excellent teacher to explain a new area to me, and Chris Barr for all the tremendous help I received for all NMR experiments.

Second lastly, I appreciate for all the help from the Chemistry Department and all the faculty members.

Lastly, my gracious heart goes to my friends - Eric, Fraser, Elvis, Brian, Dave, Abby and Paul - you guys are my *rock* and solid support I can always count on. I would like to thank my loving Hong family & Halmony and my fiancé Sean Yang for their love and support.

Dedication

For my Hong family and Halmony…

Chapter 1. Introduction and Background

1.1. Organic Dyes and Advanced Applications

Colourants absorb light in the visible region (380 – 720 nm) of the electromagnetic spectrum. Light absorption promotes electrons from the low energy ground state to a higher energy excited state. The energy difference between these electronic states determines the colour, photoluminescence and electronic properties of the material.[1]

Among the many different chemical types of colourants, organic dyes and pigments have distinctive structural features, such as the continuous alternation of single and multiple bonds, and/or incorporation of functional groups that enhance the delocalization of π-electrons in the conjugated scaffold.[2] Coloured materials have found utility in various research areas such as lasers, solar energy conversion, optical data storage, electronic displays (LCD, OLED), electrophotography, pH sensors, food additives and cosmetics.[3]

Figure 1.1 shows few examples of colourants that are used in advanced applications. *β*-Carotene (**1.1**) is a famous natural dye and owns an extended π-conjugation in its backbone, where 11 double bonds comprise the chromophore that is responsible for the orange colour of carrot; **1.1** has been incorporated into carbon nanotubes due to its excellent energy transfer capability.[4, 5] Dipyrromethene (UV-absorbing) gains fluorescent properties upon boron coordination. The BODIPY (**1.2**) dye family absorbs/emits in the visible region and is used as fluorescent switches[6], chemosensors[6], laser dyes[7] and labelling reagents for proteins[8] and DNA[9]. Incorporation of metals can be an alternative method to further tuning the energy gap of an organic dye through the interaction of the orbitals of the metal and the ligand.[2] A large π-conjugated macrocycle, phthalocyanine, can incorporate various metal centres for tailoring optical properties.[10] A copper complex (**1.3**) has been an active target in photovoltaic applications.[11]

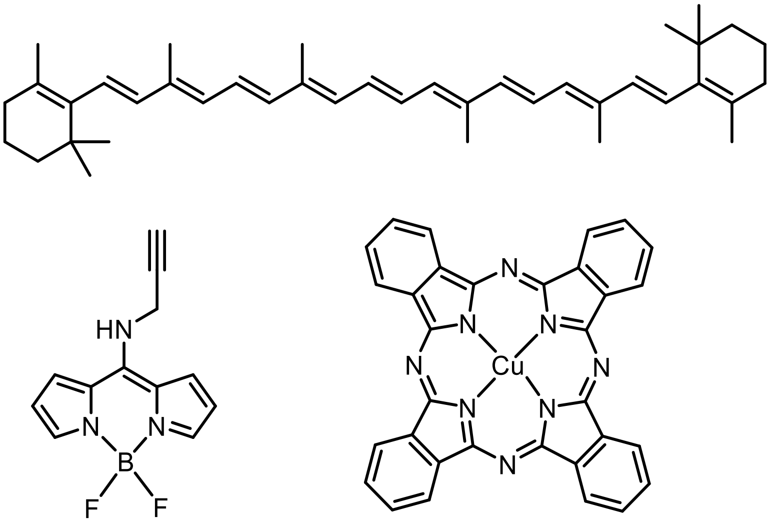

1.1

1.2

1.3

Figure 1.1 Examples of colourants: *β*-Carotene (**1.1**), boron-dipyrromethene (BODIPY, **1.2**) and copper(II) phthalocyanine (**1.3**).

1.2. History of Indigo

Indigo (**1.5**) is a famous organic dye widely used in a variety of textile and materials applications. It is best known as the "blue dye" in denim jeans, but the practice of using indigo for the colouring of fabrics has been known for 4000 years in Asia, Europe and the Americas.[12] Indigo was originally obtained from a plant source – *Indigofera tinctoria* (India, Java and China) and *Isatis tinctoria* (Europe). The naturally occurring precursor, indican, is a colourless, water-soluble glucoside of indoxyl **1.4**. Enzymatic cleavage of the sugar subunit leads to **1.4**, which upon oxidation in air yields the highly insoluble 2,2′-dimerized product, indigo **1.5**. A 2-3′ coupled product, indirubin (**1.6**), also occurs in a small quantity in the natural process.[13]

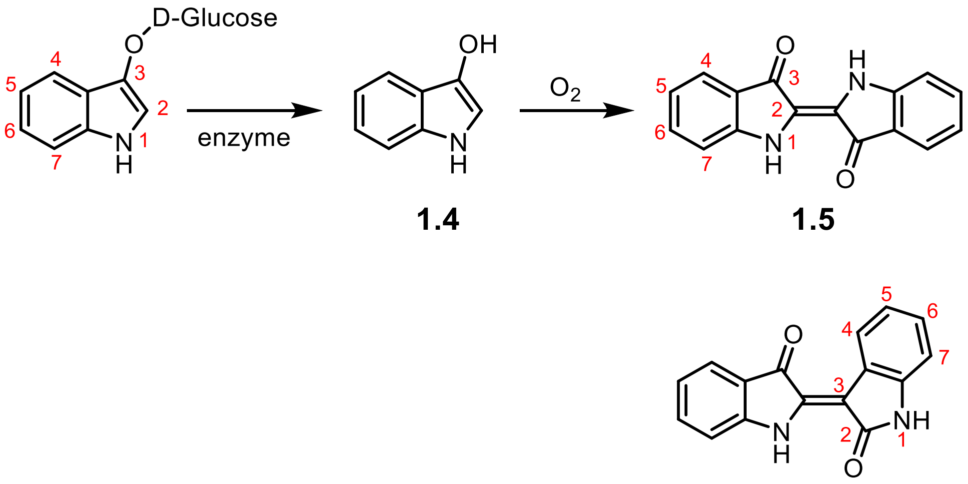

1.4 **1.5** **1.6**

Scheme 1.1 Natural synthesis of indigo (**1.5**) and numbering systems in the indole family.

The first synthetic route to indigo was reported by von Baeyer using precursors of isatin[14] (1878) and *o*-nitrobenzaldehyde[15] (1882). Von Baeyer received the Nobel Prize for his work on the synthesis and elucidation of the constitution of indigo in 1905, however, the correct *trans* configuration was not confirmed until 1928 when the X-ray crystal structure of indigo was solved.[16, 17] **Scheme 1.2** shows the industrial synthesis of indigo modified by Pfleger in 1901, which became the basis of the modern manufacturing procedure for the mass production of indigo.[1] Although indigo-producing plants are still cultivated and practiced in dyeing fabrics, the traditional preparation of indigo has been almost entirely replaced by the synthetic procedure to meet the worldwide demand. In 2011, 50,000 tons of indigo were manufactured and 95% of the dye was used in the denim industry.[18, 19]

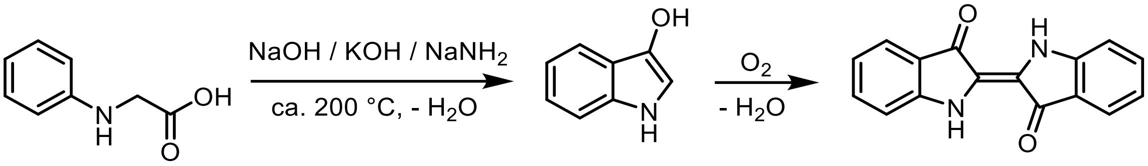

1.4 **1.5**

Scheme 1.2 Pfleger's industrial synthesis of indigo (**1.5**) in 1901.

1.3. Chemical Properties of Indigo

The dyeing process of indigo in fabrics involves a reduction in basic aqueous solutions using reducing agents such as sodium dithionite or zinc.[20, 21] Indigo (**1.5**) is insoluble in water, however, the two-electron and two-proton reduced species, leuco-indigo (**1.7**), is water-soluble. Fabrics are immersed in the yellow solution of **1.7**, and a subsequent re-oxidation converts the dye into its insoluble blue form, **1.5**. Indigo can also undergo oxidation; the two-electron and two-proton oxidized product, dehydroindigo (**1.8**), has been less explored in the literature due to its instability in the ambient environment.[22] However, **1.8** was recently discovered as a key ingredient in Maya Blue and is believed to exist inside pockets of palygorskite clay.[23]

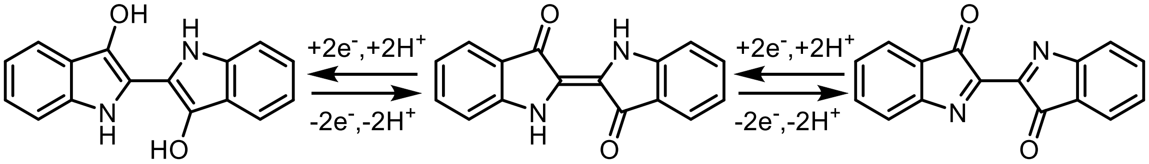

1.7 **1.5** **1.8**

Scheme 1.3 Reduction and oxidation of indigo (**1.5**).

1.4. Electronic Properties of Indigo

Indigo has absorption at λ_{max} = 605 nm (ε = 16580 $L \cdot mol^{-1} \cdot cm^{-1}$) in tetrachloroethane.[24] The dye experiences a bathochromic shift in increasing solvent polarity ranging from 540 nm in the gaseous state[25] and to λ_{max} = 610 nm (ε = 22140 $L \cdot mol^{-1} \cdot cm^{-1}$) in DMF[26]. Despite the long history, the origin of the colour was not understood until the 1960s. Lüttke and co-workers proposed that the main energy absorption of indigo derives from its structural arrangement where electron donor groups (NH) and acceptor groups (C=O) are cross-conjugated through a C=C bridge — the so-called the "H-chromophore".[27] The authors synthesized model compounds in **Figure 1.2** that are containing the central part of the indigo and showed that **1.9** and **1.10** exhibit low energy absorption at 487 nm and 529 nm in tetrachloroethane, respectively.[28] They saw an extension of the π-conjugation on 3-pyrrolidinone rings improves the absorption slightly. Therefore, the peripheral benzene rings of indigo contribute a secondary role in the absorption. Various molecular orbital calculations support this idea.[29-32] The importance of the H-chromophore can be seen in an isomer of indigo: indirubin (**1.6**) possesses both donor groups and acceptor moieties; however, its absorption wavelength is lower at 546 nm in DMF[33] due to having one intramolecular hydrogen bond for cross-conjugation.[25]

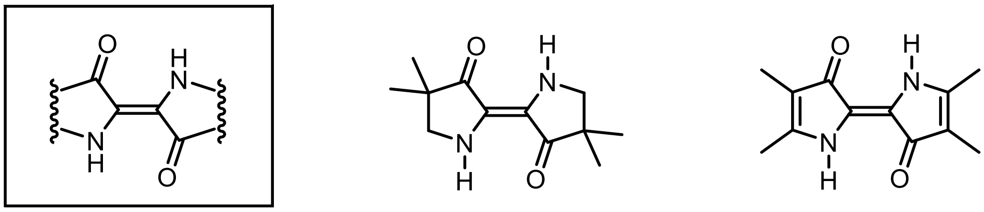

1.9

1.10

Figure 1.2 H-chromophore of indigo (left) and structures of **1.9** and **1.10**.

In contrast to azo dyes[34, 35] and stilbenes[36] which can undergo E/Z photo-isomerization about the central C=C bond, indigo does not isomerize and exists always in the *trans* conformation. Light excitation of indigo leads to an efficient non-radiative decay. The main de-excitation process is an internal conversion from S_1 to S_0 states, with a quantum yield (Φ_{IC}) of 0.991[37] in DMF. Indigo does not fluoresce nor phosphoresce appreciably and has extremely small quantum yields (Φ_F, $\Phi_T < 0.01$).[37, 38] The exceptional photostability is proposed to be induced by an ultrafast intramolecular proton transfer between adjacent carbonyl and amine groups to tautomerize indigo into an enol form in the excited state as described in **Figure 1.3**.[33, 39] However, debates still exist about this de-activation mechanism whether it involves a double-proton transfer, and/or the presence of a back proton transfer reaction, or whether to exclude a rotation about the central C=C bond in the excited state.[40-42] The most common proposal is that indigo undergoes a single proton transfer to form an enol tautomer during an excited state, followed by relaxation to the ground state in ~ 0.1 ns time-window[43, 44]. The existence of an intramolecular single proton transfer is also proposed at (millimolar) higher concentrations by femtosecond visible pump IR spectroscopy.[45]

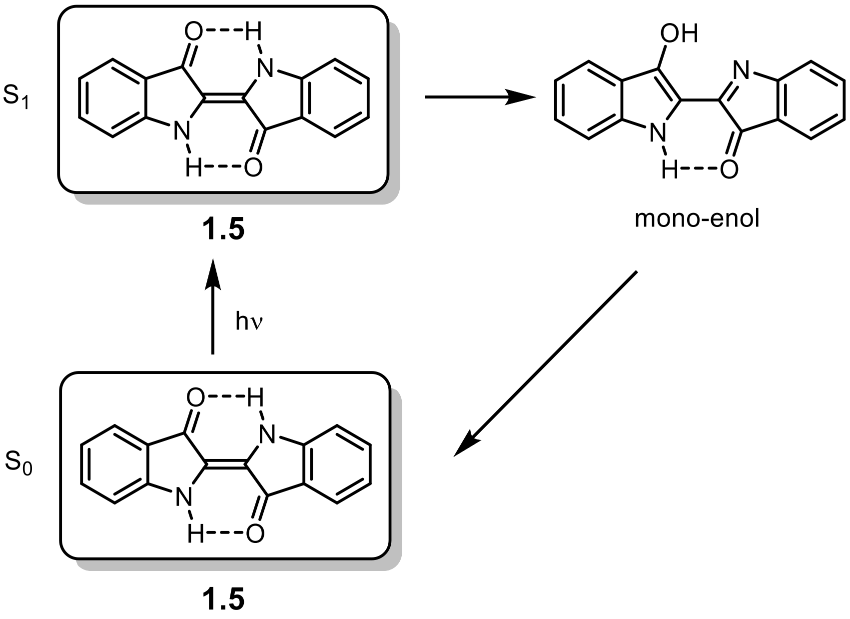

Figure 1.3 Proposed mechanism of excited-state relaxation pathway of indigo (**1.5**) via tautomerization.

1.5. Material Applications of Indigo

Indigo is a flat molecule[46] and as such experiences a strong π-stacking in the solid-state due to its outstanding intramolecular and intermolecular hydrogen bonding capability. In the solution state, indigo aggregates and becomes poorly soluble in water and most common organic solvents.[47, 48] As a result, it has been a significant hurdle to incorporate indigo in materials science applications.

In the past decade, indigo has gained significant interest as an ambipolar organic semiconductor due to its small HOMO-LUMO gap, excellent charge-carrying property derived from its packing motif, and quasi-reversibility of two-electron reduction and two-electron oxidation processes.[48, 49] Indigo has a very high melting point (390 – 392 °C) and displays good thermal stability. Its exceptional resistance towards light, air and water are attractive for utilization of this cheap, readily available dye in organic electronic applications. Indigo slowly reacts with ozone and hydroxyl radicals to decompose into isatin and anthranilic acid[50, 51], however, both compounds are non-toxic and exist in nature. Together with the low toxicity of indigo, it provides another possibility to be fused in bio-compatible materials. Currently, indigo has been explored in organic field-effect transistors (OFETs)[52], organic photodiodes[53], and bulk heterojunction solar cells.[54]

Figure 1.4 shows an example of n-type indigo polymer[55]. Initial installation using highly soluble *tert*-butoxycarbonyl (*t*BOC) *N*-protected indigo **2.1** followed by thermal deprotection has been an effective method to fabricate indigo on devices in addition to vacuum evaporation.[54, 55]

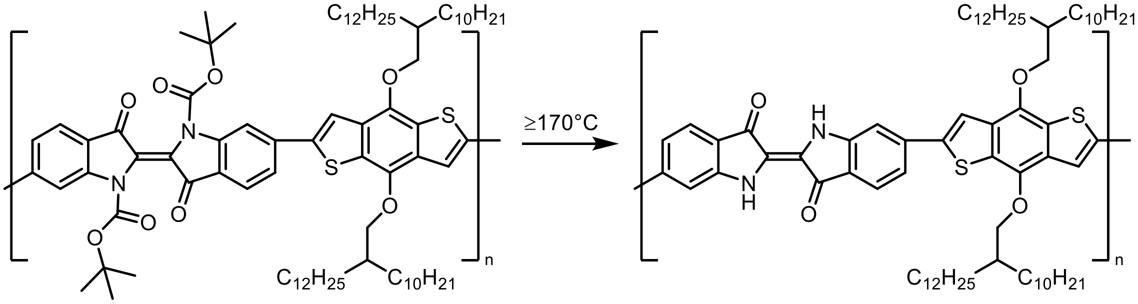

Figure 1.4 Example synthesis of n-type semiconducting indigo **1.5** polymer[55] using a di-*N,N′*-*t*BOC indigo **2.1**.

1.6. Modifications of Indigo

Structural modifications of indigo can improve the solubility, tuning absorption wavelength, degrees of conjugation, spatial orientation, redox properties, and photophysical behaviours. Five main approaches described here include substitution on benzene rings, metal coordination, *N*-substitution, bay annulation and functional group conversion.

DFT calculations of indigo (**1.5**) have shown that electron density of both HOMO and LUMO lies extensively in the H-chromophore.[32, 56, 57] **Figure 1.5** depicts the frontier molecular orbitals of indigo.[58] The electron density on the peripheral benzene ring varies in each π-molecular orbital. For example, indolyl 5- and 7-positions contain high electron density in the HOMO, yet indolyl 4- and 6-positions have a larger contribution in the LUMO. Thus, benzene substitution leads to tuning the HOMO-LUMO gap, which in turn is reflected on the absorption wavelength.

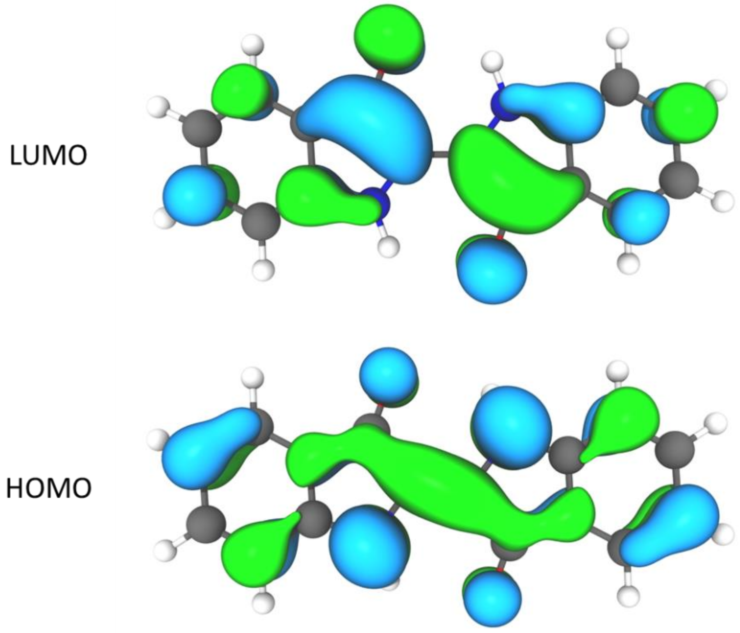

Figure 1.5 Frontier molecular orbitals (MOs) of the indigo (**1.5**). Reproduced from Reference[58].

Substitution on benzene rings has historically been the most widely used modification of indigo. **Figure 1.6** shows two historically important examples of substituted indigo derivatives. Tyrian purple (6,6′-dibromoindigo, **1.11**) is derived from an animal source and has been used in textiles.[59] The compound exhibits similar physical properties to indigo, such as poor solubility and non-luminescence.[33, 49] Bromination at the 6-position decreases both HOMO and LUMO energies at a different degree, which results in a larger bandgap[60] (1.9 eV) than indigo (1.7 eV); thus, **1.11** absorbs at a shorter wavelength at 601 nm in DMF[33]. Both **1.11** and indigo have been actively studied in OFETs[60]; especially, **1.11** serves as a coupling handle at the 6-position in the synthesis of the indigo polymer prior to the *N*-protection in **Figure 1.4**.[54, 55]

Indigo carmine (**1.12**) is obtained from sulfonation at the 5,5′-positions. It absorbs at a higher wavelength at 618 nm in DMF[33] and is used as a water-soluble food additive (E132)[61]. In addition, **1.12** has been explored as an electrode material to store sodium and lithium ions in rechargeable batteries.[62, 63]

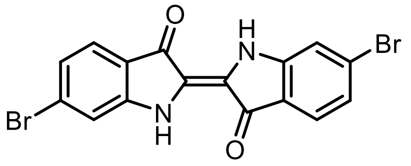

1.11

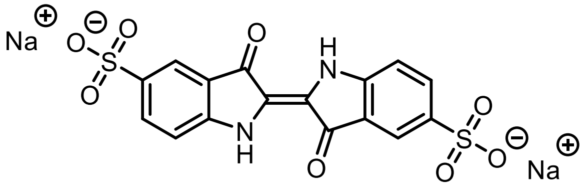

1.12

Figure 1.6 Modification on peripheral benzene rings of indigo: Tyrian purple (**1.11**) and indigo carmine (**1.12**).

Indigo (**1.5**) can coordinate to a metal in a bidentate fashion. The first metal complex is believed to be with Zinc in 1901, yet the structure has not been verified.[64] The first transition metal complexes were prepared by Beck and co-workers in 1989 with Pd and Pt metal centres.[65] Various complexes have been reported with Ru[66, 67], Re[68], Gd[69], Dy[69], Ir[70] metal centres, and indigo has demonstrated non-innocent redox behaviours as a ligand. Indigo had been known to possess two chelation modes: *trans*-(*N,O′*) and *cis*-(*N,N′*) coordination; more recently, the *cis*-(*O,O′*) coordination mode was prepared with a Cr[71] and Ti[72] metal centres.

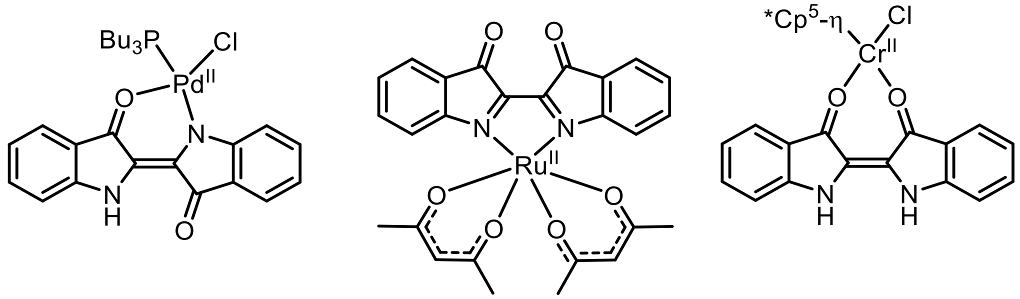

Figure 1.7 Three chelation modes of indigo (**1.5**): *trans*-(*O,N′*) (left), *cis*-(*N,N′*) (centre) and *cis*-(*O,O′*) (right).

N-substitution of indigo with organic substituents introduces steric crowding and weakens π-stacking which, in turn, improves the solubility. Furthermore, a direct modulation in the H-chromophore significantly alters absorption wavelengths. *N,N′*-dimethylindigo (*trans*-**1.13**) exhibits a red-shifted absorption at λ_{max} = 644 nm (benzene)[73]. In contrast, *N,N′*-di-acylindigo (*trans*-**1.14**) absorbs at λ_{max} = 562 nm (toluene)[74] due to weakening of the electron push-pull in the H-chromophore by electron-withdrawing substituents.[75]

Unlike the parent indigo **1.5**, the *N,N′*-substituted derivatives undergo *trans*-to-*cis* isomerization due to the absence of intramolecular hydrogen bonds that provide an efficient route for non-radiative decay to occur. Blue light induces the isomerization and the generated *cis* isomer returns to the original *trans* geometry through heat and/or red-light irradiation as shown in **Scheme 1.4**.[73, 74, 76-79] In 2017, Jacquemin, Hecht et al. synthesized *N*-aryl group-bearing indigo derivatives and observed that the lifetime of the *cis*-isomer can last as long as 408 minutes.[80] They suggested that the di-aryl *N*,*N′*-substituted indigos could function as organic photoswitches.

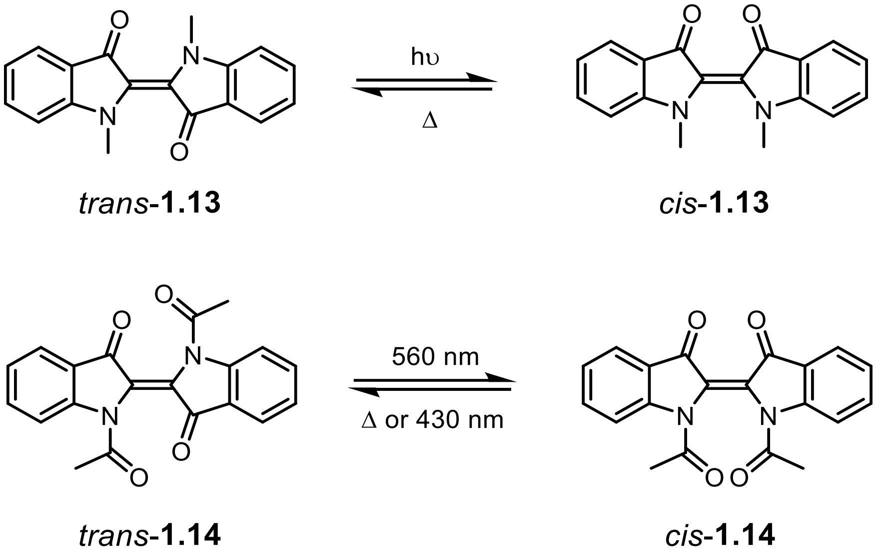

Scheme 1.4 Photo-isomerization of *N*,*N′*-disubstituted indigo derivatives (**1.13** and **1.14**).

Another structural modification involves a reaction in the “bay area” of indigo.[81, 82] **Scheme 1.5** shows a representative reaction of the bay annulation of indigo **1.5** through a condensation using arylacetoyl chloride. The resultant products contain only the partial structure of indigo, yet new interesting photophysical properties can be gained. Bay annulation removes the N-H hydrogen atoms and results in a fixed structure where the *trans*-to-*cis* isomerization is structurally prohibited. Cibalackrot (**1.15**), a doubly bay-annulated indigo, experiences a strong fluorescence as high as at Φ_F = 0.93 in methylcyclohexane since the proton transfer and *trans*-to-*cis* isomerization deactivation channels are absent.[83, 84]

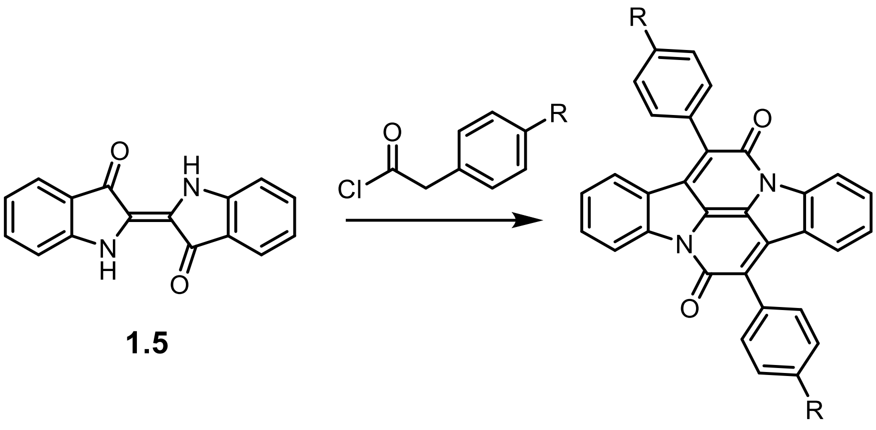

1.5

R = H, **1.15**

Scheme 1.5 Generic procedure of bay annulation of indigo **1.5**.

1.6.1. Indigo Diimines and Monoimines

In 2010, the Hicks group reported the synthesis of indigo diimines (**1.16**) —called Nindigo.[85] This one-pot reaction showed great compatibility with different types of anilines and with *t*-butyl amine. **Scheme 1.6** shows specific arylimine groups that are discussed in this research. Conversion of the carbonyl moiety to imine groups introduces steric crowding, thus Nindigo becomes highly soluble in common organic solvents. Nindigo exhibits a range of absorption wavelengths (580 – 605 nm in DCM). Similar to indigo, Nindigo forms metal complexes with various (non)metal centres such as B[86, 87], Pd[87, 88], Ru[89, 90], Co[91, 92] and serves as a redox non-innocent ligand. Monoimine derivatives (example: **1.17a**) can be easily obtained from the same reaction using lower boiling temperature solvents such as toluene[93] or tetrahydrofuran[94].

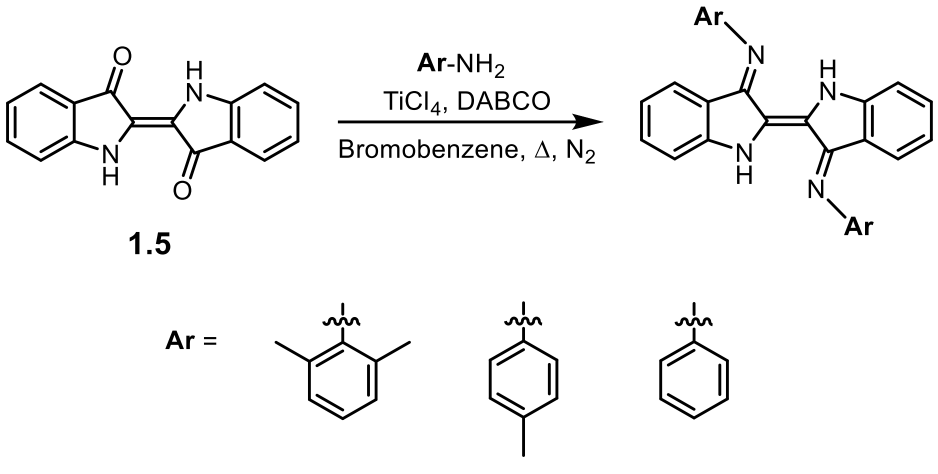

1.5

1.16a **1.16b** **1.16c**

Scheme 1.6 Hicks group’s Nindigo Synthesis (2010).

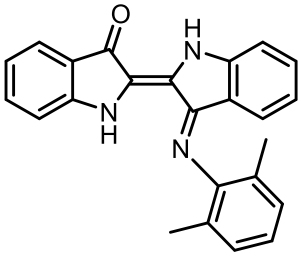

1.17a

1.7. Thesis Objectives

Indigo is a cheap textile material and is one of the most mass-produced synthetic organic dyes today. The intense blue colour and its stability towards surrounding environments such as heat, oxidation in air and photo degradation enables indigo to be a key component in the dying of denim. However, the main applications of indigo have mostly been limited to as a textile pigment due to its poor solubility. Recently, indigo and its derivatives have gained attention in organic electronics due to excellent charge transfer and electron storage abilities. Furthermore, the biocompatibility, the easy availability and the environmental sustainability of indigo render a great potential in biomedical applications to be worthwhile to develop more indigo-like compounds and study their chemistry.

This thesis explores the synthesis and characterization of a rare type of *cis* isomer of indigoids. The introduction of a short carbon chain between the two indole nitrogen atoms permanently locks the indigoid in the *cis* geometry. As a result, a new heterocycle is created on the *cis*-indigoid scaffold. Various functional groups attached to the indole nitrogen atoms may provide access to the direct tuning of the H-chromophore, thus diverse electronic systems of the *cis*-indigoid could be achieved. Since this modification focuses on the indigoid backbone, the approach is applied to both indigo and Nindigo as depicted in **Figure 1.8**.

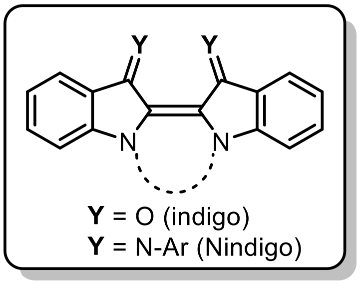

Figure 1.8 General structure of target compounds in this thesis.

Chapter 2 explores the physicochemical properties of previously reported tethered *cis*-indigos. To develop a basic understanding of the influence of the tether, structurally simple organic bridges are chosen. The *cis*-indigos are synthesized and characterized for the investigation of their spatial orientations, photophysical properties, and electrochemical properties.

The initial intention to prepare a π-conjugated tether on *cis*-indigo led unexpectedly to a new class of *cis*-indigoid; this chemistry is the subject of Chapter 3. In the reaction with a quinone, two indigoid molecules are joined together and one acted as a bridging centre. Although the bridging indigoid does not contribute π-conjugation to the core indigo, it is an interesting addition to the library of organic tethers to *cis*-indigo. The role of quinone in the product formation is also investigated by cyclic voltammetry.

The current scaffold of Nindigo is limited to mostly aromatic substituents. Due to the generic structure, the Nindigo derivatives exhibit similar absorption wavelengths and redox profiles. The above two chapters provided the *N*,*N′*-modulation can significantly alter the electronics of the indigoid. Chapter 4 discusses challenges and successful routes to *cis*-Nindigos and *cis*-indigo monoimine derivatives. The physical and chemical properties are compared to their indigo counterpart and the effects of aryl groups are examined. The pK_a of *cis*-Nindigo is also investigated.

Chapter 2. *N,N′*-Bridged Literature *cis*-Indigos

2.1. Introduction to Chapter 2

Chapter 1 provided an overview of the different ways in which the famous pigment, indigo (**1.5**), can be chemically modified. Modification at the indole nitrogen atoms is a well-adopted method in the synthesis of indigo derivatives.[74, 77, 80, 95-97] Addition of functional groups at both nitrogen atoms results in a *trans*-indigo derivative as shown in **Figure 2.1** (a). When the two substituents are connected, the *N*,*N′*-tethered indigo adopts a *cis*-conformation (b). *N*-modifications, in addition to changing the molecular configuration, have the potential to contribute to indigo's electronic structures. **Figure 2.1** shows resonance structures of *N*,*N′*-modified indigos after nitrogen lone pair delocalization in the H-chromophore.

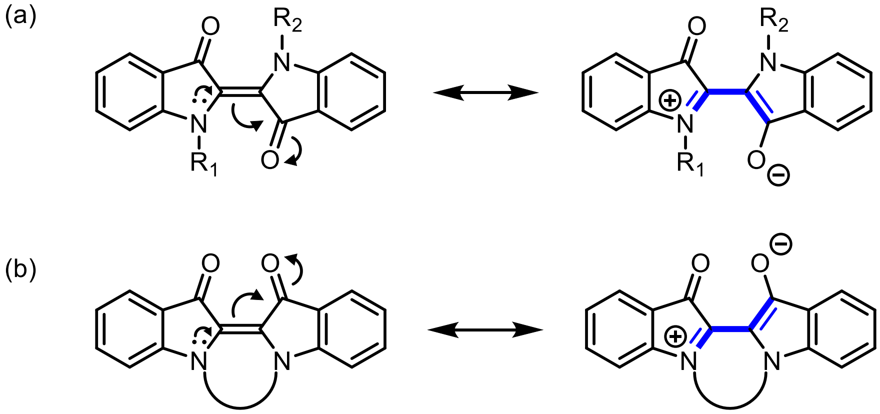

Figure 2.1 Resonance structures after electron push-pull within H-chromophore of (a) *N*,*N′*-modified *trans*-indigo and (b) *N*,*N′*-tethered *cis*-indigo.

The *cis* isomer of the unmodified indigo **1.5** in its neutral state has not been observed. The planar structure held by two intramolecular hydrogen bonds gives indigo excellent photostability. Irradiation of indigo leads predominantly to radiationless de-excitation which is enhanced by an intramolecular proton transfer between the adjacent C=O and amine group.[33, 39] In contrast, *N,N′*-substituted indigos (**Figure 2.1** (a)) exhibit a competitive photo-induced *trans*-to-*cis* isomerization; the highest conversion was reported at $\Phi_{t \rightarrow c} = 0.36$.[80] The stability of the *cis*-isomers varies depending on the size and electronics of the substituent as well as on external factors (i.e. solvents, temperature, water content).[73, 77, 80, 95, 98]

Studies on the rare *cis* geometry of indigo have been explored using singly[98] or doubly *N*-substituted *trans*-indigos under constant irradiation of light. Irradiation with light > 500 nm induces *trans*-to-*cis* isomerization in the solution state. Omote et al. quantitatively isolated the *cis* isomers by precipitation from the irradiated *trans* saturated solutions.[95] However, thermal energy reverts the isomerized indigo back to the original *trans* form upon dissolution in solvents. The *cis*-*N,N′*-substituted indigos exhibit negative photochromism; the *cis* isomer absorbs at higher energy than its *trans* counterpart. Wyman and Zenhausern proposed that the non-planar geometry of the *cis* isomer has to contribute to the weakening of H-chromophore stabilization due to a reduced conjugation in the central C=C bond, supported by higher vibrational indigoid C=O frequencies in the *N,N′*-acylated *cis*-indigos.[99] However, X-ray structures of *N,N′*-*t*BOC indigo[97] (**2.1**) and *N,N′*-Phenyl indigo[80] (**2.2**) have shown a significant twist in the *trans*-indigoid backbone at 45.8° and 31.2°, respectively; yet, these compounds still exhibit the negative photochromism.

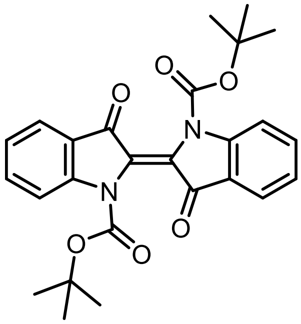

2.1

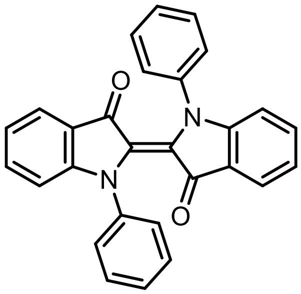

2.2

Insertion of a short organic linker between two indole nitrogen atoms permanently locks indigo in the *cis* geometry. This modification creates a new heterocycle in the *cis*-indigoid scaffold. Keller and co-workers synthesized compounds of this type[100] (**2.3**) that looks promising in biological applications. Limitations do exist in this method, as the longer carbon chains (9 and 10 carbon atoms) in **2.4** permit the corresponding indigo to exist in *trans* configuration, at which they undergo similar photo/thermal isomerization responses as to the untethered *N,N′*-substituted indigos.[77] Up to this date, there are only a handful of *cis*-*N,N′*-tethered indigo compounds reported in the literature.

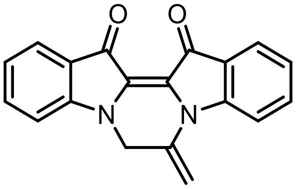

2.3

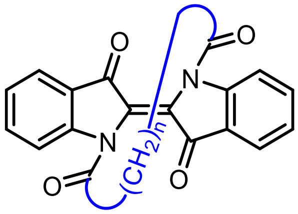

n = 7, 8

2.4

Indigoid compounds have attracted significant attention for their potential in optoelectronic applications.[48, 52-55] Understanding the spatial orientations, photophysical properties, and electrochemical properties derived by different tether systems will provide more insights in designing functional tethers on the indigoid or related indigoid compounds (i.e. Nindigo). The physicochemical characterization of the existing *cis*-fused indigos is generally lacking. Therefore, we chose the less explored, simple bridges from the literature to complete their characterization under controlled experimental conditions in order to investigate the effect of the tether group on the *cis*-indigoid electronic systems. **Figure 2.2** shows the *cis*-indigos used in our investigation.

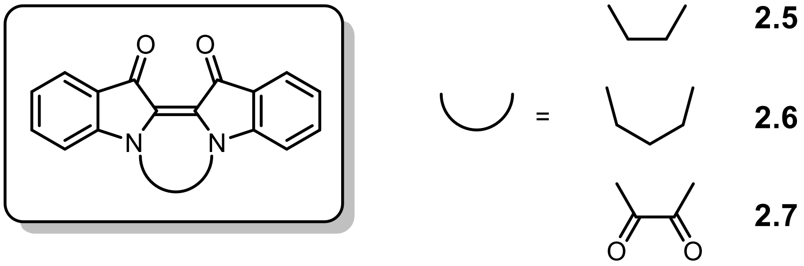

Figure 2.2 *N*,*N'*-tethered literature *cis*-indigos studied in this chapter.

The above-mentioned literature compounds are evaluated using various characterization techniques including NMR, UV-Vis, CV, photophysical methods, and X-ray crystallography in order to determine the influence of the tether on *cis*-indigoid systems.

2.2. Synthesis

The synthesis of *N,N'*-1,2-ethanoindigo (**2.5**) and *N,N'*-1,3-propanoindigo (**2.6**) was previously approached in two methods, by Pummerer and Meininger in 1954[101] and Setsune and co-workers in 1980s[96, 102]. The former reaction involved water as a solvent and sodium hydroxide as a base. Separation of the products required heating in an acidic media around 350 °C and a column separation in pyridine. We decided that this approach is not feasible due to safety concerns. The latter reaction was performed in DMF and used sodium hydride as a base. We adopted Setsune and co-worker's method in consideration of the higher solubility of indigo in organic solvents. However, the development of alternative purification methods was necessary since no information was provided by Setsune et al.

Scheme 2.1 depicts our modified synthesis of **2.5**. In the literature, indigo (**1.5**) was stirred with NaH (2 *eq.*) for 24 hours before the addition of 1,2-dibromoethane (1 *eq.*), then the reaction solution was stirred at 70 °C for 4 hours to create **2.5** in 11.4 % yield.[96] We added extra base because sodium hydride available to us was an approximately 60 % suspension in mineral oil. To ensure full deprotonation of indigo, approximately 3 equivalence was used. In addition, the time for deprotonation was shortened to 30 min since hydrogen evolution visibly decreased after this time. The yield increased from 14 % to 18 % after an extended stirring for two days at room temperature. A large quantity of indigo remained in this reaction. The initial green deprotonated solution gradually changed colour to brighter green overnight. Removal of DMF followed by water work-up gave the crude material. Recrystallization of the crude in hot toluene resulted in a purple powder of **2.5** in 18 % yield.

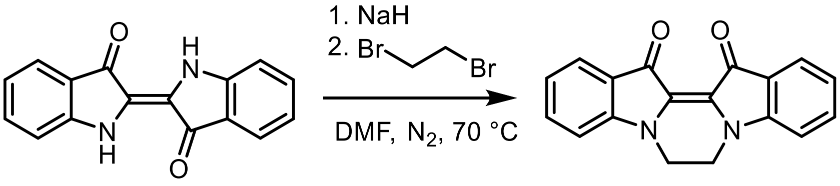

1.5

2.5

18 %

Scheme 2.1 Synthesis of **2.5**.

The synthesis of **2.6** was carried out similarly to **2.5** as shown in **Scheme 2.2**. A solution of deprotonated indigo was stirred with 1,3-dibromopropane at 55 °C overnight.

Interestingly, the initial green solution gradually deepened in colour and became fluorescent green. The reaction solution was quenched by the addition of excess water. Solid matter precipitated. Dissolution of the solid in DCM separated the product from the unreacted indigo. The condensed DCM crude material was further washed with diethyl ether and ethyl acetate to remove the remaining impurities. Recrystallization in toluene results **2.6** in purple powder in 12 % yield. 30 % (151 mg) of indigo was recovered.

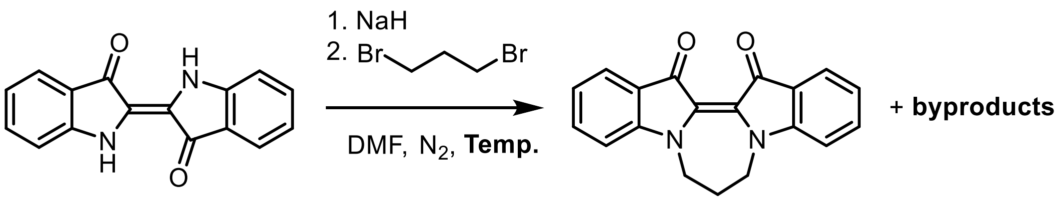

1.5

2.6

Temp. = 4 °C, 4 %
Temp. = 23 °C, 6 %
Temp. = 55 °C, 12 %

Scheme 2.2 Synthesis of **2.6**.

Before reaction optimizations, we noticed that the ^{1}H NMR spectra of the crude reaction contained multiple species. Alumina TLC revealed two intense blue spots. Column chromatography identified the second blue fraction to be **2.6** after the comparison of its ^{1}H NMR spectrum with the reported chemical shifts in the literature. Single crystals were grown from the first blue fraction and X-ray crystallographic analysis revealed the structure of *N*-allylindigo (**2.8**). Both fractions, however, were contaminated with a highly fluorescent impurity. The fluorescent impurity exhibits high affinity to alumina and resulted in a tailing inside the column to overlap with the collected fractions. In order to identify the source of the fluorescence, the loaded column was subjected to a constant washing with diethyl ether and acetonitrile. A portion of a yellow fraction was collected. Single crystal was grown, and X-ray analysis determined the structure of this fluorescent impurity to be **2.9**. Molecule **2.9** contains a cyclized arrangement where one of the indigo carbonyl groups has been intramolecularly attacked by an allyl substituent. A single crystal of **2.9** exists of a racemic mixture where the alcohol group lies above and below the re-arranged backbone. The crystal structures of the two isolated byproducts are shown in **Figure 2.3**. Both **2.8** and **2.9** consist of a *trans*-indigoid backbone, and the indigoid co-planarity was measured at 3.47° and 6.35°, respectively. The yield of the byproducts was not measured due to difficulty in the column separation.

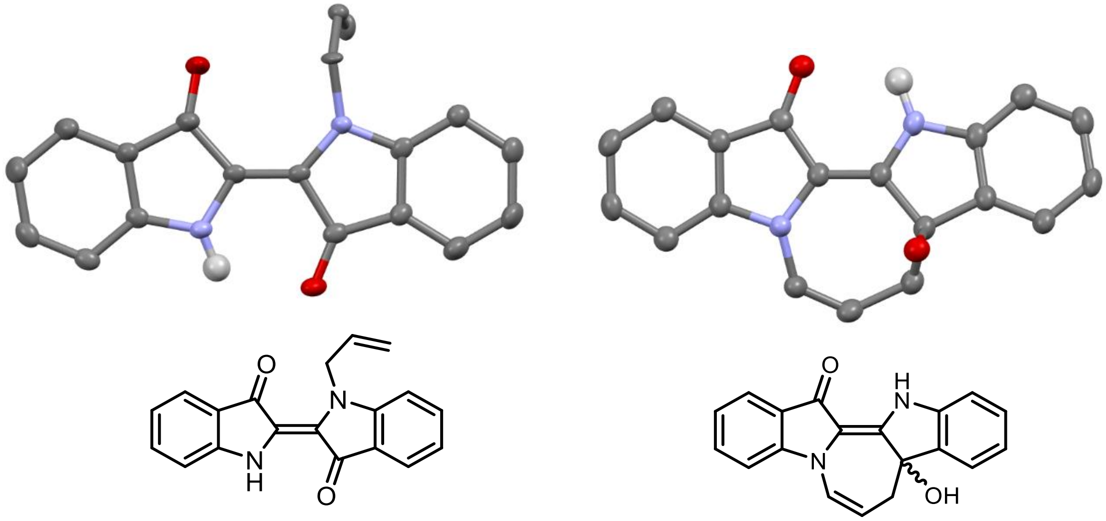

2.8 **2.9**

Figure 2.3 X-ray structures of the byproducts (**2.8** and **2.9**) obtained in **Scheme 2.2**. Hydrogen atoms except -NH are omitted for clarity. Thermal ellipsoids represented at 50%.

The product(s) distribution in the synthesis of **2.6** (**Scheme 2.2**) was affected by the reaction temperature. **2.8** is the most abundant product when the reaction was performed at a lower temperature (6 °C). At higher temperatures, **2.6** becomes the major product. **Figure 2.4** shows ^{1}H NMR spectra comparison of the crude mixtures obtained at different reaction temperatures in comparison to clean **2.8** and **2.6** references. The integration ratio of **2.6** relative to mono-allylated **2.8** increased at higher temperatures. The third reaction spectrum (55 °C) has gone through an additional ether washing, however is still included since **2.8** is poorly soluble in diethyl ether.

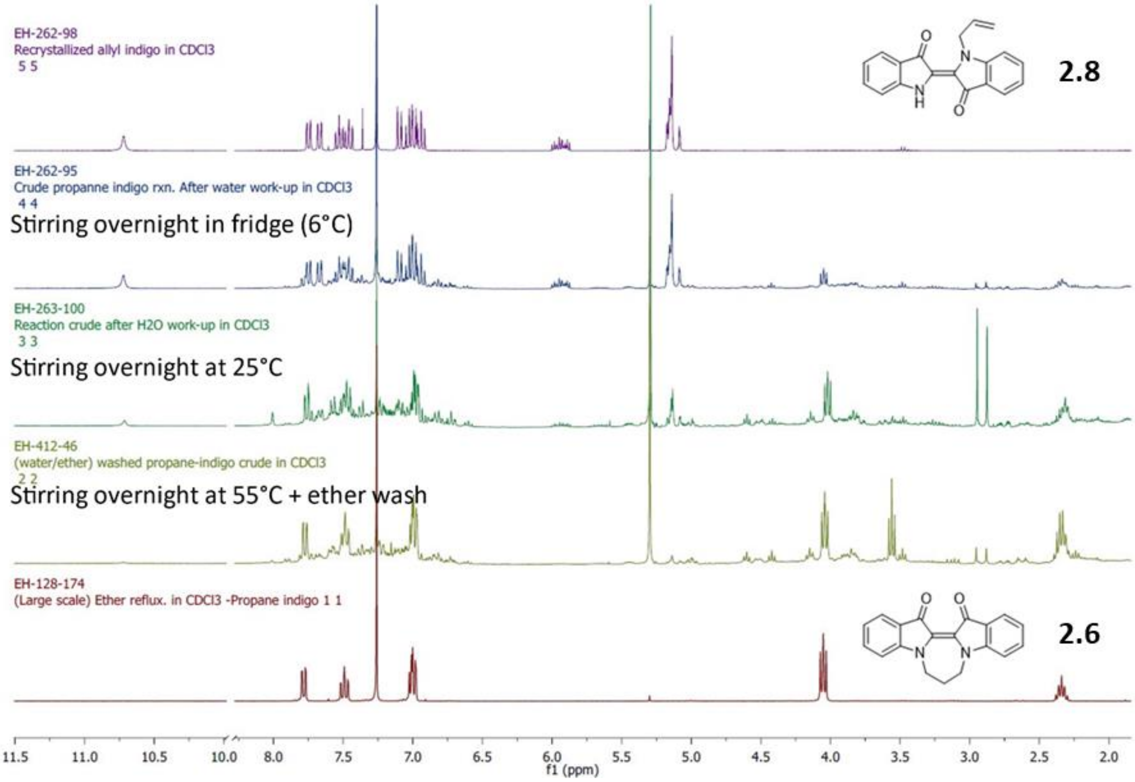

Figure 2.4 ^{1}H NMR spectral comparison of reaction mixtures obtained at varying temperatures in the synthesis of **2.6**.

Interestingly, a similar set of byproducts has been reported in the literature. Keller and co-workers investigated a reaction of deprotonated indigo with an allyl bromide in the presence of caesium carbonate.[103] **Scheme 2.3** shows the literature conditions. **2.8** was formed within 5 seconds after the introduction of the allyl bromide. A complete conversion into a new product (**2.10**) was reported after stirring the reaction solution for 1 hour. The structure of **2.10** is analogous to **2.9** where a *trans*-indigo is intramolecularly tethered between the indole nitrogen atom and the 3-position on the opposite indole by a propene bridge. This new **2.10** contains an additional allyl group at the indole nitrogen atom and was also noted to be highly fluorescent. The similar reaction outcome in our reaction setting as to Keller and co-workers synthesis led us to suspect an *in-situ* formation of allyl bromide from 1,3-dibromopropane. Thus, the decreased proton integration of **2.8** observed in **Figure 2.4** could be explained by an accelerated conversion into the fluorescent **2.9** at a higher reaction temperature.

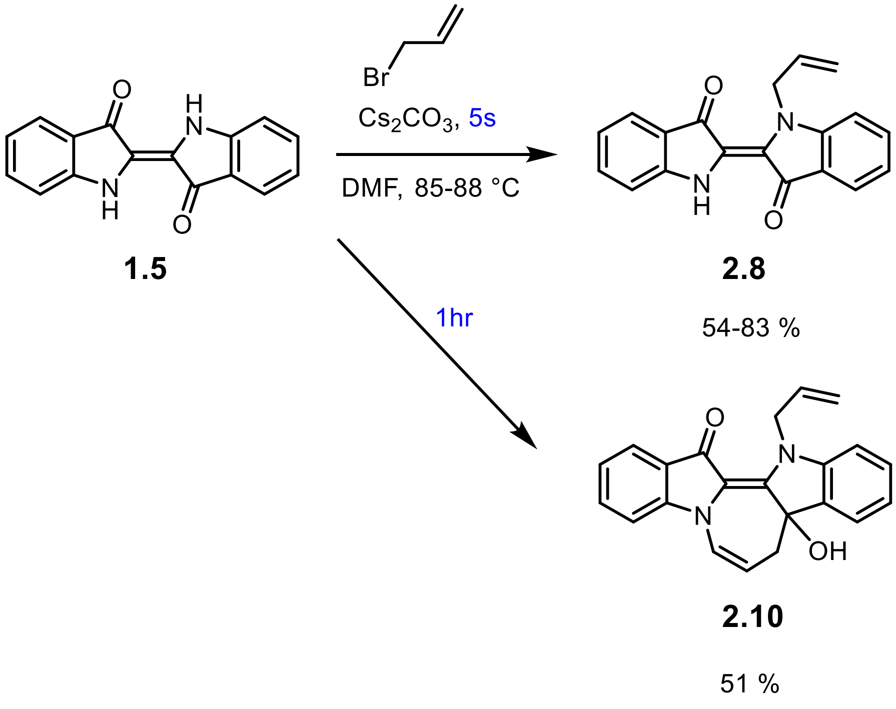

Scheme 2.3 Literature synthesis of **2.8** and **2.10**.

Scheme 2.4 shows a proposed reaction pathway in the synthesis of **2.6**. An elimination occurs at the C-2 atom of 1,3-dibromopropane to give allyl bromide. It is possible that both the deprotonated indigo and the hydride could act as a base. The acidity of indigo has been estimated to be pK_{a1} = 8.0 and pK_{a2} = 12.7 from an extrapolation of mono- and multiple sulfonated indigo derivatives in water.[104] In comparison, a hydride is a much stronger base (pK_a ~36, measured from H_2) than the deprotonated indigo. After deprotonation and elimination to form allyl bromide, the deprotonated indigo can undergo a substitution reaction at the indole nitrogen atom. Further deprotonation at the methylene carbon of the *N*-allyl group would produce an allyl anion (resonance stabilized) which then undergoes cyclization at the indigo carbonyl to form a 7-membered ring.

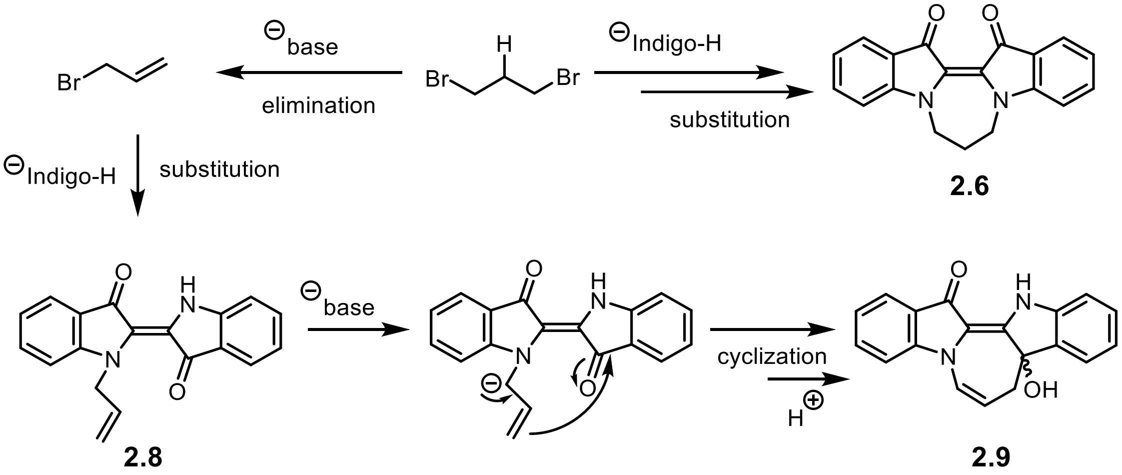

Scheme 2.4 Proposed mechanism for **Scheme 2.2**

Oxalylindigo (**2.7**) was prepared via the literature procedure reported in 1960.[99] Recrystallization from hot nitrobenzene yielded the clean product in 78 % yield. **2.7** exhibits poor solubility in all organic solvents including DMSO; its ^{13}C NMR spectrum was collected over 3 days. Two C=O signals are observed at significantly different chemical shifts at 178.44 ppm (indigoid ketone) and 152.17 ppm (oxalyl bridge).

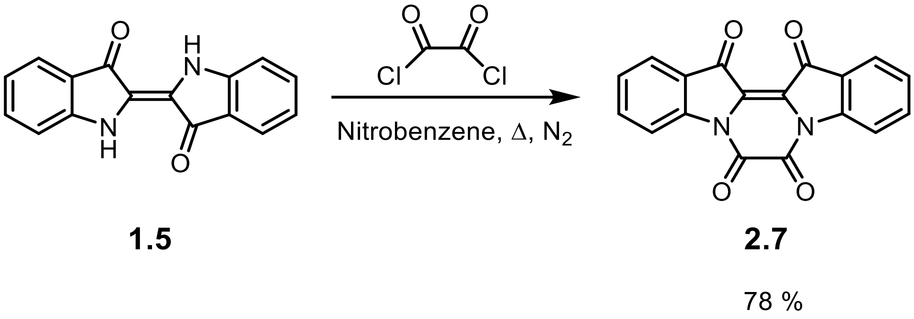

Scheme 2.5 Synthesis of **2.7**.

2.3. X-ray Crystallography

Single X-ray crystals of **2.5** and **2.6** were grown from saturated solutions of dichloromethane. Attempts to grow a single crystal of **2.7** directly from the saturated solutions were unsuccessful due to poor solubility; however, an X-ray grade crystal was obtained from hydrolysis of oxalyl DmPNindigo (**4.6a**, will be discussed in Chapter 4) in suspension solution of dichloromethane with 1M $HCl_{(aq)}$ as shown in **Scheme 2.6**.

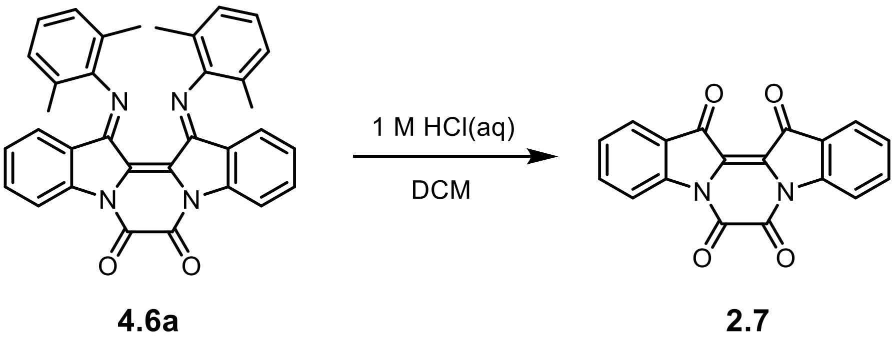

Scheme 2.6 Acid hydrolysis of Nindigo **4.6a** into indigo **2.7**.

The structures of alkyl-tethered **2.5** and **2.6** are presented in **Figure 2.5**; the structure of **2.7** is shown in **Figure 2.6**. The crystal structure of propane-bridged **2.6** was recently reported by Das et al. in 2020.[105] Our data contains the identical unit cell including packing geometries. **Table 2.1** lists a selection of structural data. In the structure of **2.6**, the two halves of the molecule are twisted by 19.78° measured from the angle between the two indole planes with respect to the central C=C bond. The measured angle is similar to that are observed in sterically crowded *N*,*N′*-dimethylindigo (*trans*-**1.13,** ~26°)[106]. In contrast, ethane-tethered **2.5** shows an almost planar *cis*-indigoid backbone where the twist angle is 3.07°.

Compound **2.7** is of interest as the first *cis*-indigo known in the literature. The possible co-planarity of **2.7** had been discussed with contradictions; Wyman and Zenhausern predicted a non-planar structure based on higher vibrational C=O stretches relative to the parent indigo.[99] Takahashi and co-workers predicted a coplanar structure using similarly found central C=C bond stretches to indigo from Raman spectroscopy.[75] Our crystallographic data revealed that **2.7** owns a planar backbone (<1°) allowing extended conjugation from sp^2 hybridized carbon atoms in the bridge.

The central C=C bond of **2.7** is within error equivalent to the corresponding bond in the parent indigo **1.5** (1.359(2) Å)[46]. In contrast, the two alkyl bridged **2.5** and **2.6** show significantly elongated C=C bond distances. Nonetheless, all observed central distances are longer than a typical Csp^2-Csp^2 length (1.33 Å)[107] found in non-conjugated carbon systems. The longer central bond arises from an effective nitrogen lone pair delocalization on the *cis*-indigo core as described in **Figure 2.1**; ring strain from the newly formed heterocycle affects the *cis*-indigoid co-planarity. This influences the interatomic

C=O···O=C distances to also vary regardless of the electronics of the tether; **2.5** exhibits a longer interatomic distance (3.005(2) Å) than **2.6** (2.935(1) Å). **2.7** shows a similar O···O distance to **2.5** as both compounds consist of a 6-membered ring.

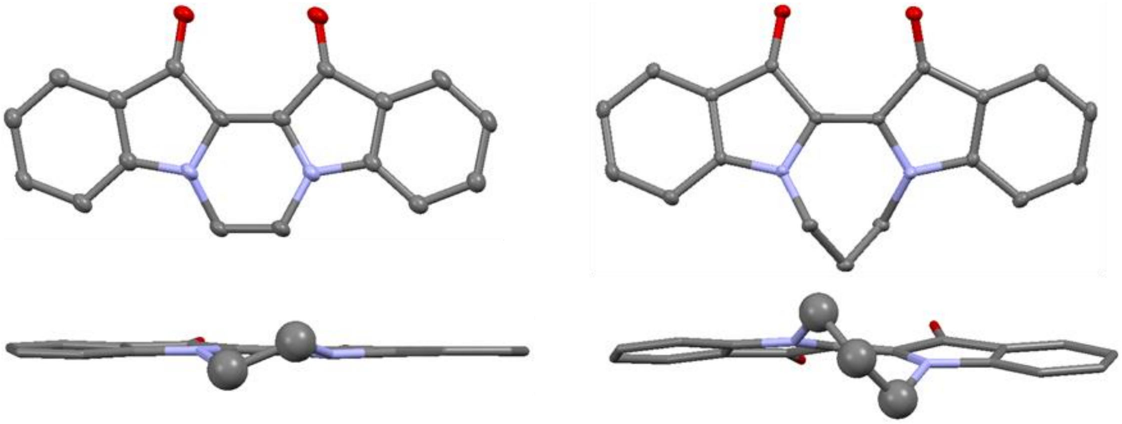

Figure 2.5 X-ray structures of **2.5** (left) and **2.6** (right). Top: front view. Bottom: rotated view. Hydrogen atoms are omitted for clarity. Thermal ellipsoids represented at 50%.

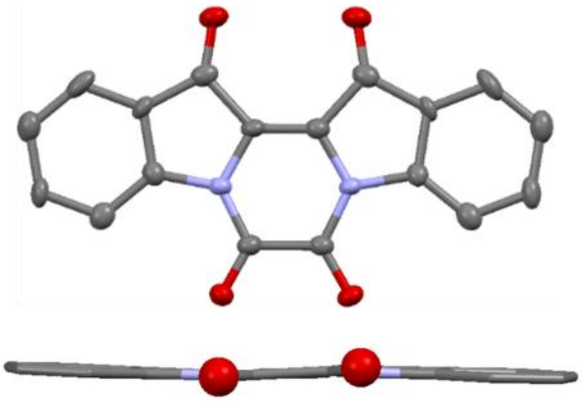

Figure 2.6 X-ray structures of **2.7**. Top: front view. Bottom: rotated view. Hydrogen atoms are omitted for clarity. Thermal ellipsoids represented at 50%.

Table 2.1 Selected distances (Å) and angles (°) in *cis*-indigos.

Parameter	**2.5**	**2.6**	**2.7**
Interatomic O···O (Å)	3.005(2)	2.935(1)	3.00(3)
Central C=C (Å)	1.374(3)	1.372(1)	1.351(7)
Backbone twist (°)	3.07	19.78	0.83

2.4. Cyclic Voltammetry

Figure 2.7 shows the cyclic voltammograms of the *cis*-indigos in dichloromethane. The alkyl-tethered two *cis*-indigos exhibit similar redox behaviours. **2.5** possesses a reversible first reduction at -1.37 V and a quasi-reversible second reduction at -1.62 V. The first oxidation event at +0.57 V is a reversible process; however, this peak becomes irreversible after additional oxidations. The second oxidation at +1.18 V is a $2e^-$ process based on the doubling in intensity compared to the 1st oxidation peak. A 3rd oxidation at +1.33 V is estimated to be a $1e^-$ event because the peak was cut-off due to avoid oxidation of the solvent. For **2.6**, a quasi-reversible reduction occurs at -1.37 V, and a reversible first oxidation was found at +0.43 V. The 1st oxidation peak also becomes irreversible after a second oxidation at +1.13 V. These irreversible oxidations of **2.5** and **2.6** cause a strong decomposition as seen in growing peaks around -0.3 V. An additional decomposition peak was also present at -1.00 V irregardless of switching directions which suggests intrinsic instability in both compounds. Compound **2.7** possesses a reversible first reduction at -0.99 V, and two quasi-reversible reductions at -1.48 V and -2.01 V. No oxidation behaviour could be seen within the dichloromethane window.

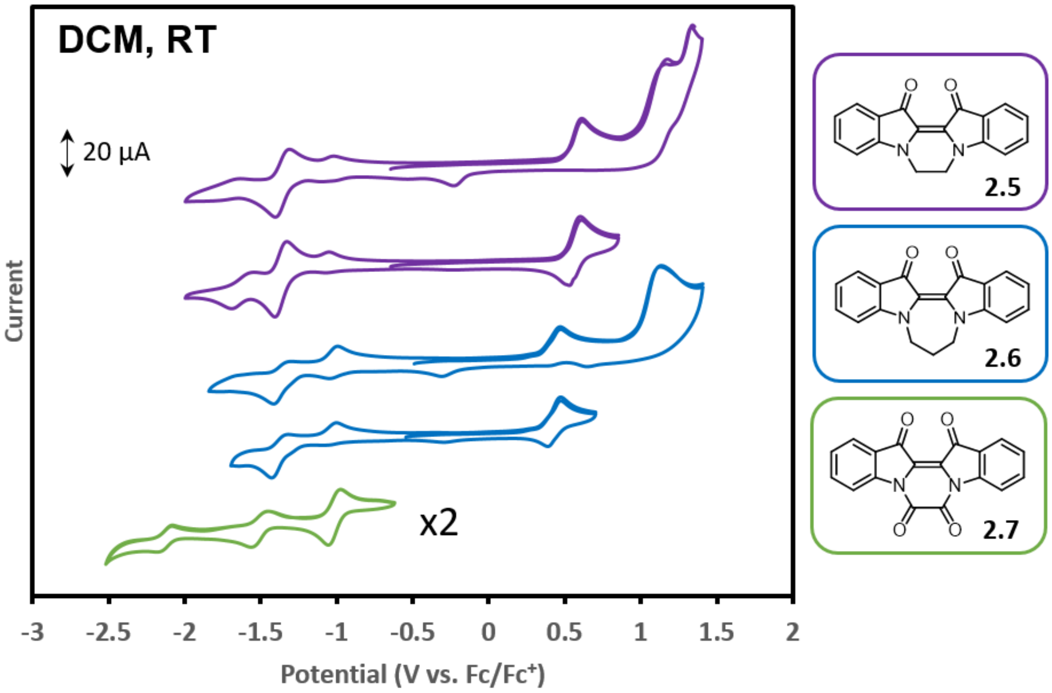

Figure 2.7 Cyclic voltammogram of *cis*-indigos (dichloromethane solution, scan rate 100 mV s^{-1}, referenced to ferrocene (Fc)/ferrocenium (Fc^{+})). 0.1 M NBu_4PF_6 electrolyte was used for **2.5** and **2.6**. 0.1 M NBu_4BF_4 was used for **2.7**.

The alkyl-tethered *cis*-indigos (**2.5** and **2.6**) possess the same first reduction potential which indicates that they have similar LUMO energies. The alkyl tether inductively donates electron density to the indole nitrogen atoms in comparison to an acyl (oxalyl) group which withdraws electron density away from the nitrogen atoms through resonance.[75] Due to this reason, **2.7** contains less electron density in the *cis*-indigo core, therefore, is more prone to reduction; the LUMO energy of **2.7** is lowered compared to both **2.5** and **2.6**. The impact of *N*-substituents was more profound on the oxidation potentials. While the two alkyl tethered *cis*-indigos still exhibit similar first oxidation potentials, the oxidation event of **2.7** could not be observed. This extended positive shift in the oxidation potential of **2.7** in comparison to **2.5** and **2.6** surpasses the observed (+0.38 V) potential shift in the reduction region. Therefore, the HOMO energy of **2.7** is located much lower than alkyl-tethered *cis*-indigos. **Table 2.2** shows the summarized redox potentials.

Table 2.2 Reduction and oxidation potentials (vs. Fc/Fc$^+$) of *cis*-indigos in DCM.

Compound	*Reduction (V)*	*Oxidation (V)*
2.5	-1.37^r, -1.62^q	+0.57^r, +1.18^i, +1.33^i
2.6	-1.37^q	+0.43^r, +1.13^i
2.7	-0.99^r, -1.48^q, -2.01^q	N/A

^{q}quasi-reversible, ^{r}reversible and ^{i}irreversible electron processes.

2.5. Electronic Absorption Spectroscopy

The three *cis*-indigo compounds show absorption wavelengths in the visible region at 585 nm, 608 nm and 429 nm in acetonitrile for **2.5**, **2.6** and **2.7** respectively. **Figure 2.8** displays the absorption spectra in acetonitrile. Similar absorption wavelengths are observed in the solution of dichloromethane. **Table 2.3** shows the absorption wavelengths in both solvents.

The two alkyl-tethered *cis*-indigos exhibit similar absorption maxima as to the parent indigo **1.5** (λ_{max} = 595 nm (ACN)). This absorption is also similar to the absorption observed in *cis*-*N*,*N′*-dimethylindigo (*cis*-**1.13**) (λ_{max} = 588 nm (benzene)), yet still blue-shifted to the *trans*-**1.13** (λ_{max} = 644 nm (benzene)).[73] The electronic contribution from the *N*-substituents is, therefore, the main determinant of the chromophore energy in *cis*-indigos. The same trend applies to **2.7**. The strong electron-withdrawing nature of the oxalyl group weakens the electron-donating ability into the indigo core due to direct conjugation to the nitrogen atoms. Its absorption wavelength (429 nm) is similar to the *cis N,N′*-di-acylindigo (*cis*-**1.14**) (λ_{max} = 435 nm (toluene)), which absorbs at higher energy than the *trans*-**1.14** (λ_{max} = 562 nm (toluene).[74]

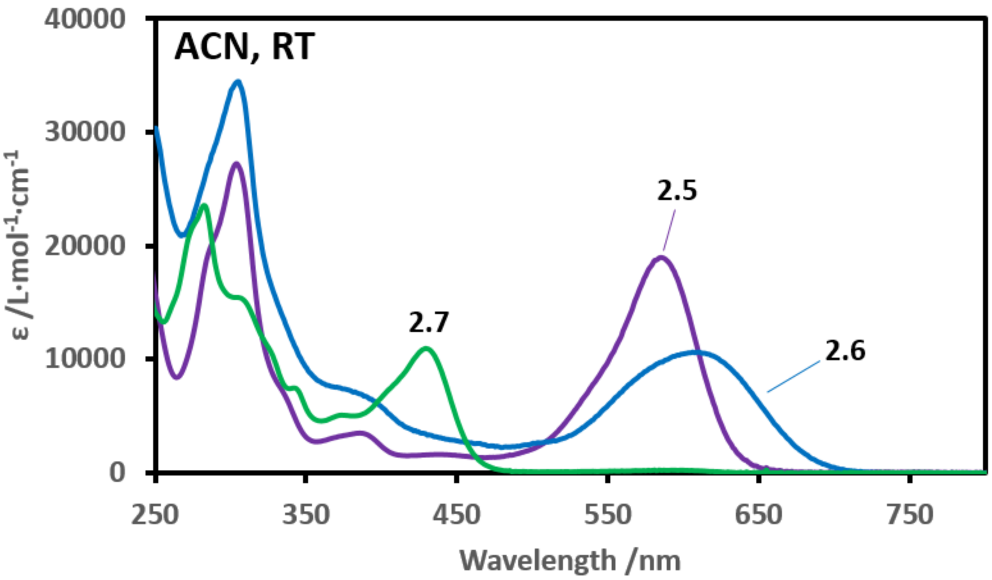

Figure 2.8 UV-Vis absorption spectra of *cis*-indigos in acetonitrile.

Table 2.3 Summary of absorption wavelengths of *cis*-indigos.

Compound	*λ_{max} (nm) (ACN) (ε (L·mol^{-1}·cm^{-1}))*	*λ_{max} (nm) (DCM)*
2.5	585 (19 000)	591
2.6	608 (11 000)	603
2.7	429 (11 000)	429

2.6. Photophysical studies

The photophysical properties of indigo (1.**5**) have been extensively studied in the literature. In contrast to its derivatives, leuco-indigo[33, 108] (**1.7**) and dehydroindigo[22] (**1.8**), indigo is considered non-fluorescent with its extremely low quantum yield ($\Phi_F < 0.01$ in DMF). The main de-excitation pathway is an internal conversion which is aided by an intramolecular proton transfer ($\Phi_{IC} = 0.991$ in DMF). This type of deactivation is absent in the *trans*-*N*,*N′*-disubstituted indigos, and the fluorescence arises in competition with other processes such as *trans*-to-*cis* isomerization, triplet excited state formation, and non-radiative decay. However, the measured fluorescence quantum yield of *trans*-*N*,*N′*-disubstituted indigos are still low: $\Phi_F \sim 0.01$ for di-alkylated species[109] and ~ 0.01 for di-acetyl derivatives[76]. While the -*trans* isomers generally exhibit fluorescence and phosphorescence, the *cis* counterparts are known to be non-luminescent.[76, 110] The bay annulated indigo, cibalackrot (**1.15**), lacks NH protons and owns a rigid *trans* geometry which does not allow the rotation about the central C=C bond. **1.15** experiences a strong fluorescence as high as at $\Phi_F = 0.93$ in methylcyclohexane with the measured singlet lifetime of 6.9 ns.[83]

The *N*,*N′*-tethered systems, similar to **1.15**, lack internal hydrogen bonds, and the structures are fixed in a *cis* geometry. We investigated the excitation behaviours of the synthesized *cis*-indigos using fluorescence spectroscopy. Our data shows that the alkyl-tethered **2.5** and **2.6** exhibit fluorescence, but no emission was detected from **2.7** as in agreement to the literature; intersystem crossing has been attributed to the non-fluorescent behaviour.[110] **Figure 2.9** shows excitation and emission spectra of **2.5** and **2.6** at 20 °C in acetonitrile. The excitation spectra (solid line) matches with the absorption peak shapes in

Figure 2.8 to confirm the purity of the sample. **2.5** shows a fluorescence maximum at 640 nm; the Stokes shift (Δ*ss*) is 1470 cm^{-1}. **2.6** exhibits a weak emission at 704 nm, yet has a greater Stokes shift of 2240 cm^{-1}. Grimme et al. have calculated that the angle twist along with the central C=C bond in *N*-substituted indigo significantly affects the ground state energy of both *trans* and *cis* form.[111] Therefore, the difference in the Stokes shifts could be regarded to different ground state structures as observed in varying co-planarity in the crystal structures of **2.5** (~3°) and **2.6** (~20°). **Table 2.4** shows a summary of the fluorescence data.

We attempted to measure the lifetimes of the singlet excited state by time-resolved fluorescence spectroscopy. However, accurate measurement of the lifetimes was not possible due to non-UV-Vis detectable decomposition of the compounds in dilute acetonitrile solutions. Our preliminary data suggest that the fluorescence lifetime of both compounds are below 0.5 ns.

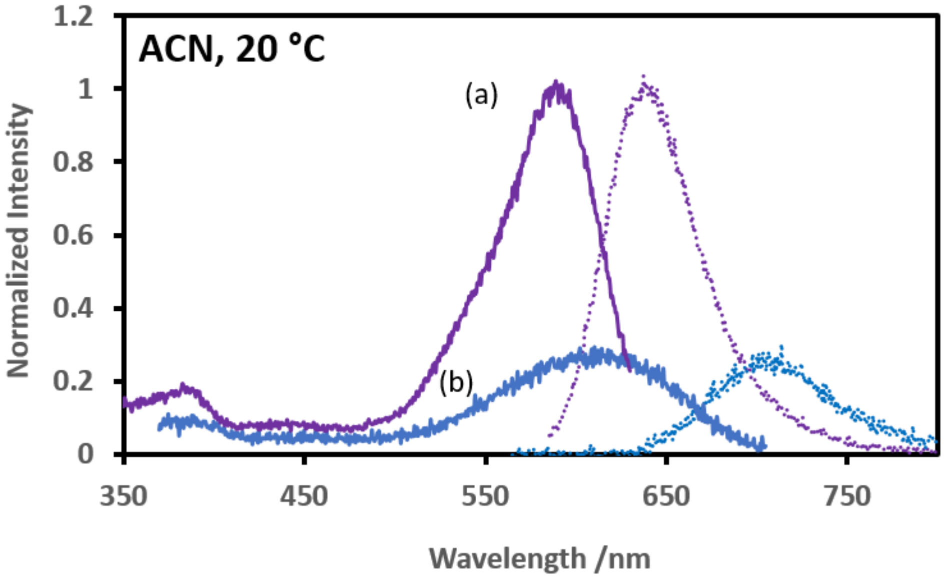

Figure 2.9 Fluorescence excitation (solid line) and emission (dotted line) spectra in acetonitrile at 20 °C: (a) **2.5** (purple colour), 6.3×10^{-6} M solution, excitation was monitored at 650 nm and emission was collected after excitation at 570 nm. (b) **2.6** (blue colour), 1.9×10^{-5} M solution, excitation was monitored at 720 nm and emission was collected after excitation at 550 nm.

Table 2.4 Absorption and emission properties of alkyl-tethered *cis*-indigos in ACN.

Compound	*λ_{abs} (nm)*	*λ_{em}(nm)*	*Δss(cm^{-1})*
2.5	585	640[a]	1470
2.6	608	704[b]	2240

[a]excitation at 570 nm. [b]excitation at 550 nm.

2.7. Conclusion

Indigo is a cheap, easily accessible compound that has shown potential in organic electronics and bioapplications. Insertion of a short carbon tether between two indole nitrogen atoms allows a permanent fixation of indigo in the *cis* geometry. This method provides a rigid structure by the formation of a fused heterocycle. Three literature *cis*-indigos were re-examined in their properties to investigate the effect of the tether on the *cis*-indigoid electronic systems.

Crystal structures of the alkyl-tethered *cis*-indigos, **2.5** and **2.6,** show an enhanced π-conjugation as supported by longer central C=C bond lengths in comparison to the parent indigo due to an inductive electron donation from the alkyl group into the *cis*-indigoid core. The electron-withdrawing oxalyl tether in **2.7** allows a neutral π-conjugation in the indigoid core, yet caused a strong hypsochromic shift in the absorption. The co-planarity in the *cis*-indigoid backbone varies, and was greatly influenced by the ring strain of the newly formed heterocycle; however, its impact on the absorption or redox properties is not observed strongly.

Alkyl-tethered **2.5** and **2.6** match maximum visible-absorption to *N,N′*-substituted *cis*-indigos that are bearing electronically similar *N*-substituents. **2.5** and **2.6** exhibit similar HOMO and LUMO energy levels; the electron-withdrawing oxalyl tether lowers both energy levels in **2.7**. In contrast to non-fluorescent untethered cis-*N,N′*-di-substituted indigos, **2.5** and **2.6** show fluorescence emission derived from the rigid structure. *N,N′*-modification through an organic tether has shown to be effective in modulating the spatial orientations, photophysical properties, and electrochemical properties of indigo.

2.8. Experimental Methods

2.8.1. General Procedure

All reagents used were commercially available. All materials were used without further purification. Dimethylformamide was dried and degassed and kept with 4 Å molecular sieves before use.

1D and 2D NMR spectra collected at room temperature were recorded on a 500 MHz Bruker instruments. NMR data were processed on Topspin 3.6 and MNOVA. FT-IR spectra were collected at room temperature on Perkin Elmer Spectrum Two spectrometer using potassium bromide pellets and processed on Perkin Elmer Spectrum program. Electronic spectra were recorded at room temperature on Agilent 8453 UV-Vis spectrometer in HPLC grade acetonitrile. Accurate masses were obtained by electrospray ionization (positive mode) high-resolution mass spectrometry (HR-MS) using an Ultimate 3000 and Thermo Scientific Exactive Plus Orbitrap LC-MS system. Cyclic voltammetry experiments were performed under argon gas at room temperature in argon sparged non-dry dichloromethane. A Bioanalytical Systems Epsilon voltammetric analyzer was used. Typical electrochemical cells consisted of a three-electrode setup including a glassy carbon working electrode, platinum counter electrode, and silver quasi-reference electrode. All solutions of the analyte (1 mM) and electrolyte (0.1 M $Bu_4N^+PF_6^-$ or $Bu_4N^+BF_4^-$) were referenced against an internal standard (1 mM Fc). X-ray single crystals were analyzed on a Bruker APEX-II CCD diffractometer at 90 K. A Mo source was used.

All X-ray structures of **2.5**, **2.6**, **2.7**, **2.8**, **2.9** were solved by Dr. Corey Sanz.

2.8.2. Photophysical Methods

Cis-indigo **2.5** and **2.6** were further purified by alumina preparative thin layer chromatography before use. Dilute solutions were prepared with HPLC grade acetonitrile, with approximate absorbance of 0.1 at one of the excitation wavelengths. Steady-state fluorescence and time-resolved fluorescence experiments were performed by the Bohne Group at the University of Victoria. Fluorescence emission was measured using a PTI QM-40 fluorimeter. Emission/excitation spectra were collected with the slits set to a 2 nm bandwidth at room temperature of 20 ºC. For **2.5**, the visible-PMT detector was used to collect emission spectra from 390 – 735 nm with an excitation wavelength of 375 nm, and from 585 – 800 nm with an excitation wavelength of 570 nm. The excitation spectra were then collected from 325 – 615 nm monitoring the emission at 630 nm and 335 – 630 nm with an emission wavelength of 650 nm. For compound **2.6**, emission spectra were collected with the visible-PMT detector from 390 – 735 nm and 760 – 800 nm with a single excitation wavelength of 375 nm, and measured from 565 – 800 with an excitation wavelength of 550 nm. The excitation scans were collected from 350 – 665 nm with an emission wavelength of 680 nm, and from 370 – 705 nm with an emission wavelength of 720 nm. Emission scans were performed with compound **2.7** from 390 – 735 nm, exciting at 375 nm, and from 465 – 800 nm, exciting at 450 nm. The ranges over which the spectra were collected was adjusted for each emission wavelength to avoid Rayleigh and Raman scattering. The solvent spectra were collected with the same conditions as each sample in order to subtract a blank from the sample.

An Edinburgh Instruments OB920 single-photon counter (SPC) was used to record time-resolved emission decays. The monochromator at the detector was set to a 16 nm bandwidth and the temperature was maintained at 20 °C with a LAUDA RMS water bath. In order to collect the instrument response function (IRF), the stop rate was set to match that of the decay and the scattering of silica in a dilute LUDOX (Aldrich) solution was recorded at the excitation wavelength. The excitation source on the SPC was an EPL-375 picosecond pulsed diode laser providing an excitation wavelength of 378 nm. The emission of **2.5** was monitored at 640 nm; the emission of compound **2.6** was monitored at 700 nm.

2.8.3. Synthesis

***N,N′*-(1,2-Ethano)indigo** (**2.5**)

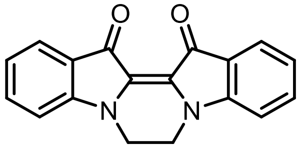

Indigo (505.4 mg, 1.927 mmol) and sodium hydride oil (60 % w/w suspension in mineral oil, 201.3 mg, ~5.0 mmol) were charged in an oven-dried, multi-neck 50 mL round bottom flask. Anhydrous DMF (15 mL) was added via syringe under a nitrogen atmosphere, and the mixture was heated to 70 °C and stirred for 30 min. 1,2-Dibromoethane (0.25 mL; 2.9 mmol) was injected, and the solution was further heated for 18 hrs, then stirred at room temperature for two days. The colour became more bright green. The solvent was removed *in vacuo* in a hot water bath. The dried powder was taken up in DCM and filtered to remove unreacted indigo. DCM residue was washed with neutral H_2O / LiCl (x4). The organic layer was dried over $MgSO_4$, filtered, and dried *in vacuo*. Recrystallization in hot toluene and washing the solids with hexanes yield product as a purple powder (96.7 mg; 18 %). Single X-ray crystals were grown from slow evaporation of a concentrated dichloromethane solution. ^1H NMR (500 MHz, CD_2Cl_2) δ 7.70 (d, 2*H*, $^3J = 7.5$ Hz, H_4), 7.55 – 7.50 (m, 2*H*, H_6), 7.03 (d, 2*H*, $^3J = 8.2$ Hz, H_7), 7.03 – 6.99 (m, 2*H*, H_5), 4.00 (s, 4*H*, H_9). ^{13}C NMR (126 MHz, CD_2Cl_2) δ 180.93 (C_2), 150.33 (C_8), 135.42 (C_6), 124.90 (C_4), 123.11 (C_3), 121.34 (C_5), 109.77 (C_7), 39.86 (C_9). IR (KBr disk, cm^{-1}): 1690s, 1611s, 1565m, 1474s, 1459s, 1380m, 1331sh,m, 1319sh,s, 1307s, 1192s, 1133s, 962s, 740s. UV-Vis (ACN; λ_{max} (nm) (ε ($L \cdot mol^{-1} \cdot cm^{-1}$))): 303 (27 000), 385 (3 000), 585 (19 000). HR-MS: Calcd for $C_{18}H_{12}N_2O_2H^+$ *m/z* = 289.09715, found *m/z* = 289.09724. mp: decomposes to purple gas >290 °C

***N,N′*-(1,3-Propano)indigo** (**2.6**)

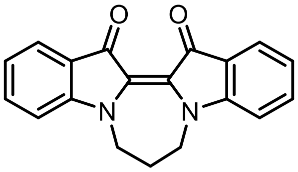

Indigo (499.4 mg, 1.904 mmol) and sodium hydride oil (60 % w/w suspension in mineral oil, 192.8 mg) were charged in an oven-dried, multi-neck 50 mL round bottom flask. Anhydrous DMF (10 mL) was added via syringe under a nitrogen atmosphere, and the mixture was heated to 60 °C and stirred for 25 min. 1,3-Dibromopropane (0.22 mL, 2.158 mmol) was injected, and the solution was further heated for 22 hrs. The colour became teal. The solution was poured into 200 mL ice and the precipitate was filtered and washed with ethyl acetate (100 mL) and ether (100 mL). The washed powder was extracted with DCM (100 mL) in sonication for 20 min. The DCM solution was filtered and the filtrate was dried on *vacuo*. The dried solid was taken up in toluene (10 mL) and recrystallized at reflux. The recrystallized powder was washed with toluene (10 mL), ether (20 mL), ethyl acetate (10 mL) and hexanes (20 mL). The product was isolated as a purple powder (73.7 mg, 13 %). Single x-ray crystals were grown from slow evaporation of concentrated dichloromethane. ^1H NMR (500 MHz, CD_2Cl_2) δ 7.69 (d, 2*H*, ^3J = 7.5 Hz, H_4), 7.54 – 7.47 (m, 2*H*, H_6), 7.04 (d, 2*H*, ^3J = 8.2 Hz, H_7), 7.02 – 6.97 (m, 2*H*, H_5), 4.08 – 3.98 (m, 2*H*, H_9), 2.37 – 2.28 (m, 2*H*, H_{10}). ^{13}C NMR (126 MHz, CD_2Cl_2) δ 182.54 (C_2), 152.67 (C_8), 135.38 (C_6), 130.11

(C_1), 124.87 (C_4), 123.16 (C_3), 121.15 (C_5), 110.30 (C_7), 46.80 (C_9), 26.33 (C_{10}). IR (KBr disk, cm^{-1}): 1698s, 1610s, 1549m, 1473s, 1462sh,s, 1359m, 1321m, 1300s, 1165s, 1147w, 1122s, 902s, 741s. UV-Vis (ACN; λ_{max} (nm) (ε (L·mol^{-1}·cm^{-1}))): 305 (27 000), 384 (3 000), 608 (11 000). HR-MS: Calcd for $C_{19}H_{14}N_2O_2H^+$ *m/z* = 303.11280, found *m/z* = 303.11287. mp: decomposes to purple gas > 300 °C.

***N,N'*-(1,2-Dioxoethano)indigo (oxalylindigo)** (**2.7**)

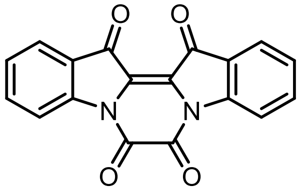

2.7 was prepared according to literature procedure[99]. ^{1}H NMR (500 MHz, DMSO-d$_6$) δ 8.49 (d, ^3J = 8.1 Hz, 2*H*, H_7), 7.97 (d, 2*H*, ^3J = 7.6 Hz, H_4), 7.95 – 7.89 (m, 2*H*, H_6), 7.57 (td, 2*H*, ^3J = 7.5 Hz, ^4J = 0.8 Hz, H_5). ^{13}C NMR (126 MHz, DMSO-d$_6$) δ 178.44 (C_2), 152.17 (C_9), 145.61 (C_8), 137.17 (C_6), 127.46 (C_5), 124.95 (C_4), 123.92 (C_3), 121.47 (C_1), 117.28 (C_7). IR (KBr disk, cm^{-1}): 1739w, 1705sh,s, 1699s, 1694sh,s, 1651s, 1597s, 1460s, 1386s, 1324m, 1301m, 1275w, 1195s, 1175m, 1154w, 1125m, 1087m, 918s, 761s. UV-Vis (ACN; λ_{max} (nm) (ε (L·mol^{-1}·cm^{-1}))): 282 (24 000), 374 (6 000), 429 (11 000). HR-MS: Calcd for $C_{18}H_8N_2O_2H^+$ *m/z* = 317.05568, found *m/z* = 317.05568. mp: decomposes to purple gas >290 °C.

Chapter 3. Dimeric *cis*-Indigoids

Parts of this work have been published in ***Org. Biomol. Chem.***, 2020,**18**, 5838-5842.[112]

3.1. Background

The effect of simple bridges on *cis*-indigoid systems was explored in Chapter 2. We were also interested in expanding the bridge moiety into more complex structures. The synthesis of *N,N′*-tethered *cis*-indigos has been seldomly discussed in the literature. In the 1940s Pummerer and co-workers explored 1,4-cycloaddition of dehydroindigo (**1.8**) with various dienophiles such as styrene, safrole and methyl acrylate, etc. as shown in **Scheme 3.1**.[113, 114] The reactivity of **1.8** towards dienophiles varies and often requires heat and pressure to achieve the product formation; yet, the reaction with styrene readily undergoes at the room temperature.[47, 115] Initially, we intended to explore the cycloaddition method; however, this approach was challenged due to the known instability of **1.8**. As the literature noted, **1.8** is readily reduced back to parent indigo (**1.5**) even during recrystallization, and an inseparable impurity was remained in the oxidation of **1.5** using Br_2[116].[22]

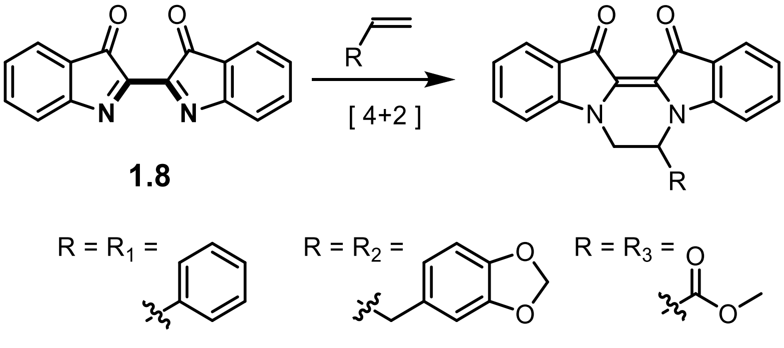

Scheme 3.1 Reported cycloaddition reactions on dehydroindigo (**1.8**).

In the search for functional organic tethers, we found a rare example of a *cis*-indigo featuring a π-conjugation in the bridge. **Scheme 3.2** depicts the literature synthesis of *N,N′*-(2,3-naphthoquinono)indigo (**3.1**) by Setsune et al.[96] Indigo **1.5** was deprotonated with NaH (2 *eq*.) in DMF and stirred for 24 hours, then stirred for an additional 24 hours after the addition of 2,3-dibromo-1,4-naphthoquinone (Br_2NQ) (1 *eq*.). Setsune and co-workers did not mention the purification methods. Characterization of **3.1** was accompanied by melting point, MS, absorption wavelength, IR and ^1H NMR spectroscopy but without presentation of any spectral data. In particular, the description of the ^1H NMR spectrum only presented a broad range of chemical shifts with no detailed information. We intended to complete the characterization of this literature compound in the hope to understand the effect of a complex tether on *cis*-indigoid systems. However, our attempt led unexpectedly to a new class of *cis*-indigoid structure type. From there, we were able to develop a new method to synthesize dimeric *cis*-indigos in presence of a base and a quinone. This chapter investigates the synthesis and characterization of newly discovered dimeric *cis*-indigos.

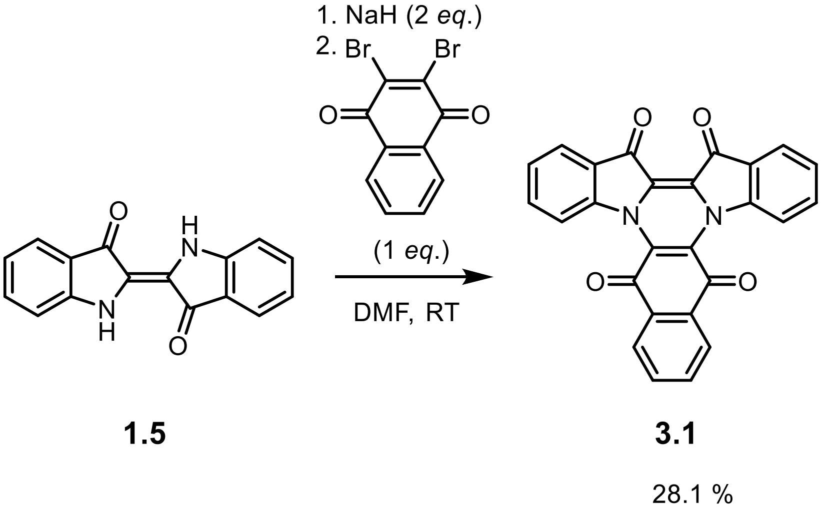

Scheme 3.2 Literature procedure of **3.1**.

3.2. Synthesis

Scheme 3.3 shows our modified version of Setsune and co-workers' procedure. The sodium hydride available to us was an approximately 60 % suspension in mineral oil. Therefore, an excess amount (2.6 *eq.*) was added to indigo **1.5** to ensure complete deprotonation. Stirring with base was only done for 25 minutes since gas evolution was visibly reduced after this time. The addition of bromanil instantly turned the green solution to brown. The mixture solution gradually changed red upon stirring overnight. Performing a water work-up followed by a silica gel chromatography separated the product from the impurities, and recrystallization in hexanes / ethyl acetate provided **3.2** as a red powder in 32 % yield. X-ray crystallography confirmed the structure of **3.2** in that a central indigo molecule is connected to a naphthoquinone unit in a structure reminiscent of the literature compound **3.1**. However, the central C–C bond of the middle indigo is a single bond, which is connected to an outer *cis*-indigo via the two indole nitrogens of the latter.

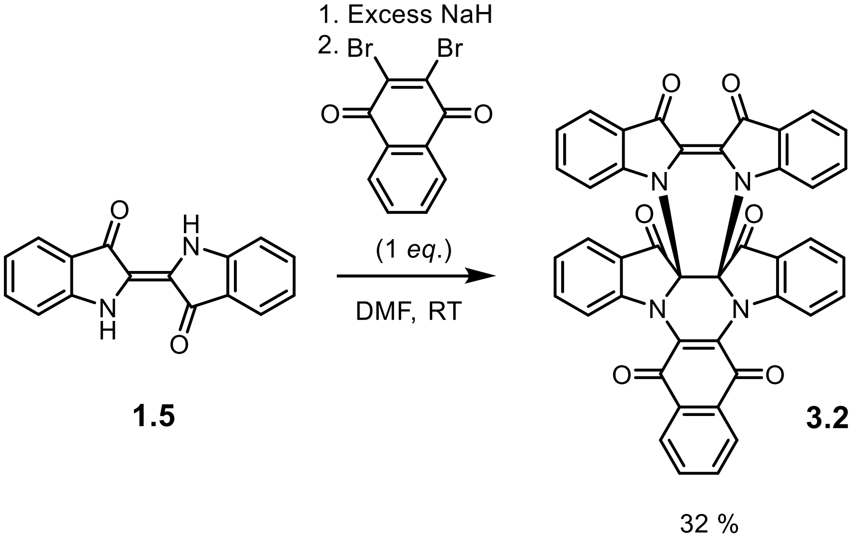

Scheme 3.3 Modified literature procedure for the synthesis of **3.2**.

The unexpected formation of **3.2** prompted us to explore similar reactions using different quinones. We chose bromanil (tetrabromo-1,4-benzoquinone) as a candidate in which mono- and di-substitution with the deprotonated indigo is possible. **Scheme 3.4** shows the possible products we imagined in the reaction with bromanil.

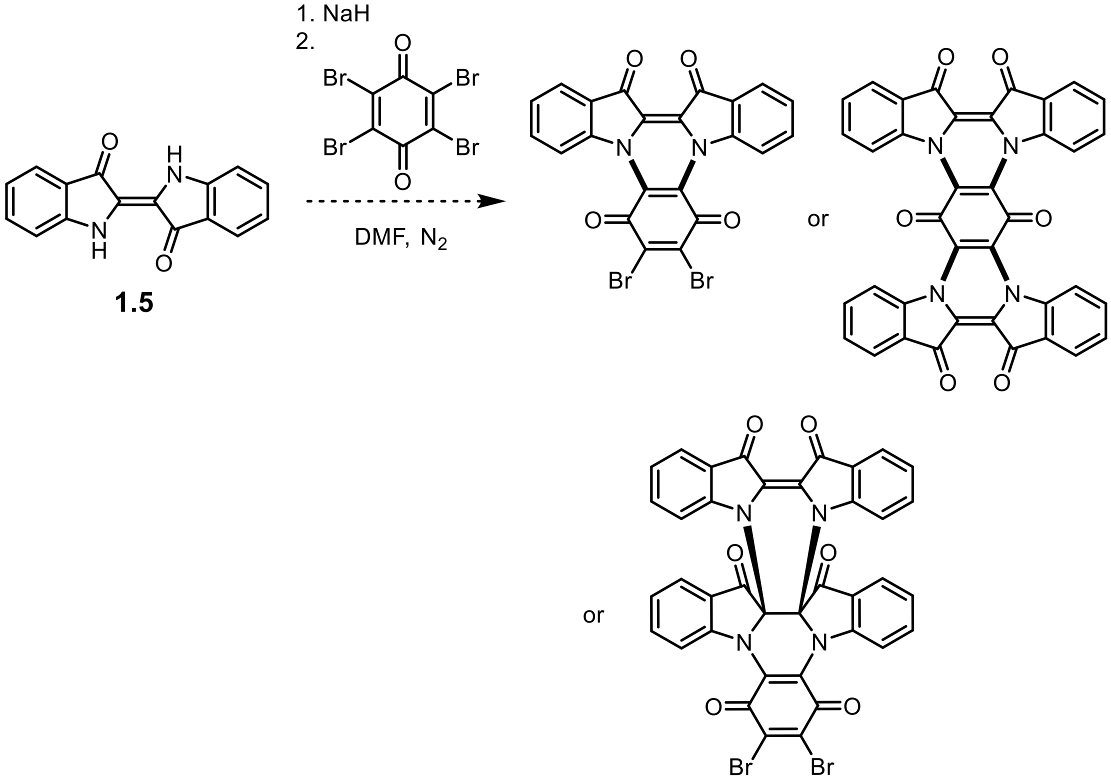

Scheme 3.4 Possible product outcomes in the reaction of deprotonated indigo **1.5** with bromanil in DMF.

In the reaction with bromanil, a similar colour change was observed to the reaction of **3.2**. In addition, heat was generated when bromanil was added into the solution of deprotonated indigo. The ^{1}H NMR of the crude mixture suggested that two species were present. Extraction of the products required several washings with 0.5M $KOH_{(aq)}$ in chloroform in order to destroy most of the unreacted quinone. Column chromatography was initially adopted to isolate the major product. Later we developed a better separation method that required a simple recrystallization in a mixture solvent of acetone / DMF. Most of the major product **3.3** precipitates out by forming a 1:1 adduct with acetone and leaving the minor product **3.4** behind. Purification of the **3.4** was challenging due to the intrinsic small quantity and contamination with the **3.3**. Column chromatography did not afford an analytically clean species because 1) major species **3.3** causes tailing inside the column and overlaps with the desired fraction 2) the obtained fraction of the minor species **3.4** still contained other inseparable contaminants. Additional recrystallization attempts failed to purify **3.4**. Fortunately, single X-ray crystals were grown from a clean saturated solution of **3.3**, and an impure saturated solution of **3.4**. **Scheme 3.5** shows the reaction condition used with bromanil and confirmed structures of isolated products. According to the X-ray analysis, each molecule is composed of two indigoid units; a flat *cis*-indigo and a bridging 2,2′-dihydroindigo. The dihydroindigo units are connected to the backbone *cis*-indigo in the same manner observed in naphthoquinone-containing **3.2**. A structural difference exists in the configurations of the bridging 2,2′-dihydroindigo unit; **3.3** contains a *trans*-2,2′-dihydroindigo and **3.4** possesses a *cis*-2,2′-dihydroindigo. Thus, two compounds are diastereomers.

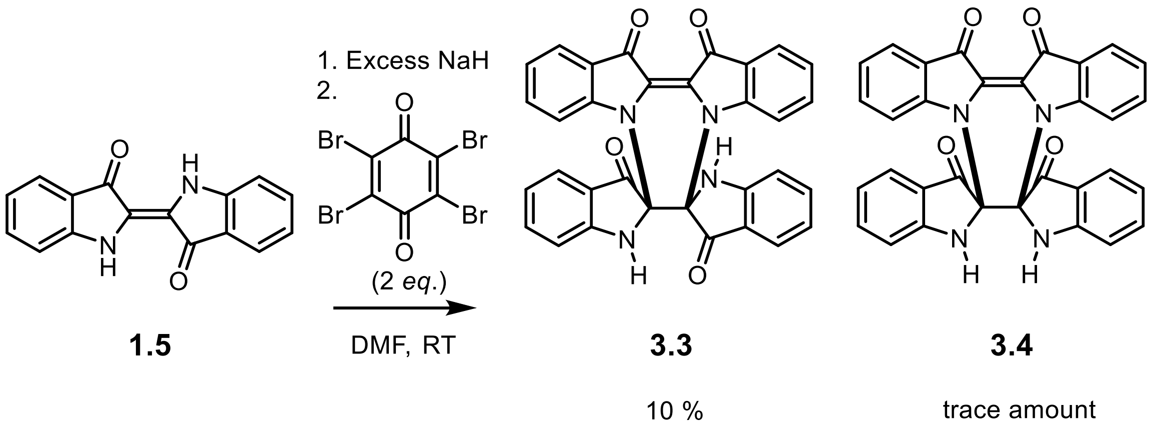

Scheme 3.5 Reaction of deprotonated indigo **1.5** with bromanil in DMF.

During reaction optimizations, we found that 2 *eq*. of bromanil gave the highest yield, where 1 *eq*. produced substantially lower yields and 10 *eq*. led to no products at all. The ratio of the two diastereomers in the optimized reaction is 1 : 0.33 based on the crude ^{1}H NMR integration using -N$\underline{\text{H}}$ singlets for **3.3** and **3.4** respectively. The product ratios were not influenced by light; the same ratio was observed in the control experiment performed in the dark.

We suspected the role of quinone in this reaction was as an oxidant since no quinone incorporation into indigo-based products were observed. We repeated the reaction using chloranil because its oxidation strength is similar to bromanil.[117] Chloranil indeed delivered the same diastereomeric products in a 1 : 0.23 ratio at room temperature. The ratio changed to 1 : 0.05 when performed at 100 °C. The overall yield of the major product **3.3** was lower in the chloranil reaction due to decomposition into isatin, which could be seen in the ^{1}H NMR spectra in the chloranil reactions only. Solvent also plays a critical role in the formation of dimeric *cis*-indigos using chloranil. **Scheme 3.6** shows an attempted reaction in THF. Multiple spots were observed on silica thin layer plates; the products described above could not be detected by ^{1}H NMR. X-ray crystallography confirmed the structure of the most intense fraction to be a re-arrangement product **3.5**. **Figure 3.1** displays the crystal structure of **3.5**. This compound was unique in the reaction in THF. The yield of **3.5** was not recorded, yet the ^{1}H NMR spectrum of the crude suggests this was the most abundant species.

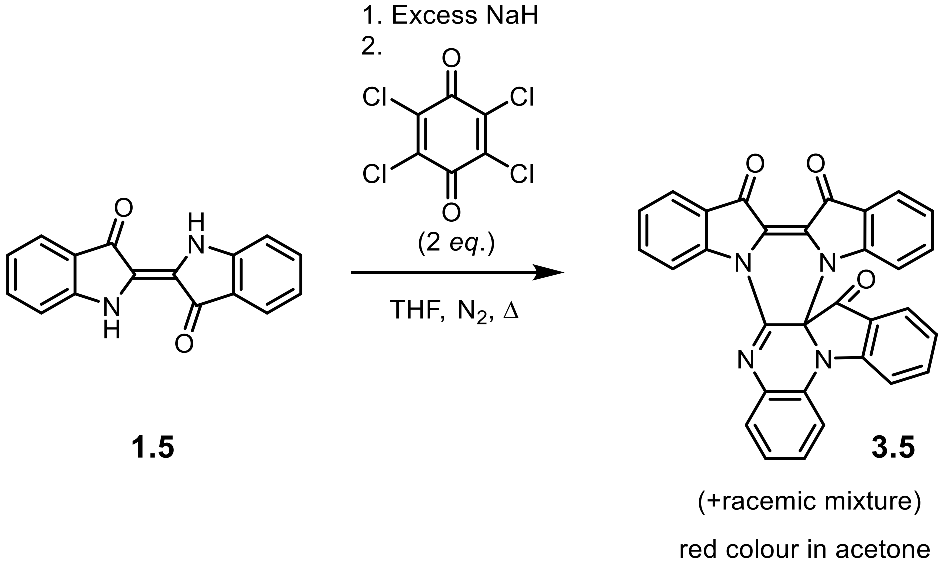

Scheme 3.6 Reaction of deprotonated indigo **1.5** with chloranil in THF.

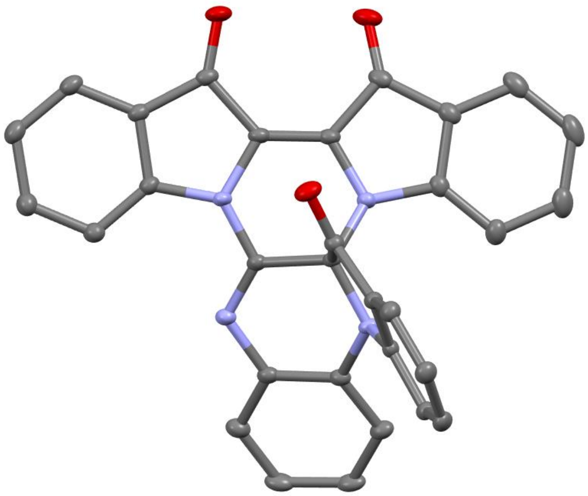

Figure 3.1 X-ray structure of **3.5**. Hydrogen atoms are omitted for clarity. Thermal ellipsoids represented at 50%.

Dimeric indigo **3.3** can be further modified at the indole nitrogen atoms. Treatment with iodomethane in presence of potassium carbonate results in the di-methylated product[118], **3.6**, as shown in **Scheme 3.7**. The yield of this reaction was 20-30 % due to using an impure starting **3.3**.

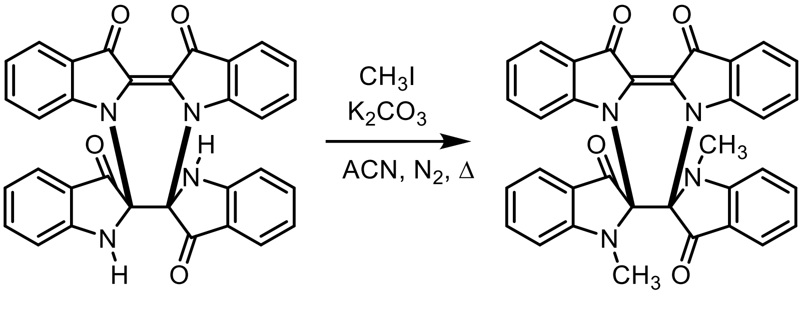

3.3

3.6

20-30 %

Scheme 3.7 Di-methylation of dimeric indigo **3.3**.

3.3. X-ray Crystallography

3.3.1. Structure of 3.2

Two crystallographically independent molecules of **3.2 (A)** and **3.2 (B)** were found in the asymmetric unit. The chemical structures of those two independent molecules are the same, yet they differ in the crystallographic symmetries: **3.2 (A)** possesses C_1 symmetry while **3.2 (B)** has pseudo C_2 symmetry. **Figure 3.2** shows the X-ray structure of **3.2 (B)** as a representative. A central 6-membered ring (C17A, C1A, N1A, C9A, C25A and N2A) adopts a twist-boat shape for **3.2 (A)** and a boat shape for **3.2 (B)**. Both shapes mimic a high energy profile of cyclohexene.[119] A second 6-membered heterocycle is present between the *cis*-2,2′-dihydroindigo and a naphthoquinone. The latter heterocycle also adopts a twist-boat for **3.2 (A)** and a boat conformation for **3.2 (B)**. The discrepancy in the crystal structures is probably due to solid-state packing effects because the solution state ^{1}H NMR spectra suggests a single species even at -90 °C.

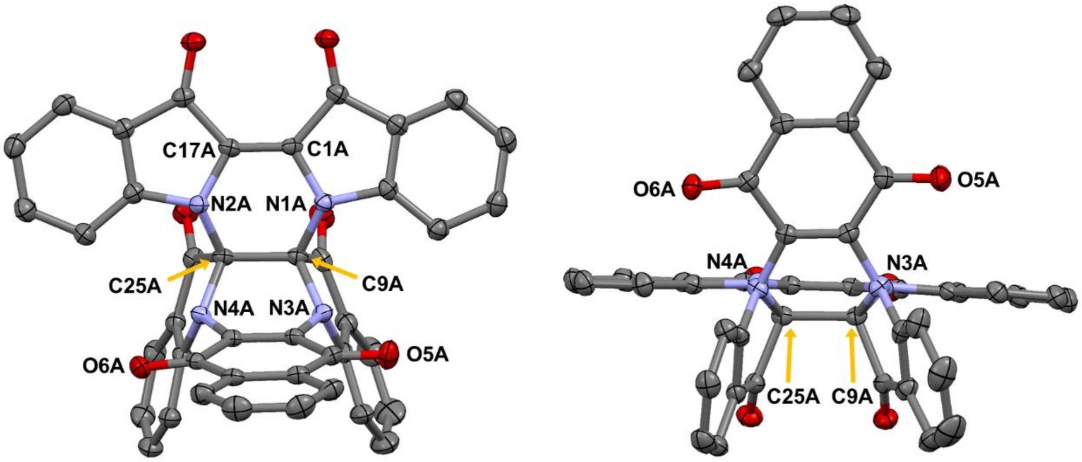

Figure 3.2 X-ray structure of **3.2 (B)**. Left: front view. Right: rotated view. Hydrogen atoms are omitted for clarity. Thermal ellipsoids represented at 50%.

3.3.2. Structures of 3.3 and 3.4

Diastereomers **3.3** and **3.4** share common constituents: a flat *cis*-indigo backbone and a 2,2-dihydroindigo as a *N,N′*-bridging substituent. The bridging dihydroindigo unit contains a central C–C bond based on observed sp^3 carbon atoms. As a result, the bridging indigo is significantly folded, and the π-conjugation is limited to separate indolyl rings. This bridging dihydroindigo moiety is connected *via* its central C–C single bond to the flat *cis*-indigo's indole nitrogen atoms as shown in **Figure 3.3**. In both compounds, the newly formed 6-membered heterocycle (C1, C1', N1', C9', C9 and N1) adopts a half-chair conformation.

Configurations of the bridging 2,2′-dihydroindigo unit resulted in different symmetries in the diastereomers: **3.3** contains a *trans*-2,2′-dihydroindigo and has pseudo C_2 symmetry while **3.4** owns a *cis*-2,2′-dihydroindigo unit and has pseudo C_s symmetry. Crystallographic data elucidated that the geometry of C=O and N-H groups on *trans*-2,2′-dihydroindigo of **3.3** cannot form intramolecular hydrogen bonds as two groups are pointing away from each other.

The central C–C carbon atoms (C9 and C9') in the bridging 2,2′-dihydroindigo are stereogenic. Both dimeric *cis*-indigos each consists of a racemic mixture. For **3.3** indigo, *S*,*S*- and *R*,*R*- configurations at the C9 and C9' carbon atoms are present in the *trans*-2,2′-dihydroindigo fragment. Similarly, a single crystal of **3.4** consists of enantiomers where the chiral C9 and C9' carbon centres adopt configurations of *S,R*- and *R,S*- in the *cis*-2,2′-dihydroindigo unit. However, the latter pair of enantiomers of **3.4** contains a pseudo-internal plane of symmetry, which is a characteristic of a *pseudo*-meso compound; thus, the enantiomeric pair of **3.4** could be interchangeable in the solution state by a ring-flip.

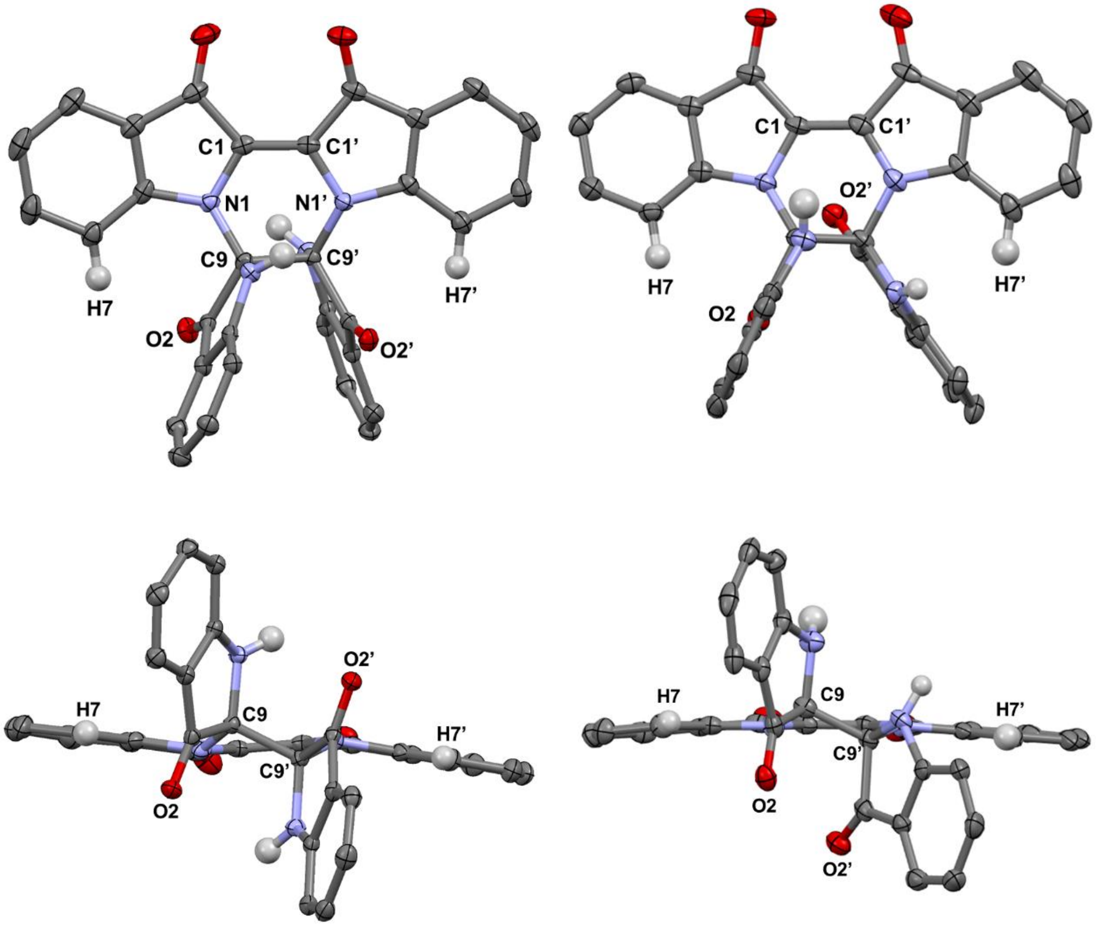

Figure 3.3 X-ray structures of diastereomers of dimeric *cis*-indigos: **3.3** (left) and **3.4** (right). Top: front view. Bottom: rotated view Hydrogen atoms except -N<u>H</u> and H7(H7') hydrogens are omitted for clarity. Thermal ellipsoids represented at 50%.

Three dimeric *cis*-indigos, **3.2**, **3.3** and **3.4**, show typical indigoid central C=C lengths that are observed in the parent indigo **1.5** (1.359(2) Å)[46] and *N*,*N′*-tethered *cis*-indigos in Chapter 2. These dimeric *cis*-indigos can be viewed as an extension of *N*,*N′*-1,2-ethanoindigo (**2.5**) where four hydrogen atoms on the ethane tether are replaced by four heteroatoms. **Table 3.1** shows a selection of structural data in comparison to the **2.5** reference. Three dimeric *cis*-indigos have similar torsion angles between the two indole halves of the nominally planar indigo core. However, the measured interatomic O···O distances do vary among the compared compounds.

The central C–C bond lengths also vary significantly. Notably, the length observed of **3.2 (B)** (1.603(2) Å) is extremely elongated in comparison to a typical Csp^3-Csp^3 length (1.54 Å)[120] in ethane. The diastereomers **3.3** and **3.4** exhibit shorter C–C bond lengths than **3.2** (**A** and **B**) owning to a smaller size of an indigoid substituent. However, despite sharing the same bridging constituent, the observed C–C bond lengths between the **3.3** and **3.4** are significantly different. This difference is not yet understood. Methyl group substitution at the *trans*-2,2′-dihydroindigo unit introduces a steric bulkiness, at which the central C–C bond becomes further elongated from 1.584(2) Å[118] in **3.3** to 1.608(2) Å in **3.6**.

Table 3.1 Selected distances (Å) and angles (°) in dimeric *cis*-indigos in comparison to reference **2.5**.

Parameter	**3.2 (A)**	**3.2 (B)**	**3.3**	**3.4**	**3.6**[a]	**2.5**
Central C=C (Å)	1.351(2)	1.349(2)	1.354(2)	1.357(3)	1.360(2)	1.374(3)
Central C–C (Å)	1.595(2)	1.603(2)	1.584(2)	1.550(3)	1.608(2)	1.528(3)
Backbone twist (°)	4.80	3.86	2.71	7.23	2.64	3.07
Interatomic O···O (Å)	2.921(2)	2.907(2)	2.871(2)	2.897(2)	2.913(2)	3.005(2)

[a] Reproduced from Reference[118].

3.4. UV-Vis Spectroscopy

Three synthesized dimeric *cis*-indigos **3.2**, **3.3** and **3.4** show absorption maxima in the visible region at 514 nm, 534 nm and 541 nm in acetonitrile, respectively. In a more polar solvent (i.e. DMSO), the absorption maxima experience a modest bathochromic shift in accordance with a characteristic of an indigoid compound.[25, 48] **Table 3.2** shows the absorption wavelengths in both solvents. For the latter two diastereomers, **3.3** and **3.4**, the main transition is derived from the flat *cis*-indigo backbone as it has the largest π-conjugation. Modification at the bridging indigoid has a minimal impact, as a dimethyl derivative, **3.6**, exhibits an absorption maximum at 531 nm in ACN and 543 nm in DMSO.[118]

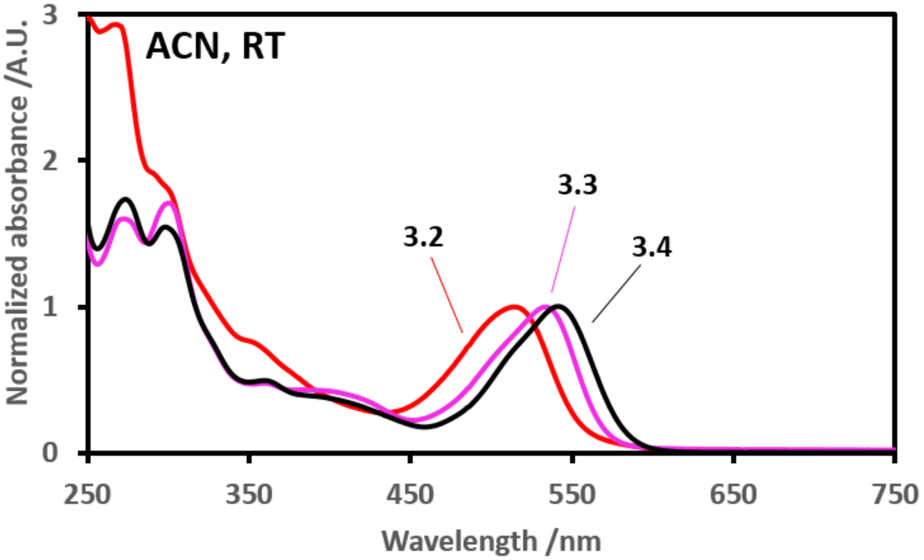

Figure 3.4 UV-Vis absorption spectra of dimeric *cis*-indigos in acetonitrile.

Table 3.2 Absorption wavelengths of dimeric *cis*-indigos.

Compound	*λ_{max} (nm) (ACN)* *(ε ($L \cdot mol^{-1} \cdot cm^{-1}$))*	*λ_{max} (nm)* *(DMSO)*
3.2	514 (14 000)	525
3.3	534 (15 000)	552
3.4	541	557

In comparison to the simple bridges explored in Chapter 2, the indigoid bridge-type on *cis*-indigo exerts a small hypsochromic shift in the maximum absorption compared to the (electronically neutral) alkane bridges on *cis*-indigo: *N*,*N′*-1,2-ethano-indigo (**2.5**) (581 nm) and *N*,*N′*-1,3-propano-indigo (**2.6**) (608 nm), yet absorbs at larger wavelengths than oxalylindigo (**2.7**) (429 nm).

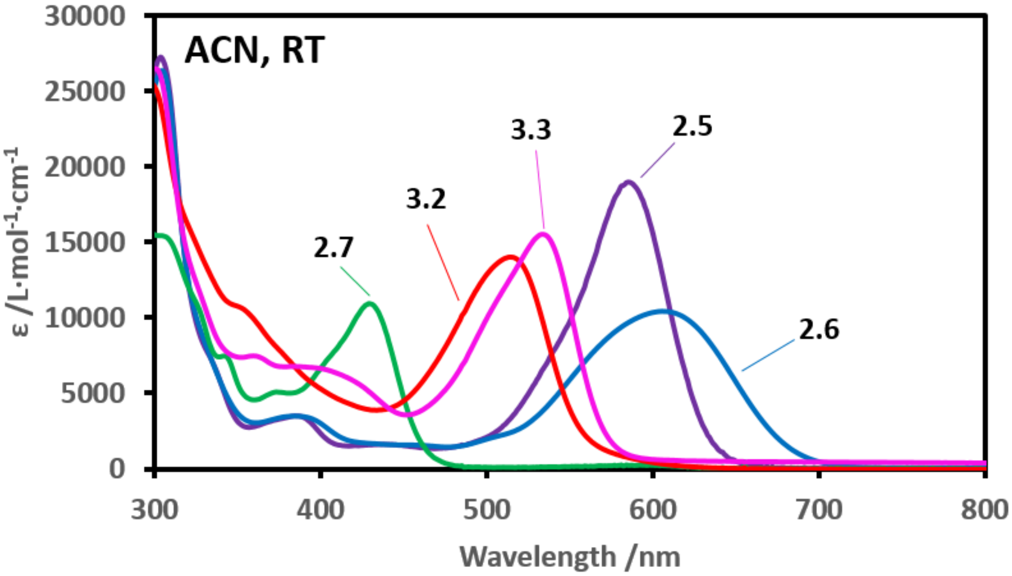

Figure 3.5 UV-Vis absorption spectra of dimeric *cis*-indigos in comparison to Chapter 2 *cis*-indigos in acetonitrile.

3.5. Cyclic Voltammetry

3.5.1. Redox Properties

Figure 3.6 shows the cyclic voltammograms of **3.2** and **3.3** in acetonitrile against ferrocene (Fc)/ferrocenium (Fc^+) internal reference. A CV of **3.4** could not be collected due to a lack of quantity and purity. Naphthoquinone containing-**3.2** undergoes one reversible oxidation at +0.95 V and three quasi-reversible reductions at -0.73 V, -1.25 V and -1.57 V. The decomposition peak at -0.89 V (denoted with *) only appears after the third reduction. The first two quasi-reversible reductions are believed to take place on the naphthoquinone moiety. A control experiment of a starting quinone (Br_2NQ) showed two reversible reductions at similar potentials and no oxidation activity in the DCM window. The oxidation of the **3.2** likely happens on the *cis*-indigo backbone since the bridging 2,2′-dihydroindigo unit has a reduced π-conjugation. As discussed in Chapter 2, alkyl-tethered **2.5** and **2.6** exhibit reversible oxidation at +0.57 V (DCM) and +0.43 V (DCM), respectively. Although a direct comparison with these potentials cannot be made since the experiments were collected in different solvents, however, three forementioned *cis*-indigos share the same indigoid backbone and exhibit positive oxidation potentials.

Compound **3.3** possesses two irreversible oxidations at +0.91 V, +1.37 V, and one irreversible reduction at -1.24 V followed by a quasi-reversible reduction at -1.40 V. A peak around -2.3 V (denoted with †) is due to cathodic decomposition of acetonitrile.[121] The voltammograms of **3.2** and **3.3** were initially collected in the dark to avoid the potential self-reduction of **3.3**. It has been reported that propane-bridged **2.6** and a derivative of oxalylindigo **2.7** undergo a photo-reduction in presence of triethylamine.[102, 122] Nonetheless, no differences in the redox behaviours were observed in the light. **Table 3.3** shows the summarized redox potentials.

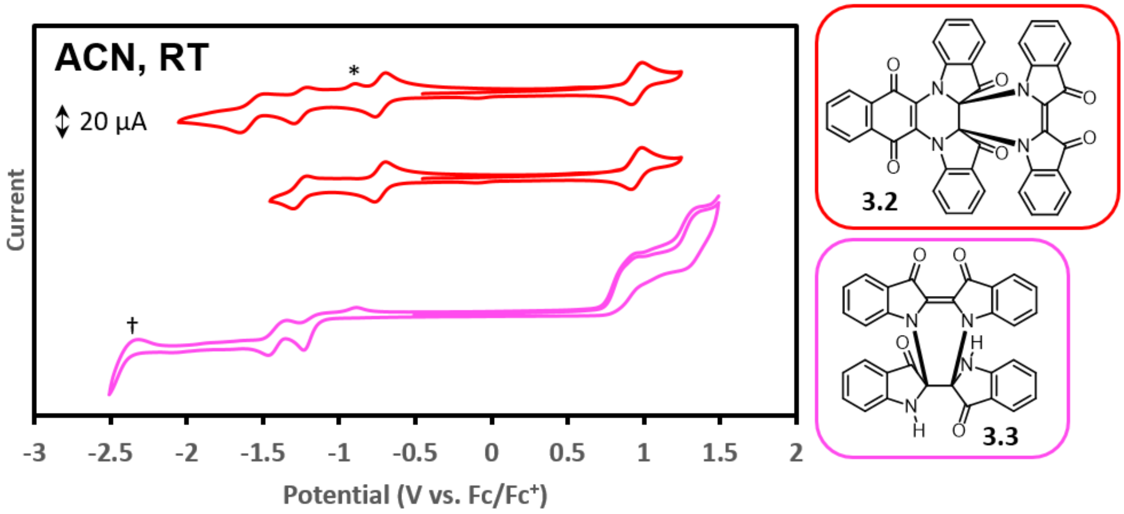

Figure 3.6 Cyclic voltammogram of **3.2** and **3.3** (acetonitrile solution in the dark, 0.1 M NBu_4PF_6 electrolyte, scan rate 100 mV s^{-1}, referenced to ferrocene (Fc)/ferrocenium (Fc^+)). See text for * and †.

Table 3.3 Reduction and oxidation potentials (vs. Fc/Fc^+) of dimeric *cis*-indigos in ACN.

Compound	*Reduction (V)*	*Oxidation (V)*
3.2	-0.73^{q}, -1.25^{q}, -1.57^{q}	+0.95^{r}
3.3	-1.24^{i}, -1.40^{q}	+0.91^{i}, +1.37^{i}

^{q}quasi-reversible, ^{r}reversible and ^{i}irreversible electron processes.

3.5.2. Mechanistic/Redox Investigations

We suspected that redox processes may be an important part of the mechanism in the formation of the dimeric *cis*-indigo products. Cyclic voltammograms of all reagents are collected to scope the interaction between deprotonated indigo and the quinone. **Figure 3.7** shows the CVs of the reagents in DMF. Excess sodium hydride (4 *eq*.) was added to a solution of indigo to represent an early reaction condition. The acidity of indigo has been estimated to pK_{a1} = 8.0 and pK_{a2} = 12.7 from an extrapolation of mono- and multiple sulfonated indigo derivatives in water.[104] A hydride can fully deprotonate indigo based on a much stronger pK_a value (~ 36, measured from H_2). By applying the same trend in polar organic solvents, indigo is presumed to be doubly deprotonated in DMF. A CV of 2,3-dichloro-5,6-dicyano-1,4-benzoquinone (DDQ) was included to provide an example of a strongly reducing quinone.

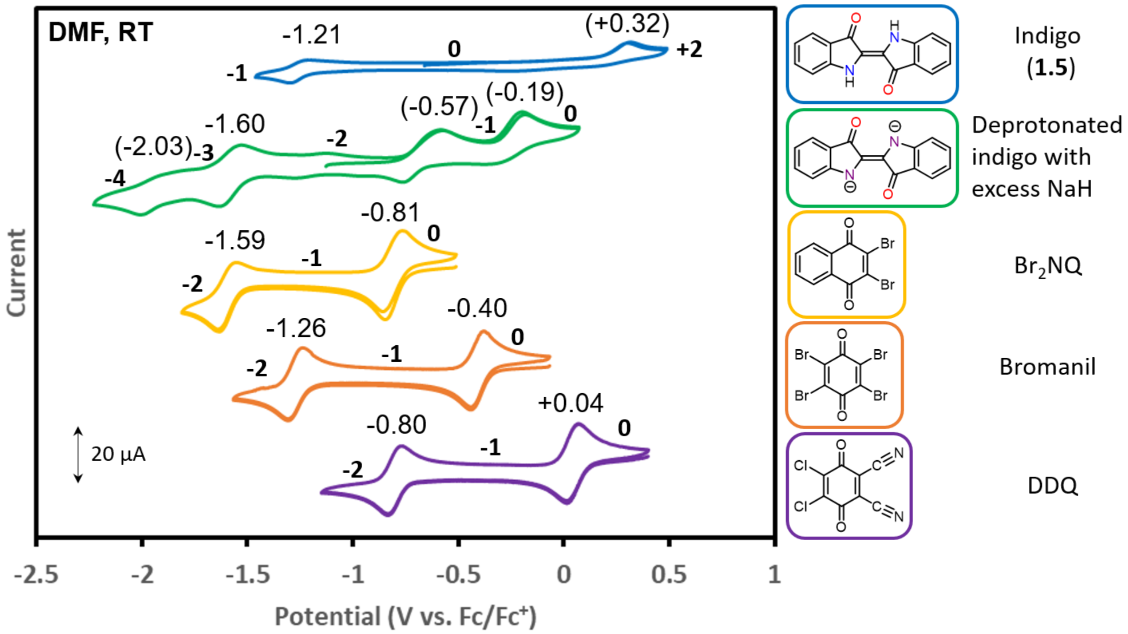

Figure 3.7 Cyclic voltammogram of reagents (DMF solution, 0.1 M NBu_4PF_6 electrolyte, scan rate 100 mV s^{-1}, referenced to ferrocene (Fc)/ferrocenium (Fc^+)). Potentials in parentheses () are irreversible events.

Indigo (**1.5**) undergoes one irreversible oxidation and one reversible reduction. Our data suggest that both processes are one electron event based on the current size in contrast to a $2e^-$ oxidation and a $1e^-$ first reduction that are observed by Compton and co-workers.[123] The CV of deprotonated indigo consists of four redox events spanning five molecular charge states ranging from -4 to 0; the latter charge state would correspond to dehydroindigo (**1.8**). Double deprotonation of indigo shifts the redox potentials to a more negative region. Thus, dianionic indigo is more easily oxidized but is harder to reduce than the parent indigo. Br_2NQ (first reduction: -0.81 V) cannot oxidize the indigo dianion to a monoanion radical due to a more negative potential than -0.57 V. In this case, the formation of the literature product **3.1** is a probable intermediate in the formation of **3.2**. However, the mechanism of the next step still needs to be validated since the properties of **3.1** are unknown. On the other hand, a stronger oxidant- bromanil (first reduction: -0.40 V), can oxidize the indigo dianion into a monoanion radical. In the reaction of **3.3** and **3.4**, the formation of the monoanion radical is probably followed by a radical addition process. It should be noted that two equivalence of bromanil was used in our reaction. We initially questioned if the indigo monoanion radical could be oxidized once more with an extra equivalent of quinone. The formation of the **1.8** was ruled out based on calculations using **equations (1)** and **(2)** which are derived from Nernst equation.[124]

$$\boldsymbol{A + Ox \underset{\leftarrow}{\rightarrow} A^{+} + Red}$$

Eq. 1

$$\boldsymbol{log\left\{\frac{[A^{+}]}{[A]}\right\} = 8.47\ \Delta E^{\circ\prime}(at\ 298\ K)}$$

Eq. 2

$$\boldsymbol{\Delta E^{\circ\prime}(in\ V) = \Delta E^{\circ\prime}\left(\frac{[Ox]}{[Red]}\right) - \Delta E^{\circ\prime}\left(\frac{[A^{+}]}{[A]}\right)}$$

In the above equations, A is the substrate and Ox is the oxidant. The ratio between one-electron oxidized substrate to the initial substrate ($[A^+]/[A]$) after stoichiometric equivalent treatment of oxidant can be calculated by using the difference in the formal potentials of the oxidant and the substrate at 298 K. Although an irreversible redox process may change the equilibrium distribution, this calculation can still provide an insight to estimate the reaction progress. In the equimolar reaction with bromanil, the ratio between the indigo monoanion radical (A^+) and the starting dianion (A) is calculated to be 25.0 : 1. This means A^+ is 25 times more present than A in the mixture solution. If two equivalents of bromanil are used, the ratio becomes 0.02 : 1 between dehydroindigo **1.8** (A^+) and indigo monoanion radical (A) in which two-electron oxidation becomes disfavoured. In the case of DDQ, a first equimolar treatment should push the one-oxidation to completeness because the ratio between indigo monoanion radical (A^+) to the starting dianion (A) is $1.5x10^5$: 1. A Second equivalence still would favour the formation of **1.8** as the calculated ratio is 101.7 : 1. Reacting indigo with one equivalent of DDQ in the synthetic procedure does lead to dimeric indigo **3.3,** which was confirmed by ^{1}H NMR spectroscopy. When two equivalents of DDQ are used, no such product formation was detected. The product observation in the reaction of equimolar DDQ along with the same result obtained from the chloranil reaction further supports a radical ion formation from deprotonated indigo in the synthesis of **3.3** and **3.4**.

3.6. NMR Spectroscopy

3.6.1. Room Temperature Measurements

1D and 2D NMR experiments are performed on **3.2** and **3.3**. The ^{1}H and ^{13}C NMR spectra are fully consistent with the molecular structures. For **3.4**, carbon chemical shifts were estimated through HSQC and HMBC experiments instead of 1D ^{13}C NMR due to a low quantity.

In the solution state ^{13}C NMR spectrum, **3.3** shows two distinctive carbonyl signals at 195.47 ppm and 179.41 ppm in DMSO-d_6. The former signal was identified as an indigoid substituent carbonyl based on its ^{3}J HMBC correlation with the indolyl -N<u>H</u> singlet. Therefore, the latter signal corresponds to the indigoid backbone carbonyl. Two different chemical shifts were observed as the result of varying electron density at the carbonyl's carbon centres. **Figure 3.8** shows resonance structures of **3.3** after delocalization of the nitrogen lone pair through the central C=C bond. This type of electron delocalization is absent for the substituent indigo; thus, the substituent carbonyl experiences more ketone-like character.

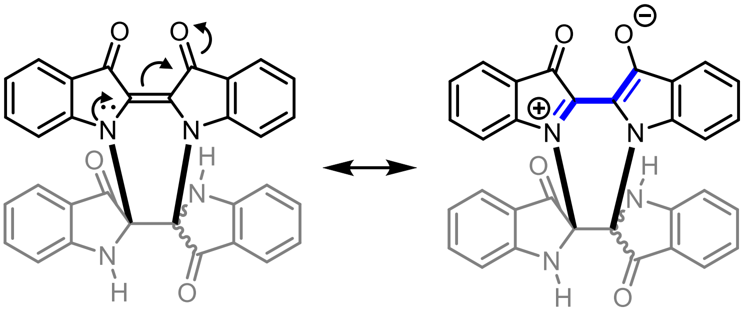

Figure 3.8 Resonance structures of **3.3**.

^{13}C NMR of **3.2** exhibits three carbonyl signals at 191.78 ppm, 180.18 ppm and 180.08 ppm in dichloromethane-d_2. 2D NMR experiments revealed a peak at 180.18 ppm corresponds to the naphthoquinone carbonyl. The first and the third signals were confirmed as indigoid carbonyls based on the ^{3}J HMBC correlation of the carbon atom with the indolyl 4th position proton. However, the exact locations could not be determined using the NMR data. Consideration of resonance structures in **Figure 3.8** suggests that similar nitrogen lone pair delocalization is possible at the *cis*-indigoid backbone as well as on the naphthoquinone moiety of **3.2** as depicted in **Figure 3.9**. Therefore, the signal at 180.08 ppm was regarded as a *cis*-indigo backbone carbonyl; a signal at 191.78 ppm was given to the indigoid substituent. **Table 3.4** summarized ^{13}C chemical shifts of dimeric *cis*-indigos.

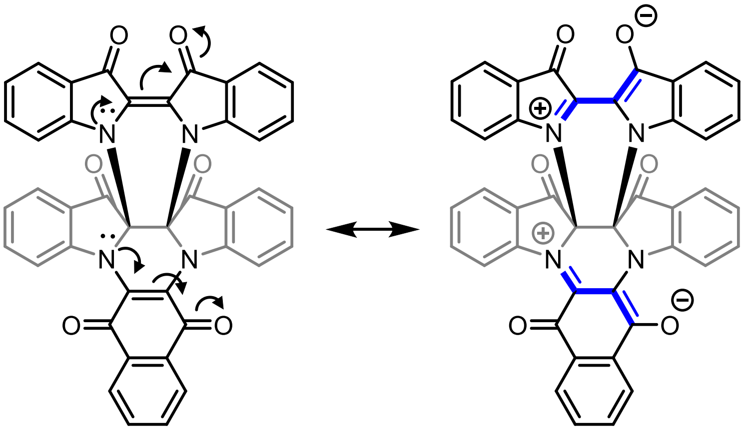

Figure 3.9 Possible resonance structures of **3.2**.

Table 3.4 Assignments of C=O ^{13}C chemical shifts in dimeric *cis*-indigos.

Compound	**3.2**	**3.3**	**3.4**
C=O location in	ppm (DCM-d_2)	ppm (DMSO-d_6)	ppm (DMSO-d_6)
Backbone	180.08	179.41	179.4
Substituent	191.78	195.47	193.1
naphthoquinone	180.18	-	-

Diastereomers **3.3** and **3.4** show almost identical proton chemical shifts except for the H7(H7') protons in the solution state ^{1}H NMR. **Figure 3.10** shows the ^{1}H NMR spectral comparison of the two diastereomers. Aromatic protons of both compounds appear within 0.01 ppm to each other except for the H7(H7') protons. H7(H7') signal on **3.3** exhibits a broad singlet while the same protons on **3.4** appear sharp. The two mentioned signals are apart by 0.12 ppm.

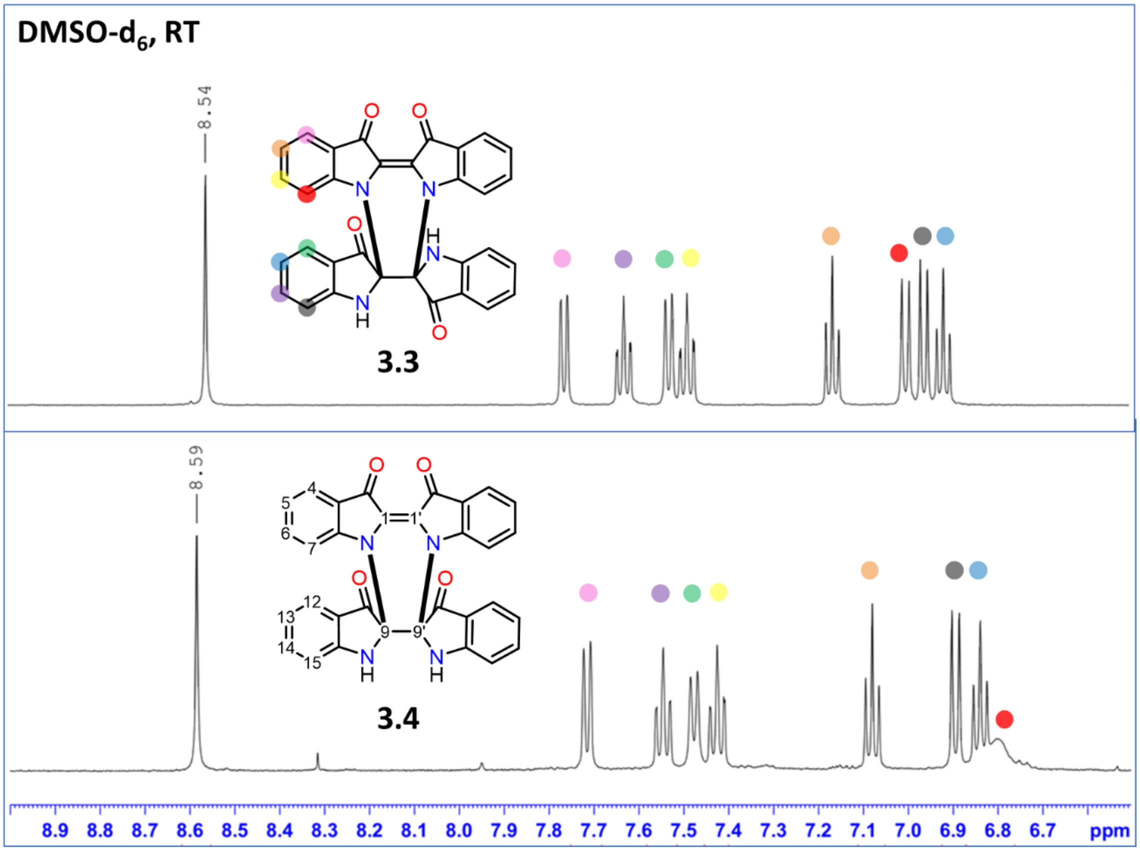

Figure 3.10 ^{1}H NMR spectral comparison of **3.3** and **3.4** in DMSO-d_6.

3.6.2. Variable Temperature Measurements

According to the X-ray structures, H7(H7’) protons of both **3.3** and **3.4** point towards the indigoid substituents. **Figure 3.11** shows the spatial distances from the carbons atoms which bear the H7(H7’) hydrogens to the centroid of the nearby indolyl rings. The average distance is shorter for **3.4**. The magnetic environment of H7(H7’) protons is greatly influenced by spatial changes of the indigoid substituents due to proximity. We propose that the observed broad signal from **3.4** is an average of exchanging ring-flip motions involving the central heterocycle as depicted in **Figure 3.12**.

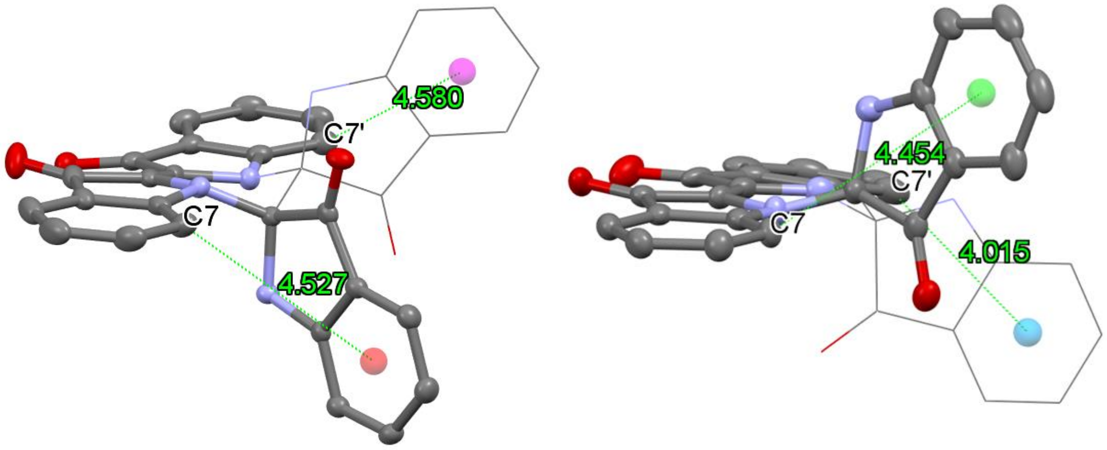

Figure 3.11 Distances measured from the C7(C7') to the nearby indolyl centroids. Left: **3.3**. Right: **3.4**.

Figure 3.12 Ring-flip conformation changes in dimeric *cis*-indigos **3.3** and **3.4**.

^{1}H NMR spectra were recorded at different temperatures to investigate the possibility of dynamic behaviour. **Figure 3.13** reveals chemical shift changes of **3.4** in DMSO-d$_6$. When heated above 57 °C, the broad H7(H7') signal becomes sharpened as the rate of ring-flip becomes faster than the NMR timescale.

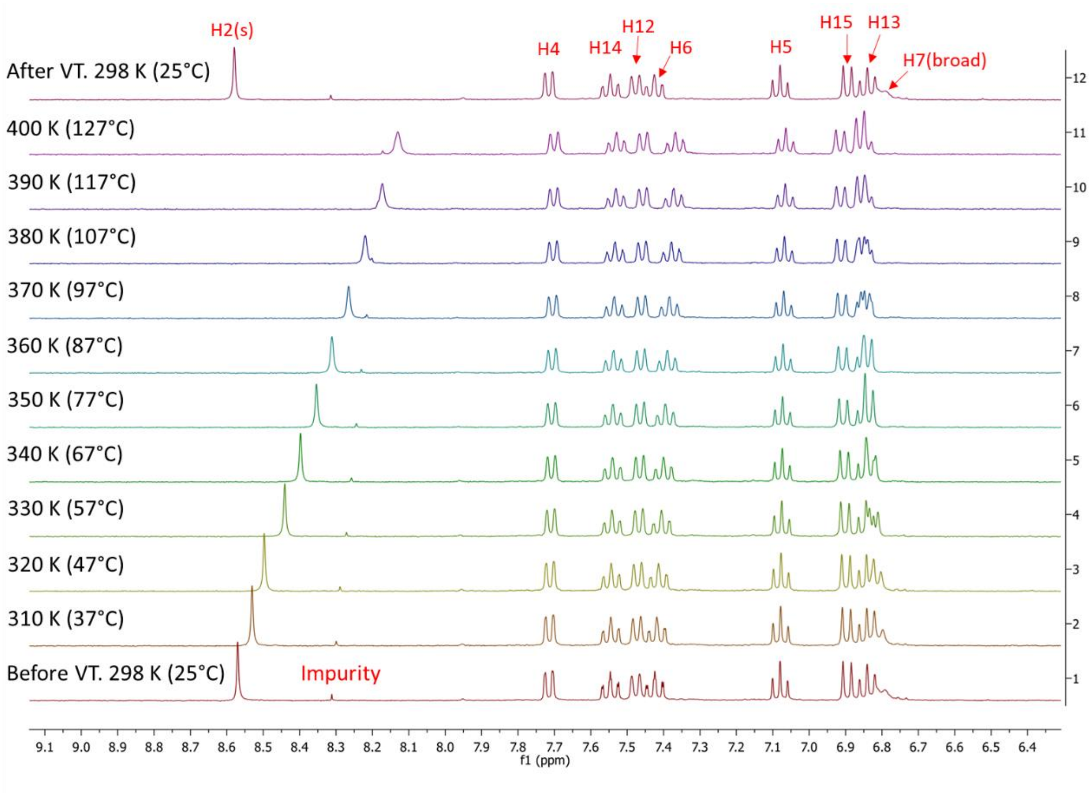

Figure 3.13 High variable temperature ^{1}H NMR spectra of **3.4** in DMSO-d_6. Reproduced from Reference[112] with permission from the Royal Society of Chemistry.

Figure 3.14 shows the low temperature ^{1}H NMR spectra of **3.4** in acetone-d_6. The -N$\underline{H}$ singlet coalesces between -33 °C ~ -43 °C while H4, H5, H6 and H15 protons persist in their peak shapes during this transition. The H4, H5 and H6 protons are located on the outer *cis*-indigo backbone where the change in the magnetic environment is least affected as pointing away from the indigoid substituent. At -63 °C, the mentioned proton signals begin to separate as well because the rate of conformation exchange becomes slower than the NMR timescale. The (apparent) molecular symmetry is lost, and two separated –N$\underline{H}$ singlets are seen in addition to the appearance of the new peaks.

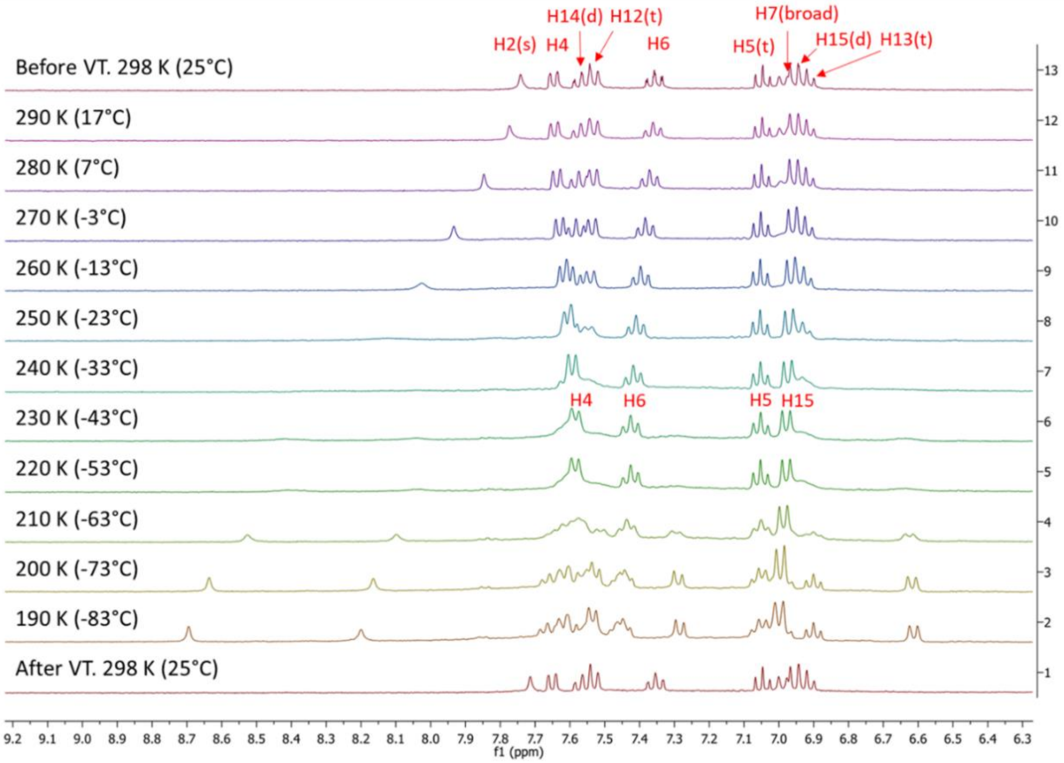

Figure 3.14 Low variable temperature ^{1}H NMR spectra of **3.4** in acetone-d$_6$. Reproduced from Reference[112] with permission from the Royal Society of Chemistry.

In the case of **3.3**, the two halves of the molecule experience symmetrical changes in the magnetic environment due to the presence of an internal C$_2$ rotation axis. **Figure 3.15** depicts the conformational changes during a ring-flip process. Three geometries shown have a unique magnetic profile, yet the molecular symmetry is retained among each exchanging conformers. In the transition state, the H7(H7’) proton is located at the closest distance to the nearby indolyl ring. As a result, the H7(H7’) protons will experience the greatest magnetic environmental changes during this transition. **Figure 3.16** shows the low VT ^{1}H NMR spectra in THF-d$_8$. A dynamic behaviour was observed at H7(H7’) protons below -23 °C. The corresponding signal coalesces while the rest signals retain their shapes.

At this stage, the rate of ring-flip is still faster than the NMR timescale while H7(H7’) protons experiencing the greatest magnetic turbulence in a similar manner observed in **3.4** (**Figure 3.10**). At below -63 °C, the signal from H7(H7’) protons re-appears as a doublet and the shape persists during the lower temperatures to suggest that a stable magnetic environment is reached. Thus, the rate of ring-flip became slower than the NMR timescale. All signals returned to the initial chemical shifts after equilibrating back to the room temperature.

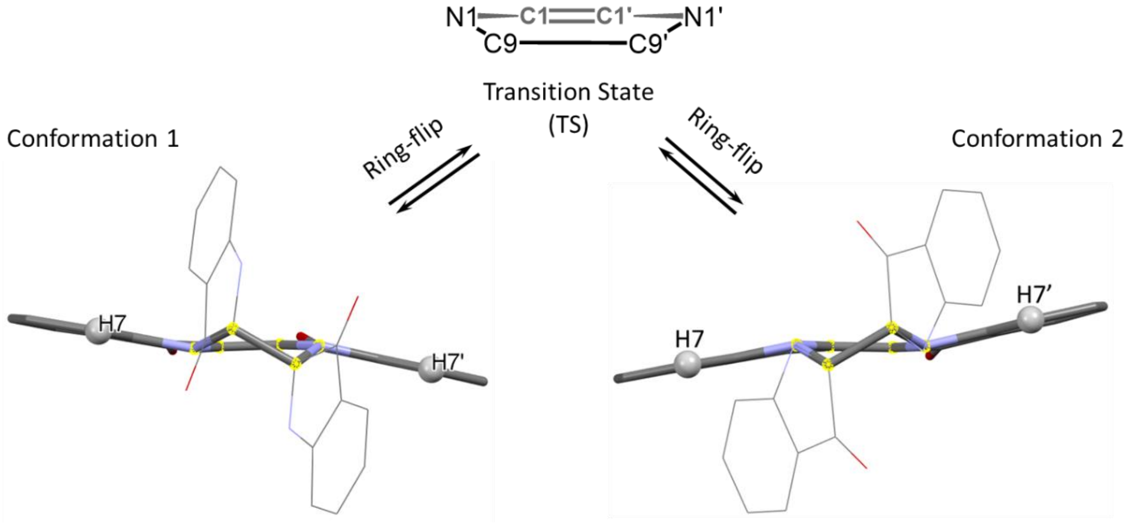

Figure 3.15 Ring-flip conformation transition in **3.3**.

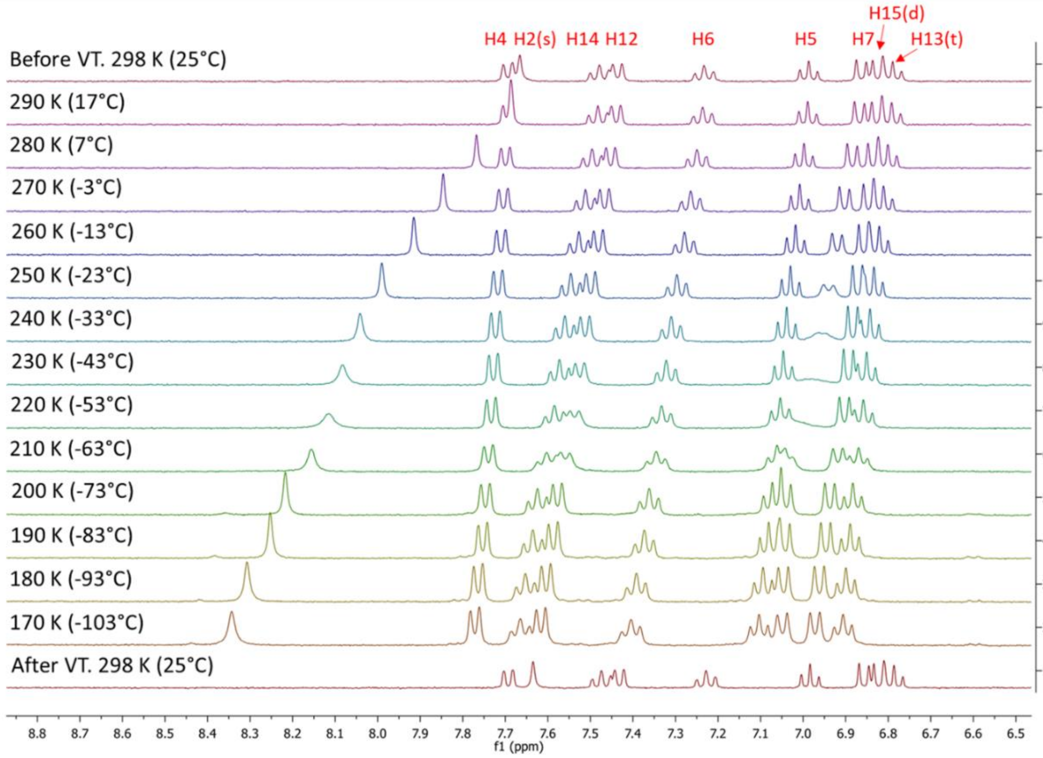

Figure 3.16 Low variable temperature ^{1}H NMR of **3.3** in THF-d_8. Reproduced from Reference[112] with permission from the Royal Society of Chemistry.

3.7. Conclusions

This chapter discovered a new structure-type of *cis*-indigo — namely dimeric *cis*-indigos. Sequential treatment of indigo with a base and a quinone introduces a 2,2′-dihydroindigo molecule as the *N*,*N*′-bridging tether to a *cis*-indigo. Quinone incorporation at the dihydroindigo unit was found in **3.2** in the reaction using 2,3-dibromo-1,4-naphthoquinone, but not in **3.3** and **3.4** when bromanil was used. Mechanistic investigation performed by CV revealed that the strength of quinone in regards to the deprotonated indigo alters the early reaction intermediates in the formation of these dimeric *cis*-indigos.

X-ray crystallography and NMR spectroscopy revealed the largest π-conjugation is located on the relatively planar *cis*-indigo backbone, whereas the indigoid substituent serves a discrete π-conjugation. The 2,2′-dihydroindigoid substituents on *cis*-indigo cause a small hypsochromic shift in the maximum visible-absorption compared to the alkane-type linkers that are discussed in Chapter 2. The dimeric *cis*-indigos exhibit rich redox properties; especially, a complete reversible redox ability was observed in naphthoquinone-bearing **3.2**. Diastereomers **3.3** and **3.4** display dynamic behaviours confirmed by solution VT ^{1}H NMR spectroscopy. These indigoid-substituted *cis*-indigos are interesting additions to the known *cis*-indigos.

3.8. Experimental Methods

See **Section 2.8.1** for general experimental details. All materials were used without further purification except DDQ, which was recrystallized in chloroform before use.

1D and 2D NMR spectra collected at room temperature were recorded on a 500 MHz Bruker instruments. Variable Temperature NMR spectra were collected on a 360 MHz Bruker instrument. All NMR spectra were collected at relaxation time (d1) = 1 second unless stated otherwise. Elemental analysis were carried out at the University of Windsor.

X-ray single crystals were analyzed on a Bruker APEX-II CCD diffractometer at 90 K. A Mo source was used for **3.2**, **3.3**, **3.5** and a Cu source was used for **3.4**.

X-ray structure of **3.2** was solved by Dr. Corey Sanz; structures of **3.3**, **3.4**, and **3.5** were solved by Dr. Dillon Hofsommer.

3.8.1. Synthesis

***N,N′*-[2,2′](*N,N′*-[2,3](1,4-naphthoquinono-2,2′-dihydroindigotino))indigo** (**3.2**)

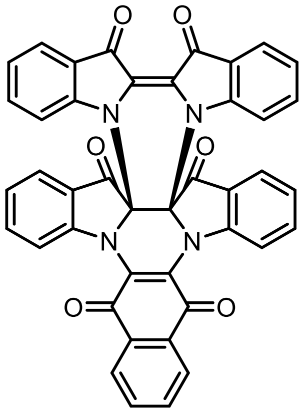

Indigo (255.6 mg; 0.9746 mmol) and sodium hydride (60 % w/w suspension in mineral oil, 103.3 mg, ~2.6 mmol) were charged in an oven dried, multi-neck 50 mL round bottom flask equipped with a nitrogen adapter and a rubber stopper. Anhydrous DMF (10 mL) was added via syringe under a nitrogen atmosphere, and the mixture was stirred at room temperature for 25 minutes. The rubber stopper was briefly removed to add 1,2-dibromo-1,4-naphthoquinone (314.3 mg; 0.9948 mmol) under a strong flow of nitrogen gas. An instant colour change occurred from green to brown. The mixture was stirred for 20 hours at room temperature under N_2 and became a wine red colour. The solution was diluted with dichloromethane (80 mL) and washed with neutral H_2O / LiCl (3 x 100 mL) then with brine (100 mL). The organic layer was dried over Na_2SO_4, filtered, and concentrated *in vacuo*. The residue was subjected to silica gel column chromatography using ethyl acetate / hexanes (70 : 30) (R_f = 0.48). Orange fraction was collected. Recrystallization in chloroform (80 mL) / hexanes (300 mL) and washing the solids with hexanes yields **3.2** as a red powder (105.5 mg, 32 %). Single X-ray crystals were grown from slow evaporation of a concentrated toluene solution. For simplification, all NMR assignments are referred to the half of the molecule. ^{1}H NMR (500 MHz, CD_2Cl_2) δ 8.13 – 8.08 (m, *2H*, H_{38}), 7.80 – 7.76 (m, *2H*, H_{39}), 7.74 (dd, *2H*, ^3J = 7.6 Hz, ^4J = 0.7 Hz, H_{20}), 7.69 (dd, *2H*, ^3J = 7.6 Hz, ^4J = 0.6 Hz, H_{28}), 7.61 (ddd, *2H*, ^3J = 8.5 Hz, ^3J = 7.4 Hz, ^4J = 1.3 Hz, H_{30}), 7.29 (ddd, *2H*, ^3J = 8.5 Hz, ^3J = 7.4 Hz, ^4J = 1.3 Hz, H_{22}), 7.19 (dd, *2H*, ^3J = 7.4 Hz, ^4J = 0.8 Hz, H_{29}), 7.08 – 7.04 (m, *4H*, H_{21} and H_{31}), 6.84

(d, *4H*, ^{3}J = 8.4 Hz, H_{23}). ^{13}C NMR (126 MHz, CD_2Cl_2) δ 191.78 (C_{26}), 180.18 (C_{41}), 180.08 (C_{18}), 157.03 (C_{32}), 147.69 (C_{24}), 140.66 (C_{42}), 139.53 (C_{30}), 135.95 (C_{22}), 135.05 (C_{38}), 131.53 (C_{40}), 127.37 (C_{39}), 125.16 (x2) (C_{19} and C_{20}), 125.07 (C_{28}), 124.93 (C_{29}), 124.30 (C_{17}), 124.00 (C_{27}), 123.63 (C_{21}), 116.04 (C_{31}), 113.81 (C_{23}), 83.12 (C_{25}). IR (KBr disk, cm^{-1}): 1739m, 1719m, 1603s, 1586sh m, 1466s, 1297m, 1196m, 908w, 749w. UV-Vis (ACN; λ_{max} (nm) (ε ($L\cdot mol^{-1}\cdot cm^{-1}$))): 268 (42 000), 302sh, 514 (14 000). HR-MS: Calcd for $C_{42}H_{20}N_4O_6H^+$ *m/z* = 677.14559, found *m/z* = 677.14524. Satisfactory elemental analysis results not obtained; Anal: Calcd for $C_{42}H_{20}N_4O_6$: C, 74.55; H, 2.98; N, 8.28. Found: C, 73.04; H, 3.58; N, 7.62.

***N,N′*-[2,2′](*trans*-2,2′-dihydroindigotino)indigo** (3.3)

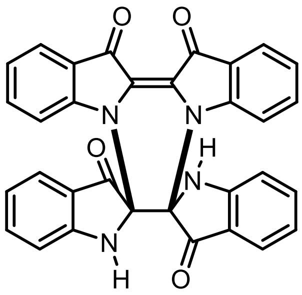

Indigo (253.9 mg; 0.9681 mmol) and sodium hydride oil (60 % w/w suspension in mineral oil, 116.3 mg, ~2.91 mmol) were charged in an oven-dried, multi-neck 50 mL round bottom flask equipped with a nitrogen adapter and a rubber stopper. Anhydrous DMF (10 mL) was added via syringe under a nitrogen atmosphere, and the mixture was stirred at room temperature for 25 minutes. The rubber stopper was briefly removed to add bromanil (808.0 mg; 1.907 mmol) under a strong flow of nitrogen. An instant colour change occurred from green to orange-brown. The mixture was stirred for 21 hours at room temperature under N_2 and became a wine red colour. The solution was diluted in chloroform (200 mL) and washed with 0.5 M $KOH_{(aq)}$ / LiCl (4 x 100 mL) followed by deionized water (100 mL). The organic layer was dried over Na_2SO_4, filtered, and concentrated in *vacuo*. The residue contained both isomers.

Separation of **3.3** was accomplished by diluting a solution of DMF (3 mL) with acetone (27 mL), heating the mixture at reflux for 15 minutes, and keeping the suspension in the freezer for 3 days. The solid was filtered and washed with cold acetone and hexanes to yield red microcrystals of **3.3** as a 1 : 1 adduct with acetone (26.8 mg, 10 %). X-ray crystals were grown from slow evaporation of a concentrated acetonitrile solution. ^{1}H NMR (500 MHz, DMSO-d_6) δ 8.54 (s, *2H*, H_2), 7.71 (d, *2H*, ^{3}J = 7.0 Hz, H_4), 7.60 – 7.54 (m, *2H*, H_{14}), 7.47 (d, *2H*, ^{3}J = 7.7 Hz, H_{12}), 7.45 – 7.39 (m, *2H*, H_6), 7.09 (t, *2H*, ^{3}J = 7.4 Hz, H_5), 6.92 (d, *2H*, ^{3}J = 8.3 Hz, H_7), 6.88 (d, *2H*, ^{3}J = 8.2 Hz, H_{15}), 6.83 (t, *2H*, ^{3}J = 7.5 Hz, H_{13}), 2.08 (s, *6H*, *acetone*). ^{13}C NMR (126 MHz, DMSO-d_6) δ 206.53 (*acetone*), 195.47 (C_{10}), 179.42 (C_2), 161.86 (C_{16}), 147.68 (C_8), 139.37 (C_{14}), 135.86 (C_6), 124.58 (C_{12}), 124.22 (C_4), 123.59 (C_3), 122.57 (C_5), 122.53 (C_1), 119.36 (C_{11}), 119.14 (C_{13}), 112.65 (C_7), 112.06 (C_{15}), 75.26 (C_9), 30.71 (*acetone*). IR (KBr disk, cm^{-1}): 3243 (broad), 1718s, 1700s, 1609s, 1573s, 1471s, 1464s, 1325s, 1295s, 1193s, 1100s, 901s, 746m, 740w. UV-Vis (ACN; λ_{max} (nm) (ε (L·mol^{-1}·cm^{-1}))): 271 (>25 000), 300 (>26 000), Note: UV acetone cutoff: 310 nm. 534 (15 000). HR-MS: Calcd for $C_{32}H_{18}N_4O_4H^+$ *m/z* = 523.14011, found *m/z* = 523.14007. Satisfactory elemental analysis results not obtained; Anal: Calcd for $C_{35}H_{24}N_4O_5$: C, 72.41; H, 4.17; N, 9.65. Found: C, 71.62; H, 4.18; N, 9.50.

Attempted isolation of *N,N′*-[2,2′](*cis*-2,2′-dihydroindigotino)indigo (3.4)

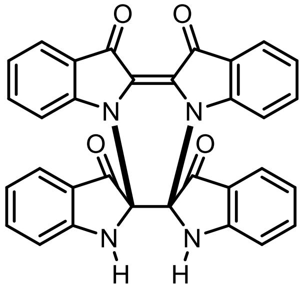

The same procedure as above was repeated. The DMF / acetone (3 mL / 27 mL) filtrate contains **3.4**. The solvent volume was reduced *in vacuo*. The resulting solid was subjected to silica gel chromatography using acetone / chloroform (20 : 80) (R_f = 0.34), and **3.4** was eluted unclean in a pink fraction. Attempts to recrystallize the residue using two-solvent systems of dichloromethane/hexanes, chloroform/hexanes were unsuccessful. X-ray crystal was grown from slow evaporation in acetonitrile. ^{1}H NMR (500 MHz, DMSO-d_6) δ 8.59 (s, *2H*, H_2), 7.72 (d, *2H*, ^3J = 7.5 Hz, H_4), 7.55 (t, *2H*, ^3J = 7.7 Hz, H_{14}), 7.48 (d, *2H*, ^3J = 7.7 Hz, H_{12}), 7.43 (t, *2H*, ^3J = 7.8 Hz, H_6), 7.08 (t, *2H*, ^3J = 7.4 Hz, H_5), 6.89 (d, *2H*, ^3J = 8.2 Hz, H_{15}), 6.84 (t, *2H*, ^3J = 7.5 Hz, H_{13}), 6.80 (s, *2H*, H_7). Carbon chemical shifts were estimated from ^{1}H-^{13}C HMBC correlations: (DMSO-d_6) δ 193.1 (C_{10}), 179.4 (C_2), 160.8 (C_{16}), 147.6 (C_8), 138.6 (C_{14}), 135.6 (C_6), 124.2 (x2) (C_4 and C_{12}), 122.2 (C_5), 119.1 (C_{13}), 112.4 (C_7), 111.8 (C_{15}), 76.5 (C_9), three carbons unassigned: 124.3, 123.6, 119.7. UV-Vis (ACN; λ_{max} (nm)): 274, 298, 541.

Chapter 4. *cis*-Nindigo and Related Compounds

4.1. Introduction to Chapter 4

Chapters 2 and 3 have demonstrated that modification at the H-chromophore using an organic *N*,*N′*-linker can effectively alter the photophysical properties, redox behaviours and spatial orientations of *cis*-indigo. With the growing interest of indigo in organic electronics such as OFETs, photodiodes and dye-sensitised solar cells, Nindigo could potentially be used in a similar manner due to characteristics derived from the common structure.

One interesting aspect of Nindigo is that while indigo can only be protonated in the gaseous state[125], Nindigo (**1.16**) and indigo monoimines (**1.17**) can readily undergo a reversible proton-induced *trans*-to-*cis* isomerization in the solution state[126]. The protonated species **4.1** and **4.2** exhibits red-shifted absorption compared to neutral *trans* isomers. Thus, protonation provides an additional means of altering the properties of Nindigoids. The *cis*-configuration of Nindigo can also be found in coordination chemistry with Pd[88] and Ru[90] (**4.3**) centres. However, recent studies from the Hicks group, Dr. Hofsommer reported that the coordination reaction of **4.1** and **4.2** can result in mixtures of *cis* and *trans* isomers.[127] *N*,*N′*-modulation in principle can simplify the coordination mode in forming metal complexes in addition to the aforementioned diverse properties derived from the tether. This chapter explores in the synthetic approaches and characterization of organically tethered Nindigo and monoimine species. The physical and chemical properties are compared with the indigoid counterpart to examine the influence of aryl groups. The acidity of *cis*-tethered Nindigo is investigated by ^{1}H NMR spectroscopy.

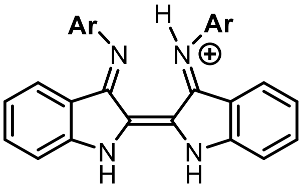

4.1

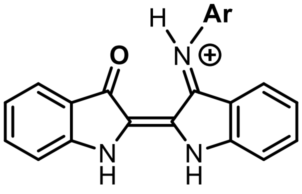

4.2

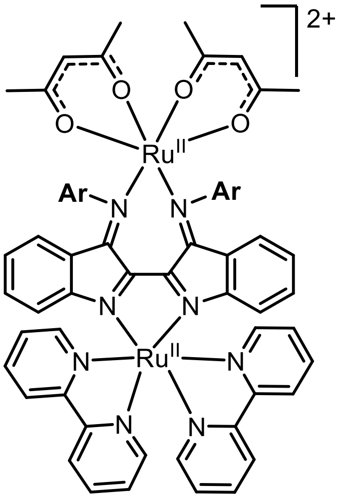

4.3

4.2. Proposed Synthesis of *cis*-Nindigos

Scheme 4.1 depicts three distinct methods we considered in accessing a bridged Nindigo. The addition of an organic linker on the Nindigo backbone could be approached by multiple synthetic routes. One way (path i) can be to react Nindigos (i.e. **1.16a**) with a cyclization reagent by analogy to established indigo chemistry. A second pathway (ii) involves taking tethered *cis*-indigos and converting them to a *cis*-Nindigo using our conventional chemistry for this. Finally (path iii), we imagined possibly performing cycloaddition chemistry on dehydro-Nindigo (i.e. **4.4a**) as a diene in the same manner dehydroindigo (**1.8)** reacts with dienophiles to yield a *cis*-indigo as explained in Chapter 3.

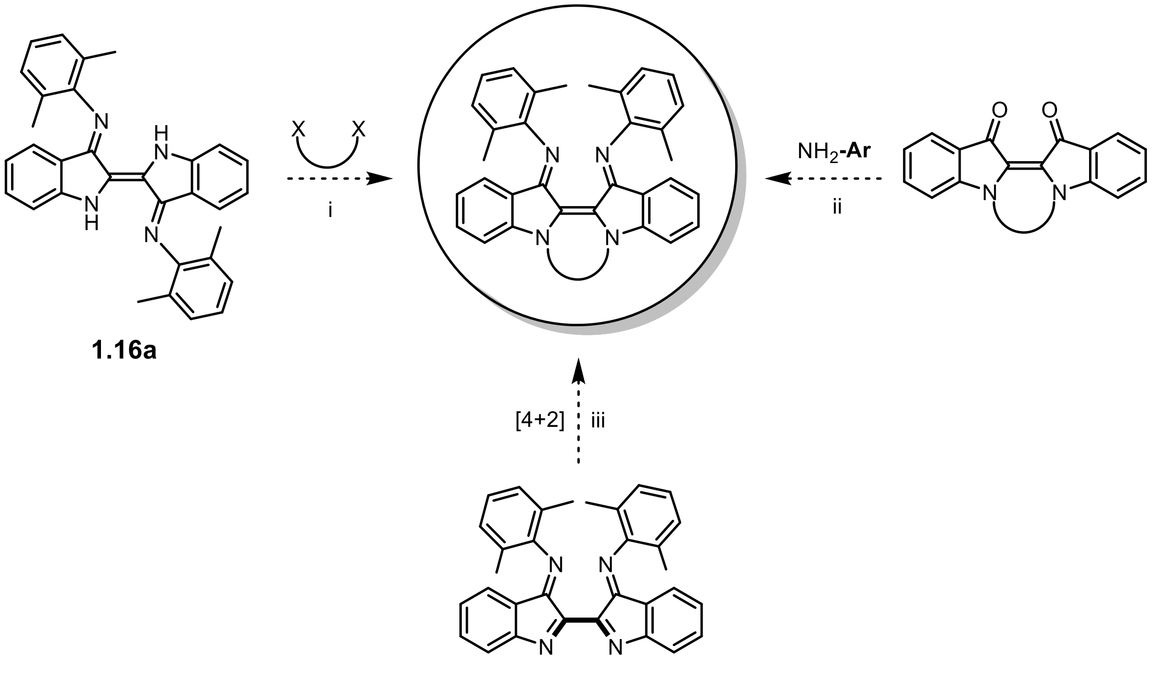

1.16a

4.4a

Scheme 4.1 Possible approaches to *cis*-Nindigo: i) Nindigo alkylation or acylation, ii) ketone to imine group conversion on *cis*-indigo and iii) cycloaddition on dehydro-Nindigos. **Ar** is an aryl group.

4.2.1. Nindigo Alkylation

Nindigo **1.16a** was reacted with a base and then a dihaloalkane in **Scheme 4.2** in the same way indigo was *N,N'*-alkylated in Chapter 2. However, deprotonated Nindigo, unlike deprotonated indigo, did not undergo an S$_N$2 substitution upon the addition of 1,2-dihaloethane. A green solution of the deprotonated Nindigo gradually changed colour back to purple after stirring overnight with 1,2-dibromoethane. The bulk of the reaction mixture was confirmed to be the starting Nindigo **1.16a** according to ^{1}H NMR spectroscopy.

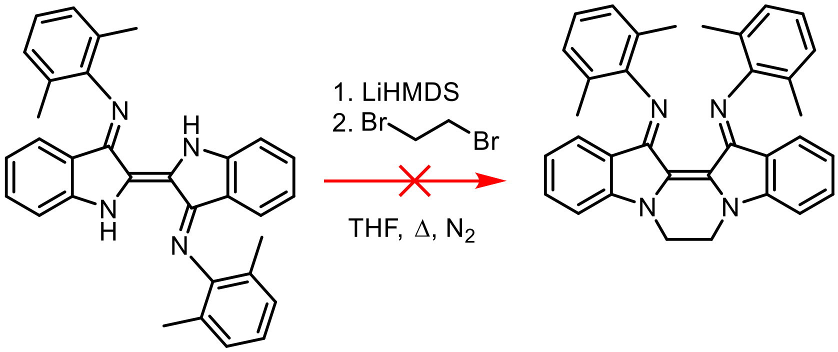

1.16a

Scheme 4.2 Failed synthesis of *N,N'*-ethane-bridged *cis*-Nindigo.

The unexpected full recovery of the starting Nindigo begs the question of the origin of the proton source. In Chapter 2, when deprotonated indigo was reacted with 1,2-dibromoethane, the successful *N,N′*-substitution product was isolated with only 18 % of yield while the starting indigo was recovered as the major quantity. In a similar reaction of deprotonated indigo with a 1,3-dibromopropane, a *beta* hydrogen abstraction on the electrophile produced an allyl bromide, then a subsequent substitution lead to an isolation of allyl indigo (**2.8**) as a byproduct. Applying the same analogy, an *alpha* hydrogen abstraction by the deprotonated Nindigo species on 1,2-dibromoethane could be imagined producing a vinyl bromide and the starting (neutral) Nindigo. However, detection of the vinyl bromide in this reaction by ^{1}H NMR was unsuccessful. This could be due to the low boiling point (15.8 °C) of the vinyl bromide which could have evaporated during the reflux under a constant stream of nitrogen gas as well as/or during the solvent evaporation process. It is suspected that a deprotonated Nindigo favours proton abstraction instead of nucleophilic substitution due to its strong basicity. Changing the reaction conditions did not improve the substitution pathway; recovery of the starting Nindigo was still observed in different reaction conditions with switching an alkyl halide source (X=I), solvent (ACN) and base (NaH). In all attempts, the diagnostic singlet (-C$\underline{H}_2$-) of an ethane tether was not found in the crude ^{1}H NMR spectra.

An attempt to introduce a three-carbon atom tether on Nindigo **1.16a** in **Scheme 4.3** using 1,3-dibromopropane did not result in a productive outcome either. In addition, the ^{1}H NMR spectrum of the crude possessed weak signals of a triplet at 3.98 ppm and a multiplet at 2.36 ppm along with the high intensity of a neutral Nindigo. Although the first two noted signals might indicate a distinctive feature of a propane bridge, an accurate comparison of their proton integrations was difficult due to a messiness in the nearby region. Although this reaction may have produced a trace amount of the desired compound **4.5a**, it was not further pursued because of the low suspected yield.

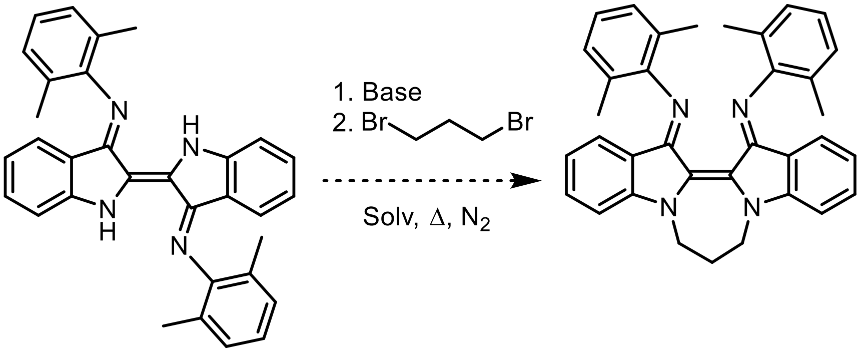

1.16a **4.5a**

Scheme 4.3 Attempted S_N2 reaction of deprotonated Nindigo **1.16a** with 1,3-dibromopropane.

Overall, the attempted *N,N'*-alkylation on Nindigo **1.16a** using alkyl dihalides did not lead to a successful synthesis of *cis*-Nindigo. The main reaction pathway is suspected to be a hydrogen atom abstraction from the electrophile. In order to block this elimination pathway, a new cyclization reagent was chosen. 2,3-dibromo-1,4-naphthoquinone (Br_2NQ) does not possess α- or β- hydrogen atoms and has previously reacted with deprotonated indigo to provide a quinone substituted sub-structure (**Scheme 3.3**). However, in the attempted reaction with Nindigo **1.16a**, a redox reaction took a place between the quinone and the deprotonated Nindigo as shown in **Scheme 4.4**. Treatment of **1.16a** with an equimolar amount of the quinone resulted in a 2 : 1 mixture of dehydro-Nindigo **4.4a**, a $2e^-$ and $2H^+$ oxidized form of Nindigo, and the starting material as determined by ^1H NMR spectroscopy.

The formation of the oxidized Nindigo suggests that the first oxidation potential of the deprotonated Nindigo locates in a similar range with the first reduction potential of the quinone, in which the quinone was consumed as an oxidant rather than an electrophile.

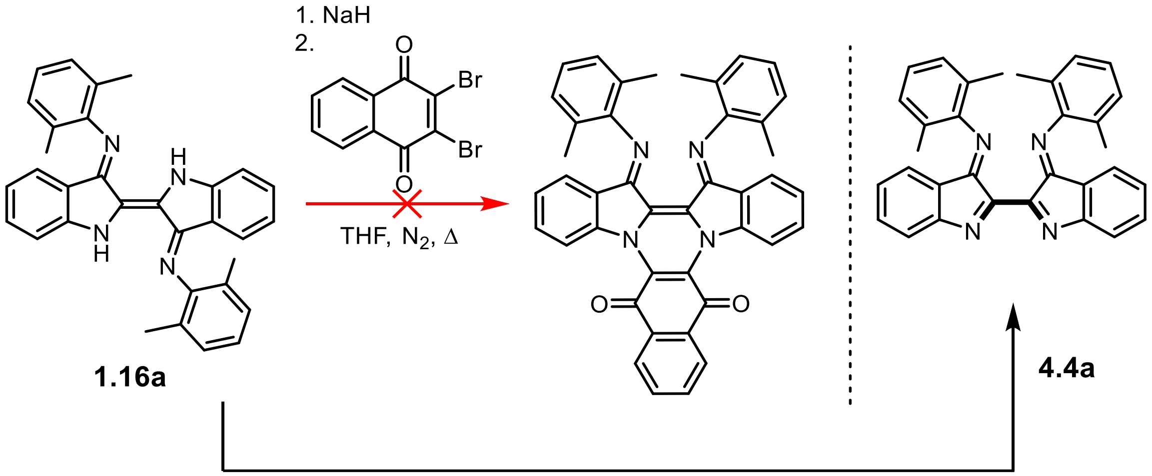

Scheme 4.4 Attempted reaction of deprotonated Nindigo **1.16a** with 2,3-dibromo-1,4-naphthoquinone, and the isolated oxidized Nindigo **4.4a**.

4.2.2. Imine Group Installation on *cis*-indigos

The second main approach to *cis*-Nindigo suggested in **Scheme 4.1** involves the Hicks group's conventional Nindigo synthesis.[85] *Cis*-indigos **2.5** and **2.6** were treated with excess $TiCl_4$ in presence of DABCO and 2,6-dimethyl aniline in high-boiling aromatic solvents. When **2.5** was subjected to the Nindigo procedure in bromobenzene, the ^1H NMR spectrum of the reaction mixture did not reveal the diagnostic -CH_2- singlet. The reaction did not produce the desired *cis*-Nindigo, although the starting material was destroyed. In the case of **2.6** treated in *m*-xylene, the crude ^1H NMR spectrum featured a small triplet at 3.98 ppm which agreed with the previous observation of **4.5a**. However, attempts to purify and isolate the desired compound using were unsuccessful partly due to the low quantity of putative product. In addition, the non-tethered Nindigo **1.16a** was identified in the reaction mixture suggesting that the organic tether was destroyed in the reaction with $TiCl_4$.

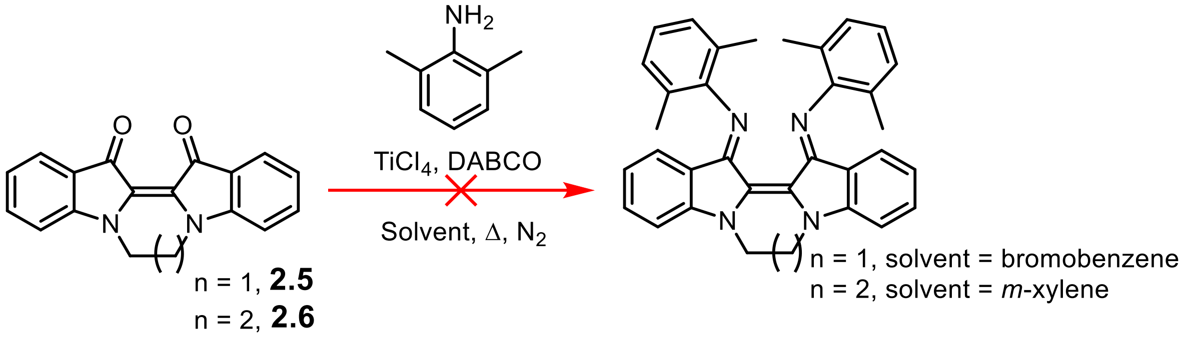

Scheme 4.5 Unsuccessful ketone to imine group conversion on *cis*-*N*,*N'*-alkyl-tethered indigos, **2.5** and **2.6**, using the Hicks group procedure[85].

The formation of the non-tethered Nindigo **1.16a** in the conventional Nindigo reaction setting could be explained by a redox event between the alkyl-substituted indole nitrogen moiety and the Ti(4+). Hall, Jr. and co-workers observed the formation of black tar in the reaction of tertiary amines with titanium tetrachloride.[128] **Scheme 4.6** depicts their proposed mechanism for the decomposition of triethylamine. Triethylamine undergoes a one-electron oxidation by Ti(4+) and loses an α-hydrogen atom to become an iminium ion. With a structural similarity of alkyl-tethered indole nitrogen with triethylamine, it is suspected that Ti(4+) could also initiate an N–C bond cleavage by a similar electron transfer; however, understanding the different stability observed of two *cis*-indigos as a starting material requires a further investigation.

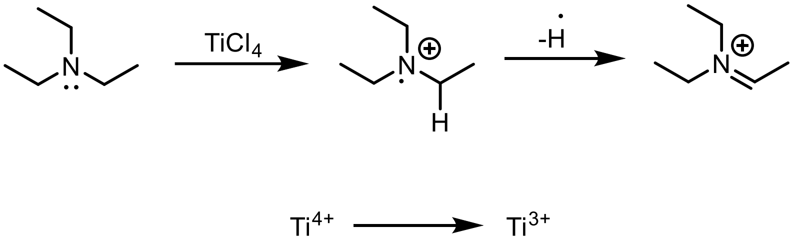

Scheme 4.6 Proposed reaction of electron transfer between triethylamine and titanium (4+).

Next, we applied the ketone-to-imine conversion reaction on oxalylindigo (**2.7)**. **Scheme 4.7** shows the reaction performed in THF with *p*-toluidine. Despite the oxalyl bridge being different from the alkyl tether due to direct conjugation with the indigoid backbone and lacks a hydrogen atom, thin layer chromatography spotted the formation of a non-tethered *p*TolNindigo (**1.16b**) along with multiple products. Column chromatography enabled the isolation of the major species as an intense yellow fraction. **Figure 4.1** shows the ^{1}H NMR spectrum of this isolated species with respect to the starting oxalylindigo **2.7**. The isolated compound retained the proton chemical shifts of the starting material, yet new aromatic signals appeared in the 7.6 – 6.8 ppm region. An alkyl singlet appeared at 2.42 ppm which was integrated to 3H. The overall proton integration was close to 12H and the newly formed methyl signal supports that one imine group is installed on **2.7**. This imine group could be added on indigoid ketone moiety or on the oxalyl bridge, both would result in a total of 12H protons. The location of the imine group could not be definitively assigned based on the ^{1}H NMR. Also, single crystals were grown but failed to diffract. Nonetheless, a strong similarity in the locations of the chemical shifts to a ^{1}H NMR spectrum of DmP monoimine analogue **4.7a** (will be discussed in section **4.2.5**) suggests that installation of one *p*Tol group occurred on the indigoid carbonyl moiety. Performing the same reaction at higher temperatures in *m*-xylene did not lead to the desired diimine species **4.6b**. The suspected *p*Tol monoimine compound **4.7b** was found less, instead of more non-tethered Nindigo **1.16b** was formed. This reaction was not further pursued due to a low yield of the suspected compound.

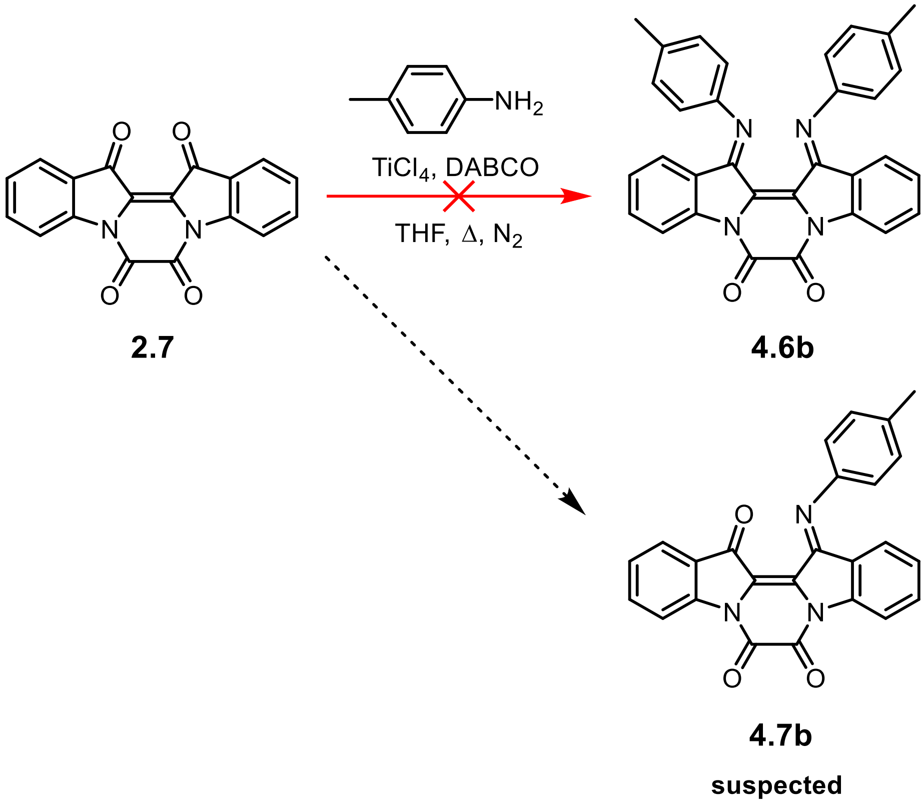

Scheme 4.7 Attempted ketone to imine group conversion on oxalylindigo **2.7** with *p*-toluidine.

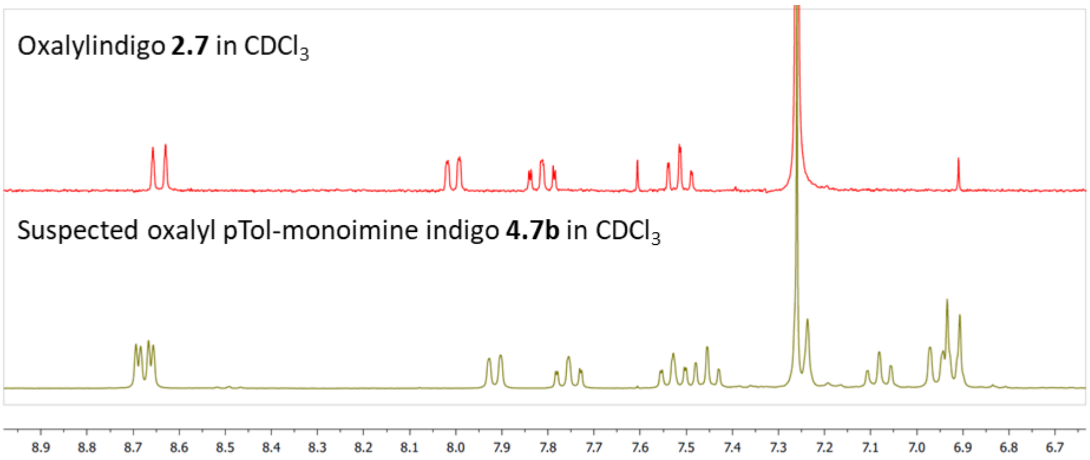

Figure 4.1 ^{1}H NMR spectral comparison of oxalylindigo **2.7** and suspected mono *p*Tol imine indigo **4.7b** in CDCl$_3$.

4.2.3. *Cis*-Nindigo Derivatives from Reactions of Dehydro-Nindigo

Cycloaddition reactions of dehydro-Nindigos (**4.4**) were briefly explored as shown in **Scheme 4.8**. Preparation of the dehydro-Nindigo reactants was carried out according to the group's procedure using excess Ag_2O.[88] In order to generalize the reactivity, dehydro-Nindigos of both bulky (DmP **4.4a**) and non-bulky (*p*Tol **4.4b**) aromatic substituents are tested. Dehydro-Nindigo was stirred with dienophiles of methyl propiolate, diphenylacetylene, anethole, safrol, styrene and cyclohexene in aromatic solvents at reflux and studied by ^{1}H NMR to observe possible cycloaddition products. In some attempted reactions, we saw the formation of reduced Nindigo (**1.16**) which may have resulted from the non-dry reaction settings, however much of the starting **4.4a** and **4.4b** remained even after the overnight reflux. In no cases was any evidence of cycloaddition seen. Current data suggests that dehydro-Nindigos do not undergo [4+2] cycloaddition with the said dienophiles where they are previously known to react with dehydroindigo (**1.8**) to form *cis*-indigos.[113, 115]

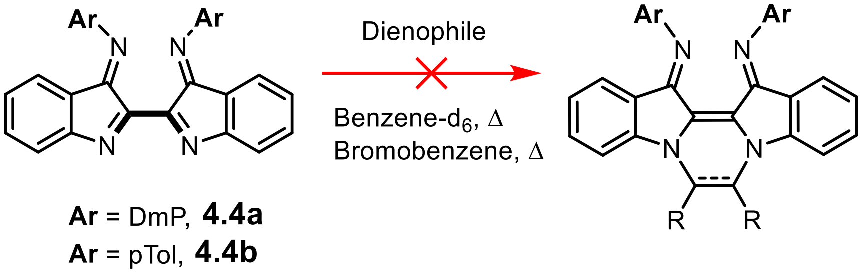

Scheme 4.8 Failed cycloaddition reactions on dehydro-Nindigo **4.4**.

4.2.4. Synthesis of *cis*-oxalyl Nindigo Derivatives

Up to this date, there is only one *N*,*N′*-organically tethered *cis*-Nindigo was reported in the literature. In 1939, van Alphen reported the isolation of red-violet crystals of "oxalylindigo-dianil" (oxalyl PhNindigo, **4.6c**) from a reaction of phenylNindigo **1.16c** with oxalyl chloride.[129] **Scheme 4.9** shows the literature procedure where the two said reagents are sitting in diethyl ether for two weeks at room temperature. His proof for the formation of **4.6c** was based solely on nitrogen elemental analysis.

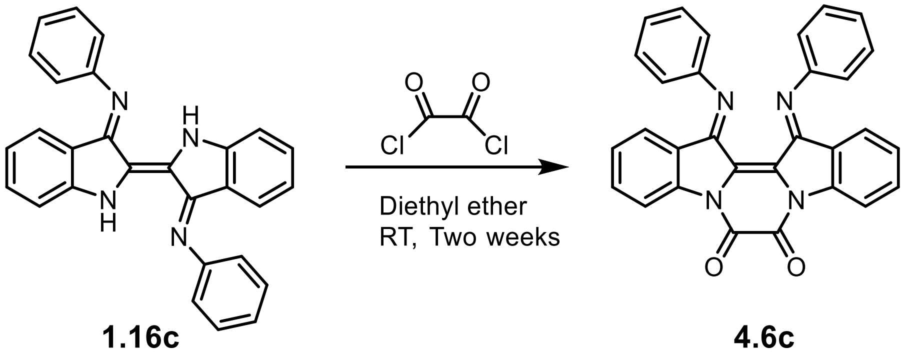

Scheme 4.9 Literature synthesis of **4.6c** by J. van Alphen (1939).

Our attempt at the literature procedure on Nindigo **1.16a** led to an untethered protonated Nindigo **4.1a** as shown in **Scheme 4.10**. The reaction solution stayed in a teal colour and the ^{1}H NMR spectrum confirmed the major species is **4.1a**. The desired product formation (**4.6a** in a protonated form, will be discussed in **Scheme 4.11**) was detected after 8 days. However, the conversion was very slow and column chromatography was unable to isolate the desired product due to decomposition during the separation.

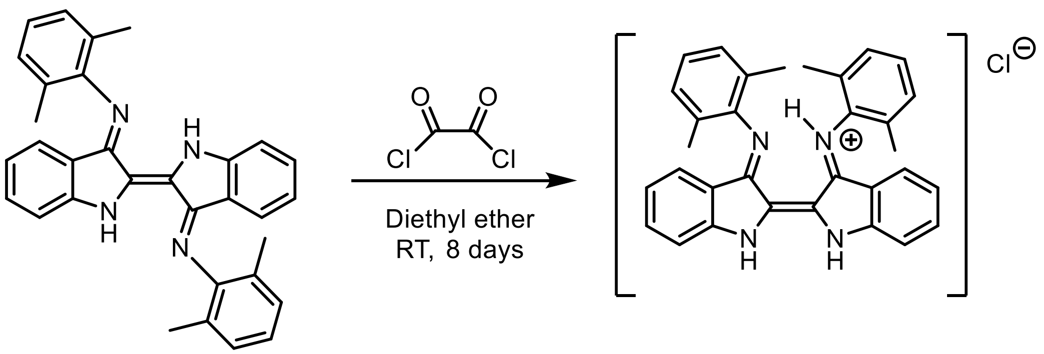

1.16a **4.1a**

Scheme 4.10 Unsuccessful acylation by following the literature procedure (1939) on **1.16a** and the obtained reaction product **4.1a**.

Therefore, we explored a modified route to obtain the oxalyl DmP Nindigo **4.6a**. **Scheme 4.11** shows our modified synthesis in toluene. After the injection of oxalyl chloride, the purple solution of **1.16a** instantly changed colour to teal which agrees with the previous observation of the formation of **4.1a**. Upon heating, the mixture solution becomes red. Red crystals precipitate out upon cooling. The ^{1}H NMR spectrum of the red crystals contained a singlet at 17.81 ppm. Treatment of triethylamine changed the colour to yellow, and the singlet at 17.81 ppm disappeared. The ^{1}H NMR spectrum of the yellow solution contained similar aromatic chemical shifts, but the overall proton integration was less by 1H. X-ray crystallography confirmed the final yellow product to be a neutral oxalyl-tethered **4.6a**. We suspected that the initially obtained red precipitate was the protonated form, **4.6aH$^+$**, with a chloride counter-anion. Growing single crystals directly from the red solution was unsuccessful due to decomposition. Instead, X-ray crystals were grown from a suspension solution of neutral **4.6a** in diethyl ether with added trifluoroacetic acid. The red crystals were confirmed to be **4.6aH$^+$** with a trifluoroacetate counter-anion. In regard to J. van Alphen's observations, we suspect the red-violet crystals that he discovered was a protonated oxalyl Nindigo **4.6cH**$^+$ with a chloride based on the red crystal colour and the absence of a base in the synthesis.

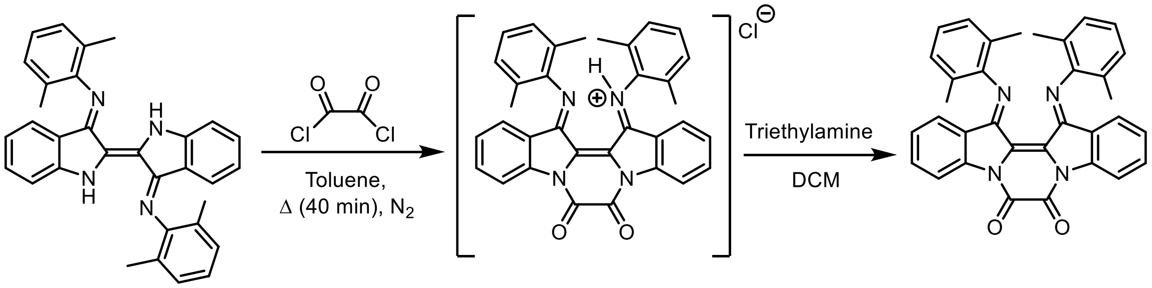

1.16a **4.6aH$^+$Cl$^-$** < 79% **4.6a** 70%

Scheme 4.11 Successful synthesis of **4.6a**.

Characterization of the **4.6aH**$^+$Cl$^-$ was not possible because of the rapid decomposition that occurred in an ambient environment. The compound was unstable towards moisture. For example, a decomposition was observed over 13 hours of ^{13}C NMR collection period. In order to investigate the decomposition pathway, a separate experiment was performed in **Scheme 2.6** where a DCM solution of **4.6a** was suspended with 1M $HCl_{(aq)}$ at room temperature for 24 hours. Brown crystals precipitated from the suspension solution, and the X-ray diffraction confirmed the formation of oxalylindigo (**2.7**) in which both imine groups are hydrolyzed.

Elemental analysis of isolated **4.6aH**$^+$Cl$^-$ showed that the carbon content is 4.4 % below the calculated value and nitrogen is 0.9 % lower. This result suggests that the red precipitate contains non-carbon containing impurities. Since the result was obtained despite our best effort to keep in a dry condition, the yield of **4.6aH**$^+$Cl$^-$, therefore, can only be estimated. Furthermore, neutralization into **4.6a** proceeded as soon as **4.6aH**$^+$Cl$^-$ was recovered in order to avoid hydrolysis. For characterization of the protonated Nindigo, we attempted direct acidification of **4.6a**. TFA could have been used, however, in the previous X-ray structure, the protonated species carried one extra molecule of TFA. Therefore, tetrafluoroboric acid (HBF_4) was chosen for the bulk synthesis in the hopes of preparing a protonated species without an extra equivalent of acid. **Scheme 4.12** shows the protonation of the **4.6a** in toluene. The **4.6aH**$^+BF_4^-$ salt precipitate as a red powder and the recrystallization in $CHCl_3$/hexanes yields the product in a microcrystalline form in quantitative yield. However, **4.6aH**$^+BF_4^-$ was easily neutralized to **4.6a** upon contact with ambient moisture, yet hydrolysis of the imine group did not occur. The **4.6aH**$^+BF_4^-$ salt was stable when kept in a water-free environment, therefore used for further characterizations of the protonated Nindigo.

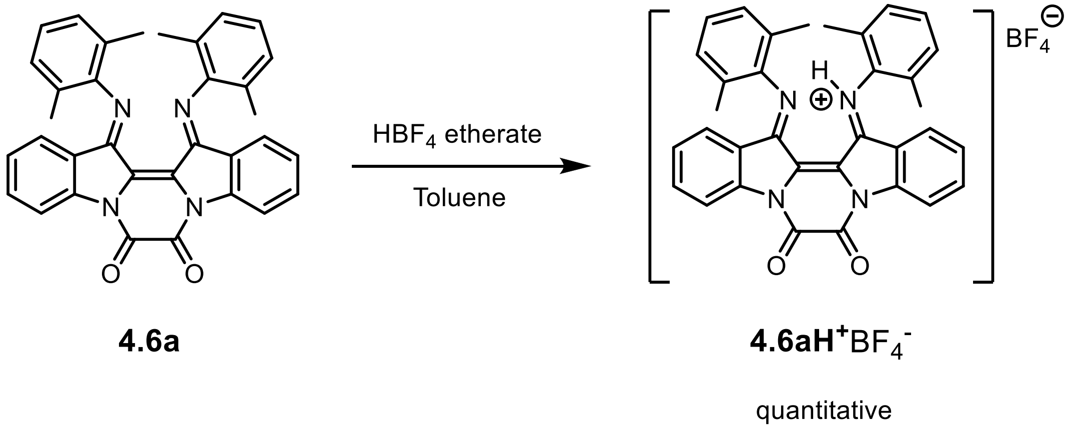

Scheme 4.12 Protonation of **4.6a** using HBF_4 etherate.

The synthesis of the oxalyl Nindigo with a DmP substituent in toluene (**Scheme 4.11**) was successful, and a reaction with a less bulky group on Nindigo was explored. *p*Tol Nindigo **1.16b** was initially subjected to the toluene reflux as shown in **Scheme 4.13**. The solution was rather yellow even without adding a base. The ^1H NMR spectrum revealed the presence of multiples species. X-ray crystals were grown from the reaction solution and two structures were identified in **Figure 4.2**. Compounds **4.8** and **4.8-Cl** co-crystallized with a composition ratio of 75 : 25 %, respectively. The two compounds differ by a single chlorine atom at the *meta* to the indole nitrogen. Their generic structure composes of a reduced **1.16b** as the core, one oxalyl group connecting an indole nitrogen atom and a (formally) imine nitrogen, and lastly a carbonyl group was inserted in the same way on the opposite bay area of the molecule. Column chromatography could not separate **4.8** and **4.8-Cl** due to similar polarities derived from the common structure.

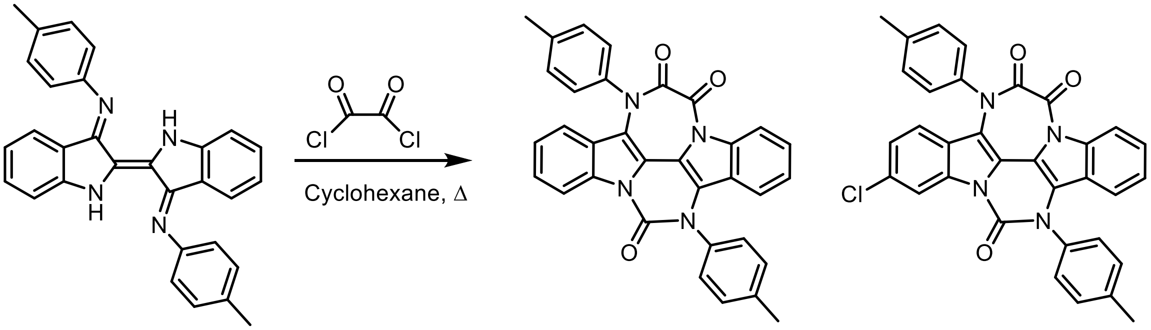

1.16b **4.8** **4.8-Cl**

Scheme 4.13 Reaction of *p*Tol Nindigo **1.16b** with oxalyl chloride and observed insertion compounds, **4.8** and **4.8-Cl**.

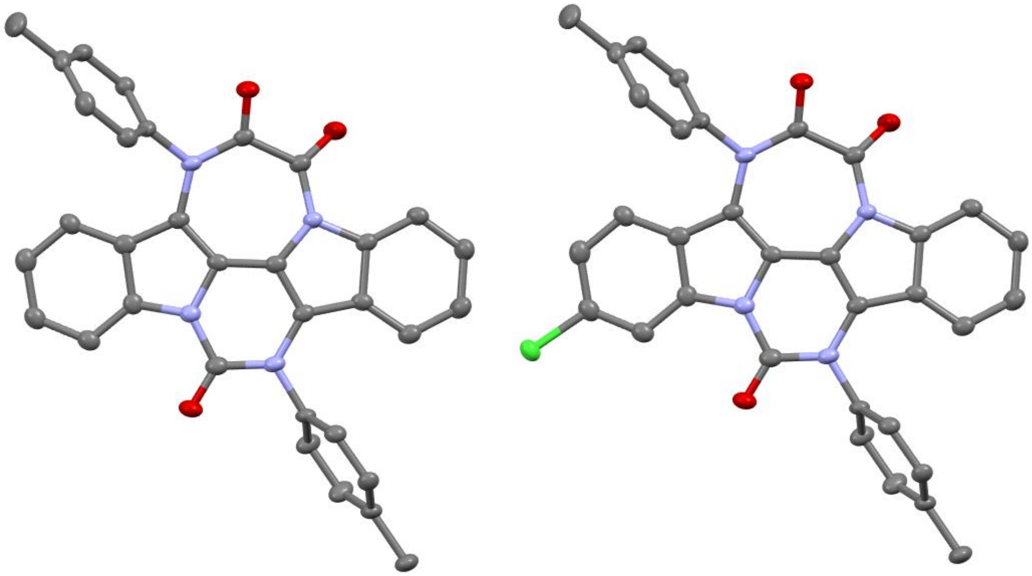

Figure 4.2 X-ray structures of **4.8** (left) and **4.8-Cl** (right). Hydrogen atoms are omitted for clarity. Thermal ellipsoids represented at 50%.

The source of the carbonyl group and the chloride can be explained from the known light-induced decomposition of oxalyl chloride in **Scheme 4.14**. Oxalyl chloride is known to react with saturated hydrocarbon solvents (i.e. *n*-heptane, cyclohexane) in the light to cause insertion of half of the molecule into the solvent. The remaining fragment results in the liberation of carbon monoxide and HCl.[130] A gas-phase photolysis study proposed that the wavelength of the radiation predominates specific bond cleavage to liberate a free radical and atoms.[131] The formation of the chlorine radical is supported by the observed chlorine substitution at the 5th position on the **1.16b**'s indolyl ring. If it were to be an electrophilic aromatic substitution, the 6th position would have been favoured. Although the literature noted aromatic hydrocarbon solvents (such as toluene, benzene) inhibit this photo-degradation due to an absorption of the activation radiation by the solvents, the successful acylation with **1.16a** (but not in **1.16b**) raises a question about the reactivity of Nindigo also plays a role.

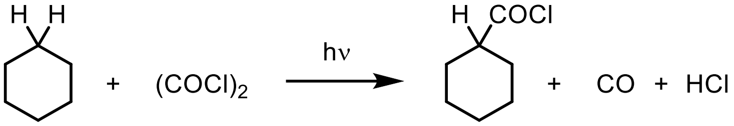

Scheme 4.14 Light-induced decomposition of oxalyl chloride in cyclohexane.

4.2.4.1. Chemical Reduction of the Oxalyl Nindigo Bridge

In order to expand *cis*-Nindigo derivatives, modification of the oxalyl Nindigo **4.6a** is explored. **Scheme 4.15** shows a reduction of oxalyl group in tethered diindole into an ethane-bridge using $LiAlH_4$ reducing agent.[132]

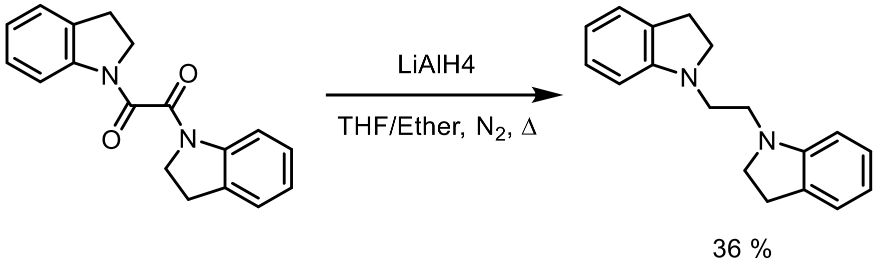

Scheme 4.15 Literature reduction of the oxalyl group using $LiAlH_4$.

Attempt to reduce oxalyl tether on Nindigo **4.6a** using $LiAlH_4$ in **Scheme 4.16** led to the destruction of the bridge, and resulted in unbridged *trans*-Nindigo **1.16a** as confirmed by ^1H NMR.

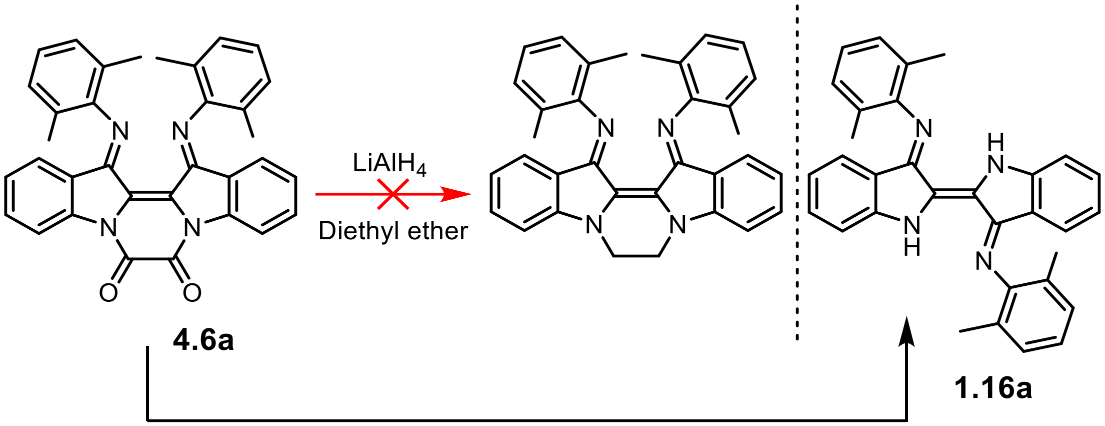

Scheme 4.16 Failed reduction on oxalyl group on **4.6a** using LiAlH$_4$.

A milder reducing agent, Sodium borohydride (NaBH$_4$), was able to reduce the oxalyl ketones into an alkane chain. **Scheme 4.17** shows the formation of protonated ethane-type bridged Nindigo **4.9aH$^+$** from a treatment of **4.6a** with NaBH$_4$ in methanol, followed by quenching with ammonium chloride. X-ray crystallography confirmed that the product contains a racemic mixture in which two alcohol groups on the bridge moiety are *trans* to each other. Notably, the **4.9aH$^+$** was only stable while protonated; attempts to neutralize with triethylamine caused a loss of the bridge that leads to an untethered *trans*-Nindigo **1.16a**. Recrystallization from hot ethyl acetate results in a product containing a varying ratio of product : ethyl acetate (between 0.6–1.1).

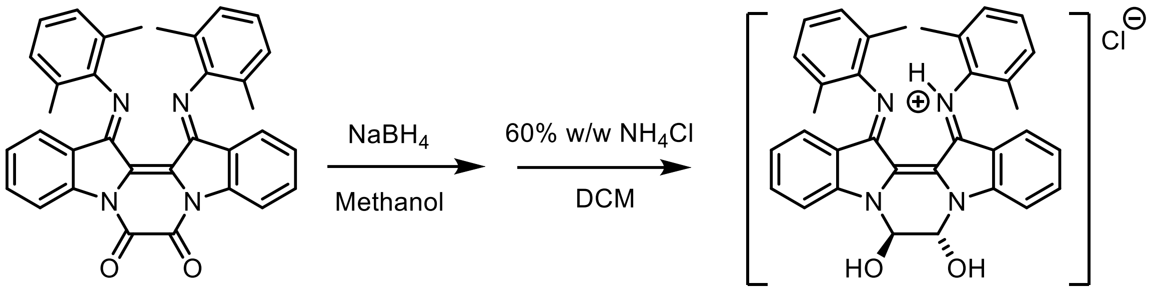

4.6a

4.9aH$^+$

(+racemic mixture)

54-65 %

Scheme 4.17 Synthesis of **4.9aH$^+$** from the reduction of oxalyl group on **4.6a** using NaBH$_4$.

4.2.5. Synthesis of Oxalyl Indigo Monoimine

Oxalyl tethered indigo monoimine (**4.7a**) was synthesized using similar conditions to the ones used for Nindigo **4.6a** synthesis. Acylation of indigo monoimine **1.17a** did not require heat, however, overnight stirring was necessary. During the initial injection of the oxalyl chloride, the purple solution of the **1.17a** instantly became teal, however, the colour quickly turned red within the first 5 seconds of the injection. Soon thereafter, a red powder precipitated out from the reaction mixture. Similar to the protonated di-imine analogue, the red protonated mono-imine species was extremely water-sensitive. Therefore, neutralization with triethylamine was conducted immediately upon isolation of the protonated species. The addition of triethylamine into the red solution of the precipitates results in a rapid colour change into yellow. Recrystallization in methanol yields a brown powder of **4.7a** in pure form in a 65 % yield. X-ray crystallography confirmed the structure of **4.7a**.

Performing this reaction with external heat produces a byproduct. **Figure 4.3** shows the ^{1}H NMR spectral comparison of the reaction outcome with heat (top) and at room temperature (bottom). The presence of the byproduct can be easily noticed by subtraction of the two spectra's proton integrations. The byproduct possesses almost the same chemical shifts as the **4.7a** except for an additional doublet at 6.6 ppm and an absence of a triplet at 7.6 ppm. The two said signals correspond to the Nindigo's indolyl moiety. Subtraction of the proton integrations between the two spectra indicates the byproduct contains a total of 16H in comparison to 17H protons of the desired product. HR-MS of the mixture solution indeed confirmed a presence of a mono-chlorinated byproduct (**4.7a-Cl**). It is suspected that chlorination occurred at the Nindigo's indolyl 6-position where it caused the disappearance of the triplet at 7.6 ppm in the desired product. Chlorination at the Nindigo's indole 6th position was previously observed in **Scheme 4.13**. Column chromatography was unable to separate **4.7a-Cl** from the mixture solution of **4.7a** since two species have identical R_f values.

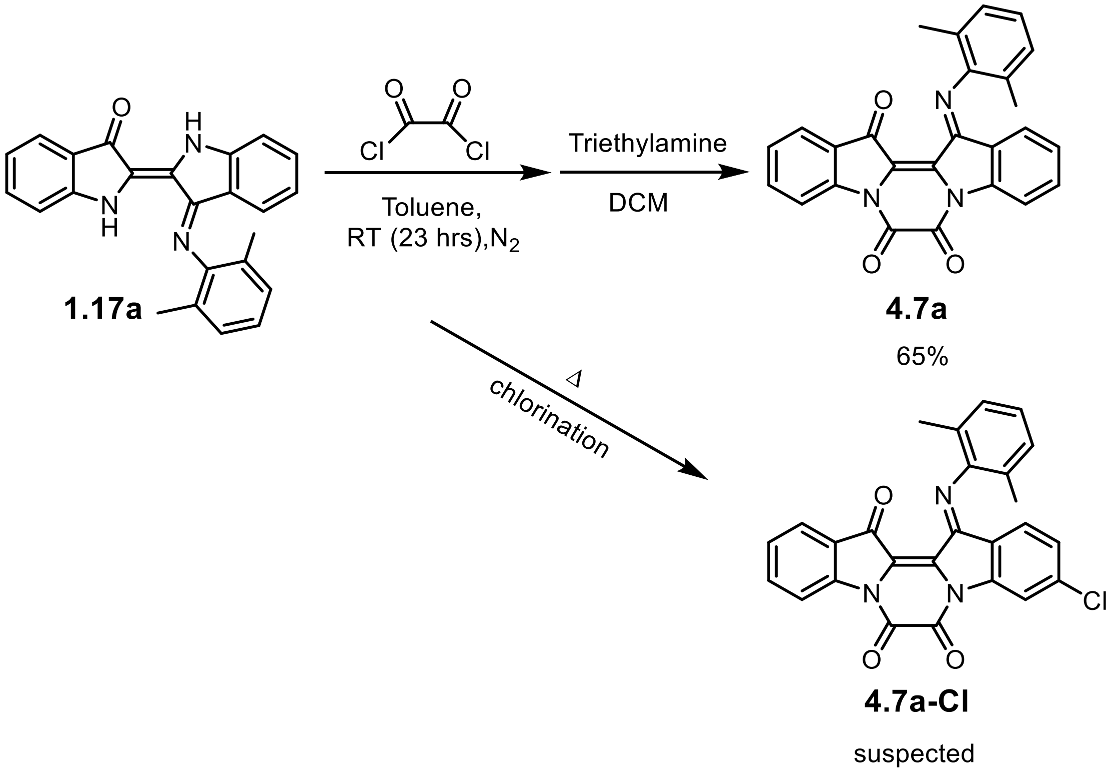

Scheme 4.18 Different reaction outcomes in the synthesis of **4.7a** based on of presence of external heat.

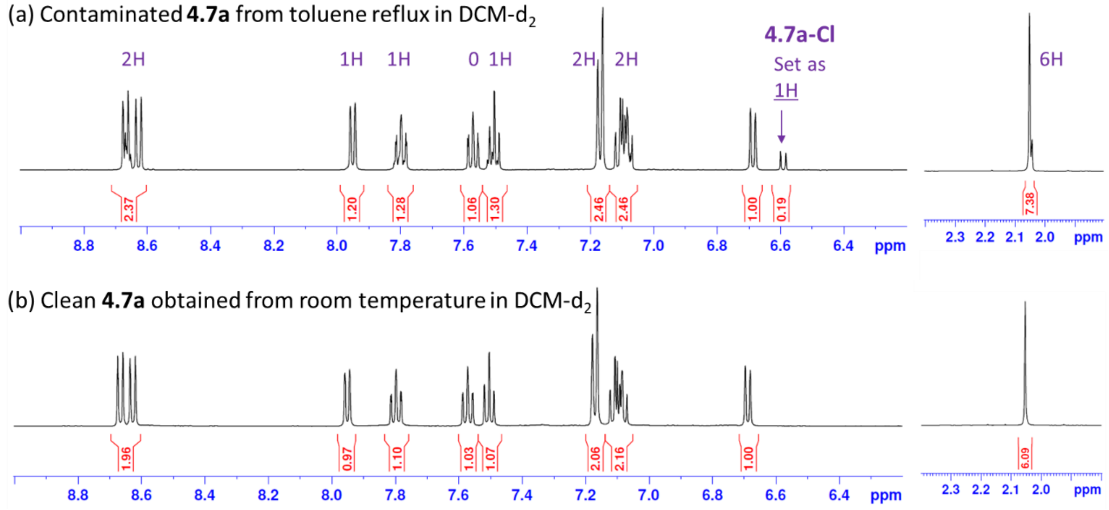

Figure 4.3 ^{1}H NMR spectral comparison of formation of **4.7a**: (a) reaction crude from toluene reflux (b) the clean product obtained at room temperature. Subtraction in the proton integrations between two spectra indicates the presence of the **4.7a-Cl**.

4.3. NMR Characterization

Figure 4.4 shows ^{1}H NMR spectral comparison of the tethered *cis*-(N)indigoid compounds with respect to oxalylindigo (**2.7**) as a reference. All hydrogen atoms are fully assessed based on additional 2D NMR experiments. An indigoid system (i.e. indigo, Nindigo, thioindigo, etc) generally follows a numbering system of an indole, however, the backbone hydrogen atoms are re-labelled in order to differentiate the indolyl groups derived from the indigo moiety and the Nindigo compartments. **Figure 4.5** depicts the hydrogen atom labelling used in this discussion. An example of the proton assignment involves 1) grouping of the nearby indolyl protons by ^{3}J ^{1}H-^{1}H COSY; 2) identification of the ‘a’ proton through a ^{3}J ^{1}H-^{13}C correlation with a carbon atom on the indigoid carbonyl and 3) locating the ① proton on the Nindigo’s indolyl moiety through a NOESY correlation with a -CH_3 signal derived from the imine substituent.

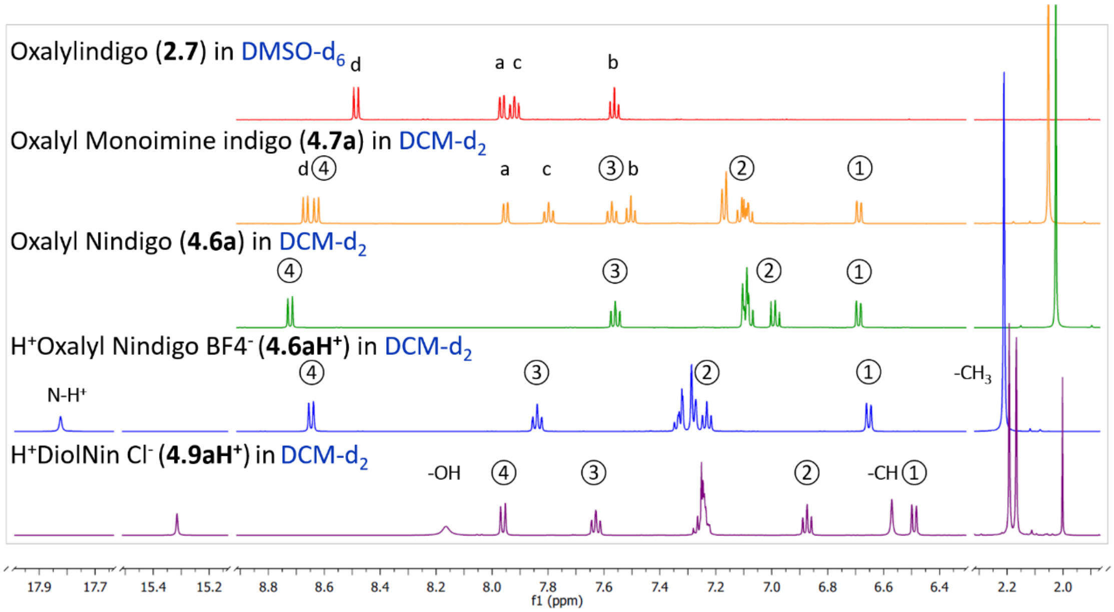

Figure 4.4 ^{1}H NMR spectral comparison of cis-tethered (N)indigoids.

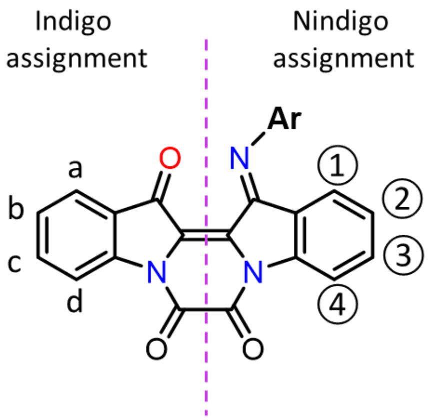

Figure 4.5 A diagram of hydrogen atom labels on indigo/Nindigo moiety.

The indolyl protons experience different chemical shift patterns in the given *cis*-indigoid and related cis-Nindigo analogues. The Nindigoid indolyl protons appear in the lower ppm. The aryl substituent causes a through-space shielding in the adjacent Nindigo indolyl moiety. The extent of shielding roughly correlates to the spatial distance from the imine group. The ①, ② and ③ protons of Nindigo **4.6a** experience upfield chemical shifts by 1.28 ppm, 0.48 ppm and 0.36 ppm, respectively in comparison to **2.7**. An example of a through-space shielding is demonstrated on 1-methyl-8-phenylnaphthalene.[133] The methyl group is upfield shifted by 0.68 ppm in comparison to its initial chemical shift in 1-methylnaphthalene. Indigo monoimine **4.7a** presents chemical shift patterns of both Nindigo and indigo.

Two protonated *cis*-Nindigos contain a single -N$\underline{H}$ signal. These compounds contain a mirror symmetry in the solution state in an NMR timescale. Protonation of Nindigo (**4.6aH$^+$**) causes a slight downfield shift in protons ② and ③ as well as in the -CH_3 singlet. The chemical shifts of **4.9aH$^+$** are consistently upfield relative to the corresponding protons on **4.6aH$^+$** due to an enhanced electron delocalization of the indole nitrogens into the Nindigo core. **Figure 4.6** depicts resonance structures of **4.9aH$^+$** after the lone pair electron delocalization, in which greater electron density is located at the ④ proton. The indole nitrogen atoms on the oxalyl-tethered compounds have less available electron density that could participate in delocalization into the Nindigo core due to a direct conjugation with the electron-withdrawing carbonyl group to form an amide.

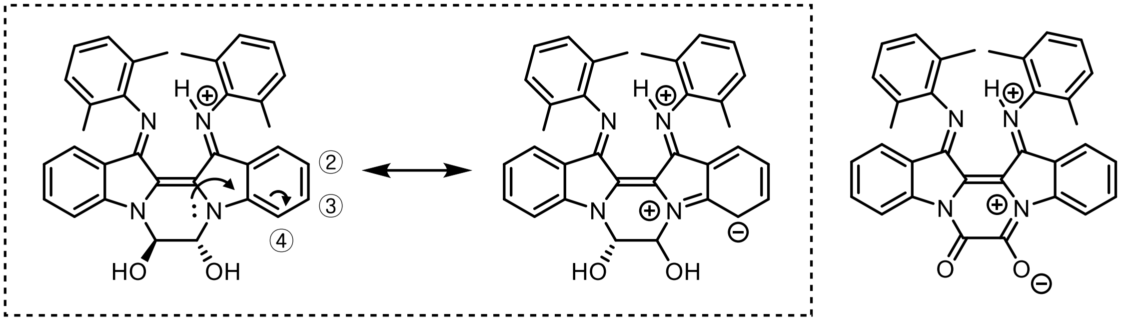

4.9aH⁺ **4.6aH⁺**

Figure 4.6 Resonance structures of **4.9aH$^+$** in comparison to **4.6aH$^+$**.

Interestingly, **4.9aH$^+$** shows splitting in the -CH$_3$ peaks in both ^{1}H NMR and ^{13}C NMR. X-ray crystallographic data found that two different magnetic environments are created due to spatial distances to the alcohol groups (see **Section 4.4.2**). The magnetic environments are interchangeable after a heterocycle ring-flip; however, the rate is slower than the NMR timescale.

4.3.1. p*K*$_a$ Estimation using ^{1}H NMR Spectroscopy

^{1}H NMR spectroscopy has become widely used for the determination of relative acidity owning to its simple requirements of sample preparation and a rapid experimental time.[134-136] We initially intended to determine the relative acidity of the protonated oxalyl Nindigo **4.6aH$^+$**. This approach turned out not to be feasible due to two problems. First, although the protonated Nindigo shows good solubility, the neutral species is poorly soluble in most common solvents such as THF, ACN and DMSO including water. Among the former three organic solvents, DMSO was chosen for our pK_a exploration because it provided a better solubility; however, 3.2 mg of Nindigo did not fully dissolve in 0.6 mL

DMSO-d_6. The second problem is the intrinsic instability of the protonated species towards ambient water. Neutralization was mostly observed in DMSO-d_6 even after pre-drying the solvent over molecular sieves (**Figure 4.8**). However, getting an estimation of the pK_a will provide a basic understanding of the compound's nature and it could benefit the future reactions with the oxalyl Nindigo **4.6a**. Therefore, we decided to use ^{1}H NMR spectroscopy to find an acidity range by monitoring the changes against known standards. To make sure our initial baseline consists of one species, **4.6a** was used as a starting point. The standards are converted into conjugate acid to carry a BF_4^- counter-anion in order to study the acidity of the **4.6aH$^+$**BF_4^-. The purity of all reagents is verified by ^{1}H NMR. All glassware was pre-dried in the oven and the compounds were kept in dry condition. Note that this approach cannot avoid partial neutralization. Therefore, the measured pK_a window will underestimate the relative acidic strength; thus, the pK_a ranges appear lower than their true value. Prior to DMSO-d_6 investigation, we have observed in **Figure 4.7** that neutral Nindigo becomes fully protonated in acetonitrile-d_3 upon addition of 1.0 equivalence of anilinium BF_4^-. This information provided us that pK_a of **4.6aH$^+$**BF_4^- is greater than 10.64[137] in acetonitrile.

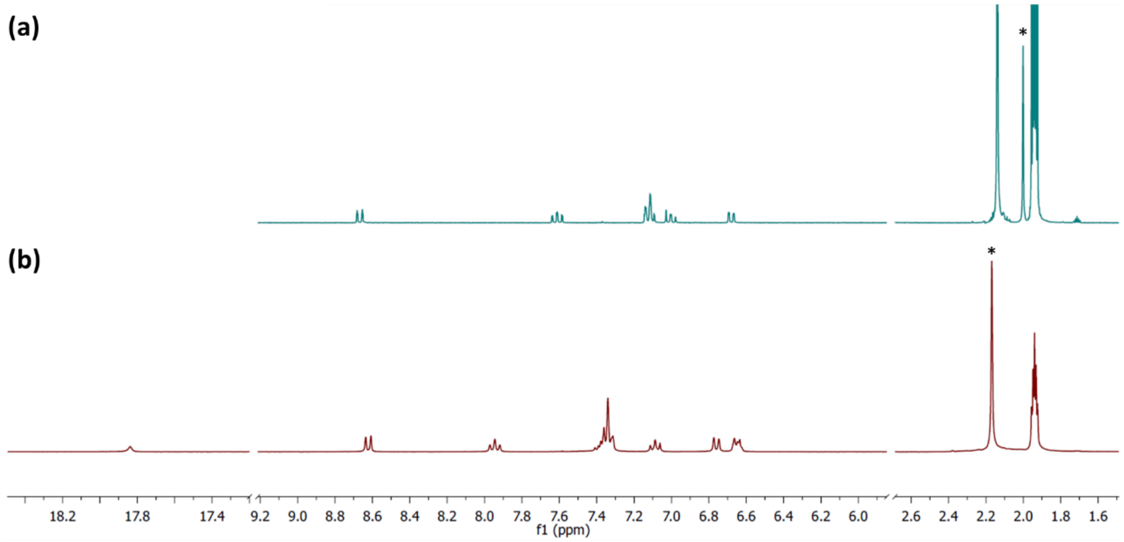

Figure 4.7 ^{1}H NMR spectra of (a) neutral Nindigo **4.6a** in ACN-d_3 (b) after addition of 1.0 *eq.* of anilinium BF_4^-. Methyl peaks are denoted with (*).

Dissolution of **4.6aH**$^+$$BF_4^-$ in DMSO-d_6 causes a partial neutralization despite our effort to keep in a dry condition. **Figure 4.8** shows the peaks broadening in the aromatic region due to the exchange between two species in the NMR timescale. However, the -CH_3 peaks are well-separated and are used as NMR handles to identify each species.

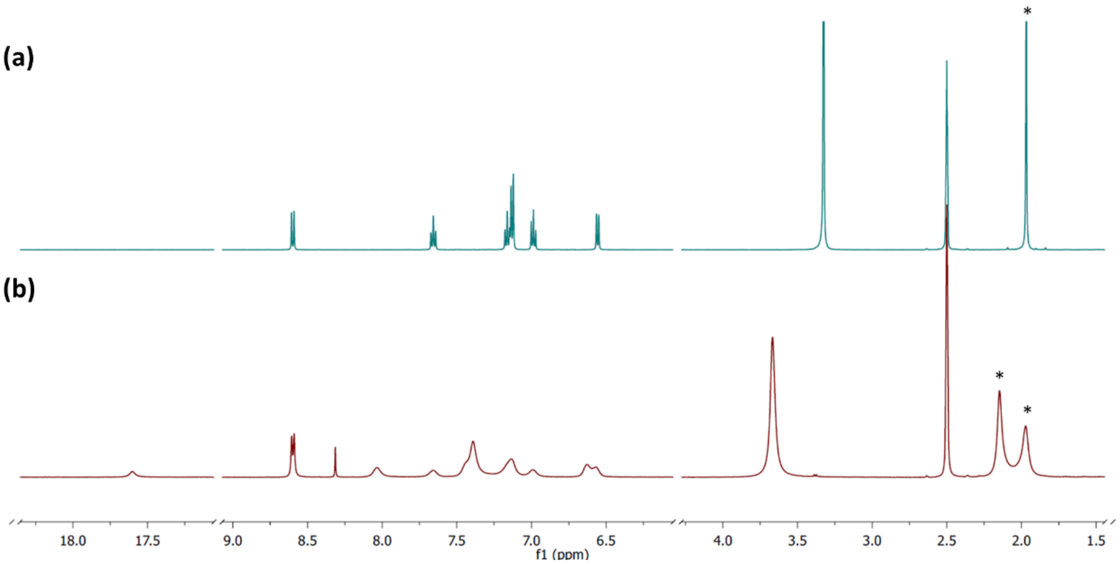

Figure 4.8 ^{1}H NMR spectra of (a) reference neutral Nindigo **4.6a** in DMSO-d_6 (b) partial neutralization of **4.6aH**$^+$BF$_4^-$ after dissolution in DMSO-d_6. Methyl peaks are denoted with (*).

When **4.6a** was treated with 1.0 equivalence of anilinium BF$_4^-$ in DMSO-d_6, partial pronation was observed as seen in **Figure 4.9** where the growing of the protonated species' -CH$_3$ signal was detected (indicated by a red arrow). Lutidinium BF$_4^-$ was able to partially protonate to a lesser degree but collidinium BF$_4^-$ did not protonate at all. Therefore, the pK_a window of the **4.6aH**$^+$BF$_4^-$ spans the ranges of anilinium (pK_a = 3.6)[137] and lutidinium (pK_a = 4.46)[138] in DMSO.

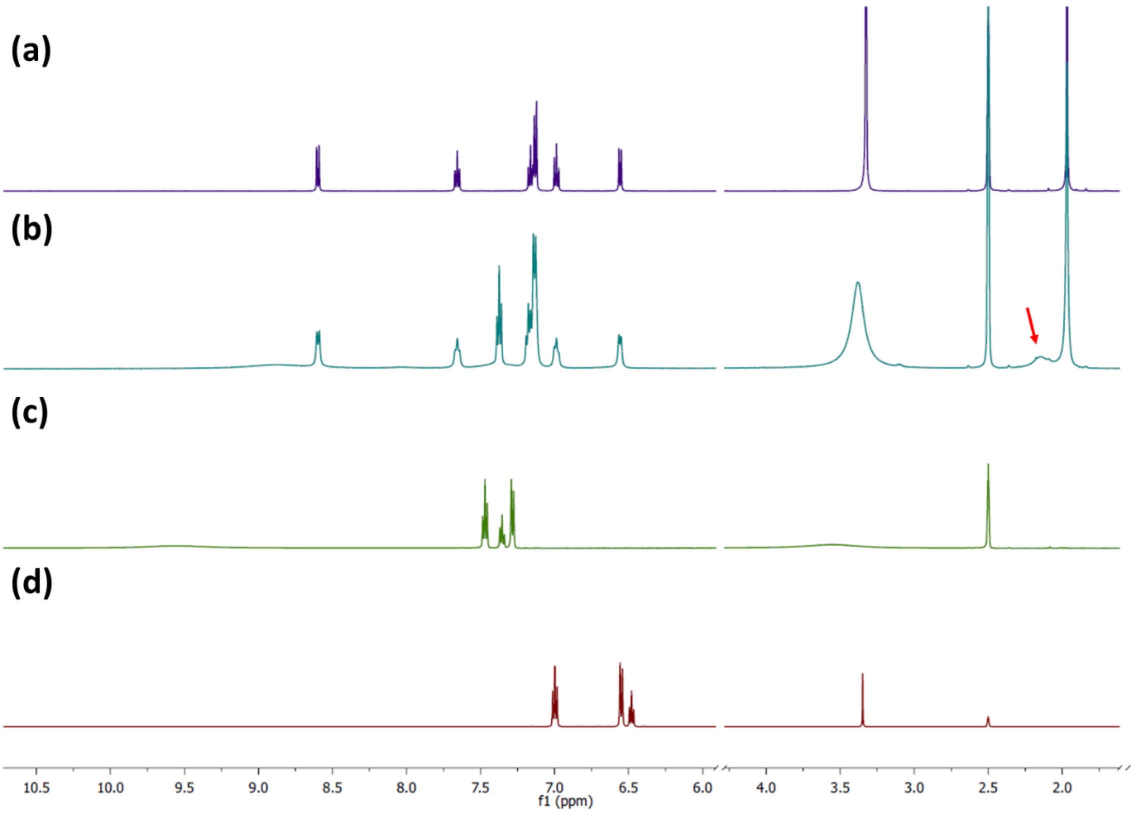

Figure 4.9 ^{1}H NMR spectra of (a) neutral Nindigo **4.6a** in DMSO-d_6 (b) after addition of 1.0 *eq*. anilinium BF_4^- (c) reference anilinium BF_4^- in DMSO-d_6 (d) reference aniline in DMSO-d_6. The red arrow indicates growing of the protonated species **4.6aH**$^+BF_4^-$.

In the case of indigo monoimine **4.7a**, no spectral changes were detected after treatment of anilinium BF_4^- nor diphenylammonium triflate (pK_a: -1.1)[137] in DMSO-d_6. Therefore, pK_a of protonated **4.7aH**$^+BF_4^-$ is estimated to be less than -1.1 in DMSO. The stronger acidity of the N···O system is due to the more electronegative oxygen atom being less basic than nitrogen.

4.4. X-ray Crystallography

Single X-ray crystals of monoimine **4.7a** and Nindigo **4.6a** were obtained from saturated solutions of DCM and slow evaporation of DCM / ACN, respectively. The X-ray structure of indigo **2.7** was previously discussed in Chapter 2. A single X-ray crystal of **4.6aH**$^+$ was obtained with a trifluoroacetate anion from in-situ protonation with TFA in diethyl ether. A single crystal of **4.9aH**$^+$ was grown as a chloride salt from a saturated solution of acetonitrile.

4.4.1. Neutral Oxalylindigoids

The imine group containing compounds in **Figure 4.10** are compared with indigoid counterpart **2.7** in order to understand the effect of imine group on the compounds' structures. **Table 4.1** lists a selection of the structural data. All three oxalyl group containing molecules show a fairly planar backbone where the twist angle measured between the two half indolyl planes is consistently less than 10°. Notably, monoimine **4.7a**'s O2 and N2A atoms locate below and above the average plane of the backbone as seen in **Figure 4.10**. As the ketone group is replaced with the imine moiety, the sterics of the imine substituent brings non-bonded distance between two heteroatoms (oxalylindigo: O2···O2A; indigo monoimine: O2···N2A, Nindigo: N2···N2A) closer. The aryl substituents lie between 84-86° with respect to the plane of the nearby indolyl group, therefore causing a poor overlap with the π-orbitals in the backbone. The structurally symmetric compounds (oxalylindigo **2.7**, oxalyl Nindigo **4.6a**) contain statistically equivalent bond lengths between the two indolyl halves of the molecule. On the other hand, the bonds observed for **4.7a** show statistically different bond lengths between the two indolyl groups especially among the atoms located in the H-chromophore (C2–C1 vs. C2A–C1A and C1–N1 vs. C1A–N1A also N1–C9 vs. N1A–C9A).

The observed central C=C bond lengths are similar for all three compounds. However, the central C–C bond length of **2.7** was notably shorter compared to the rest of the imine group containing compounds. These three oxalyl indigoids show similar C=C bond lengths to those of the parent *trans*-indigo (1.359(2) Å)[46], *trans*-indigo monoimine **1.17a** (1.354(2) Å)[93] but they are significantly shorter than *trans*-Nindigo **1.16a** C=C (1.402(2) Å)[93]. In the Nindigoid systems, the electron-withdrawing nature of the oxalyl group in the **4.6a** exerts more defined alternation of the single/double bond in the H-chromophore region compared to untethered **1.16a**. For example, the imine C=N lengths and the central C=C length in **4.6a** were shortened while the other four distances in the pyrrole ring became significantly elongated.

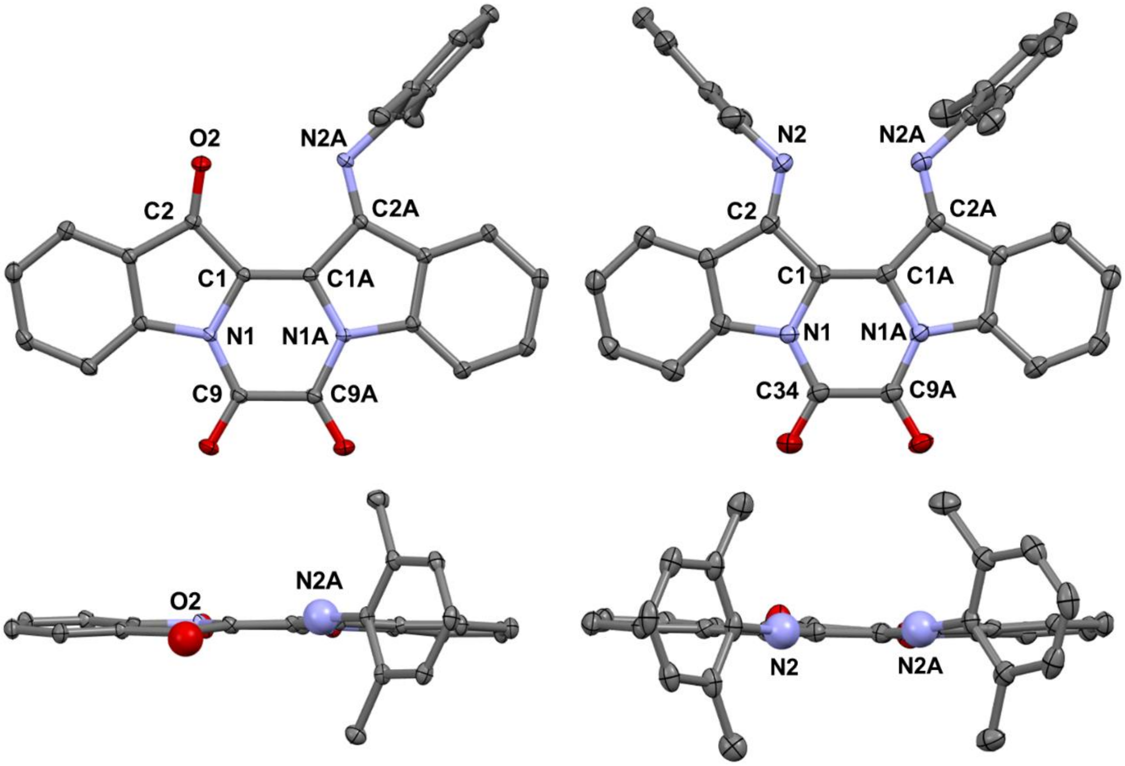

Figure 4.10 X-ray structures of **4.7a** (left) and **4.6a** (right). Top: front view. Bottom: rotated view. Hydrogen atoms are omitted for clarity. Thermal ellipsoids represented at 50%.

Table 4.1 Selected bond distances (Å) and angles (°) in neutral oxalyl indigoids.

Distance(A)	**2.7**	**4.7a**	**4.6a**
Interatomic distance	*O···O*	*O···N*	*N···N*
(Å)	3.00(3)	2.950(1)	2.899(1)
C=O distance (Å) or	1.23(2)	1.212(1)	**1.282(2)**
***C=N distance** (Å)*	1.22(2)	**1.278(1)**	**1.283(2)**
Central C=C (Å)	1.351(7)	1.352(2)	1.360(2)
Central C-C (Å)	1.510(5)	1.524(2)	1.521(2)
Backbone twist (°)	0.83	8.35	6.69
DmP1∠ Indole1 (°)	-	-	84.90
DmP2∠ Indole2 (°)	-	85.67	84.14

4.4.2. Protonated *cis*-Nindigos

Figure 4.11 shows X-ray structures of **4.6aH$^+$** and **4.9aH$^+$**. Both protonated *cis*-Nindigos exhibit asymmetric NH···N hydrogen bonding, however, the fitting model determined that two imine nitrogen atoms within the molecule are equally protonated. **4.6aH$^+$**, similar to its neutral counterpart **4.46a**, exhibit statistically equivalent bond lengths between the two halves of the molecule. **4.9aH$^+$** displays a similar bond length symmetry except for a minor discrepancy in one set of bonds; C1–C2 (1.470(2) Å) and C1–C2A(1.460(2) Å).

Table 4.2 lists a selection of structural data in comparison to the untethered protonated Nindigo[126] **4.1a**. All protonated Nindigos show significantly shortened N···N distances compared to the neutral oxalyl Nindigo **4.6a**. Compound **4.6aH$^+$** and untethered **4.1a** exhibit similar N···N distance. However, **4.9aH$^+$** exhibits the longest distance. It is important to note that these protonated species contain the same aryl group, the difference observed in bond lengths/ distances provides a qualitative measure of effect derived from the organic tether. Therefore, this comparison provides an interesting proof-of-concept that a bridge moiety could be a means to tune the size of the imine pocket, which will in turn relate to the compound's acidic strength. The oxalyl bridged **4.6aH$^+$** produced a noticeable alternation of the single/ double bond lengths in the H-chromophore region; the strong electron-withdrawing character inhibits effective delocalization of the nitrogen lone pair in the Nindigo's backbone. The central C=C bond length and the N=C distances in one half of the molecule were shorter than **4.9aH$^+$**. In addition, the average angle between the aryl groups with respect to the plane of the nearby indolyl group is lowered in **4.6aH$^+$,** from ~

84° to ~ 69° when compared to its neutral counterpart. A slight increase in π-conjugation from the imine pendant group is suggested upon protonation.

The single crystal of **4.9aH⁺** consists of a racemic mixture in a 1:1 ratio. Stereochemistry is derived from its ethane bridge where two stereogenic carbon centres have R,R and S,S configurations. In **Figure 4.11**, R,R is shown. In the previous discussion in section 4.3, the ^{1}H NMR spectrum of **4.9aH⁺** showed the splitting of the -CH_3 singlets. According to the X-ray structure, the four alkyl carbon atoms can be sorted into two groups based on the spatial distances to an alcohol oxygen atom located on the same plane. The measured distances between C17···O1A (6.178(2) Å) and C17A···OA1 (6.016(2) Å) are significantly shorter than the distances between C16···O1 (6.716(2) Å) and C16A···O1 (6.698(2) Å). Spatial interaction between the methyl group and the oxygen moiety creates two different magnetic environments.

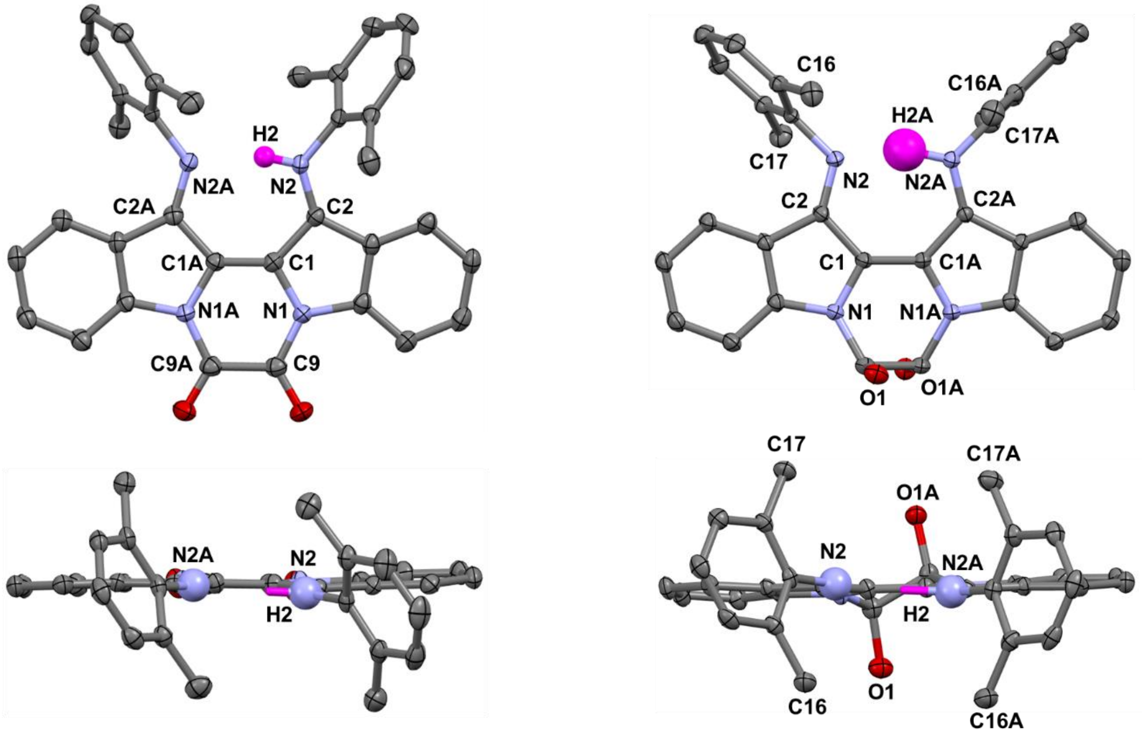

Figure 4.11 X-ray structures of **4.6aH**$^+$ (left) and **4.9aH**$^+$ (right). Top: front view. Bottom: rotated view. Hydrogen atoms except H2 and H2A are omitted for clarity. Thermal ellipsoids represented at 50%.

Table 4.2 Selected bond distances (Å) and angles (°) in protonated *cis*-Nindigoids.

Parameter	**4.6aH**$^+$	**4.9aH**$^+$	**4.1a**^{a}
Interatomic N⋯N (Å)	2.618(3)	2.707(2)	2.613(1)
C=N distance (Å)	1.286(4) 1.296(4)	1.311(2) 1.306(2)	1.315(1) 1.301(2)
Central C=C (Å)	1.355(4)	1.372(2)	1.385(2)
tether C-C (Å)	1.524(4)	1.537(2)	-
Backbone twist (°)	4.99	8.63	9.08
DmP1∠ Indole1 (°)	67.62	79.46	85.51
DmP2∠ Indole2 (°)	69.53	82.05	83.13

^{a} Reproduced from Reference[126].

4.5. UV-Vis Spectroscopy

The three oxalyl-tethered neutral indigoid compounds exhibit absorption wavelengths in the visible region at 429 nm, 426 nm and 419 nm in acetonitrile for oxalylindigo (**2.7**) indigo monoimine **4.7a** and Nindigo **4.6a**, respectively. This $\pi\rightarrow\pi^*$ transition is due to electron "push-pull" between the indole nitrogen donor and the acceptor group (C=O in indigo; C=N in indigo monoimine and Nindigo).[86] An oxalyl bridge weakens the electron-donating ability of the indole nitrogens due to a direct conjugation of the electron-withdrawing carbonyl groups. As the number of imine groups increases, a slight decrease in the absorption wavelength was observed. This trend was also seen in the *trans*-(N)indigoids: Indigo **1.5** (λ_{max} = 605 nm in CCl_4), monoimine **1.17a** (λ_{max} = 592 nm in DCM)[93] and Nindigo **1.16a** (λ_{max} = 584 nm in DCM)[93].

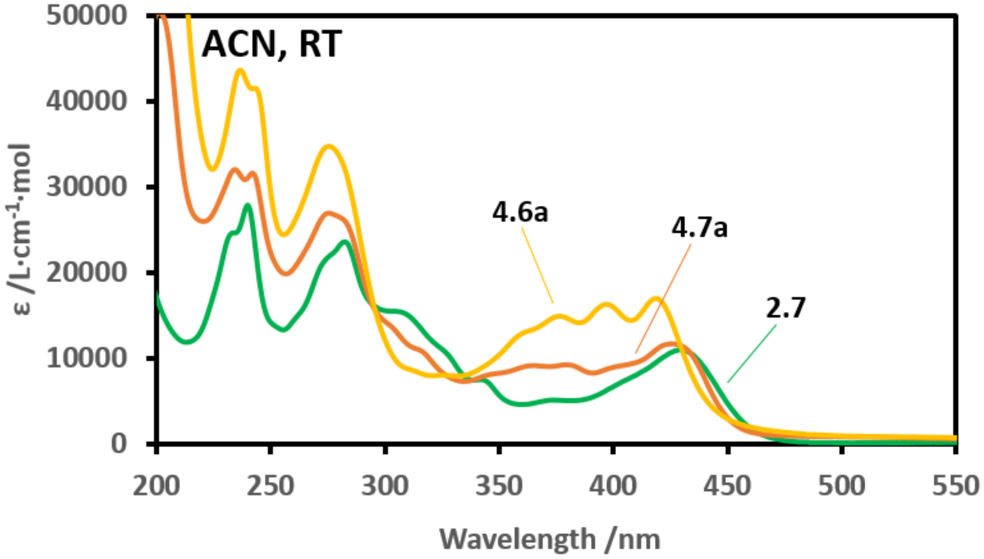

Figure 4.12 UV-Vis absorption spectra of neutral oxalyl indigoids: indigo **2.7** Nindigo **4.6a** and monoimine **4.7a** in acetonitrile.

The UV-Vis spectrum of the protonated oxalyl Nindigo **4.6aH**$^+$ was obtained from in-situ protonation of the neutral **4.6a** with excess (1.2 *eq*.) of the anilinium BF_4. The presence of anilinium BF_4 and aniline did not interfere in the absorption in the visible region. Protonated Nin **4.6aH**$^+$BF4$^-$ has an absorption maximum at 496 nm, and the alkane-type tethered **4.9aH**$^+$Cl$^-$ showed a much blue-shifted absorption wavelength at 627 nm in acetonitrile. As described above, the electron-withdrawing oxalyl bridge weakens the "push-pull" nature of the indigoid H-chromophore. On the other hand, then (electronically innocent) ethane-bridge exhibits similar absorption to untethered **4.1a**CF_3COO^- (λ_{max} = 650 nm)[139] in DCM. **Table 4.3** summarizes absorption wavelengths of tethered compounds.

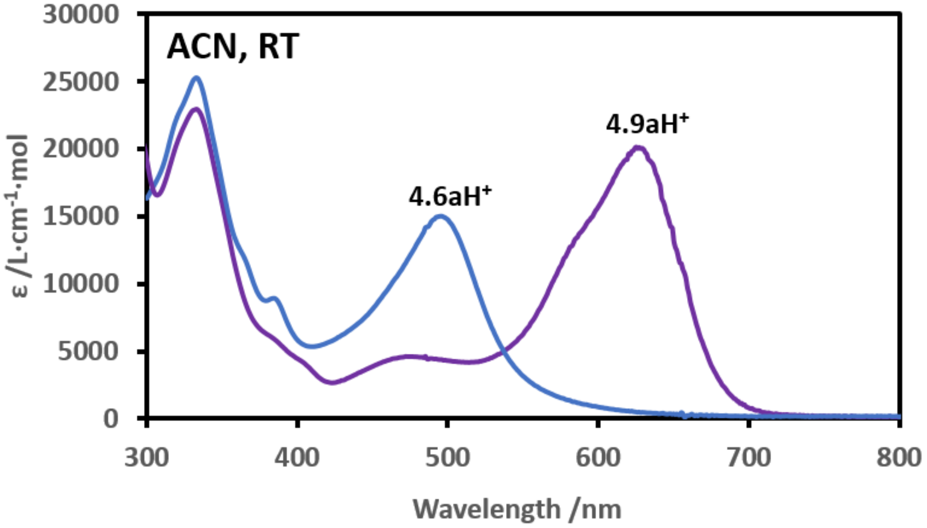

Figure 4.13 UV-Vis absorption spectrum of protonated tethered *cis*-Nindigo derivatives: **4.6aH**$^+$BF4$^-$and **4.9aH**$^+$Cl$^-$in acetonitrile.

Table 4.3 Absorption wavelengths of *cis*-Nindigo and related compounds in ACN.

Compound	λ_{max} *(nm) (ACN)*	ε *(L·mol⁻¹·cm⁻¹)*
2.7	429	11 000 (1000)
4.7a	426	11 800 (300)
4.6a	419	17 000 (400)
4.6aH$^+$BF4$^-$	496	14 800 (200)
4.9aH$^+$Cl$^-$	627	20 400 (400)

4.6. Cyclic Voltammetry

4.6.1. Neutral Oxalylindigoids

Figure 4.14 shows the cyclic voltammograms of the oxalyl-bridge containing neutral indigoid compounds with respect to ferrocene/ferrocenium reference in acetonitrile. The redox behaviours of oxaylindigo (**2.7**) in DCM was previously discussed in Chapter 2. Compound **2.7** possesses one reversible reduction at -0.92 V and two quasi-reversible reductions at -1.32 V and -2.05 V in acetonitrile. No oxidation processes were observed within the acetonitrile potential window. The monoimine species **4.7a** contains two quasi-reversible reductions at -1.28 V, -2.18 V which are negatively shifted compared to indigo **2.7,** and an irreversible oxidation event at +0.91 V. The peak at -0.89 V coincides with the first reduction of **2.7**, and growing in the returning wave suggests that an imine group hydrolysis occurs as the monoimine compound is reduced. Additional decomposition peaks at – 2.12 V, -1.76 V and +0.60 V further support the instability of **4.7a** in both negative and positive directions. The Nindigo **4.6a** possesses a single reduction at -1.50 V and a single oxidation at +0.82 V; both processes are irreversible. Decomposition of **4.6a**

was also observed in both directions based on the growth of new peaks at +0.35 V and -0.92 V. Increasing imine groups on the *cis*-indigoid system shifted both reduction and oxidation processes in more negative potential; thus, both LUMO and HOMO energy levels are lowered. **Table 4.4** shows the summarized redox potentials.

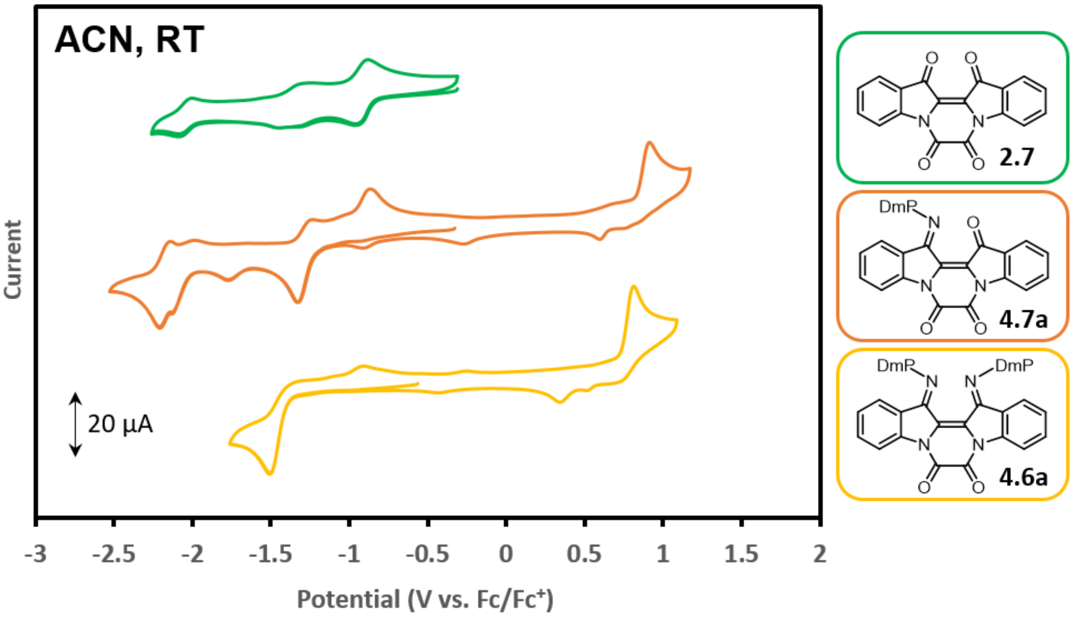

Figure 4.14 Cyclic voltammogram of oxalyl-tethered indigo **2.7**, monoimine **4.7a** and Nindigo **4.6a** (acetonitrile solution, 0.1 M NBu_4PF_6 electrolyte, scan rate 100 mV s^{-1}, referenced to ferrocene (Fc)/ferrocenium (Fc^+)).

4.6.2. Protonated *cis*-Nindigos

Figure 4.15 shows voltammograms of protonated *cis*-Nindigos. The cyclic voltammogram of oxalyl-tethered **4.6aH$^+$** was recorded with both chloride and tetrafluoroborate counterions. For the chloride salt **4.6aH$^+$**Cl$^-$, first irreversible reduction occurred at -0.43 V followed by two quasi-reversible reductions at -1.68 V and -0.43 V. Two irreversible oxidations are observed at +0.72 V and +1.06 V. Decomposition arises with a chloride anion, as the silver electrode was coated with a black tar after each CV experiment. Switching the counteranion to BF_4^- did not lead to the same coating on the electrode and resulted in different redox behaviours. **4.6aH**$^+$BF4$^-$ presented four reductions; two reversible reductions at +0.41 V and -1.11 V followed by quasi-reversible reductions at -2.12 V, -2.28 V. An irreversible oxidation was found at +1.06 V. The extra peak at -1.50 V is believed to be decomposition as the corresponding return peak was smaller. In comparison to the neutral counterpart **4.6a**, protonation of Nindigo resulted in a higher electron affinity and resistance to oxidation as indicated by a positive shift in the first reduction and first oxidation potentials in **4.6aH**$^+$BF4$^-$.

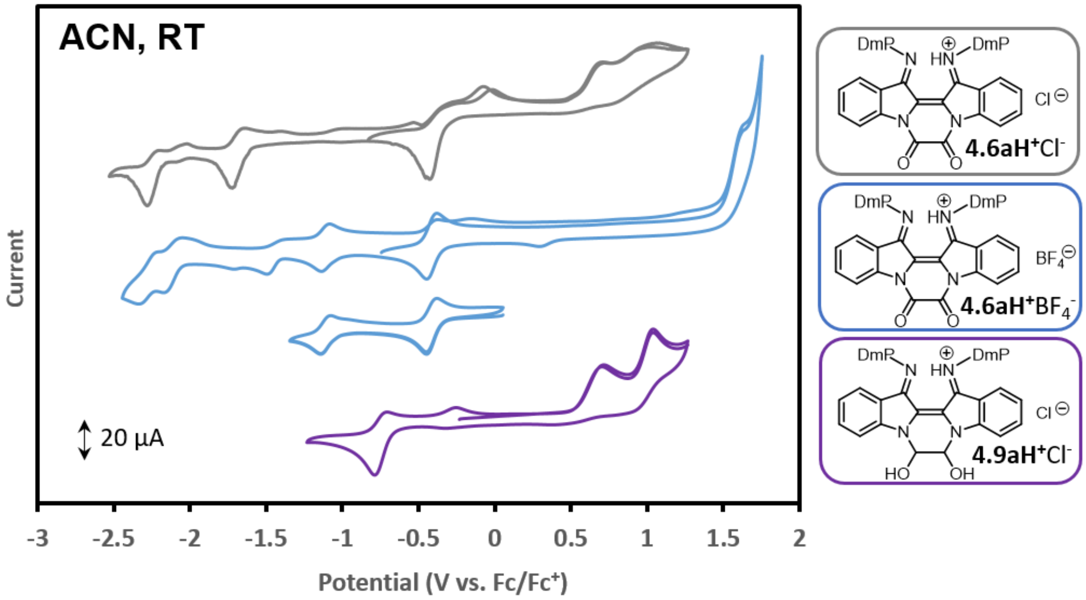

Figure 4.15 Cyclic voltammogram of protonated tethered *cis*-Nindigo species (acetonitrile solution, 0.1 M NBu_4PF_6 electrolyte, scan rate 100 mV s^{-1}, referenced to ferrocene (Fc)/ferrocenium (Fc^+)). Numbers in parentheses are derived from peak potentials.

An ethane-type tethered Nindigo **4.9aH**$^+$Cl$^-$ (**Figure 4.15**) contains one quasi-reversible reduction at -0.75 V and two irreversible oxidations at +0.72 V and +1.06 V. Interestingly, these oxidation potentials coincide with the oxidations observed from oxalyl-tethered **4.6aH**$^+$Cl$^-$. However, the irreversible oxidation events are not from a chloride activity as attempted CVs of tetrabutylammonium chloride and ferrocenium chloride failed to reproduce the said oxidations. At this moment it is unclear the origin of the two questionable oxidations.

Table 4.4 Reduction and oxidation potentials of *cis*-Nindigoids and **2.7** in ACN.

Compound	*Reduction (V)*	*Oxidation (V)*
2.7	-0.92^r, -1.32^q, -2.05^q	N/A
4.7a	-1.28^q, -2.18^q	+0.91^i
4.6a	-1.50^i	+0.82^i
4.6aH$^+$Cl$^-$	-0.43^i, -1.68^q, -2.24^q	+0.72^i, +1.06^i
4.6aH$^+$BF4$^-$	-0.41^r, -1.11^r, -2.12^q, -2.28^q	+1.06^i
4.9aH$^+$Cl$^-$	-0.75^q	+0.72^i, +1.06^i

^{q}quasi-reversible, ^{r}reversible and ^{i}irreversible electron processes.

4.7. Conclusions

Synthetic explorations to prepare *cis*-Nindigo derivatives encounter challenges due to the different reactivity of Nindigo in comparison to indigo. Established methods of nucleophilic substitution and [4+2] cycloaddition were unsuccessful. The group's Nindigo procedure on oxalylindigo (**2.7**) showed a promise in the installation of one imine group.

So far, successful synthetic methods to *cis*-Nindigo are achieved via acylation using oxalyl chloride and a subsequent reduction of the oxalyl tether.

Oxalyl Nindigo **4.6a** and indigo monoimine **4.7a** exhibit similar absorption wavelengths to their indigoid counterpart **2.7** at 419 nm, 426 nm and 429 nm, respectively. Thus, the electronics of oxalyl tether dictates the *cis*-indigoid absorption. ^{1}H NMR spectroscopy revealed that the imine group causes a through-space shielding in the nearby indolyl protons, yet, its spatial contribution in compounds' co-planarity was found minimal. In contrast, increasing imine groups on the oxalyl indigoid structure raised both HOMO and LUMO energies.

Protonation of Nindigo **4.6a** (to give H$^+$oxalyl Nindigo **4.6aH$^+$**) causes a bathochromic shift in the lowest energy visible absorption. The absorption wavelength of alkane-type tethered **4.9aH$^+$** is much higher due to restoration of the nitrogen lone pair delocalization by switching the electron-withdrawing tether into an electronically neutral ethane-type; this absorption is similar to the untethered protonated Nindigo (**4.1a**). The acidity (pK_a) of **4.6aH$^+$** is estimated between 3.6 – 4.46 in DMSO. The monoimine analogue **4.7aH$^+$** is suspected to have a lower pK_a at below -1.1 in DMSO.

Incorporation of the aryl groups on the *cis*-indigoid structure has shown a fine-tuning in the redox potentials and introduced an acid/base chemistry that can provide additional means to alter the electronic systems on *N,N′*-tethered indigoids.

4.8. Experimental Methods

See **Section 2.8.1** for general experimental details.

Nindigos **1.16a** and **1.16b**, and monoimine indigo **1.17a** were prepared according to the literature procedure.[85, 94]

For pK_a investigations, lutidinium tetrafluoroborate, collidinium tetrafluoroborate were synthesized according to the literature method.[140] Preparation of diphenylammonium triflate was followed by a procedure from Ohno et al.[141] Anilium tetrafluoroborate was given by Dr. Dillon Hofsommer. Reagents were checked for purity by ^{1}H NMR. All prepared reagents were vacuum-dried and kept in a desiccator prior to use. A solvent of DMSO-d_6 was pre-dried with 4 Å molecular sieves. Glassware such as vials and NMR tubes were pre-dried in an oven. A typical preparation method follows a weighing of Nindigo (~5 mg) in a glass vial, then one equivalence of pK_a standard was calculated and added. 0.8 mL of dry DMSO-d_6 was injected into the mixture powder via a 1-mL disposable syringe equipped with a disposable needle. The mixture solution was dissolved repeatedly by withdrawing the solution using the syringe and purging back into the vial. The same syringe was used to transfer the mixture solution into an NMR tube.

X-ray structures of **4.6a**, **4.6aH$^+$** were solved by Dr. Dillon Hofsommer; structures of **4.7a**, **4.8/4.8-Cl** and **4.9aH$^+$** were solved by Dr. Corey Sanz.

4.8.1. Synthesis

***N*,*N′*-(1,2-dioxoethano)indigo 3,3′-bis(2,6-dimethylphenylimine)** (**4.6a**)

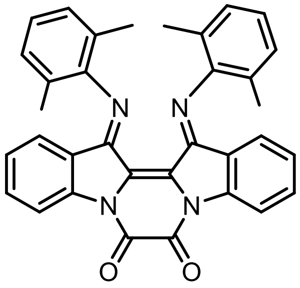

Nindigo **1.16a** (0.9985 g, 0.002131 mmol) was charged in a flame-dried, multi-neck 250 mL round bottom flask equipped with a nitrogen adapter and a rubber stopper. Dry toluene (60 mL) was added via syringe under a nitrogen atmosphere, and the mixture was briefly stirred for 5 minutes. Oxalyl chloride (1.00 mL, 1.48 mmol, 5.5 eq) was injected via syringe and instant colour change occurred from purple to green. The mixture solution was brought to reflux and stirred for 40 minutes under nitrogen atmosphere. The mixture solution was kept in the freezer overnight and red microcrystals of protonated chloride salt (**4.6aH$^+$**) precipitated. The crystals were filtered and washed with hexanes (3 x 30 mL), then immediately transferred into a pre-prepared solution of DCM (100 mL) / triethylamine (2 mL) in a 1-neck 250 mL flask. The neutralized yellow solution was stirred for 10 minutes. The DCM solution was dried on *vacuo*. The product was recrystallized in methanol (60 mL) reflux for 30 minutes. The product solution was filtered and washed with cold methanol (3 x 20 mL) and hexanes (3 x 20 mL). Brown microcrystalline (778.3 mg, 70 %). X-ray crystals were obtained from slow evaporation of dichloromethane/acetonitrile. ^{1}H NMR (500 MHz, CD_2Cl_2) δ 8.72 (d, *2H*, ^3J = 8.2 Hz, H_7), 7.56 (ddd, *2H*, ^3J = 8.6, ^{3}J = 7.6 Hz, ^4J = 1.2 Hz, H_6), 7.10 (d, *2H*, ^3J = 7.5 Hz, H_{22}), 7.10 – 7.06 (m, *2H*, H_5), 7.02 – 6.95 (m, *2H*, H_{21}), 6.69 (dd, *2H*, ^3J = 7.6 Hz, ^4J = 0.8 Hz, H_4), 2.03 (s, *6H*, H_{24}). ^{13}C NMR (126 MHz, CD_2Cl_2) δ 153.19 (C_2 or C_{34}), 152.50 (C_2 or C_{34}), 149.18 (C_{17}), 142.62 (C_8), 133.47 (C_6), 128.68 (C_{22}), 127.78 (C_5), 125.26 (C_4), 124.02 (C_{23}), 123.89 (C_1), 123.82 (C_{21}), 123.33 (C_3), 118.35 (C_7), 18.00 (C_{24}). IR (KBr disk, cm^{-1}): 1707s, 1662m, 1610w, 1590w, 1579m, 1460m, 1384m, 1300w, 1197s, 1157w, 1095w, 936w, 767w, 755m. UV-Vis (ACN; λ_{max} (nm) (ε (L·mol^{-1}·cm^{-1}))): 278, 376 (14 900), 397 (16 400), 419 (17 000). HR-MS: Calcd for $C_{34}H_{26}N_4O_2H^+$ m/z = 523.21285, found m/z = 523.21287; Satisfactory elemental analysis results not obtained; Anal: Calcd for $C_{34}H_{26}N_4O_2$: C, 78.14; H, 5.01; N, 10.72. Found: C, 77.42; H, 4.99; N, 10.44. mp: decomposes at 286 °C.

N,N′-(1,2-dioxoethano)indigo 3,3′-bis(2,6-dimethylphenylimine) hydrochloride (**4.6aH**$^+$Cl$^-$)

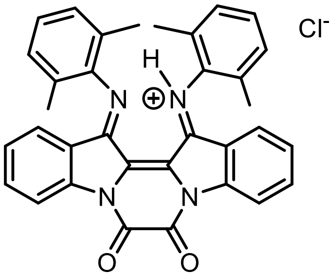

The same procedure as above was repeated. Due to a catalytic hydrolysis during 12 hrs scan time, only ^{1}H NMR signals are assigned. ^{1}H NMR (500 MHz, CD_2Cl_2) δ 17.81 (s, *1H*, H_2), 8.65 (d, *2H*, ^3J = 8.3 Hz, H_7), 7.84 (t, *2H*, ^3J = 7.9 Hz, H_6), 7.36 – 7.21 (m, *6H*, H_{12}, H_{13} and H_{14}), 7.24 (t, *2H*, ^3J = 7.7 Hz, H_5), 6.67 (d, *2H*, ^3J = 8.0 Hz, H_4), 3.38 (impurity), 2.23 (s, *12H*, $H_{16A\text{-}C}$ and $H_{17A\text{-}C}$). ^{13}C NMR (126 MHz, CD_2Cl_2) δ 160.66, 151.29, 145.84, 138.95, 137.37, 130.48, 130.06, 129.40, 129.31, 128.65, 127.91, 127.30, 125.62, 119.94, 118.98, 18.52. IR (KBr disk, cm^{-1}): 3424br, 1726s, 1631sh, 1603m, 1480w, 1461m, 1381m, 1360w, 1207m, 1096w, 778w, 753w. Satisfactory elemental analysis results not obtained; Anal: Calcd for $C_{34}H_{27}ClN_4O_2$: C, 73.05; H, 4.87; N, 10.02. Found: C, 68.74; H, 4.74; N, 9.14.

N,N′-(1,2-dioxoethano)indigo 3,3′-bis(2,6-dimethylphenylimine) hydrotetrafluoroborate (**4.6aH**$^+$BF4$^-$)

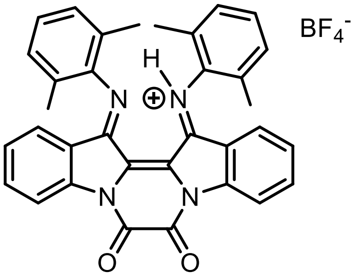

In a 100 mL 1-neck rb flask, oxalyl Nindigo **4.6a** (51.7 mg, 0.09893 mmol) was dissolved in dry toluene (10 mL). HBF4·etherate (0.02 mL, 0.147 mmol, 1.5 eq) was injected via syringe and the yellow-brown solution was stirred under nitrogen atmosphere for 5 minutes. The mixture solution was filtered and red precipitate was washed with diethyl ether. Recrystallized from chloroform (40 mL) / diethyl ether (80 mL) and washing the solids with excess diethyl ether yields **4.6aH**BF4$^-$ as red shiny microcrystalline. Yield: 63.0 mg (104 %). ^{1}H NMR (500 MHz, CD_2Cl_2) δ 17.82 (s, *1H*, H_2), 8.65 (d, *2H*, ^3J = 8.3 Hz, H_7), 7.84 (t, *2H*, ^3J = 8.0 Hz, H_6), 7.36 – 7.31 (m, *2H*, H_{13}), 7.28 (d, *4H*, ^3J = 7.6 Hz, H_{12} and H_{14}), 7.23 (t, *2H*, ^3J = 7.7 Hz, H_5), 6.65 (d, *2H*, ^3J = 8.0 Hz, H_4), 2.21 (s, *12H*, $H_{16A\text{-}C}$ and $H_{17A\text{-}C}$). ^{13}C NMR (126 MHz, CD_2Cl_2) δ 160.95 (C_2), 151.39 (C_9), 145.87 (C_8), 138.95 (C_{10}), 138.90 (C_6), 130.54 (C_{15}), 130.03 (C_{14}), 129.36 (C_{13}), 128.57 (C_5), 127.81 (C_1), 127.27 (C_4), 119.84 (C_3), 118.80 (C_7), 18.16 (C_{17}). IR (KBr disk, cm^{-1}): 1768sh, 1727s, 1638w, 1602m, 1463m, 1385m, 1304w, 1243w, 1208w, 1097w, 1054m, 902w, 777w, 753w. UV-Vis (ACN; λ_{max} (nm) (ε (L·mol^{-1}·cm^{-1}))): 333 (25 000), 496 (14 800). HR-MS: Calcd for $C_{34}H_{27}N_4O_2^+$ m/z = 523.21285, found m/z = 523.21287; Calcd for $[(C_{34}H_{27}N_4O_2^+)_2BF_4]^+$ m/z = 1133.42917, found m/z = 1133.43205. mp: decomposes at 194 °C.

_N,N′_-(1,2-dioxoethano)indigo 3-(2,6-dimethylphenylimine) (**4.7a**)

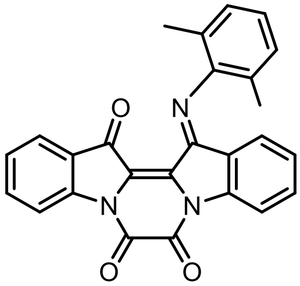

Indigo monoimine **1.17a** (197.9 mg, 0.542 mmol) was charged in a flame-dried, multi-neck 50 mL round bottom flask equipped with a nitrogen adapter and a rubber stopper. Dry toluene (10 mL) was added via syringe under a nitrogen atmosphere, and the mixture was briefly stirred for 5 minutes. Oxalyl chloride (0.34 mL, 4.0 mmol, 7.3 eq) was injected via syringe. Instant colour change was observed from purple to green which lasts < 5 sec, then the solution became a red suspension. The mixture solution was stirred 23 hours at room temperature under nitrogen atmosphere. The suspension solution was filtered. The red solid residue was washed with hexanes (1 x 30 mL), then immediately transferred into a pre-prepared solution of dichloromethane (20 mL) / triethylamine (2 mL) in a 50 mL round bottom flask. The neutralized solution was stirred for 5 minutes then was subjected to dry on *vacuo*. Anhydrous ethanol (~ 20 mL) was added to the flask and the solution was briefly sonicated then filtered. The isolated powder was washed with anhydrous ethanol (3 x 10 mL) and hexanes (3 x 10 mL) to yield **4.7a** as a brown powder (148.5 mg, 65.3 %). X-ray crystals were grown from saturated solution in DCM. ^{1}H NMR (500 MHz, CD_2Cl_2) δ 8.67 (d, *1H*, ^3J = 8.2 Hz, H_7), 8.63 (d, *1H*, ^3J = 8.2 Hz, H_{7A}), 7.95 (d, *1H*, ^3J = 7.6 Hz, H_4), 7.83 – 7.76 (m, *1H*, H_6), 7.60 – 7.54 (m, *1H*, H_{6A}), 7.50 (td, *1H*, ^3J = 7.5, ^4J = 0.5 Hz, H_5), 7.17 (d, *2H*, ^3J = 7.5 Hz, H_{12} and H_{14}), 7.14 – 7.05 (m, *2H*, H_{5A} and H_{13}), 6.69 (d, *1H*, ^3J = 7.5 Hz, H_{4A}), 2.05 (s, *6H*, $H_{16A\text{-}C}$ and $H_{17A\text{-}C}$). ^{13}C NMR (126 MHz, CD_2Cl_2) δ 178.47 (C_2), 153.68 (C_{2A}), 152.77 (C_9 or C_{9A}), 151.68 (C_9 or C_{9A}), 148.74 (C_{10}), 145.31 (C_8), 143.09 (C_{8A}), 136.59 (C_6), 134.03 (C_{6A}), 128.89 (C_{12} and C_{14}), 128.09 (C_{5A}), 127.97 (C_5), 127.07 (C_1 or C_{1A}), 125.92 (C_3), 125.62 (C_{4A}), 125.09 (C_4), 124.63 (C_{13}), 124.20 (C_{11} and C_{15}), 122.57 (C_{3A}), 119.39 (C_1 or C_{1A}), 118.48 (C_7), 118.27 (C_{7A}), 17.98 (C_{16} and C_{17}). IR (KBr disk, cm-1): 1708s, 1595sh, 1657w, 1620w, 1601w, 1589w, 1460m, 1381m, 1326w, 1300w, 1198s, 1152w, 1129w, 1089w, 926m, 772w, 754m, 671w. UV-Vis (ACN; λ_{max} (nm) (ε (L·mol^{-1}·cm^{-1}))): 275, 426 (11 800). HR-MS: Calcd for $C_{26}H_{17}N_3O_3H^+$ m/z = 420.13427, found m/z = 420.13434. mp: decomposes at 280 °C.

N,N′-(1,2-dihydroxyethano)indigo 3,3′-bis(2,6-dimethylphenylimine) hydrochloride (4.9aH$^+$Cl$^-$)

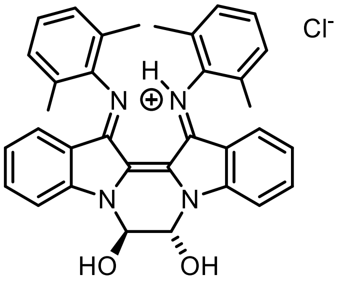

Oxalyl Nindigo **4.6a** (150.7 mg; 0.2884 mmol) and sodium borohydride (112.2 mg; 2.966 mmol) were dissolved in methanol (30 mL) in a one-neck, 100 mL round bottom flask. The mixture solution was stirred for 1 hour. A gradual colour change occurred from yellow-purple to green-purple. The solution strongly fluoresces blue under UV-light. Excess ammonium chloride (690.2 mg; 12.90 mmol) was added, and the mixture solution and instantly darkened blue colour and became teal. After stirring for 15 min, the teal solution was transferred into a separatory funnel and diluted in dichloromethane (40 mL). The organic layer was washed with 20 % NH_4Cl solution (2 x 40 mL) then 1M HCl solution (1 x 40 mL). The collected DCM layer was dried over $MgSO_4$, removed *in vacuo*. The solid residue was re-dissolved in ethyl acetate (40 mL) and heated at reflux for 20 min. The suspension solution was kept in the freezer overnight. The solid was filtered and washed with ethyl acetate until the washings lost the initial green-purple colour, then washed with hexanes. Black staticky fine powder of **4.9aH$^+$** was isolated (123.8 mg). Ethyl acetate remained after drying for 3 days under vacuum. The product : ethyl acetate ratio was inconsistent between the batches. In this instance, the product mixture contained a ratio of 1: 1.08 as determined by proton integration on 500 MHz NMR. (New effective MW = 658.5697 g/mol, yield of product: 65.2 % yield). ^{1}H NMR (500 MHz, CD_2Cl_2) δ 15.31 (s, *1H*, H_{2A}), 8.16 (s, *2H*, H_1), 7.96 (d, *2H*, ^3J = 8.4 Hz, H_7), 7.63 (t, *2H*, ^3J = 7.6 Hz, H_6), 7.32 – 7.19 (m, *6H*, H_{12}, H_{13} and H_{14}), 6.88 (t, *2H*, ^3J = 7.6 Hz, H_5), 6.57 (s, *2H*, H_9), 6.49 (d, *2H*, ^3J = 8.1 Hz, H_4), 2.19 (s, *6H*, H_{16A-C} or H_{17A-C}), 2.17 (s, *6H*, $H_{16A\text{-}C}$ or $H_{17A\text{-}C}$). ^{13}C NMR (126 MHz, CD_2Cl_2) δ 158.43 (C_2), 148.60 (C_8), 140.65 (C_{10}), 136.62 (C_6), 131.01 (C_{11} or C_{15}), 130.97 (C_{11} or C_{15}), 129.55 (C_{12} and C_{14}), 128.75 (C_1), 128.20 (C_{13}), 125.97 (C_4), 123.60 (C_5), 118.11 (C_3), 113.50 (C_7), 76.54 (C_9), 18.48 (C_{16} or C_{17}), 18.43 (C_{16} or C_{17}). IR (KBr disk, cm^{-1}): 3067br, 1730w, 1604s, 1586sh, 1573sh, 1480w, 1465w, 1411w, 1328sh, 1312m, 1200m, 1137m, 1091w, 1063w, 971w, 771w, 747w. UV-Vis (ACN; λ_{max} (nm) (ε ($L\cdot mol^{-1}\cdot cm^{-1}$))): 296 (21 100), 333 (23 500), 627 (20 400). HR-MS: Calcd for $C_{34}H_{31}N_4O_2^+$ m/z = 527.24415, found m/z = 527.24406; Calcd for $[(C_{34}H_{31}N_4O_2)_2Cl]^+$ m/z = 1089.45771, found m/z = 1089.45926. mp: decomposes at 211-218 °C.

Chapter 5. Summary and Future Work

The usage of indigo has expanded from textile pigment to organic electronics. The properties of indigo can be tempered via structural modifications, yet most methods in the literature focus on preserving the *trans* geometry. This dissertation explored the conversion of indigo into its rare *cis* form through an introduction of a short organic tether between two indole nitrogen atoms. The characterized *cis*-indigoids demonstrated ranges of absorption wavelengths, rich redox behaviours, varying spatial orientations in addition to gained photo-responsiveness. This work showed direct modulation at the H-chromophore is an effective means to diversify properties of indigo. In addition, the work has provided a basic understanding of the influence of the organic tether that can be beneficial to the future design of functional tethers on *cis*-indigoid for tailoring properties for the application of interest.

In the first two chapters, *N,N′*-tethered *cis*-indigos were investigated to scope the effect of the tether. In chapter 2, structurally simple bridges were chosen from the literature. The electronics of tether posed strong impacts on the absorption wavelengths and electrochemical properties. However, indigoid co-planarity rather depended on the chain lengths of the organic linker. The alkyl bridged indigos (**2.5** and **2.6**) show fluorescence behaviour derived from the rigid *cis*-structure in contrast to untethered *cis*-*N,N′*-substituted indigos. In Chapter 3, a complex tether consisting of dihydroindigo units were synthesized from the reaction with a quinone. These indigoid substituents caused a small-hypsochromic shift in the absorption in comparison to alkyl tethers where the effect was neutral, however, the effect was weaker than an electron-withdrawing oxalyl tether (in **2.7**) which caused a strong hysochromic behaviour. The role of the quinone in the formation of dimeric *cis*-indigos depended on its oxidation strength: naphthoquinone substitution occurs in **3.2** but not with bromanil in **3.3** and **3.4**. VT ^{1}H NMR spectroscopy revealed that diastereomeric indigos **3.3** and **3.4** possess a dynamic behaviour.

Most of the syntheses of *cis*-indigos suffer from a low yield. *N,N′*-alkylation using a bromide source resulted in a 12 – 18 % yield for **2.5** and **2.6**. In the future, a milder base (e.g. Cs_2CO_3) instead of NaH could be explored; an alkylation with propagyl bromide on indigo in DMF was effective in 90 % yield.[100] The current purification procedure for the dimeric indigos that are presented in Chapter 3 is challenged by the low solubility of the major product **3.3**. The minor product **3.4** has not been isolated in analytically pure form due to contamination with the major species and an impurity. Using soluble indigo (such as a derivative with solubilizing substituents at the -5,5′ or -6,6′ positions, (see **Figure 5.1**) may allow isolation of both diastereomers by simple column chromatography. However, in this case, the corresponding starting material (in a deprotonated form) must be carefully examined for their oxidation potentials. A suitable oxidant then could be chosen.

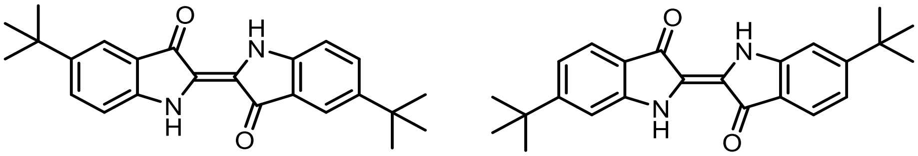

Figure 5.1 Examples of soluble *tert*-butyl substituted indigo[142].

Utilization of the *cis*-indigos can be applied in metal coordination chemistry. Current *cis*-(*O,O′*) coordination reaction using parent indigo requires an extensive workup or a reductive method to bring two oxygen atoms close together.[71, 72] However, one may access an easier interaction with the metal and avoid unwanted coordination modes using the tethered *cis*-indigoid structure. Prospective metals are Co, Zn, Cu and Ni where the complex formation was observed with the neutral *β*-diketone ligands.[143] **Figure 5.2** shows a coordination geometry comparison of *cis*-indigo with 3-(salicylidene)-*β*-diketone. Thus, *cis*-indigos could chelate in a neutral state and could act as a metal sensor/detector using their characteristic chromophore.

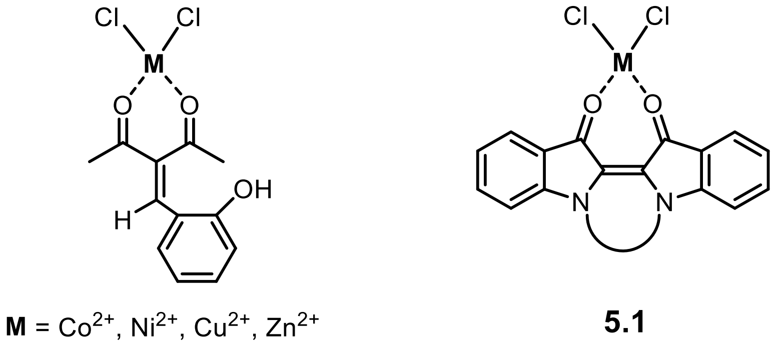

Figure 5.2 Coordination of neutral *β*-diketone derivative on metal (II) centres and prospecting cis-(*O,O′*) chelation mode of *cis*-indigo.

In Chapter 4, the installation of an organic tether on Nindigo and monoimine indigo was explored. Synthetic challenges arose due to the different reactivity of the imine containing species compared to indigo. Acylation was achieved from the reaction with oxalyl chloride. Oxalyl Nindigo (**4.6a**) and monoimine (**4.7a**) were compared with their indigoid counterpart **2.7** to assess the effect of the aryl groups. The arylimine groups raise both HOMO and LUMO energies, yet did not impact much on the absorption nor backbone co-planarity. pK_a investigation suggested that the acidity of protonated Nindigo **4.6aH$^+$** lies between that of anilinium (pK_a = 3.6)[137] and lutidinium (pK_a = 4.46)[138] in DMSO. The monoimine analogue **4.7aH$^+$** is suspected to have a much lower pK_a. An ethane-type-tethered protonated Nindigo **4.9aH**$^+$ was obtained from the reduction of the oxalyl group on Nindigo **4.6a**.

One of the advantages of Nindigo over indigo is an accessible protonation in the imine pocket. As a preliminary investigation in the relationship between the linker and characteristics of the *cis*-Nindigo system, Chapter 4 focused on one derivative of Nindigo, *bis*-2,6-dimethyl phenyl (DmP) Nindigo. Protonated tethered Nindigos have successfully demonstrated that the distance between two imine groups can be altered by switching bridges. For future considerations, incorporation of different imine substituents could further tune the acidity since the imine pendant groups are in close proximity and exerting steric hindrance to the protonation site as depicted in **Figure 5.3**. The steric introduction is a common method used in tuning the acidity of 1,8-bis(dimethylamino)naphthalene ("proton sponge").[144]

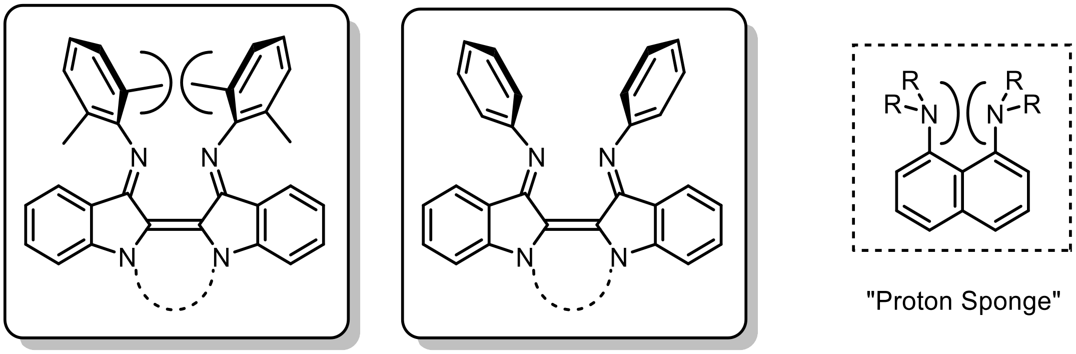

Figure 5.3 Structural comparison of *cis*-Nindigo and proton sponge.

So far, the organic tethers explored in this research were not in π-conjugation with the indigoid core with exception of the oxalyl tether. A π-conjugated bridge moiety will be an interesting addition to the library of *cis*-indigos as it is anticipated that absorption wavelengths, redox potentials and acidity (for Nindigo) could be expanded.

Anmportant consideration must be made in designing a *cis*-indigoid framework with a benzene-type bridge. The newly formed heterocycle would have **8 π-electrons** – which is Hückel anti-aromatic (**4n π**). However, Bunz et al. analyzed dihydroazacenes (*N* = 4, 5) and calculated that although the anti-aromatic character is localized on the heterocycle (8 π), yet the compounds are overall weakly aromatic. [145, 146] They proposed a rationale that anti-aromatic character can be spread over and be diluted in larger 4n π systems.[147] In fact, isolation of dihydroazatetracene (**Figure 5.4**, left) is limited in the oxygen-free environment, yet the pentacene analogue (**Figure 5.4**, right) is remarkably stable in the air.

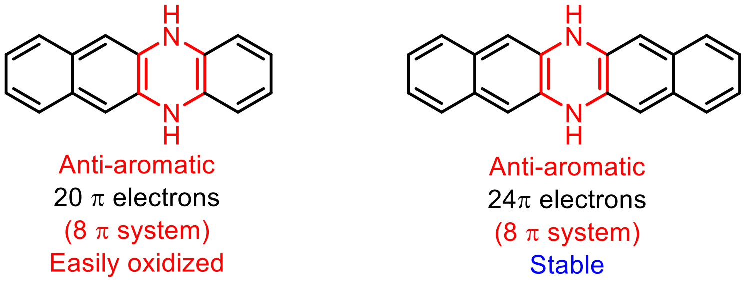

Figure 5.4 Hückel electron count and physical characteristics of diazaacenes (*N* = 4, 5).

Cis-indigoid molecules have proven a relatively planar structure. Expansion of electron delocalization through the indigoid backbone could benefit the stabilization of the anti-aromatic character. In addition, increasing effective π-conjugation through the bridge moiety should lower the HOMO-LUMO energy gap; a red-shift in λ_{max} is expected. **Scheme 5.1** suggests two synthetic approaches to install a benzene tether on Nindigo. Unlike dehydroindigo, dehydro-Nindigos (example: **4.4a**) are easy to prepare and are stable enough to be isolated and stored. So far, cycloaddition reactions on dehydro-Nindigos have been unsuccessful as explored in Chapter 4, yet a reactive dienophile such as benzyne could push the reaction forward (**Route 1**).

A second possible route to a benzene bridge is through a copper-mediated coupling reaction (**Route 2**). Installation of aryl groups on the indole[148] and indigo[80] using a copper source have been explored in the literature. After coupling with the first indole ring, steric crowding from the inserted moiety with the adjacent imine substituent in **1.16a** should induce the *trans*-to-*cis* isomerization. Thus, increases the chance of the second intramolecular coupling.

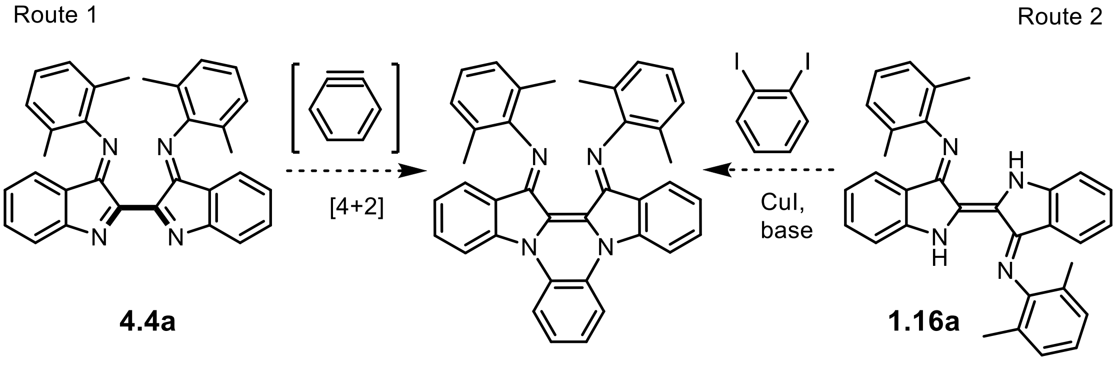

5.2

Scheme 5.1 Proposed synthesis to benzene-bridged *cis*-Nindigo. Route 1) [4+2] cyclization. Route 2) Cu coupling.

An alternative structure to the benzene-type bridge is a naphthalene analogue of azaacene. Fluoflavine (**5.3**) is isoelectronic to naphthalene and is an air-stable, fluorescent compound that has been a target of study in organic electronics.[149, 150] Despite being formally anti-aromatic (20 π), **5.3** can be easily synthesized and stored. **Scheme 5.2** suggests an acid-catalyzed condensation reaction at the oxalyl moiety with *o*-phenylenediamine using acetic acid.[151] This reaction could potentially be applied to both indigo **2.7** and Nindigo **4.6a** depending on their reactivity towards the acid used. One could imagine proceeding with the condensation reaction using an indigo monoimine **4.7a** first, and then install a different aryl group by the group's Nindigo synthesis.

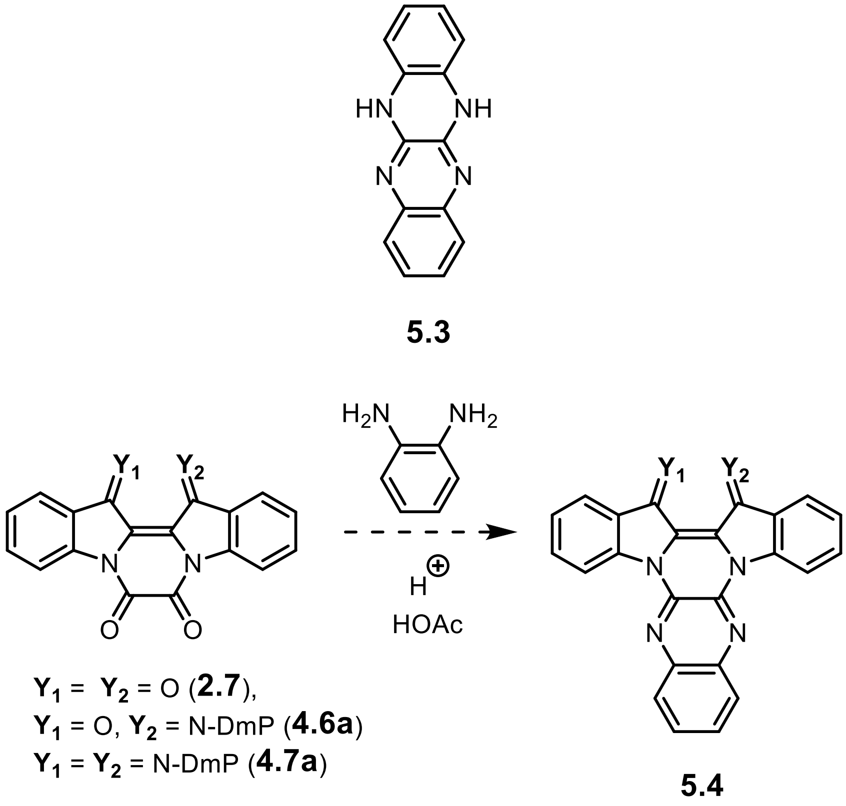

Scheme 5.2 Proposed synthesis of diazanaphthalene-bridged *cis*-indigoids.

The reaction of Nindigo with oxalyl chloride (**Scheme 4.11**) was a simple and efficient way to obtain two related *cis*-Nindigos in a straightforward manner. Therefore, a reaction with bis(acyl chloride) is a promising route to create another acid/neutral pair of *cis*-Nindigo. **Scheme 5.3** proposes a reaction with malonyl chloride. Malonyl indigo has been reported in the literature, yet it is not fully characterized.[122] A malonyl bridge is electronically similar to an oxalyl bridge yet will probably exert a larger ring strain, which would affect the acidity and solubility by twisting the backbone of the compound.

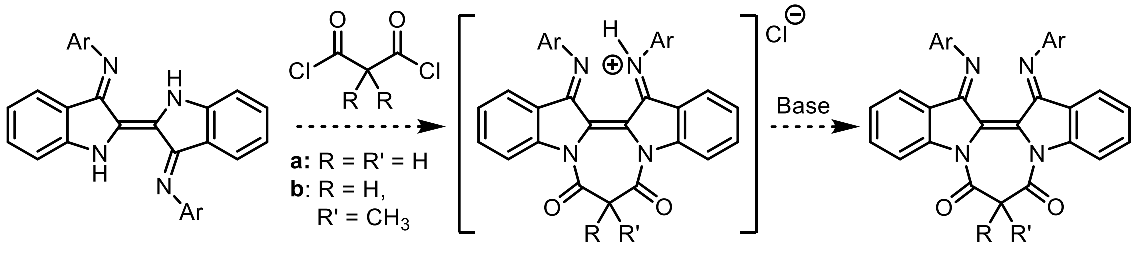

1.16 **5.5a/b**

Scheme 5.3 Proposed reaction of malonyl-type-bridged *cis*-Nindigo.

The reaction with α-methylated malonyl bridge will be particularly interesting as deprotonation at α-hydrogen would result in a π-conjugated heterocycle in **Scheme 5.4**. In addition, the electron-withdrawing nature of the malonyl C=O groups will be weaker due to a delocalization of the negative charge on the bridge moiety as suggested in the resonance structures below. This modification may have interesting implications for absorption energies as opposed to an oxalyl tether. Furthermore, a secondary reaction area is introduced to the system, which expands the potential chemistry of *cis*-Nindigo through its bridge.

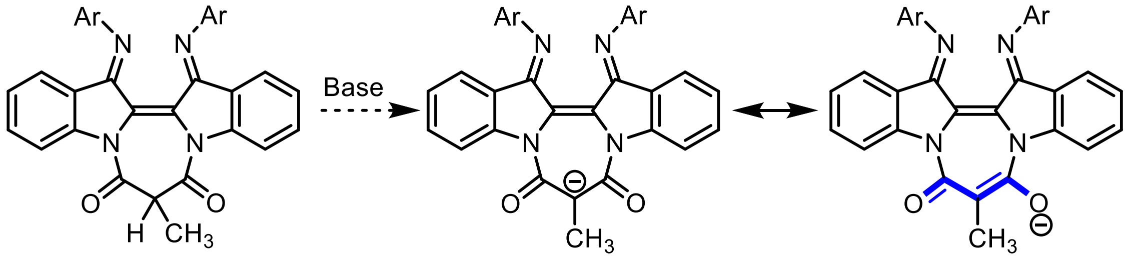

5.5b **5.5b^{-}**

Scheme 5.4 Proposed deprotonation of α-methylated malonyl-bridged *cis*-Nindigo.

Bibliography

1. M. R. Christie, *Colour Chemistry*, The Royal Society of Chemistry, Cambridge, UK, 2nd edn., **2015**.
2. Z. Y. Wang, *Near-Infrared Organic Materials and Emerging Applications*, CRC Press, UK, 1st edn., **2013**.
3. O. Ostroverkhova, *Chemical Reviews*, **2016**, 116, 13279-13412.
4. K. Yanagi, Y. Miyata and H. Kataura, *Advanced Materials*, **2006**, 18, 437-441.
5. K. Abe, D. Kosumi, K. Yanagi, Y. Miyata, H. Kataura and M. Yoshizawa, *Physical Review B*, **2008**, 77, 165431-165436.
6. B. Sui, S. Tang, T. Liu, B. Kim and K. D. Belfield, *ACS Applied Materials & Interfaces*, **2014**, 6, 18408-18412.
7. C. F. Gomez-Duran, I. Garcia-Moreno, A. Costela, V. Martin, R. Sastre, J. Banuelos, F. Lopez Arbeloa, I. Lopez Arbeloa and E. Pena-Cabrera, *Chemical Communications*, **2010**, 46, 5103-5105.
8. T. Kálai and K. Hideg, *Tetrahedron*, **2006**, 62, 10352-10360.
9. P. Guixens-Gallardo, Z. Zawada, J. Matyasovsky, D. Dziuba, R. Pohl, T. Kraus and M. Hocek, *Bioconjugate Chemistry*, **2018**, 29, 3906-3912.
10. H. Tian and L. Sun, *8.16 Organic Photovoltaics and Dye-Sensitized Solar Cells*, in *Comprehensive Inorganic Chemistry II*, eds. J. Reedijk and K. Poeppelmeier, Elsevier, Amsterdam, 2nd edn., **2013**, pp. 567-605.
11. R. F. Salzman, J. Xue, B. P. Rand, A. Alexander, M. E. Thompson and S. R. Forrest, *Organic Electronics*, **2005**, 6, 242-246.
12. M. Seefelder, *Indigo in culture, science and technology*, Ecomed, Landsberg, Germany, 2nd edn., **1994**.
13. Y. Shin, D. I. Yoo and K. Kim, *Textile Coloration and Finishing*, **2012**, 24, 253-259.
14. R. Huisgen, *Angewandte Chemie International Edition in English*, **1986**, 25, 297-311.
15. A. Baeyer and V. Drewsen, *Berichte der Deutschen Chemischen Gesellschaft*, **1882**, 15, 2856-2864.
16. A. Reis and W. Sehneider, *Zeitschrift für Kristallographie - Crystalline Materials*, **1928**, 68, 543-566.
17. A. de Meijere, *Angewandte Chemie International Edition in English*, **2005**, 44, 7836-7840.
18. *Nature*, Chemists go green to make better blue jeans, **2018**, Editorial Article, 553.
19. T. M. Hsu, D. H. Welner, Z. N. Russ, B. Cervantes, R. L. Prathuri, P. D. Adams and J. E. Dueber, *Nature Chemical Biology*, **2018**, 14, 256-261.
20. P. Westbroek, K. De Clerck, P. Kiekens, E. Gasana and E. Temmerman, *Textile Research Journal*, **2003**, 73, 1079-1084.
21. R. S. Blackburn, T. Bechtold and P. John, *Coloration Technology*, **2009**, 125, 193-207.
22. R. Rondão, J. S. Seixas de Melo, V. D. B. Bonifácio and M. J. Melo, *The Journal of Physical Chemistry A*, **2010**, 114, 1699-1708.

23. M. Sánchez del Río, E. Boccaleri, M. Milanesio, G. Croce, W. van Beek, C. Tsiantos, G. D. Chyssikos, V. Gionis, G. H. Kacandes, M. Suárez and E. García-Romero, *Journal of Materials Science*, **2009**, 44, 5524-5536.
24. P. W. Sadler, *The Journal of Organic Chemistry*, **1956**, 21, 316-318.
25. R. M. Christie, *Biotechnic and Histochemistry*, **2007**, 82, 51-56.
26. J. S. de Melo, R. Rondao, H. D. Burrows, M. J. Melo, S. Navaratnam, R. Edge and G. Voss, *Chemphyschem*, **2006**, 7, 2303-2311.
27. M. Klessinger and W. Lüttke, *Tetrahedron*, **1963**, 19, 315-335.
28. E. Wille and W. Lüttke, *Angewandte Chemie International Edition in English*, **1971**, 10, 803-804.
29. M. Klessinger, *Dyes and Pigments*, **1982**, 3, 235-241.
30. L. Serrano-Andrés and B. O. Roos, *Chemistry – A European Journal*, **1997**, 3, 717-725.
31. H. Bauer, K. Kowski, H. Kuhn, W. Lüttke and P. Rademacher, *Journal of Molecular Structure*, **1998**, 445, 277-286.
32. V. Barone, M. Biczysko, C. Latouche and A. Pasti, *Theoretical Chemistry Accounts*, **2015**, 134.
33. J. Seixas de Melo, A. P. Moura and M. J. Melo, *The Journal of Physical Chemistry A*, **2004**, 108, 6975-6981.
34. T. Schultz, J. Quenneville, B. Levine, A. Toniolo, T. J. Martínez, S. Lochbrunner, M. Schmitt, J. P. Shaffer, M. Z. Zgierski and A. Stolow, *Journal of the American Chemical Society*, **2003**, 125, 8098-8099.
35. P. J. Coelho, C. M. Sousa, M. C. R. Castro, A. M. C. Fonseca and M. M. M. Raposo, *Optical Materials*, **2013**, 35, 1167-1172.
36. D. H. Waldeck, *Chemical Reviews*, **1991**, 91, 415-436.
37. R. Rondao, J. Seixas de Melo, F. A. Schaberle and G. Voss, *Physical Chemistry Chemical Physics*, **2012**, 14, 1778-1783.
38. J. S. Seixas de Melo, H. D. Burrows, C. Serpa and L. G. Arnaut, *Angewandte Chemie International Edition in English*, **2007**, 46, 2094-2096.
39. T. Kobayashi and P. M. Rentzepis, *The Journal of Chemical Physics*, **1979**, 70, 886-892.
40. M. Moreno, J. M. Ortiz-Sánchez, R. Gelabert and J. M. Lluch, *Physical Chemistry Chemical Physics*, **2013**, 15, 20236-20246.
41. I. Iwakura, A. Yabushita and T. Kobayashi, *Chemistry Letters*, **2009**, 38, 1020-1021.
42. S. Yamazaki, A. L. Sobolewski and W. Domcke, *Physical Chemistry Chemical Physics*, **2011**, 13, 1618-1628.
43. J. Pina, D. Sarmento, M. Accoto, P. L. Gentili, L. Vaccaro, A. Galvao and J. S. Seixas de Melo, *The Journal of Physical Chemistry B*, **2017**, 121, 2308-2318.
44. N. D. Bernardino, S. Brown-Xu, T. L. Gustafson and D. L. A. de Faria, *The Journal of Physical Chemistry C*, **2016**, 120, 21905-21914.
45. X. He, F. Yang, S. Li, X. He, A. Yu, J. Chen, J. Xu and J. Wang, *The Journal of Physical Chemistry A*, **2019**, 123, 6463-6471.
46. P. Süsse and A. Wolf, *Naturwissenschaften*, **1980**, 67, 453-453.
47. C. D. Hurd and T. T. S. Wang, *Journal of Chemical & Engineering Data*, **1964**, 9, 582-583.

48. E. D. Glowacki, G. Voss and N. S. Sariciftci, *Advanced Materials*, **2013**, 25, 6783-6800.
49. R. Shinar, E. D. Glowacki, I. Kymissis, L. Leonat, G. Voss, M. Bodea, Z. Bozkurt, M. Irimia-Vladu, S. Bauer and N. S. Sariciftci, presented in part at the Organic Semiconductors in Sensors and Bioelectronics IV, 2011.
50. C. Iuga, E. Ortíz, J. R. Alvarez-Idaboy and A. Vivier-Bunge, *The Journal of Physical Chemistry A*, **2012**, 116, 3643-3651.
51. S. J. M. Nassar, D. Sirbu and A. Harriman, *Photochemical and Photobiological Sciences*, **2019**, 18, 2875-2883.
52. J. H. L. Ngai, G. Y. Chang, X. Gao, X. Zhou, A. D. Hendsbee and Y. Li, *RSC Advances*, **2019**, 9, 26230-26237.
53. I. K. Kim, X. Li, M. Ullah, P. E. Shaw, R. Wawrzinek, E. B. Namdas and S. C. Lo, *Advanced Materials*, **2015**, 27, 6390-6395.
54. C. Liu, S. Dong, P. Cai, P. Liu, S. Liu, J. Chen, F. Liu, L. Ying, T. P. Russell, F. Huang and Y. Cao, *ACS Applied Materials & Interfaces*, **2015**, 7, 9038-9051.
55. C. Guo, J. Quinn, B. Sun and Y. Li, *Journal of Materials Chemistry C*, **2015**, 3, 5226-5232.
56. C. Ma, H. Li, Y. Yang, D. Li and Y. Liu, *Chemical Physics Letters*, **2015**, 638, 72-77.
57. Z. Ju, J. Sun and Y. Liu, *Molecules*, **2019**, 24.
58. S. MacLean, Frontier molecular orbitals (MOs) of the indigo -Optimization and energy calculations performed in ORCA 4.2.1 at ωB97X-D3BJ/def2-TZVPP level of theory. Images rendered using VMD 1.9.4a51 with Tachyon 0.99.1 for ray tracing. unpublished work, 2021.
59. R. J. H. Clark, C. J. Cooksey, M. A. M. Daniels and R. Withnall, *Endeavour*, **1993**, 17, 191-199.
60. E. D. Głowacki, G. Voss, L. Leonat, M. Irimia-Vladu, S. Bauer and N. S. Sariciftci, *Israel Journal of Chemistry*, **2012**, 52, 540-551.
61. A. D. Durnev, A. V. Oreshchenko, A. V. Kulakova and N. F. Beresten, *Voprosy Meditsinskoi Khimii*, **1995**, 41, 50-53.
62. M. Yao, M. Araki, H. Senoh, S.-i. Yamazaki, T. Sakai and K. Yasuda, *Chemistry Letters*, **2010**, 39, 950-952.
63. M. Yao, K. Kuratani, T. Kojima, N. Takeichi, H. Senoh and T. Kiyobayashi, *Scientific Reports*, **2014**, 4, 3650.
64. W. Beck and K. Sünkel, *Zeitschrift für Anorganische und Allgemeine Chemie*, **2020**, 646, 248-255.
65. W. Beck, C. Schmidt, R. Wienold, M. Steimann and B. Wagner, *Angewandte Chemie International Edition in English*, **1989**, 28, 1529-1531.
66. P. Mondal, M. Chatterjee, A. Paretzki, K. Beyer, W. Kaim and G. K. Lahiri, *Inorganic Chemistry*, **2016**, 55, 3105-3116.
67. P. Mondal, A. Das and G. K. Lahiri, *Inorganic Chemistry*, **2016**, 55, 1208-1218.
68. J. Y. Wu, C. H. Chang, P. Thanasekaran, C. C. Tsai, T. W. Tseng, G. H. Lee, S. M. Peng and K. L. Lu, *Dalton Transactions*, **2008**, 6110-6112.
69. F. S. Guo and R. A. Layfield, *Chemical Communications*, **2017**, 53, 3130-3133.

70. D. V. Konarev, L. V. Zorina, S. S. Khasanov, A. F. Shestakov, A. M. Fatalov, A. Otsuka, H. Yamochi, H. Kitagawa and R. N. Lyubovskaya, *Inorganic Chemistry*, **2018**, 57, 583-589.
71. D. V. Konarev, S. S. Khasanov, A. V. Kuzmin, A. F. Shestakov, A. Otsuka, H. Yamochi, G. Saito and R. N. Lyubovskaya, *Dalton Transactions*, **2016**, 45, 17095-17099.
72. D. V. Konarev, A. V. Kuzmin, S. S. Khasanov, A. M. Fatalov, E. I. Yudanova and R. N. Lyubovskaya, *Chemistry*, **2018**, 24, 8415-8423.
73. C. Giuliano, L. Hess and J. Margerum, *Journal of the American Chemical Society*, **1968**, 90, 587-594.
74. J. Blanc and D. L. Ross, *The Journal of Physical Chemistry*, **1968**, 72, 2817-2824.
75. S. Itoh, S. Ohno, N. Hasegawa and H. Takahashi, *Journal of Raman Spectroscopy*, **1989**, 20, 423-430.
76. J. Pouliquen, V. Wintgens, V. Toscano, B. Jaafar, S. Tripathi, J. Kossanyi and P. Valat, *Canadian Journal of Chemistry*, **1984**, 62, 2478-2486.
77. O. Yoshimori, T. Atsushi, A. Hiromu, N. Takehiko and K. Choji, *Bulletin of the Chemical Society of Japan*, **1984**, 57, 470-472.
78. D. Farka, M. Scharber, E. D. Glowacki and N. S. Sariciftci, *The Journal of Physical Chemistry A* **2015**, 119, 3563-3568.
79. H. Nakagawa, A. Matsumoto, A. Daicho, Y. Ozaki, C. Ota and Y. Nagasawa, *Journal of Photochemistry and Photobiology A: Chemistry*, **2018**, 358, 308-314.
80. C. Y. Huang, A. Bonasera, L. Hristov, Y. Garmshausen, B. M. Schmidt, D. Jacquemin and S. Hecht, *Journal of the American Chemical Society*, **2017**, 139, 15205-15211.
81. M. A. Kolaczkowski, B. He and Y. Liu, *Organic Letters*, **2016**, 18, 5224-5227.
82. T. Furuyama, D. Tamura, H. Maeda and M. Segi, *Tetrahedron Letters*, **2018**, 59, 2913-2916.
83. G. Haucke and R. Paetzold, *Journal für Praktische Chemie*, **1979**, 321, 978-986.
84. J. L. Ryerson, A. Zaykov, L. E. Aguilar Suarez, R. W. A. Havenith, B. R. Stepp, P. I. Dron, J. Kaleta, A. Akdag, S. J. Teat, T. F. Magnera, J. R. Miller, Z. Havlas, R. Broer, S. Faraji, J. Michl and J. C. Johnson, *The Journal of Chemical Physics*, **2019**, 151, 184903.
85. S. R. Oakley, G. Nawn, K. M. Waldie, T. D. MacInnis, B. O. Patrick and R. G. Hicks, *Chemical Communications*, **2010**, 46, 6753-6755.
86. G. Nawn, S. R. Oakley, M. B. Majewski, R. McDonald, B. O. Patrick and R. G. Hicks, *Chemical Science*, **2013**, 4, 612-621.
87. G. Nawn, R. McDonald and R. G. Hicks, *Inorganic Chemistry*, **2013**, 52, 10912-10919.
88. G. Nawn, K. M. Waldie, S. R. Oakley, B. D. Peters, D. Mandel, B. O. Patrick, R. McDonald and R. G. Hicks, *Inorganic Chemistry*, **2011**, 50, 9826-9837.
89. P. Mondal, F. Ehret, M. Bubrin, A. Das, S. M. Mobin, W. Kaim and G. K. Lahiri, *Inorganic Chemistry*, **2013**, 52, 8467-8475.
90. P. Mondal, S. Plebst, R. Ray, S. M. Mobin, W. Kaim and G. K. Lahiri, *Inorganic Chemistry*, **2014**, 53, 9348-9356.
91. S. Fortier, O. G.-d. Moral, C.-H. Chen, M. Pink, J. J. Le Roy, M. Murugesu, D. J. Mindiola and K. G. Caulton, *Chemical Communications*, **2012**, 48, 11082-11084.

92. S. Fortier, J. J. Le Roy, C. H. Chen, V. Vieru, M. Murugesu, L. F. Chibotaru, D. J. Mindiola and K. G. Caulton, *Journal of the American Chemical Society*, **2013**, 135, 14670-14678.
93. G. Nawn, Synthesis, Redox and Spectroscopic Properties of Nindigo and a Variety of Nindigo Coordination Compounds, University of Victoria, 2013.
94. S. R. Oakley, Synthesis, characterization and coordination chemistry of indigo diimines, University of Victoria, 2008.
95. O. Yoshimori, I. Satoshi, M. Ryuichi, F. Kiyoko, N. Takehiko and K. Choji, *Bulletin of the Chemical Society of Japan*, **1979**, 52, 3397-3399.
96. J. Setsune, T. Fujiwara and T. Kitao, *Chemischer Informationsdienst*, **1986**, 17, 299-302.
97. E. D. Glowacki, G. Voss, K. Demirak, M. Havlicek, N. Sunger, A. C. Okur, U. Monkowius, J. Gasiorowski, L. Leonat and N. S. Sariciftci, *Chemical Communications*, **2013**, 49, 6063-6065.
98. L. A. Huber, P. Mayer and H. Dube, *ChemPhotoChem*, **2018**, 2, 458-464.
99. G. M. Wyman and A. F. Zenhäusern, *The Journal of Organic Chemistry*, **1965**, 30, 2348-2352.
100. A. Shakoori, J. B. Bremner, A. C. Willis, R. Haritakun and P. A. Keller, *The Journal of Organic Chemistry*, **2013**, 78, 7639-7647.
101. R. Pummerer and F. Meininger, *Justus Liebigs Annalen der Chemie*, **1954**, 590, 173-194.
102. S. Jun-ichiro, M. Toshikazu, F. Takashi and K. Teijiro, *Chemistry Letters*, **1984**, 13, 1755-1758.
103. A. Shakoori, J. B. Bremner, M. K. Abdel-Hamid, A. C. Willis, R. Haritakun and P. A. Keller, *Beilstein Journal of Organic Chemistry*, **2015**, 11, 481-492.
104. J. N. Etters, *Journal of the Society of Dyers and Colourists*, **1993**, 109, 251-255.
105. B. Das, A. K. Guha and A. Wahab, *Journal of Physical Organic Chemistry*, **2020**, 33.
106. G. Miehe, P. Süsse, V. Kupcik, E. Egert, M. Nieger, G. Kunz, R. Gerke, B. Knieriem, M. Niemeyer and W. Lüttke, *Angewandte Chemie International Edition in English*, **1991**, 30, 964-967.
107. F. H. Allen, O. Kennard, D. G. Watson, L. Brammer, A. G. Orpen and R. Taylor, *Journal of the Chemical Society, Perkin Transactions 2*, **1987**, S1-S19.
108. R. Rondao, J. Seixas de Melo, M. J. Melo and A. J. Parola, *The Journal of Physical Chemistry A*, **2012**, 116, 2826-2832.
109. D. Pinheiro, M. Pineiro, A. M. Galvão and J. S. Seixas de Melo, *Chemical Science*, **2021**, 12, 303-313.
110. H. Görner, J. Pouliquen and J. Kossanyi, *Canadian Journal of Chemistry*, **1987**, 65, 708-717.
111. G. Grimme, P. Boldt, S. Grimme and P. G. Jones, *Chemische Berichte*, **1993**, 126, 1015-1021.
112. H. Hong, C. M. Conover, D. T. Hofsommer, C. A. Sanz and R. G. Hicks, *Organic and Biomolecular Chemistry*, **2020**, 18, 5838-5842.
113. R. Pummerer and H. Fiesselmann, *Justus Liebigs Annalen der Chemie*, **1940**, 544, 206-239.

114. R. Pummerer and E. Stieglitz, *Berichte der deutschen chemischen Gesellschaft (A and B Series)*, **1942**, 75, 1072-1085.
115. M. Lora-Tamayo and J. L. Soto, *Chapter 7 - Dienes Containing Two Nitrogen Atoms in the Conjugated System*, in *Organic Chemistry*, ed. J. A. N. Hamer, Elsevier, Amsterdam, **1967**, vol. 8, pp. 179-204.
116. L. Kalb, *Berichte der deutschen chemischen Gesellschaft*, **1909**, 42, 3642-3652.
117. M. T. Huynh, C. W. Anson, A. C. Cavell, S. S. Stahl and S. Hammes-Schiffer, *J Am Chem Soc*, **2016**, 138, 15903-15910.
118. W. Thomas, Synthesis and Characterization of a New Dimeric Indigo Compound, University of Victoria, 2019.
119. S. V. Shishkina, O. V. Shishkin and J. Leszczynski, *Chemical Physics Letters*, **2002**, 354, 428-434.
120. Y. Ishigaki, T. Shimajiri, T. Takeda, R. Katoono and T. Suzuki, *Chem*, **2018**, 4, 795-806.
121. S. Pons and S. B. Khoo, *Electrochimica Acta*, **1982**, 27, 1161-1169.
122. S. Jun-ichiro, F. Takashi, M. Kazutoshi, M. Yasufumi and K. Teijiro, *Chemistry Letters*, **1986**, 15, 1393-1396.
123. A. M. Bond, F. Marken, E. Hill, R. G. Compton and H. Hügel, *Journal of the Chemical Society, Perkin Transactions 2*, **1997**, 1735-1742.
124. N. G. Connelly and W. E. Geiger, *Chemical Reviews*, **1996**, 96, 877-910.
125. M. U. Munshi, J. Martens, G. Berden and J. Oomens, *The Journal of Physical Chemistry A* **2019**, 123, 8226-8233.
126. E. C. Nicholls-Allison, G. Nawn, B. O. Patrick and R. G. Hicks, *Chemical Communications*, **2015**, 51, 12482-12485.
127. D. T. Hofsommer, Indigo Mono- and Diimine Ligands as Proton and Electron Reservoirs, University of Victoria, 2019.
128. H. K. Hall, Jr., A. B. Padias, P. A. Williams, J.-M. Gosau, H. W. Boone and D.-K. Park, *Macromolecules*, **1995**, 28, 1-8.
129. J. van Alphen, *Recueil des Travaux Chimiques des Pays-Bas*, **1939**, 58, 378-386.
130. M. S. Kharasch and H. C. Brown, *Journal of the American Chemical Society*, **1942**, 64, 329-333.
131. K. B. Krauskopf and G. K. Rollefson, *Journal of the American Chemical Society*, **1936**, 58, 443-448.
132. C. Aubry, A. J. Wilson, D. Emmerson, E. Murphy, Y. Y. Chan, M. P. Dickens, M. D. Garcia, P. R. Jenkins, S. Mahale and B. Chaudhuri, *Bioorganic and Medicinal Chemistry*, **2009**, 17, 6073-6084.
133. C. W. Anson and D. M. Thamattoor, *Journal of Organic Chemistry*, **2012**, 77, 1693-1700.
134. A. D. Gift, S. M. Stewart and P. Kwete Bokashanga, *Journal of Chemical Education*, **2012**, 89, 1458-1460.
135. M. J. Bezdek, S. Guo and P. J. Chirik, *Science*, **2016**, 354, 730-733.
136. A. Kütt, S. Selberg, I. Kaljurand, S. Tshepelevitsh, A. Heering, A. Darnell, K. Kaupmees, M. Piirsalu and I. Leito, *Tetrahedron Letters*, **2018**, 59, 3738-3748.
137. S. Tshepelevitsh, A. Kütt, M. Lõkov, I. Kaljurand, J. Saame, A. Heering, P. G. Plieger, R. Vianello and I. Leito, *European Journal of Organic Chemistry*, **2019**, 2019, 6735-6748.

138. G. Izzet, X. Zeng, H. Akdas, J. Marrot and O. Reinaud, *Chemical Communications*, **2007**, 810-812.
139. E. C. Nicholls-Allison, Part I: The Synthesis and Characterization of Scorpionate Ligands for Lanthanide Complexation for Potential PARACEST Applications Part II: The Synthesis and the Characterization of New and Old Organic Dyes, University of Victoria, 2015.
140. H. Ohmori, T. Takanami, H. Shimada and M. Masui, *Chemical and Pharmaceutical Bulletin*, **1987**, 35, 2558-2560.
141. M. Hirao, H. Sugimoto and H. Ohno, *Journal of The Electrochemical Society*, **2000**, 147, 4168.
142. H. Langhals, *New Journal of Chemistry*, **2008**, 32, 21-23.
143. S. A. Samath, M. Raman, N. Raman, K. T. Jeyasubramanian and S. K. Ramalingam, *Transition Metal Chemistry*, **1992**, 17, 13-15.
144. V. Raab, E. Gauchenova, A. Merkoulov, K. Harms, J. Sundermeyer, B. Kovačević and Z. B. Maksić, *Journal of the American Chemical Society*, **2005**, 127, 15738-15743.
145. S. Miao, S. M. Brombosz, P. v. R. Schleyer, J. I. Wu, S. Barlow, S. R. Marder, K. I. Hardcastle and U. H. F. Bunz, *Journal of the American Chemical Society*, **2008**, 130, 7339-7344.
146. J. I. Wu, C. S. Wannere, Y. Mo, P. v. R. Schleyer and U. H. F. Bunz, *The Journal of Organic Chemistry*, **2009**, 74, 4343-4349.
147. U. H. Bunz, *Chemistry*, **2009**, 15, 6780-6789.
148. S. Matsumoto, M. Akazome, S. Qu, T. Kobayashi, M. Kanehiro and K. Ogura, *Heterocycles*, **2010**, 80, 645-656.
149. K. Isoda, T. Abe and M. Tadokoro, *Chemistry An Asian Journal*, **2013**, 8, 2951-2954.
150. K. Hatakeyama-Sato, T. Akahane, C. Go, T. Kaseyama, T. Yoshimoto and K. Oyaizu, *ACS Energy Letters*, **2020**, 5, 1712-1717.
151. U. H. F. Bunz and J. Freudenberg, *Accounts of Chemical Research*, **2019**, 52, 1575-1587.

Appendix A: List of Appendix Contents

Appendix B: NMR Spectra

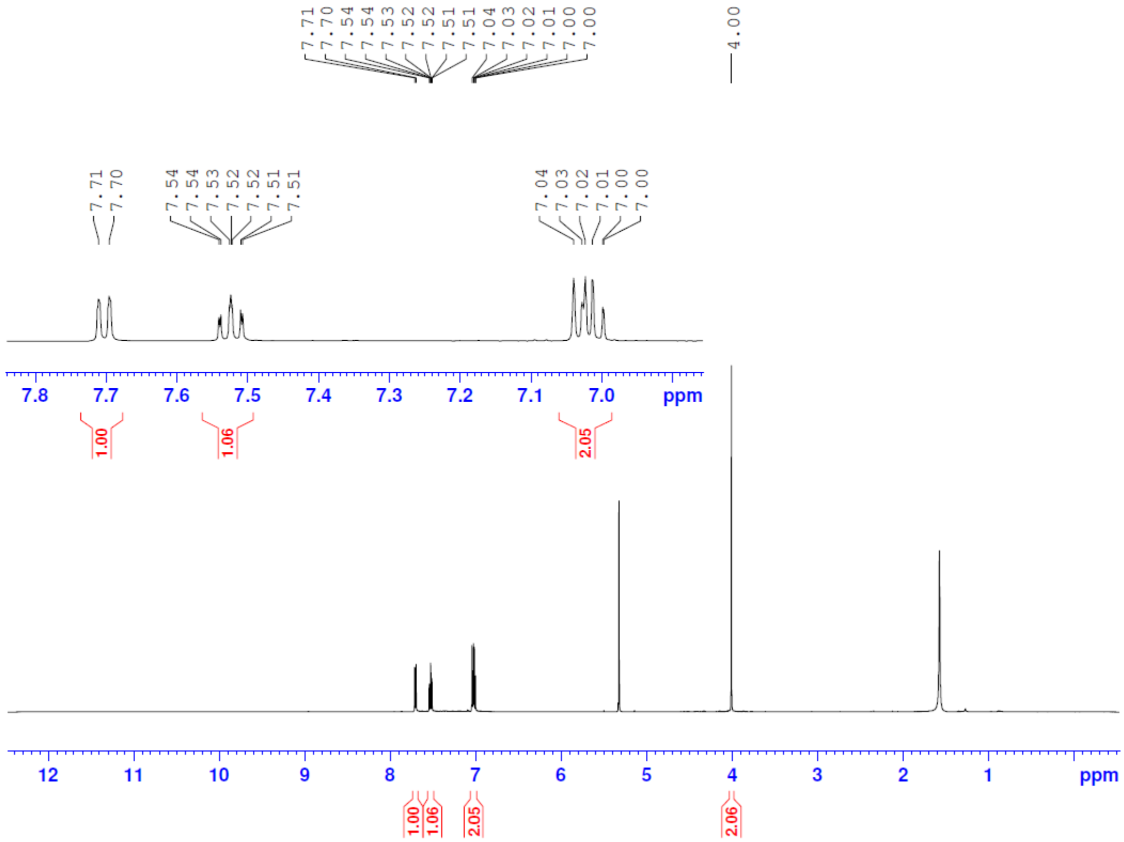

Appendix B-1 ^{1}H NMR spectrum of **2.5** in CD_2Cl_2 at 500 MHz.

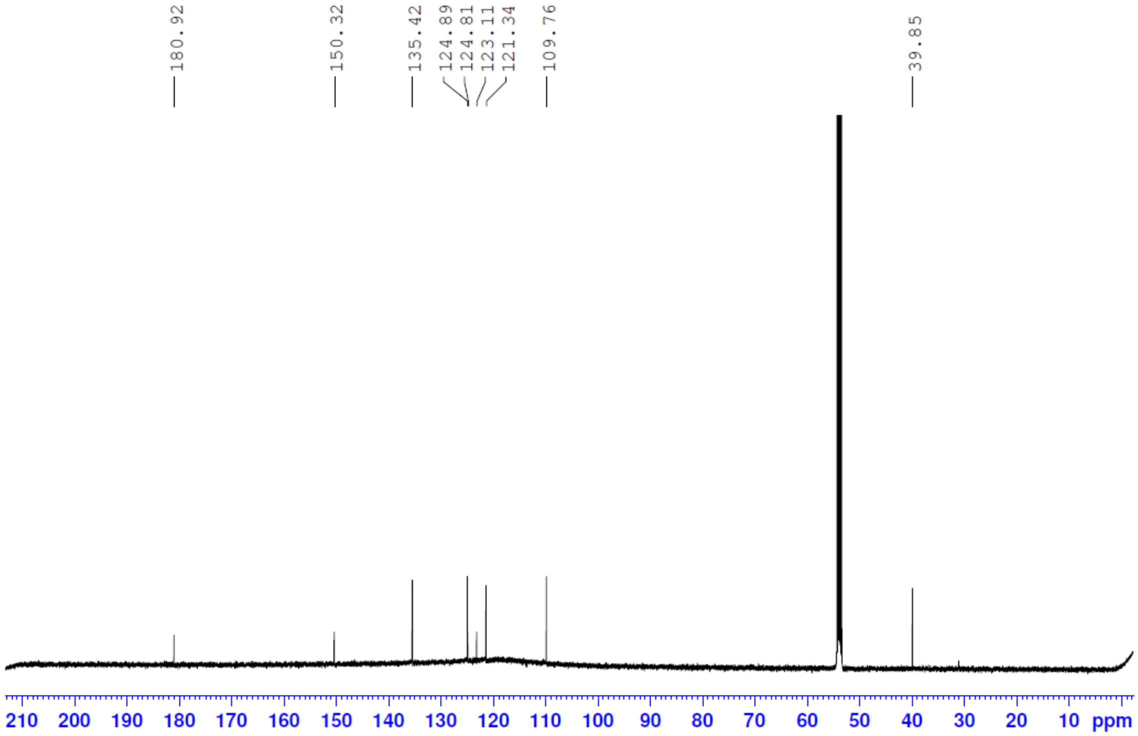

Appendix B-2 ^{13}C NMR spectrum of **2.5** in CD_2Cl_2 at 126 MHz.

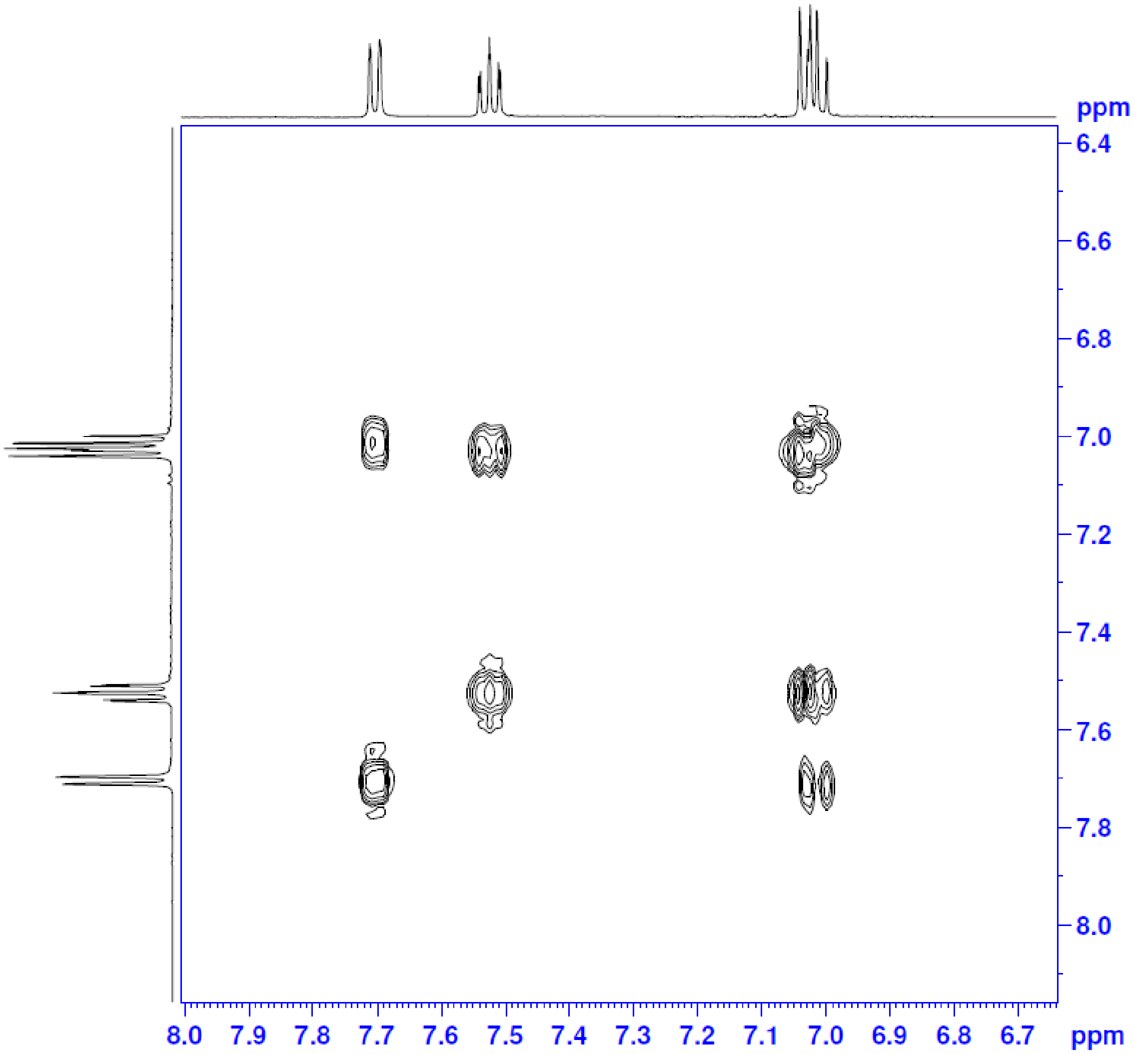

Appendix B-3 2D ^{1}H-^{1}H COSY spectrum of **2.5** in CD_2Cl_2 at 500 MHz.

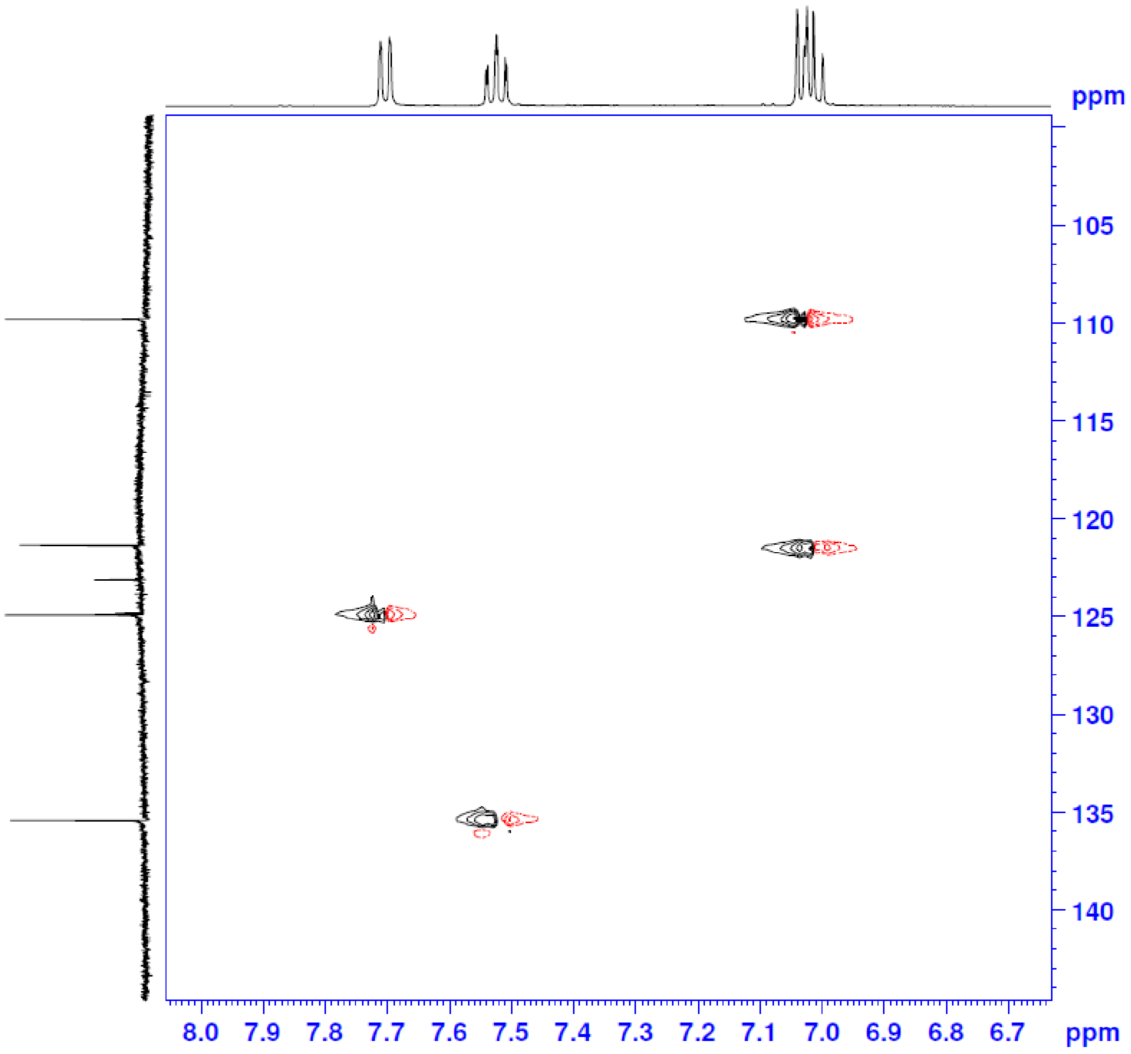

Appendix B-4 2D ^{1}H-^{13}C HSQC spectrum of **2.5** in CD_2Cl_2.

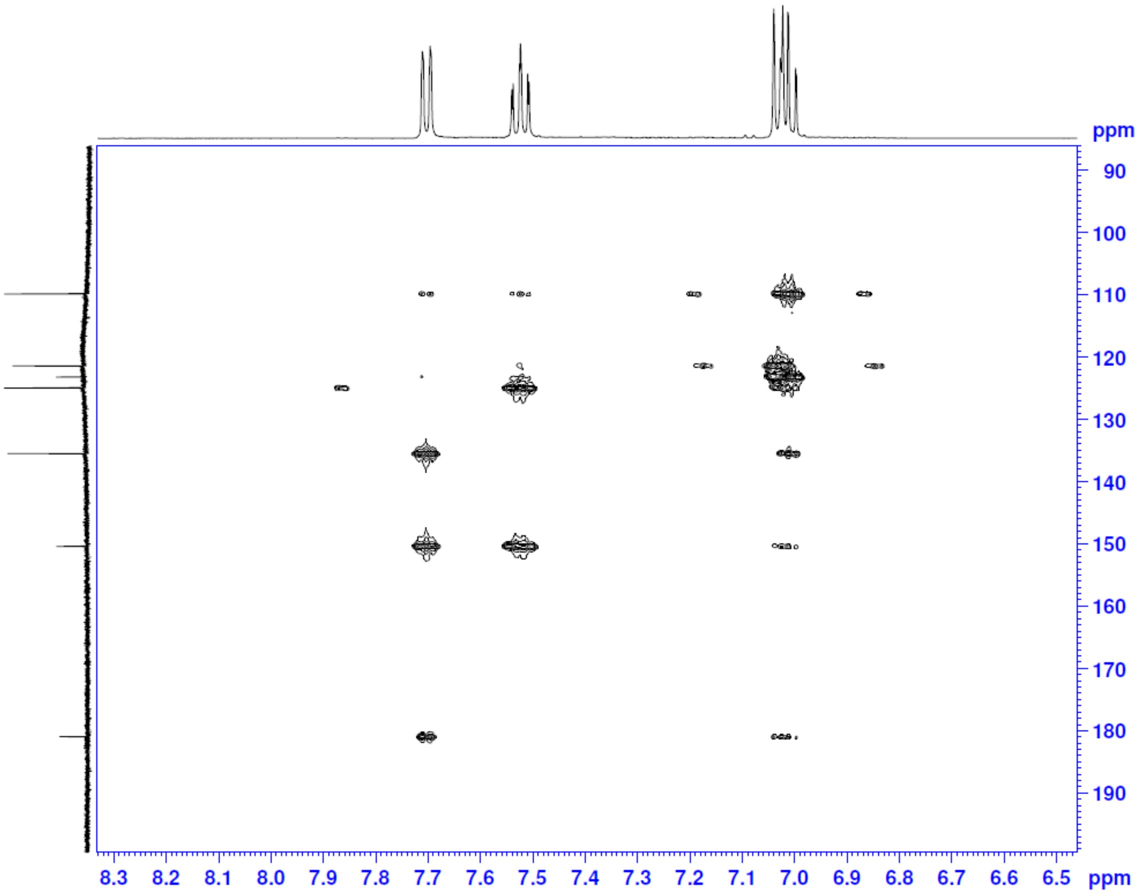

Appendix B-5 2D ^{1}H-^{13}C HMBC spectrum of **2.5** in CD_2Cl_2.

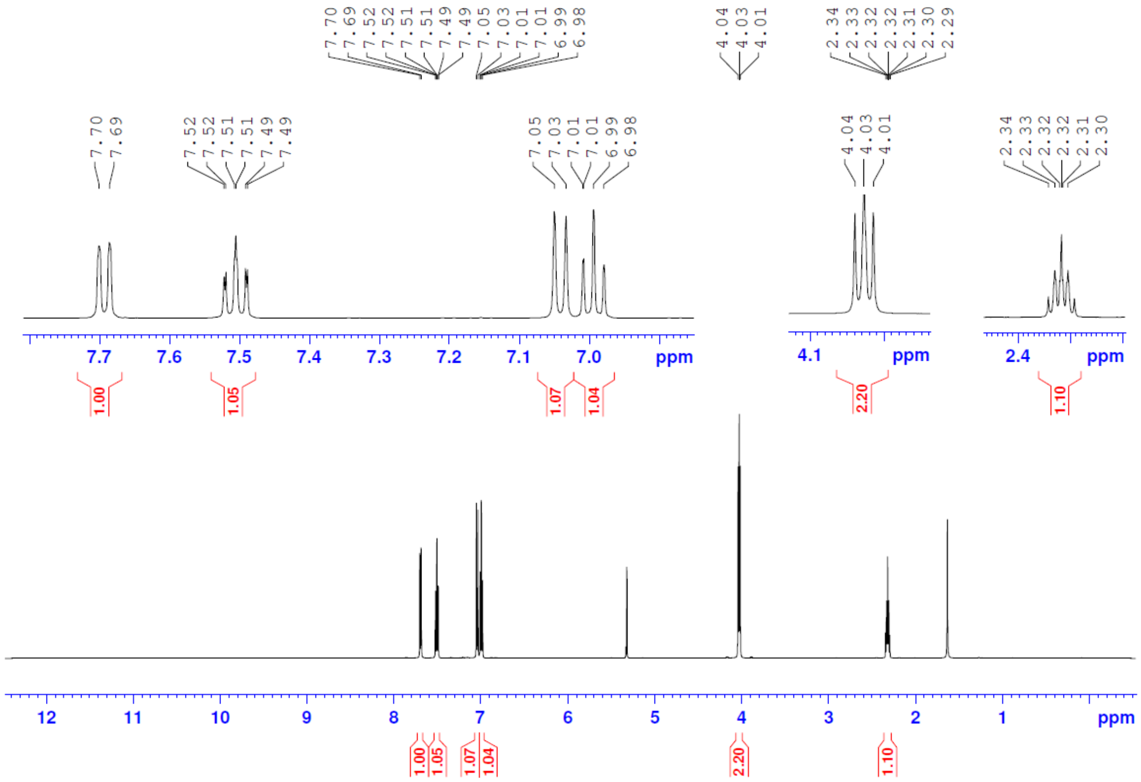

Appendix B-6 ^{1}H NMR spectrum of **2.6** in CD_2Cl_2 at 500 MHz.

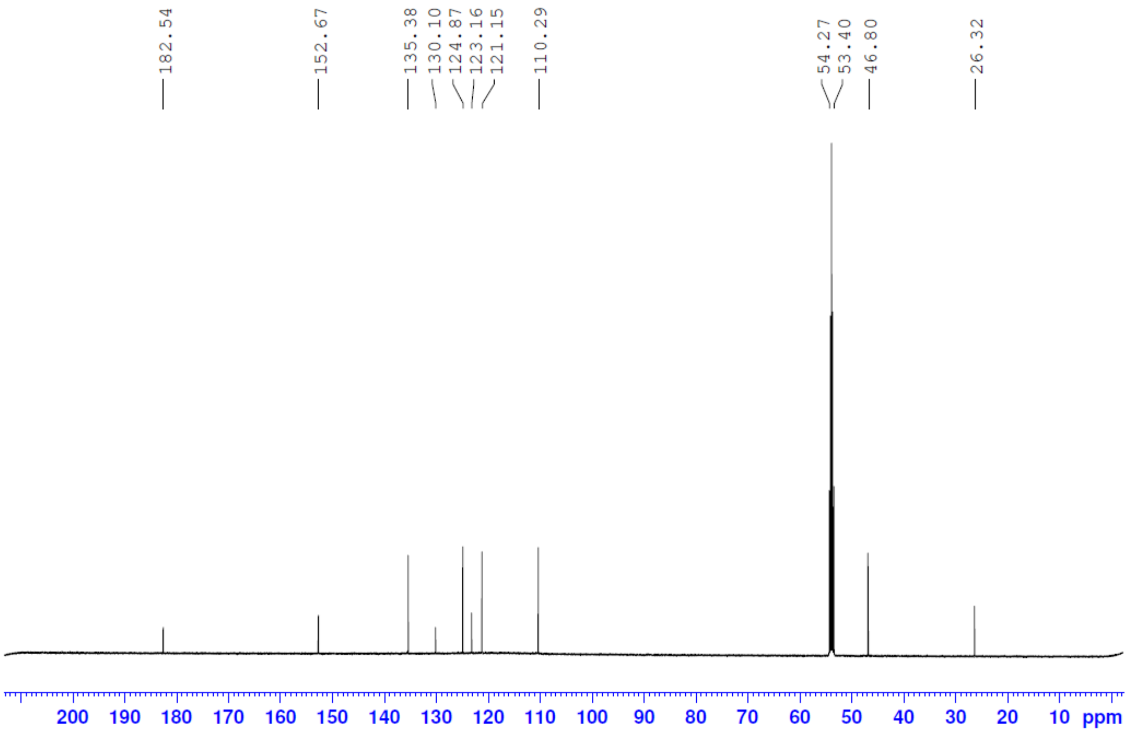

Appendix B-7 ^{13}C NMR spectrum of **2.6** in CD_2Cl_2 at 126 MHz.

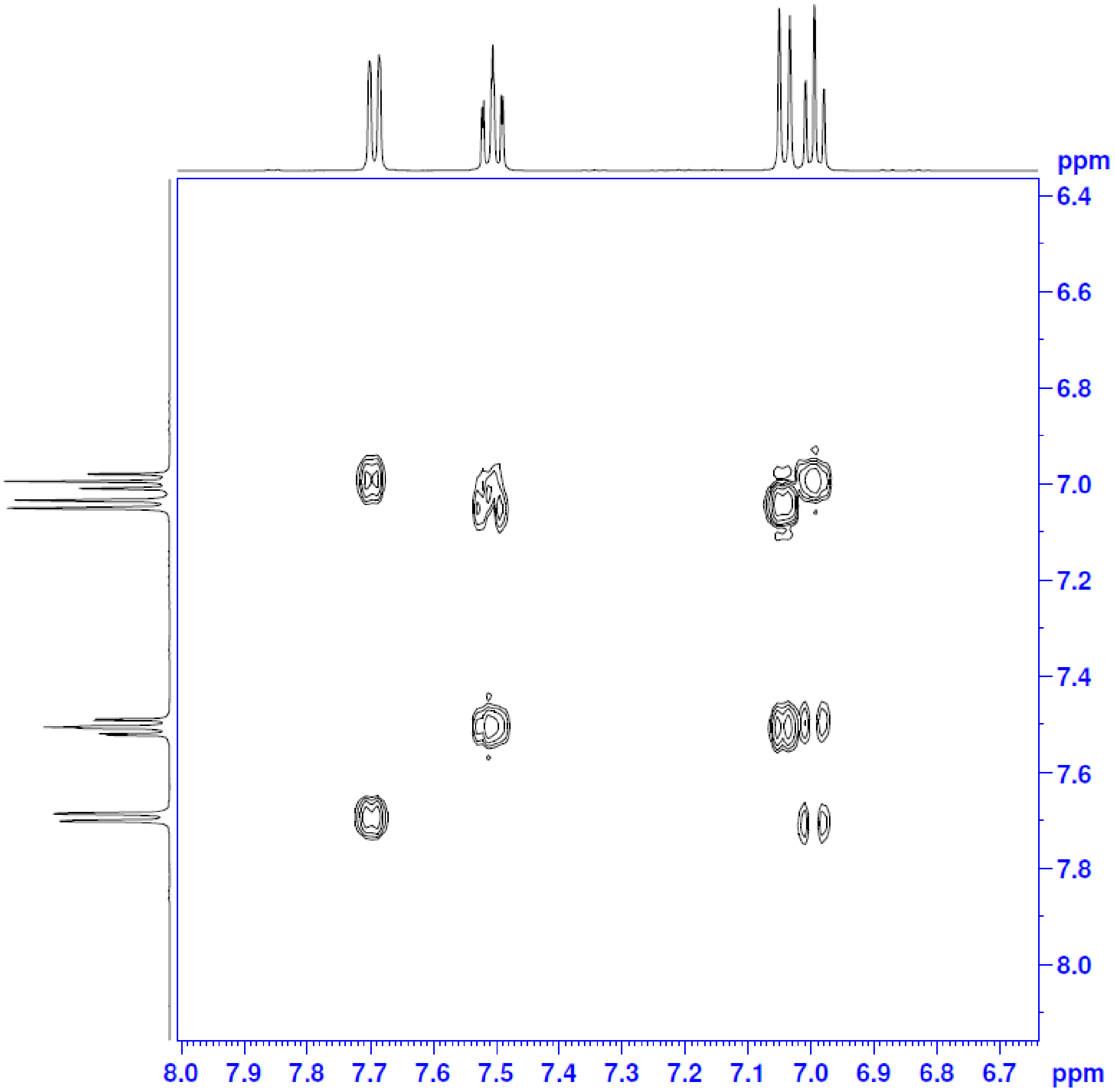

Appendix B-8 2D ^{1}H-^{1}H COSY spectrum of **2.6** in CD_2Cl_2 at 500 MHz.

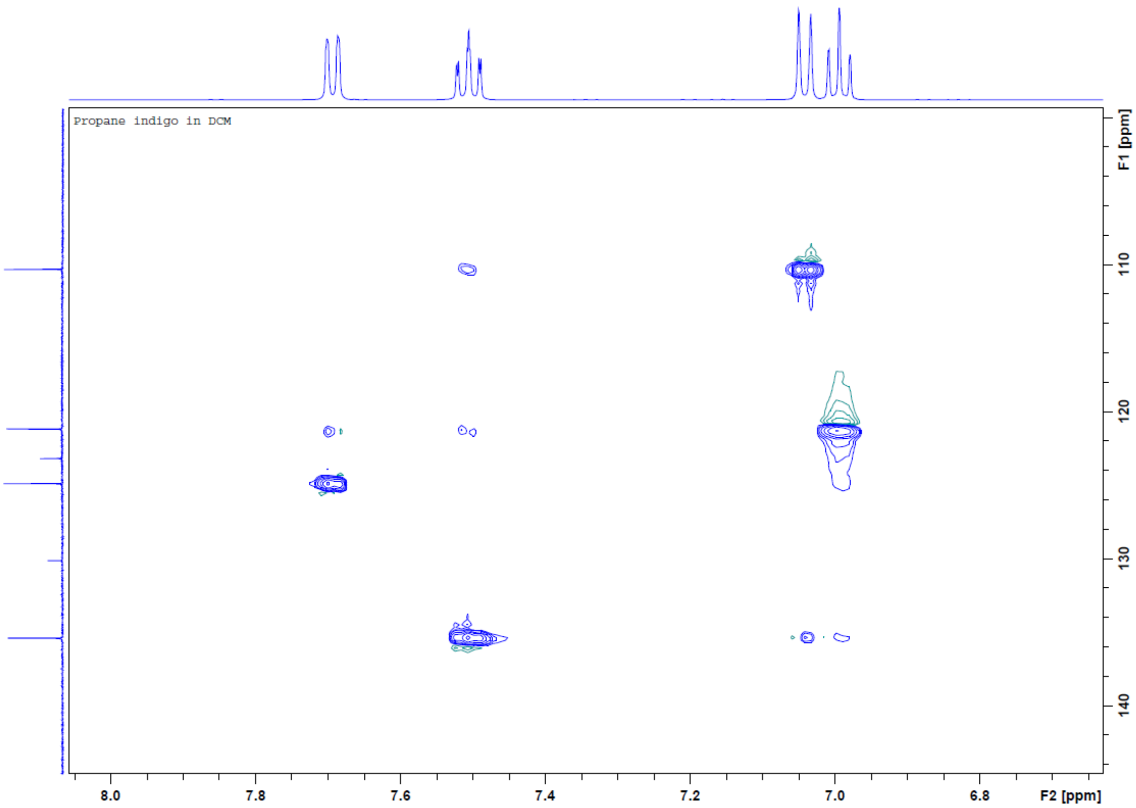

Appendix B-9 2D ^{1}H-^{13}C HSQC spectrum of **2.6** in CD_2Cl_2.

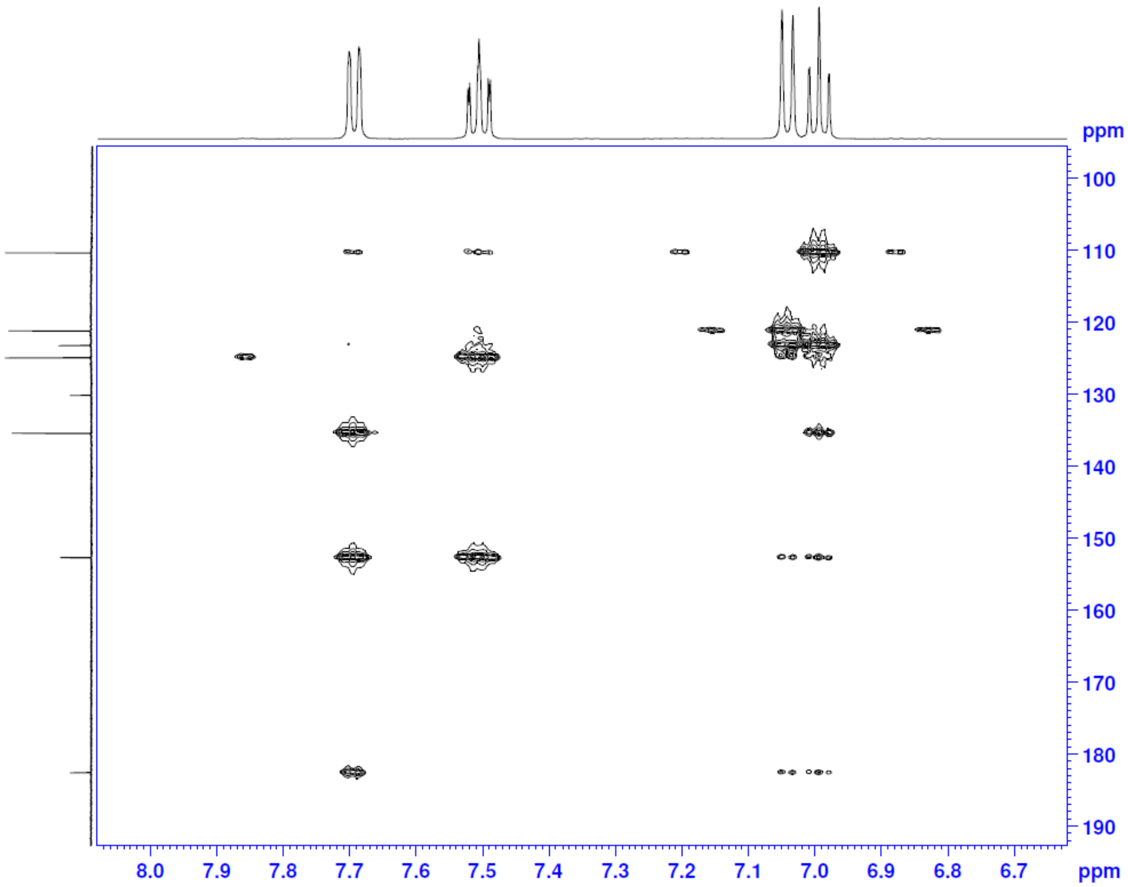

Appendix B-10 2D ^{1}H-^{13}C HMBC spectrum of **2.6** in CD_2Cl_2.

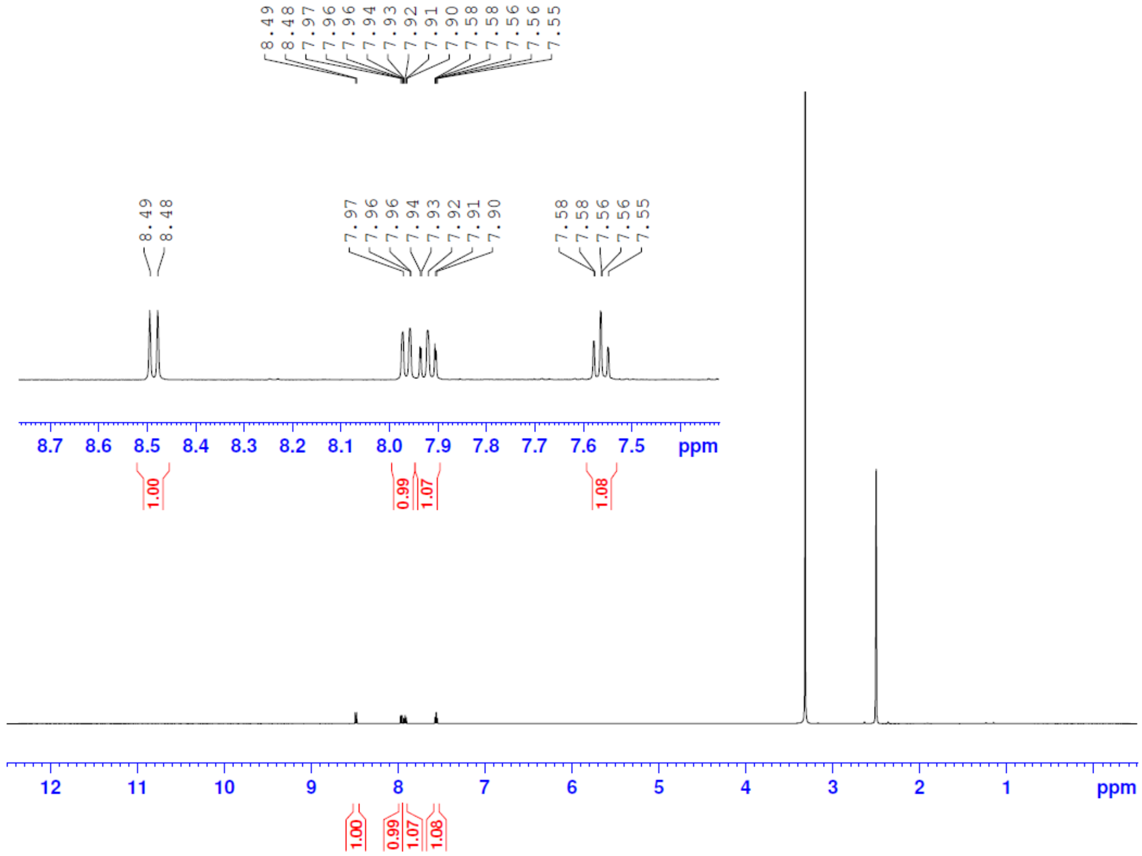

Appendix B-11 ^{1}H NMR spectrum of **2.7** in DMSO-d$_6$ at 500 MHz.

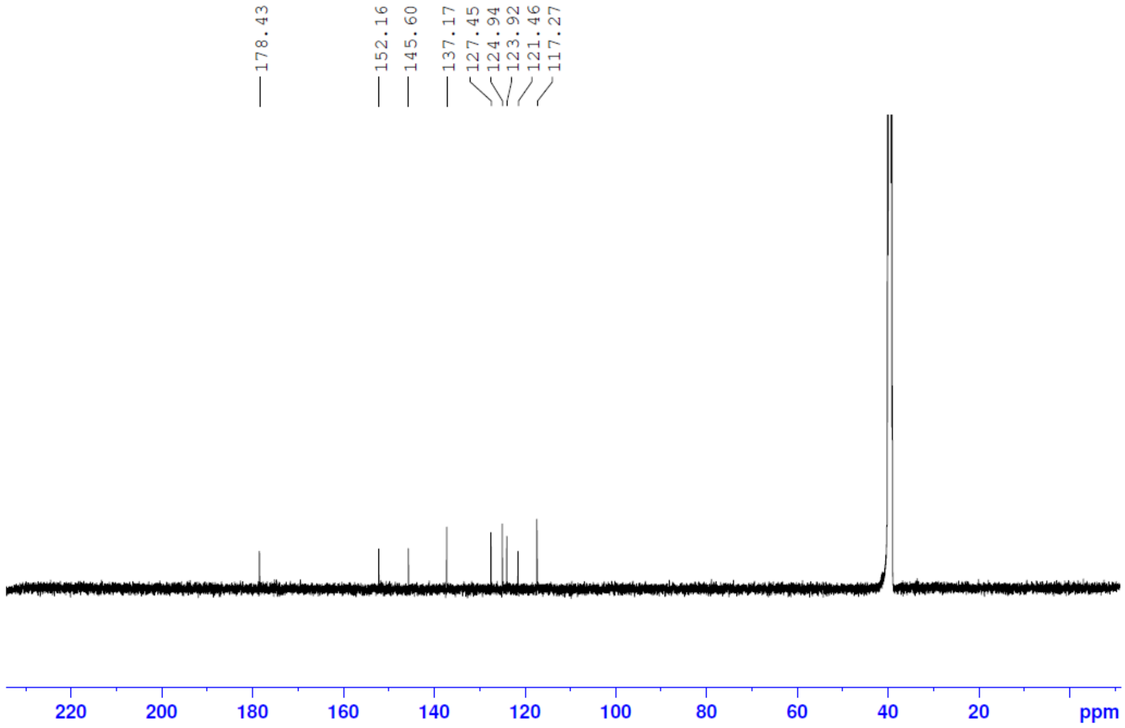

Appendix B-12 ^{13}C NMR spectrum of **2.7** in DMSO-d_6 at 126 MHz.

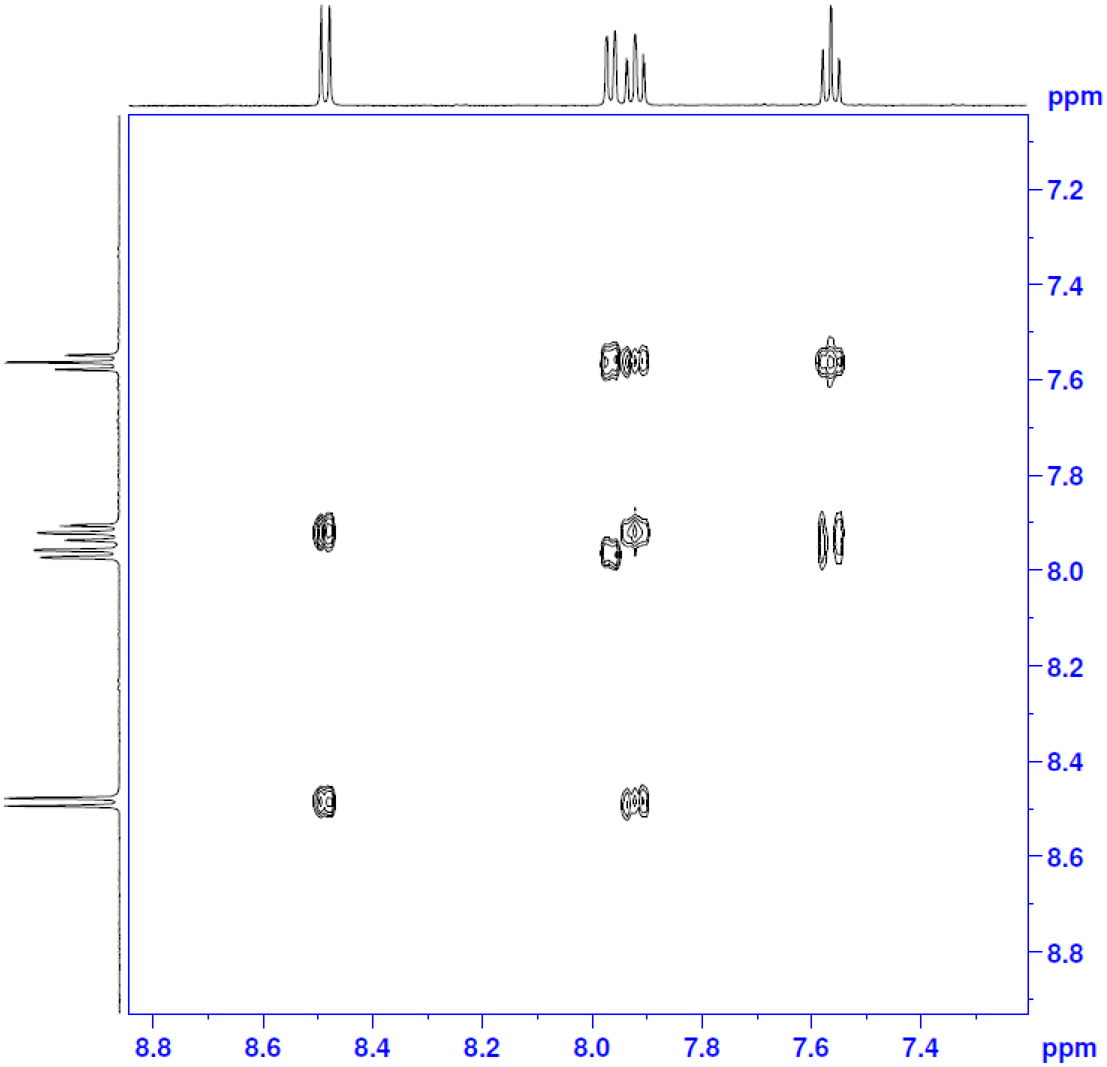

Appendix B-13 2D ^{1}H-^{1}H COSY spectrum of **2.7** in DMSO-d_6 at 500 MHz.

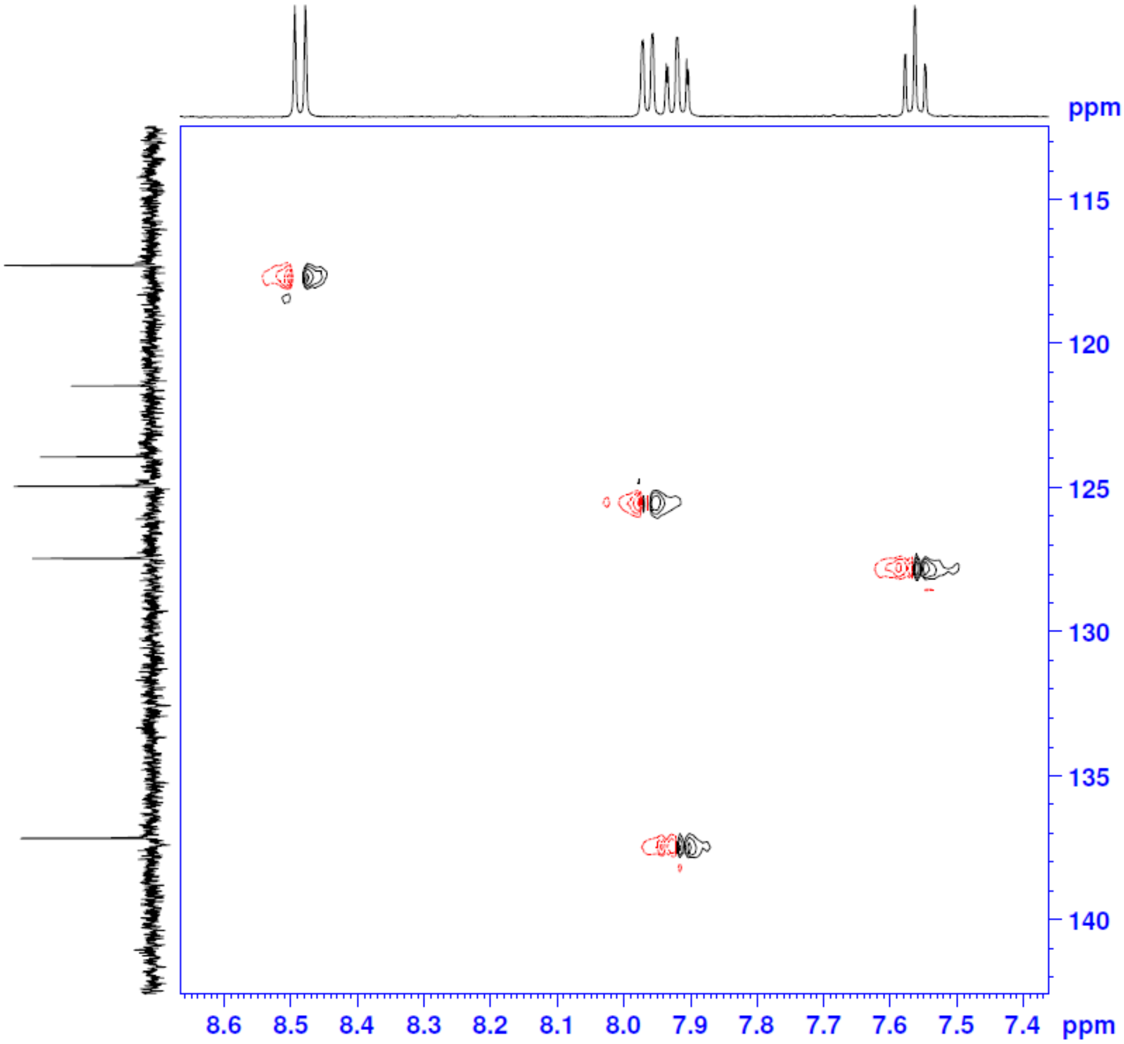

Appendix B-14 2D ^{1}H-^{13}C HSQC spectrum of **2.7** in DMSO-d$_6$.

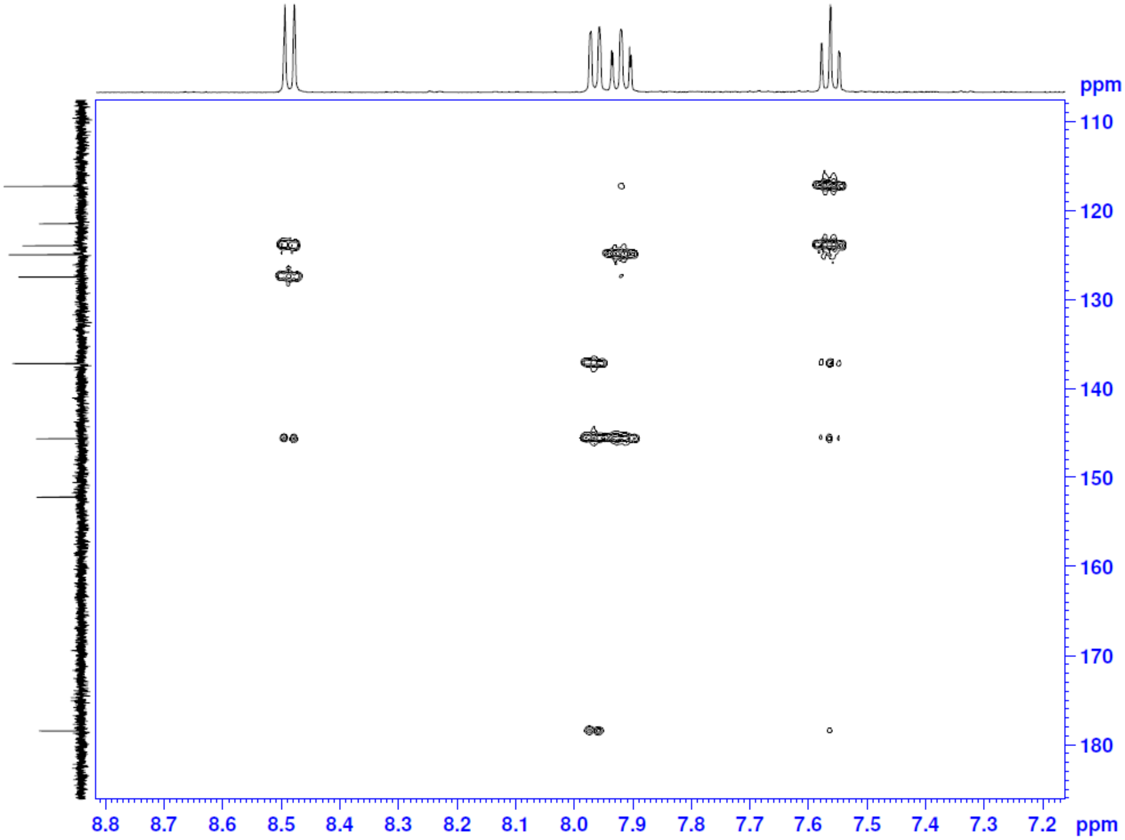

Appendix B-15 2D ^{1}H-^{13}C HMBC spectrum of **2.7** in DMSO-d$_6$.

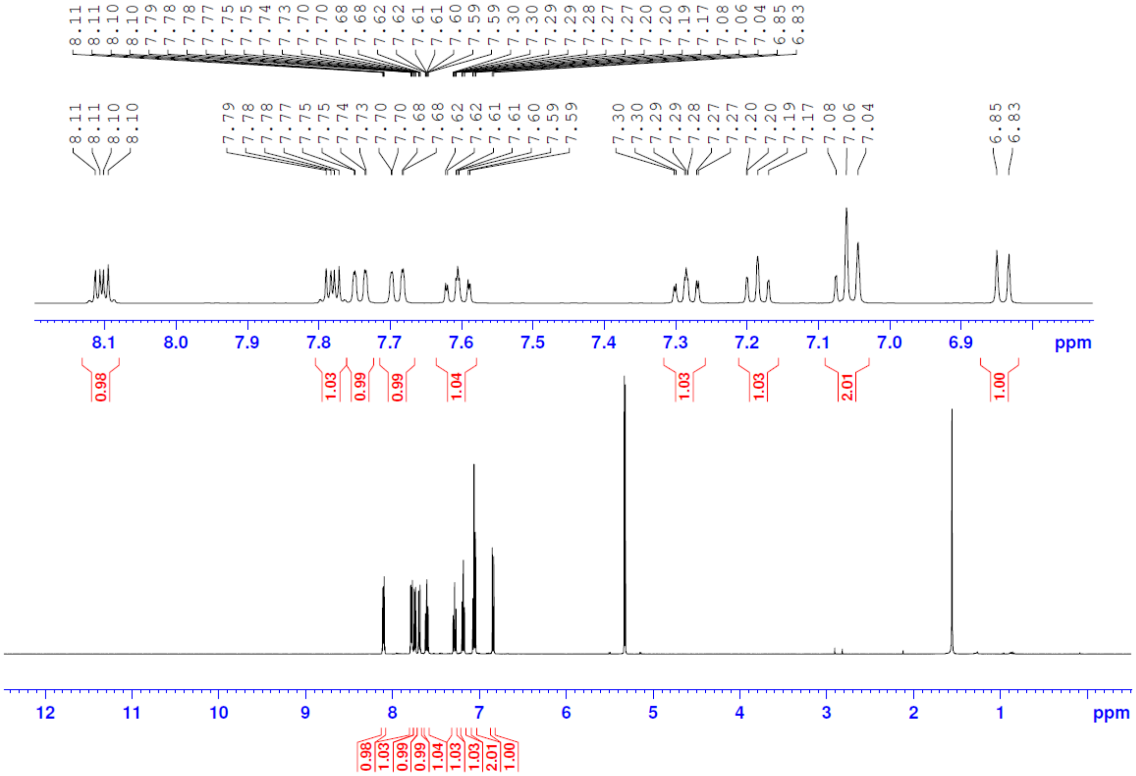

Appendix B-16 ^{1}H NMR spectrum of **3.2** in CD_2Cl_2 at 500 MHz.

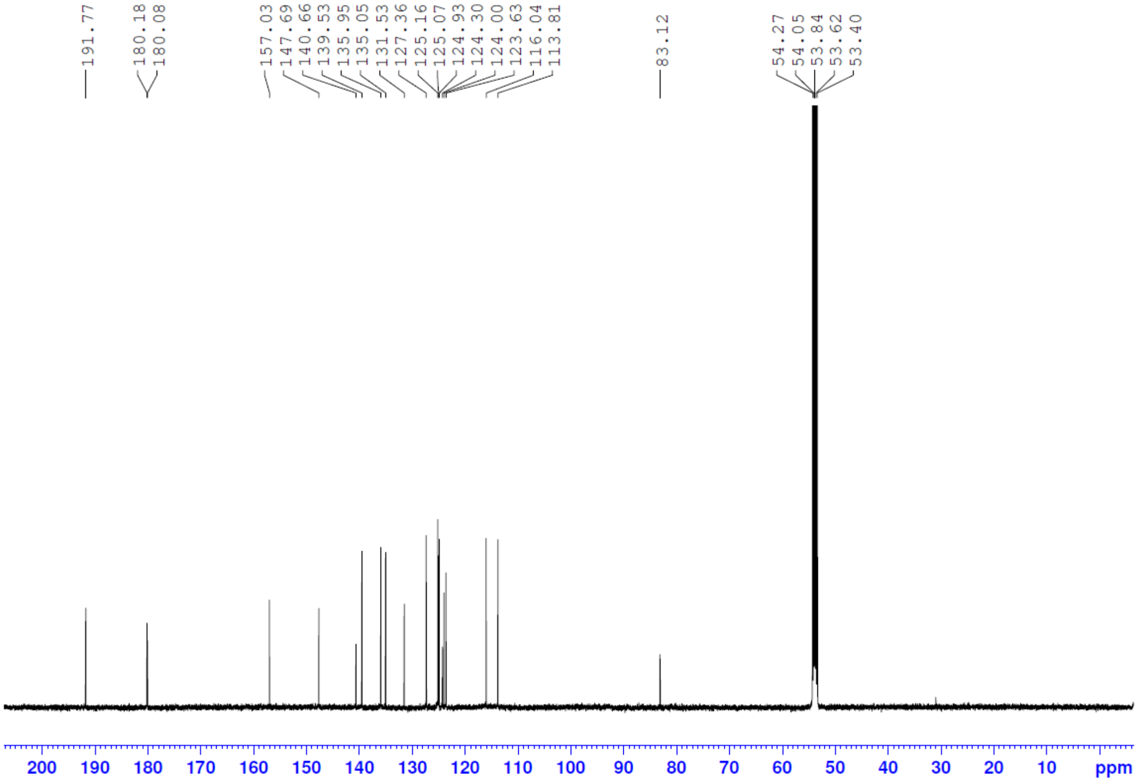

Appendix B-17 ^{13}C NMR spectrum of **3.2** in CD_2Cl_2 at 126 MHz.

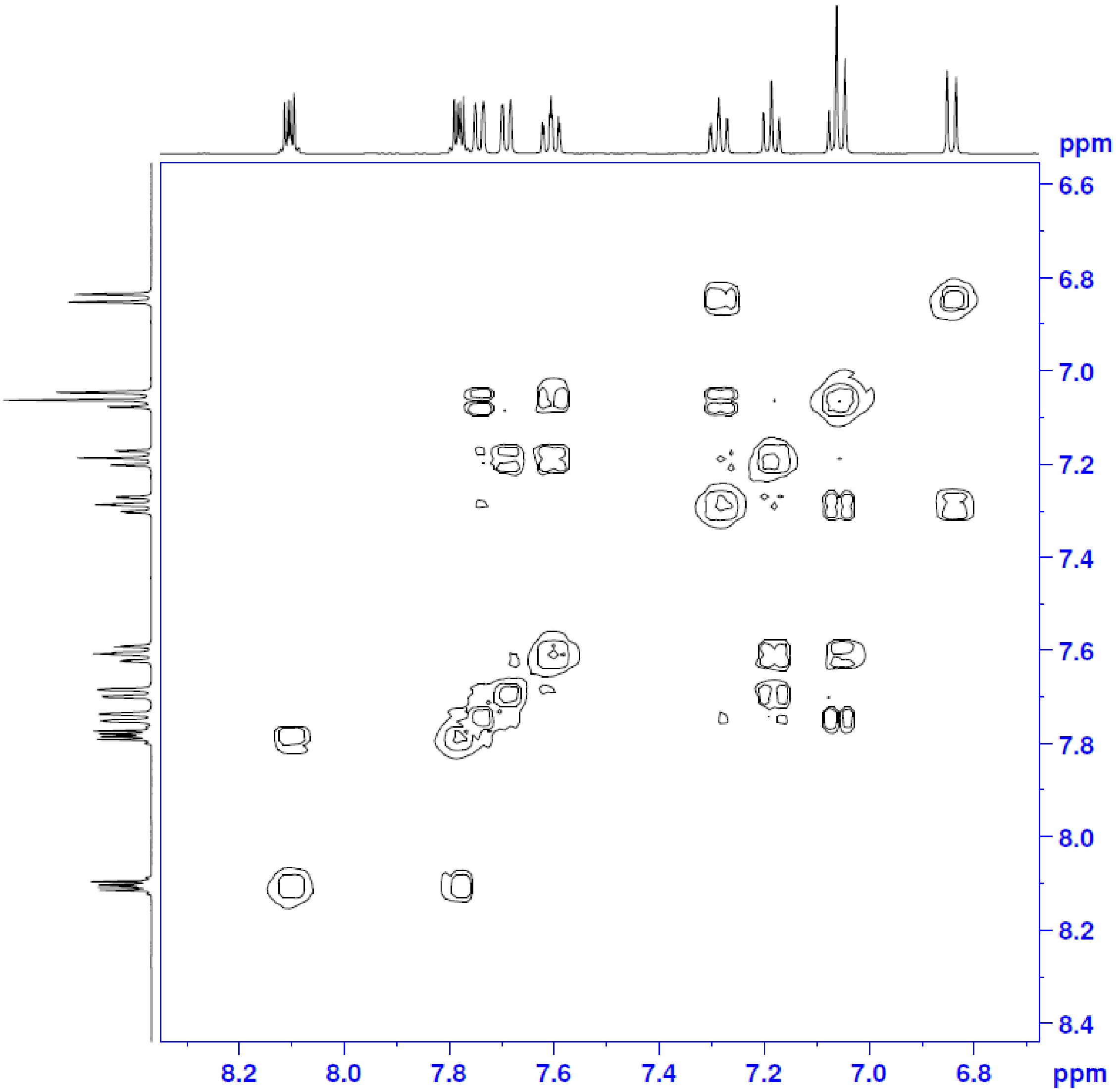

Appendix B-18 2D ^{1}H-^{1}H COSY spectrum of **3.2** in CD_2Cl_2 at 500 MHz.

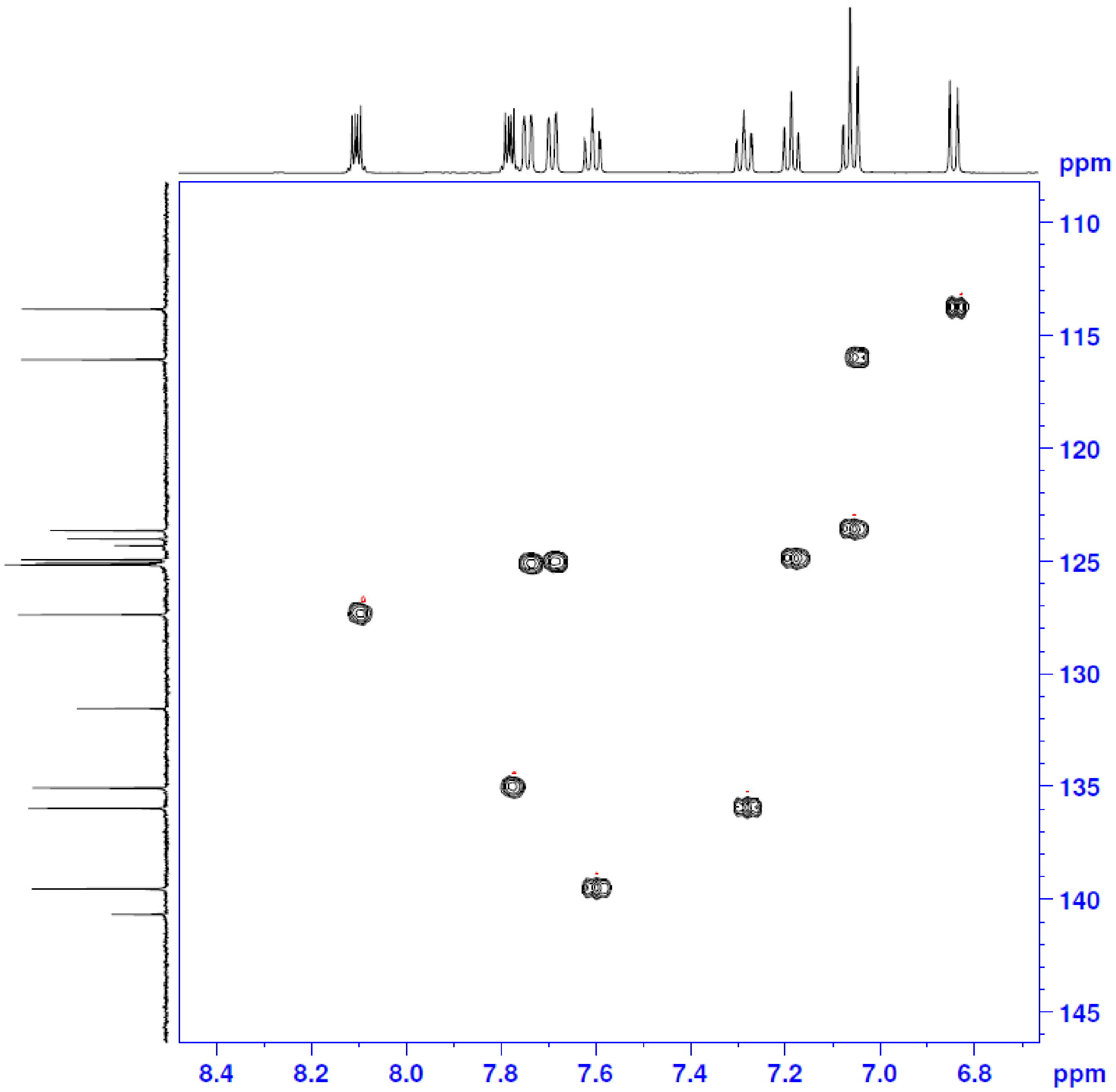

Appendix B-19 2D ^{1}H-^{13}C HSQC spectrum of **3.2** in CD_2Cl_2.

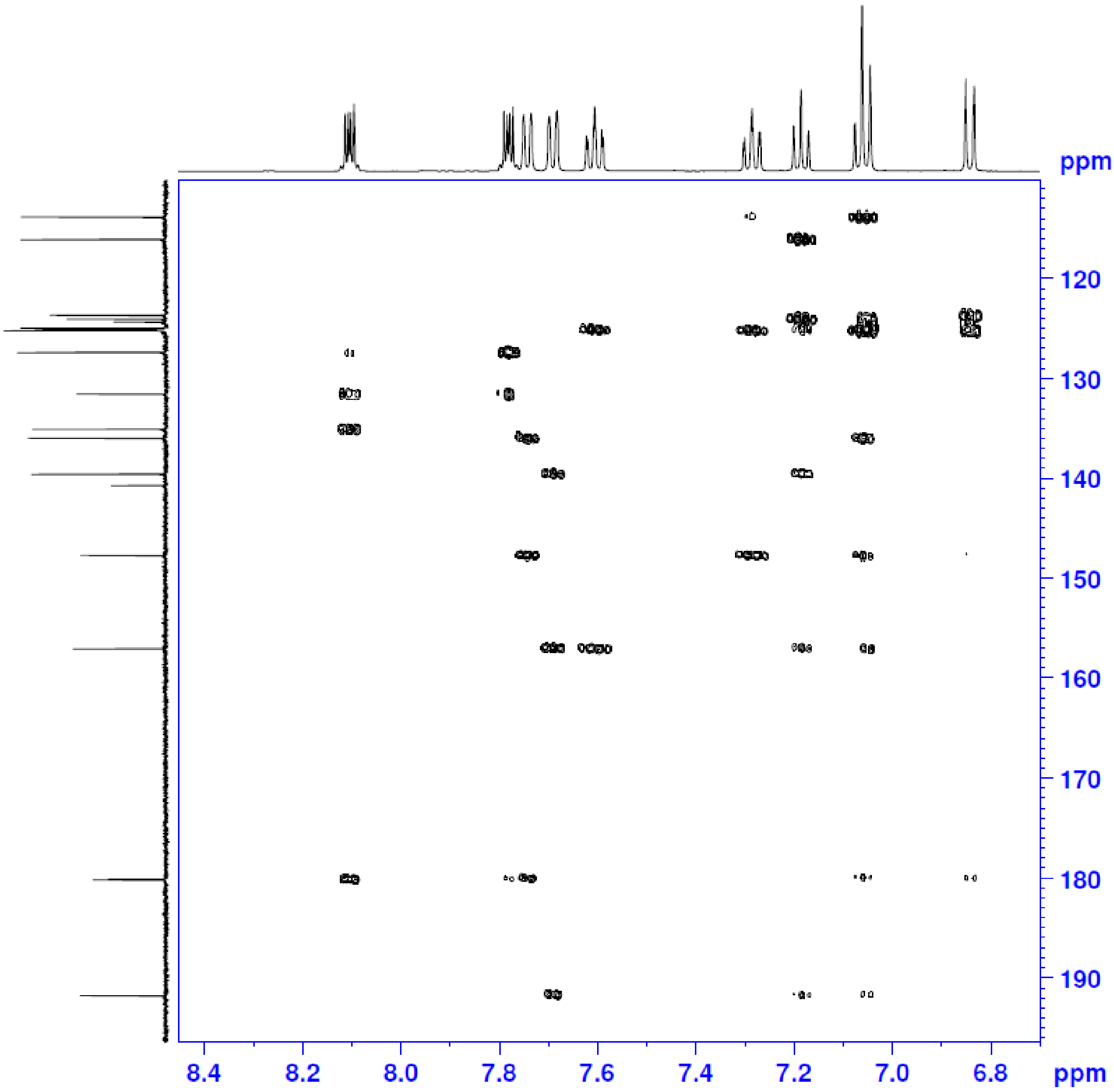

Appendix B-20 2D ^{1}H-^{13}C HMBC spectrum of **3.2** in CD_2Cl_2.

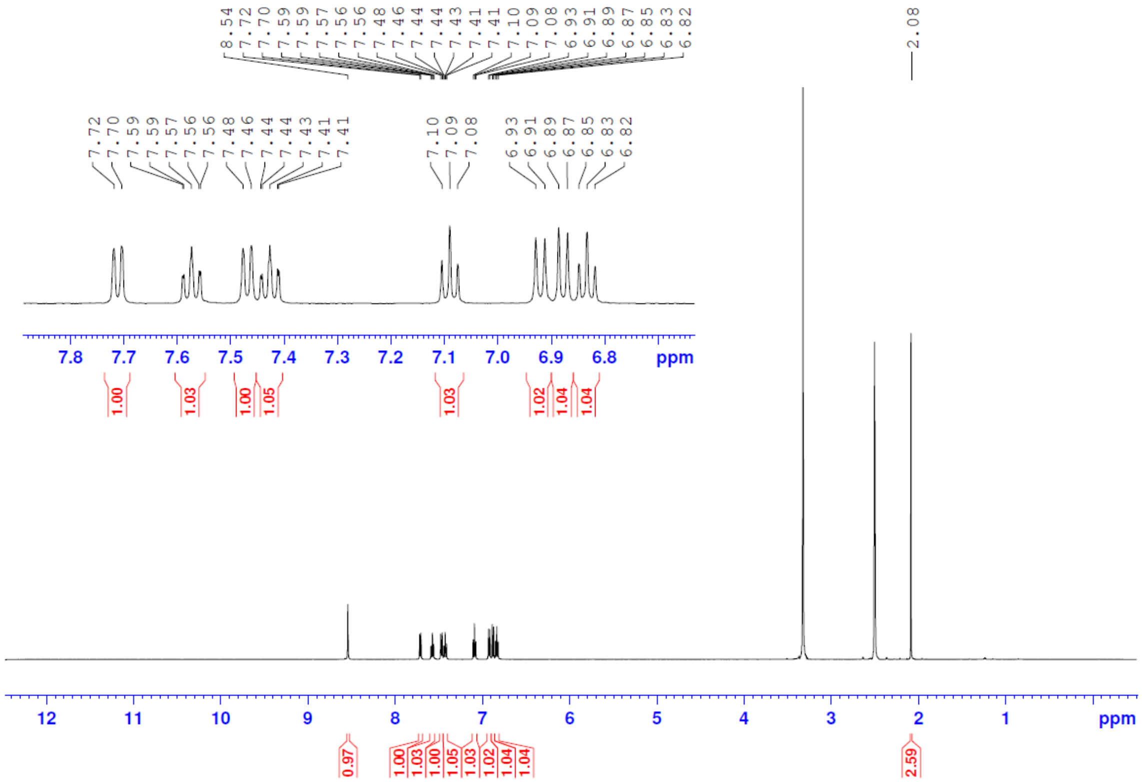

Appendix B-21 ^{1}H NMR spectrum of **3.3·acetone** in DMSO-d_6 at 500 MHz.

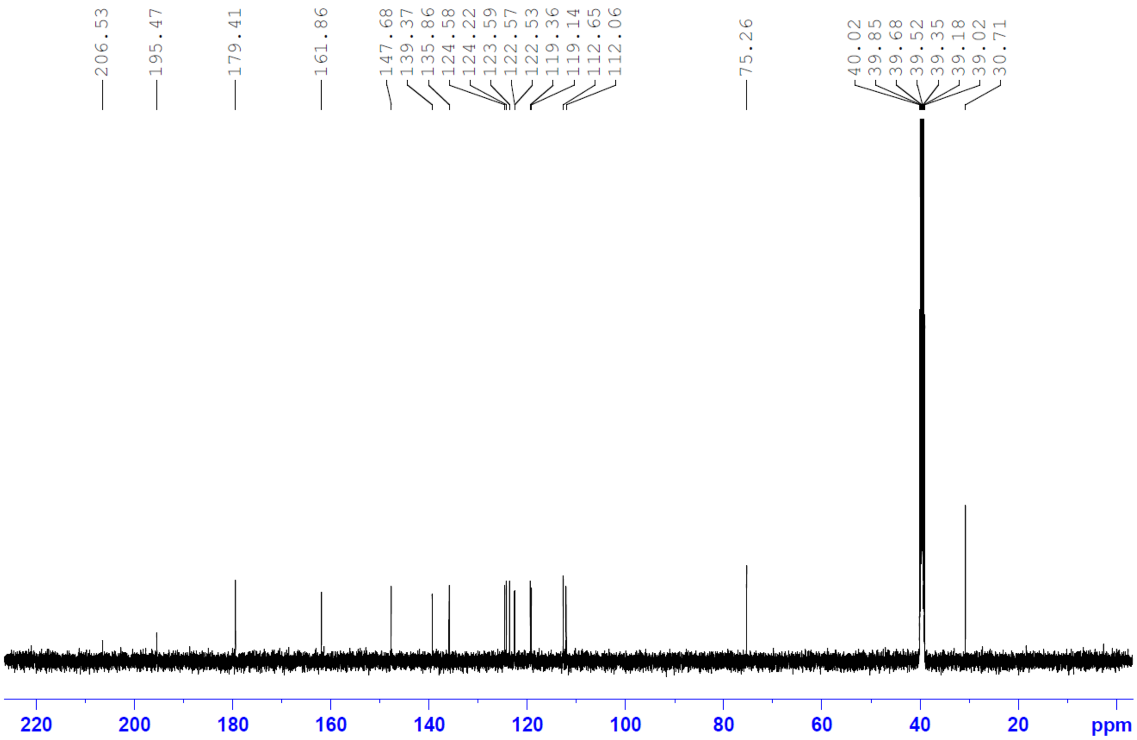

Appendix B-22 ^{13}C NMR spectrum of **3.3·acetone** in DMSO-d_6 at 126 MHz.

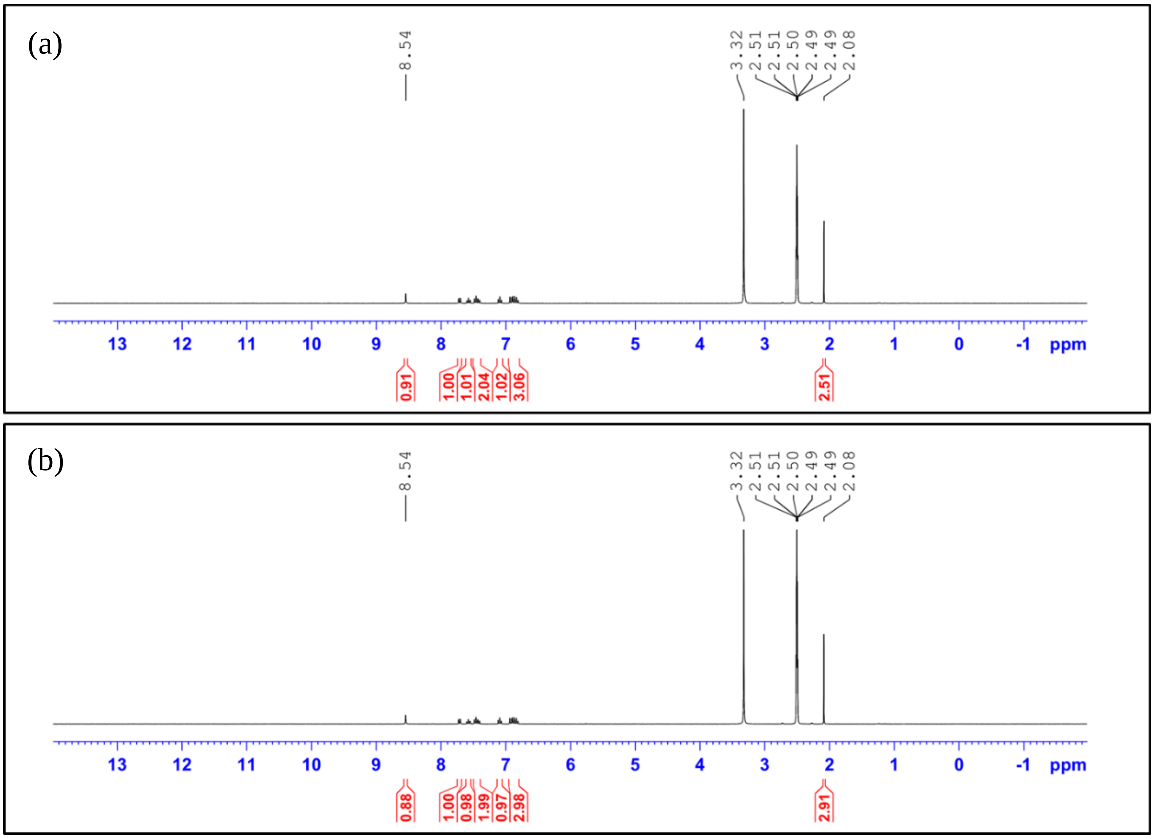

Appendix B-23 Evidence of 1:1 (product : acetone) adduct formation of **3.3** after recrystallization in acetone: 1H NMR spectra of the same tube with varying relaxation delay (d_1) time in DMSO-d_6 at 300 MHz, (a) $d_1 = 1$ second, (b) $d_1 = 30$ seconds. Acetone (δ 2.08) integration increases with longer d1. Reproduced from the Reference[112] with permission from the Royal Society of Chemistry.

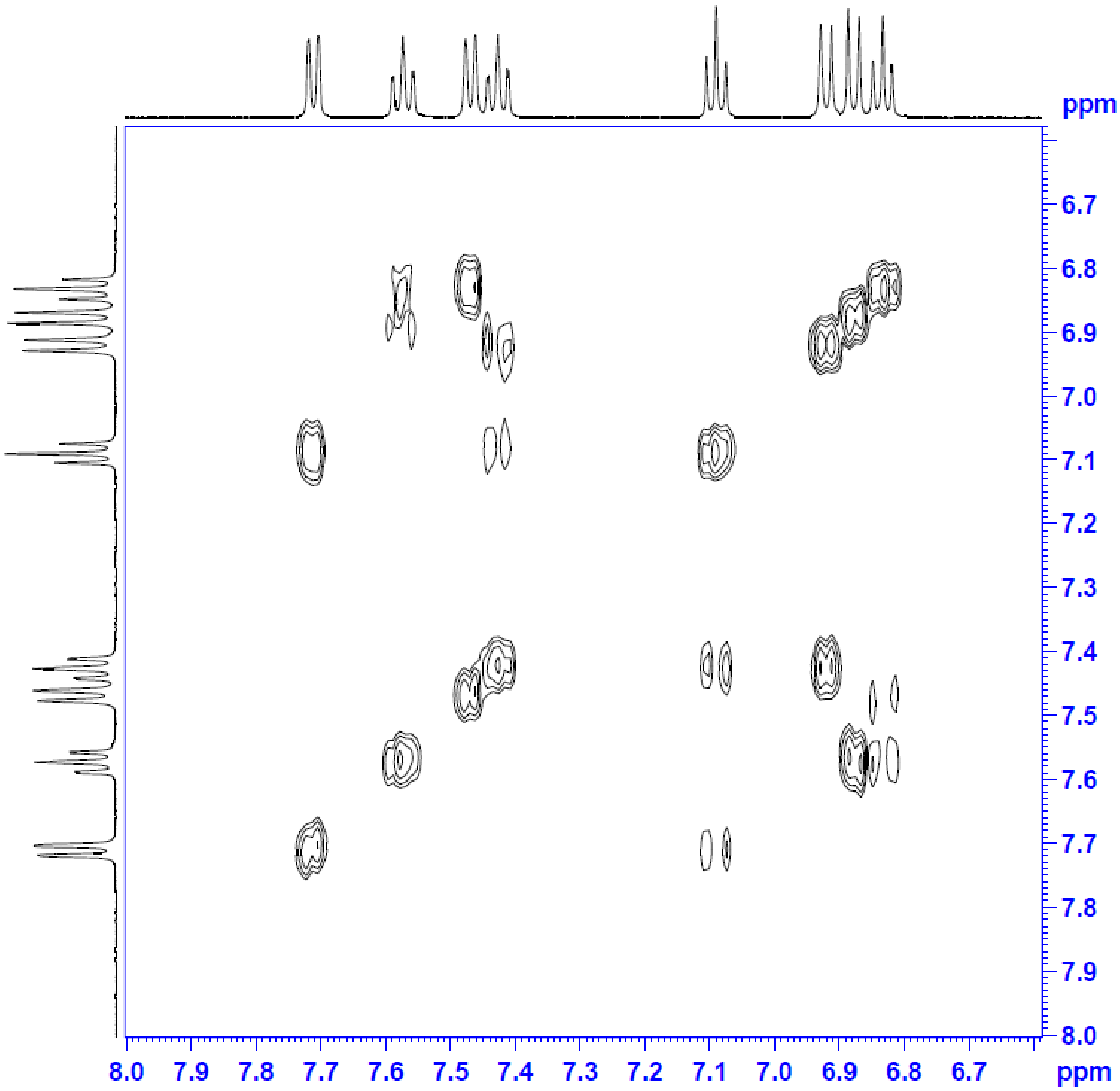

Appendix B-24 2D ^1H-^1H COSY spectrum of **3.3·acetone** in DMSO-d_6 at 500 MHz.

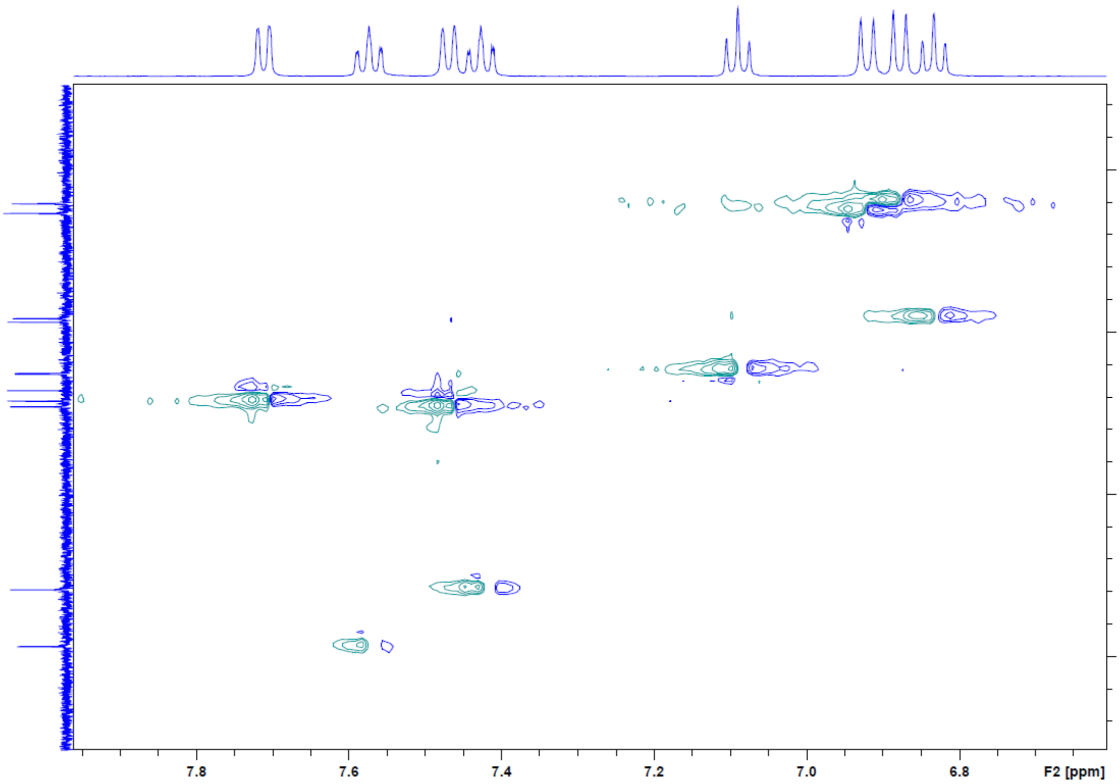

Appendix B-25 2D ^{1}H-^{13}C HSQC spectrum of **3.3·acetone** in DMSO-d$_6$.

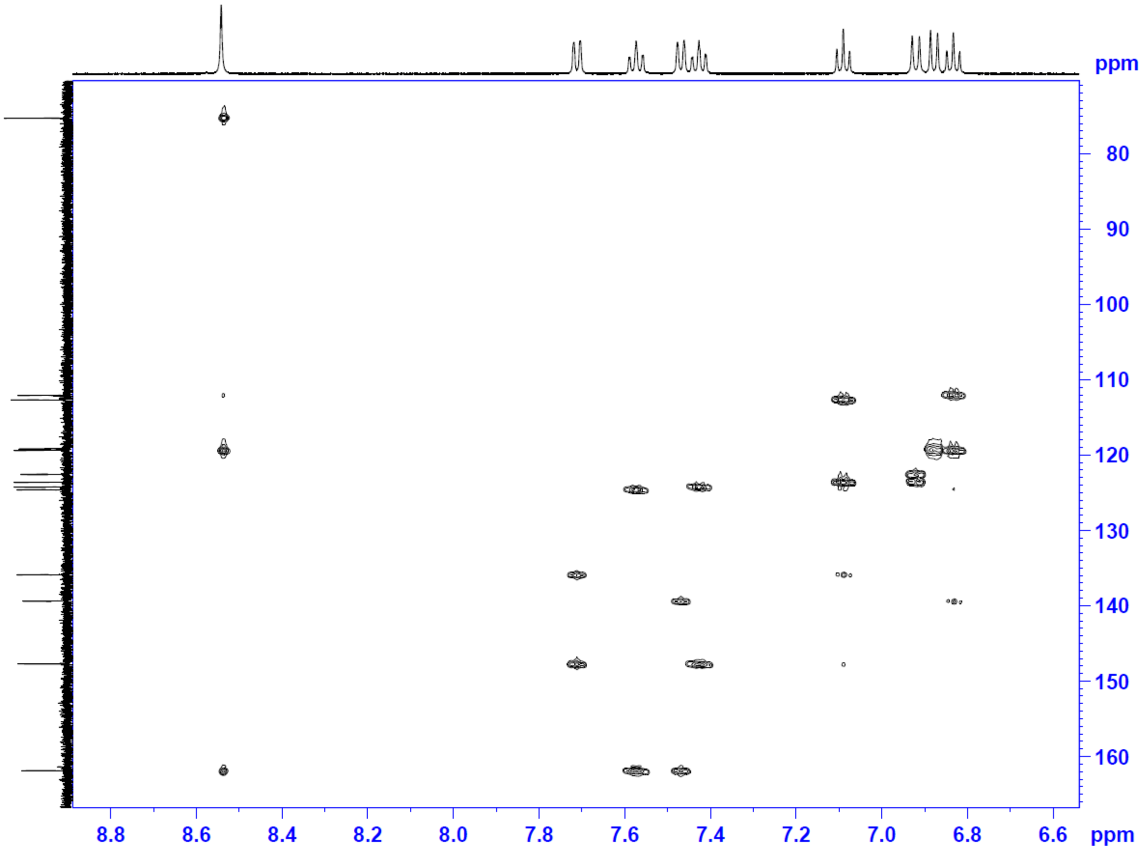

Appendix B-26 2D ^{1}H-^{13}C HMBC spectrum of **3.3·acetone** in DMSO-d_6.

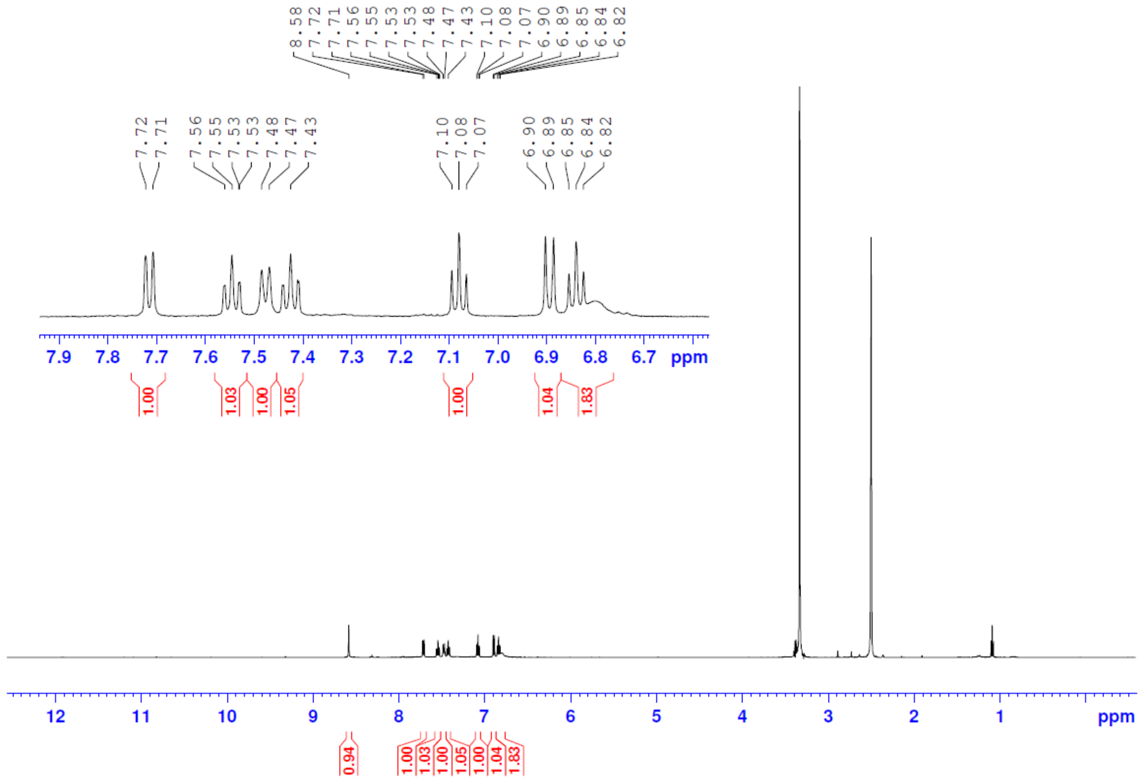

Appendix B-27 ^{1}H NMR spectrum of **3.4** in DMSO-d_6 at 500 MHz.

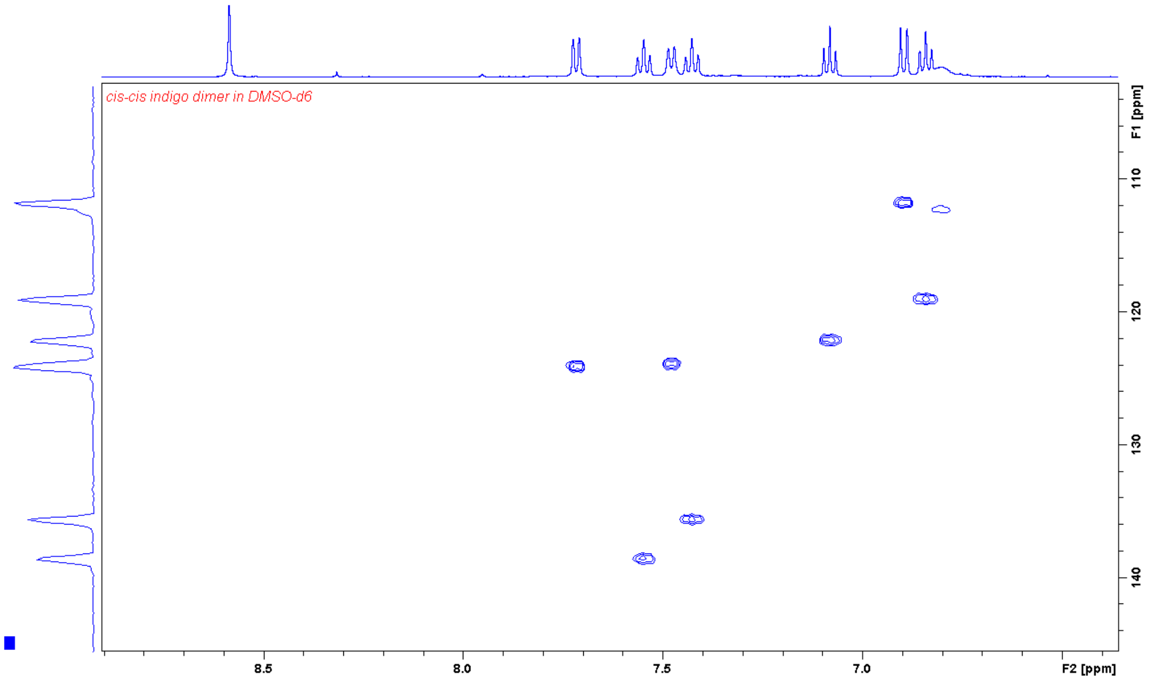

Appendix B-28 2D ^{1}H-^{13}C HSQC spectrum of **3.4** in DMSO-d$_6$.

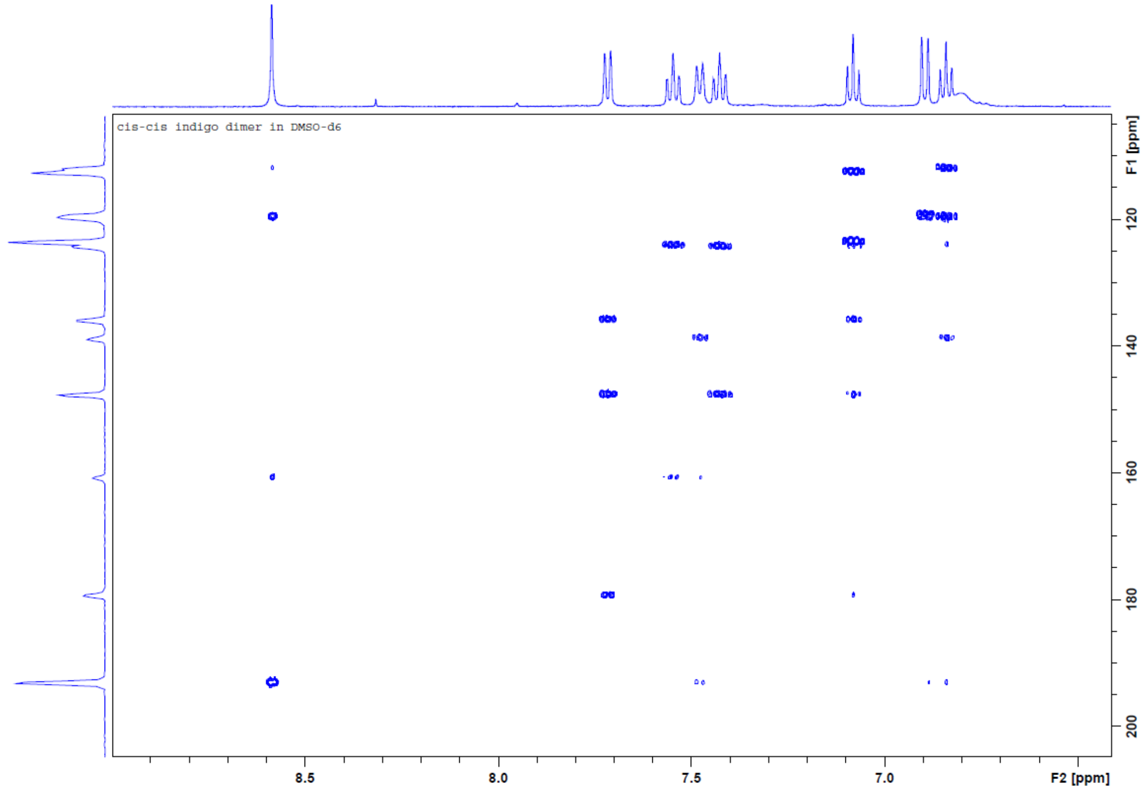

Appendix B-29 2D ^{1}H-^{13}C HMBC spectrum of **3.4** in DMSO-d$_6$.

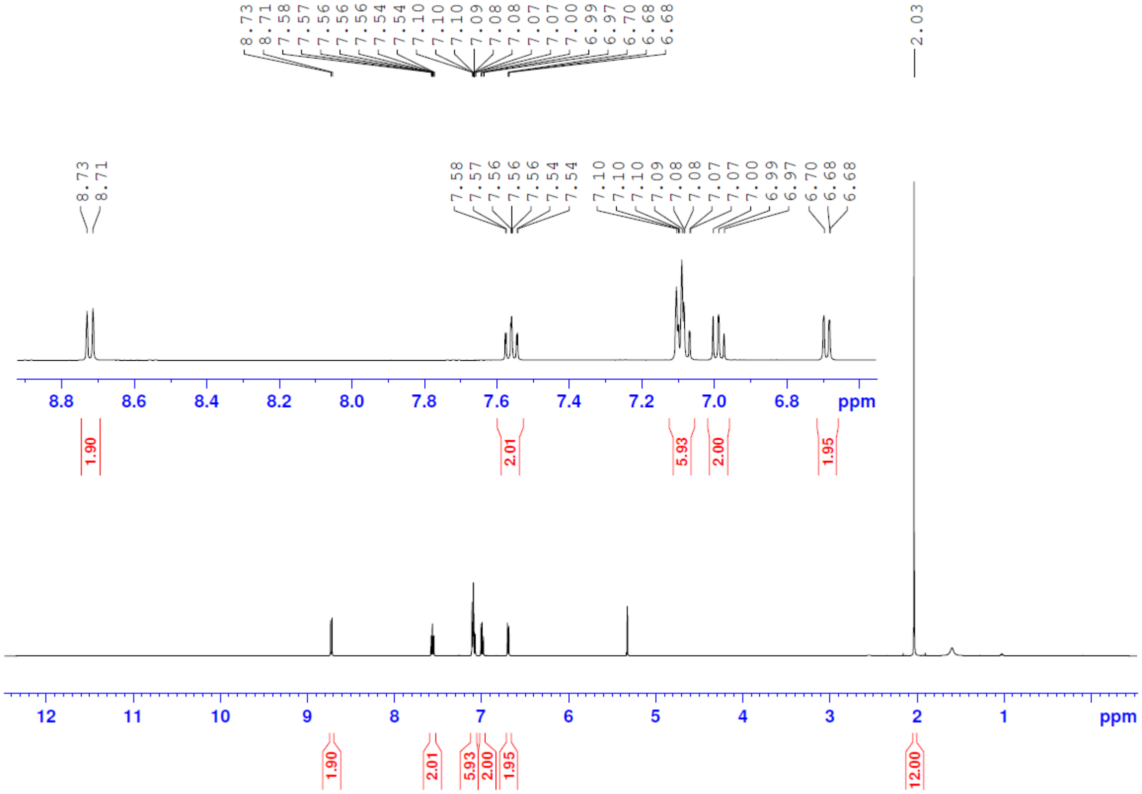

Appendix B-30 ^{1}H NMR spectrum of **4.6a** in CD_2Cl_2 at 500 MHz.

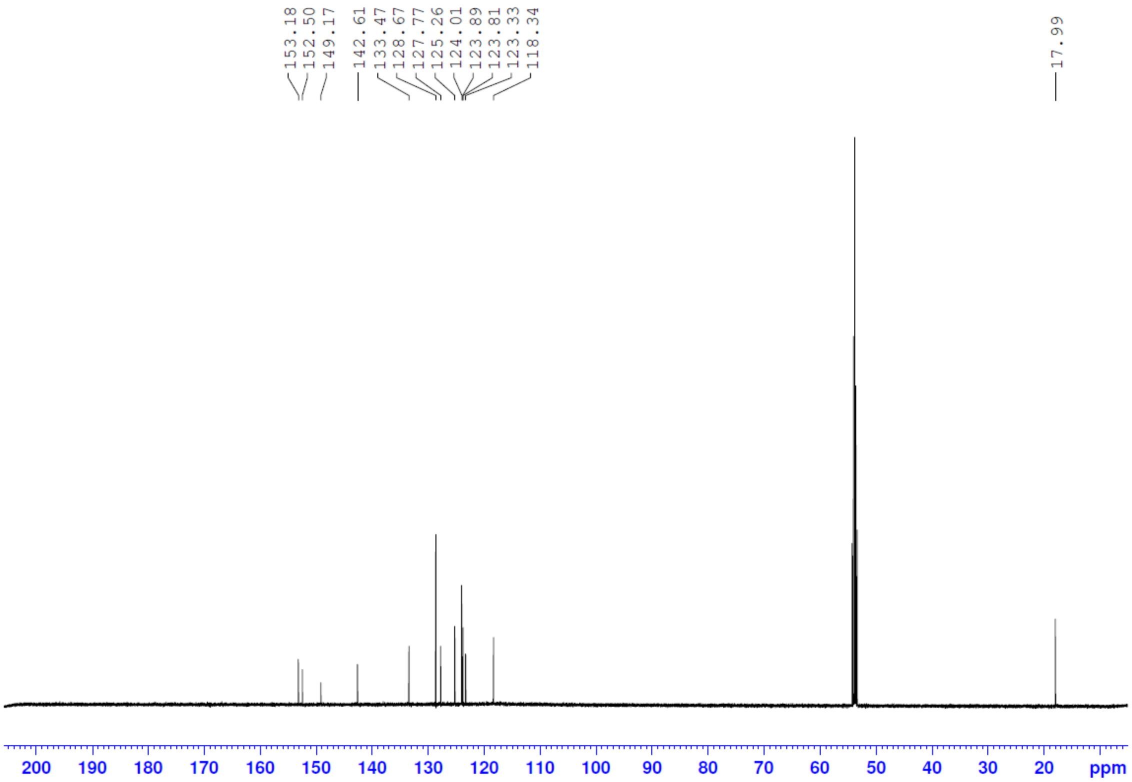

Appendix B-31 ^{13}C NMR spectrum of **4.6a** in CD_2Cl_2 at 126 MHz.

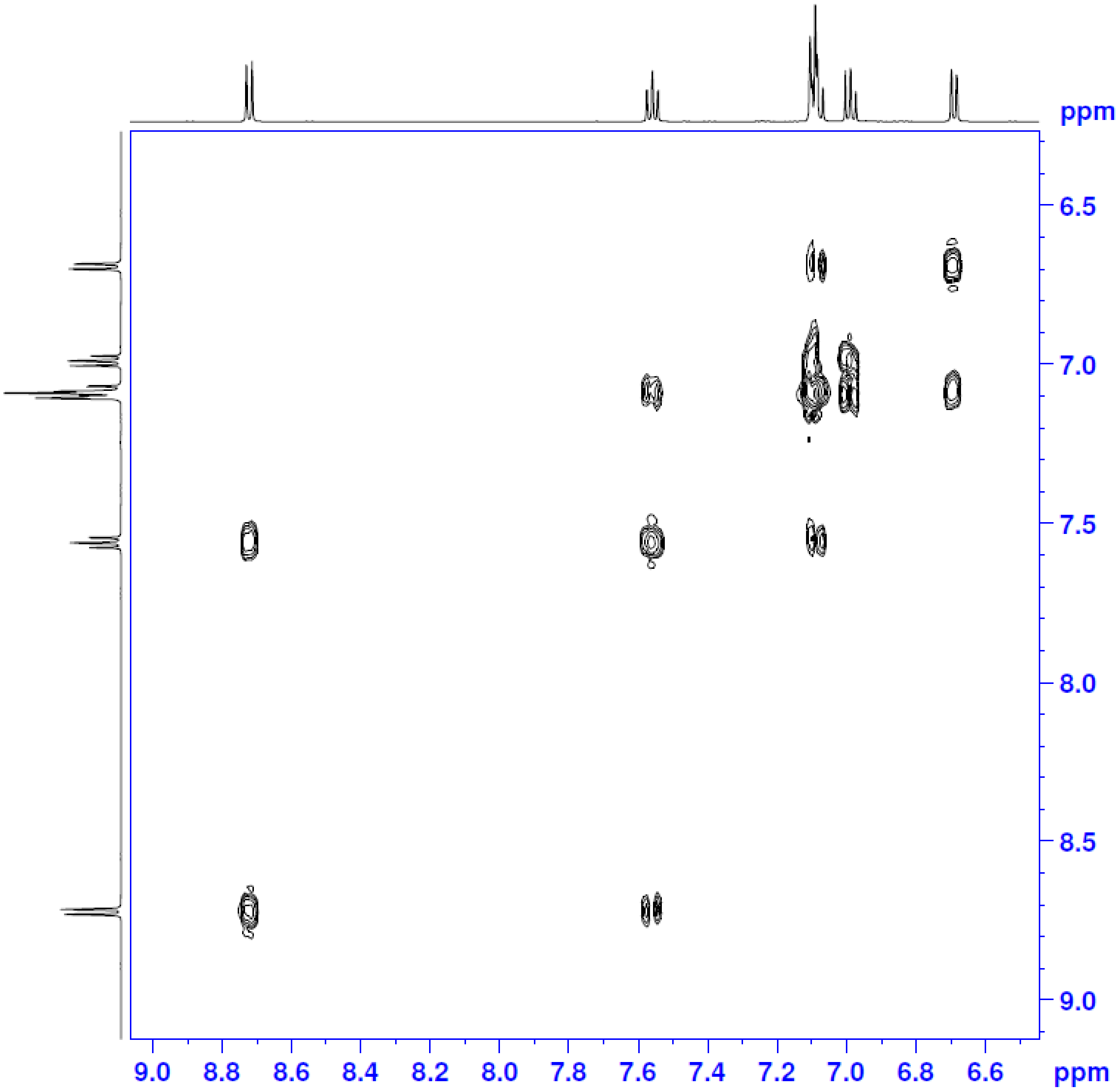

Appendix B-32 2D ^{1}H-^{1}H COSY spectrum of **4.6a** in CD_2Cl_2 at 500 MHz.

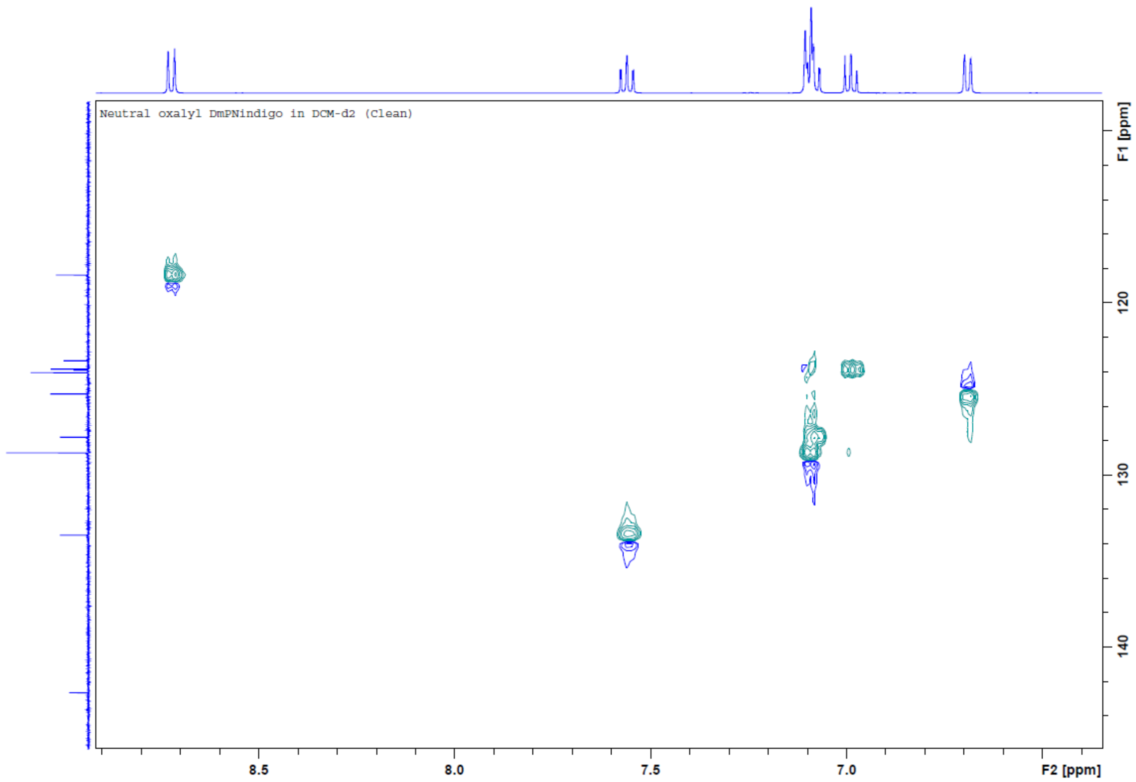

Appendix B-33 2D ^{1}H-^{13}C HSQC spectrum of **4.6a** in CD_2Cl_2.

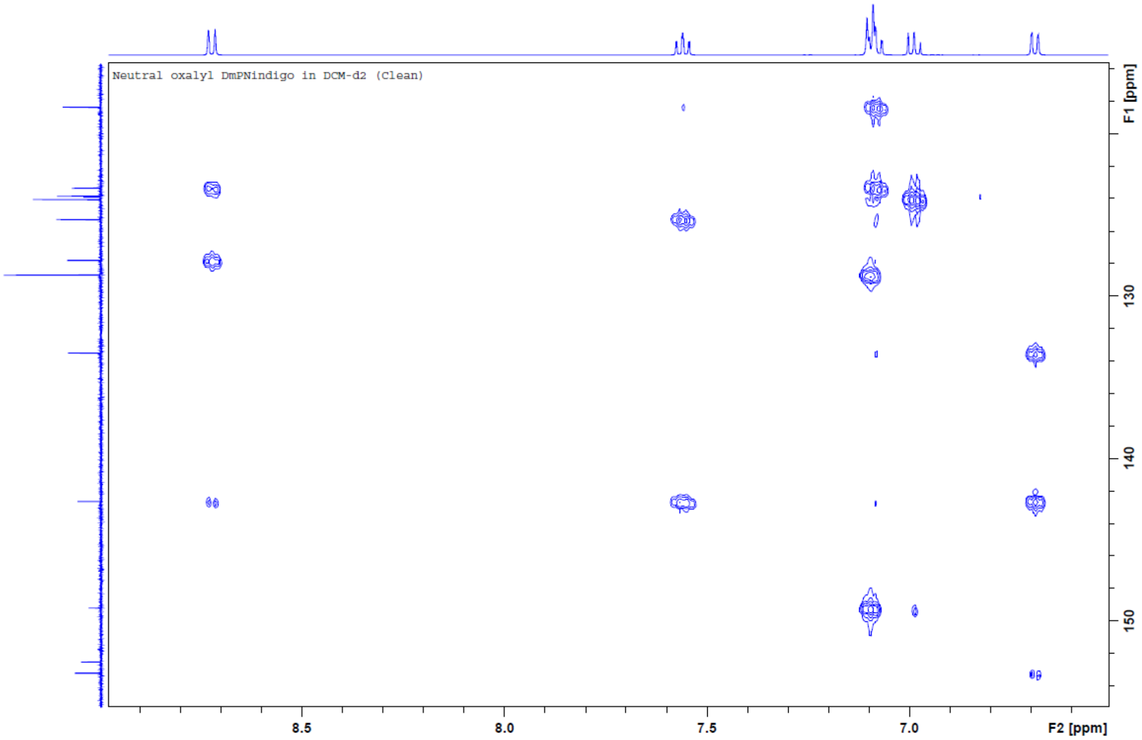

Appendix B-34 2D ^{1}H-^{13}C HMBC spectrum of **4.6a** in CD_2Cl_2.

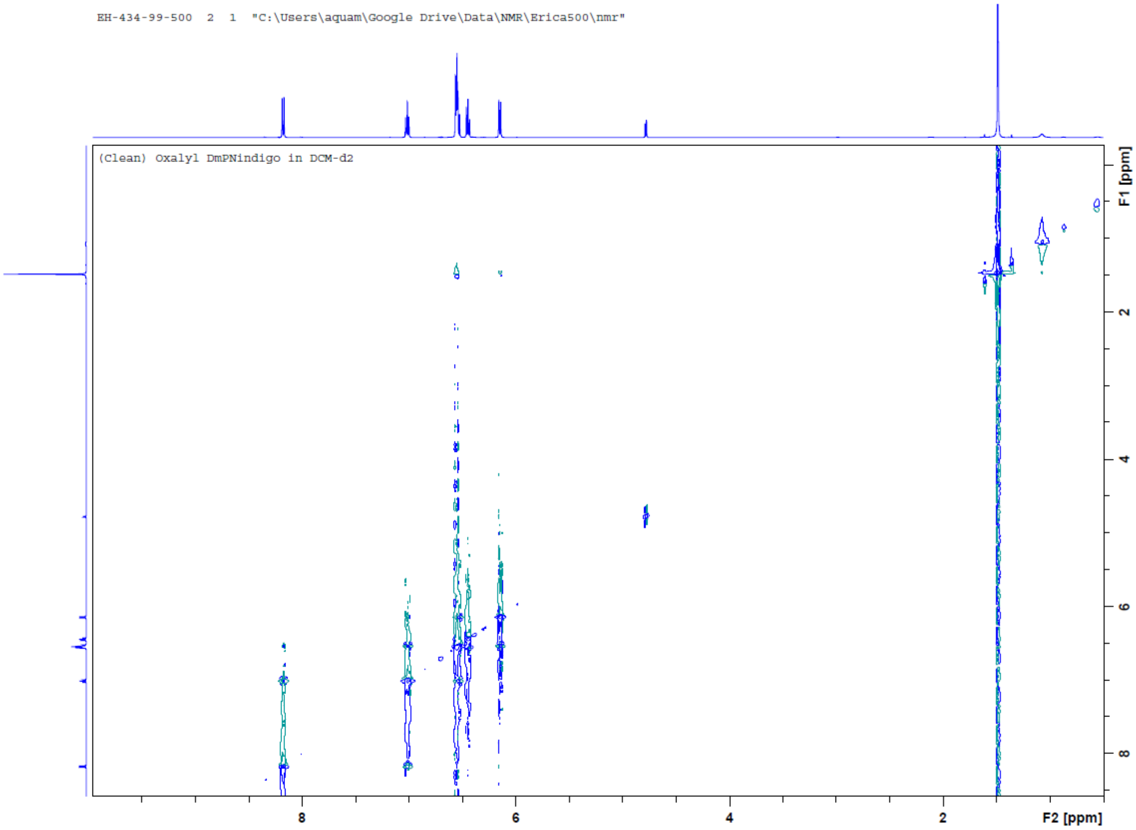

Appendix B-35 2D ^{1}H-^{1}H NOESY spectrum of **4.6a** in CD_2Cl_2 at 500 MHz.

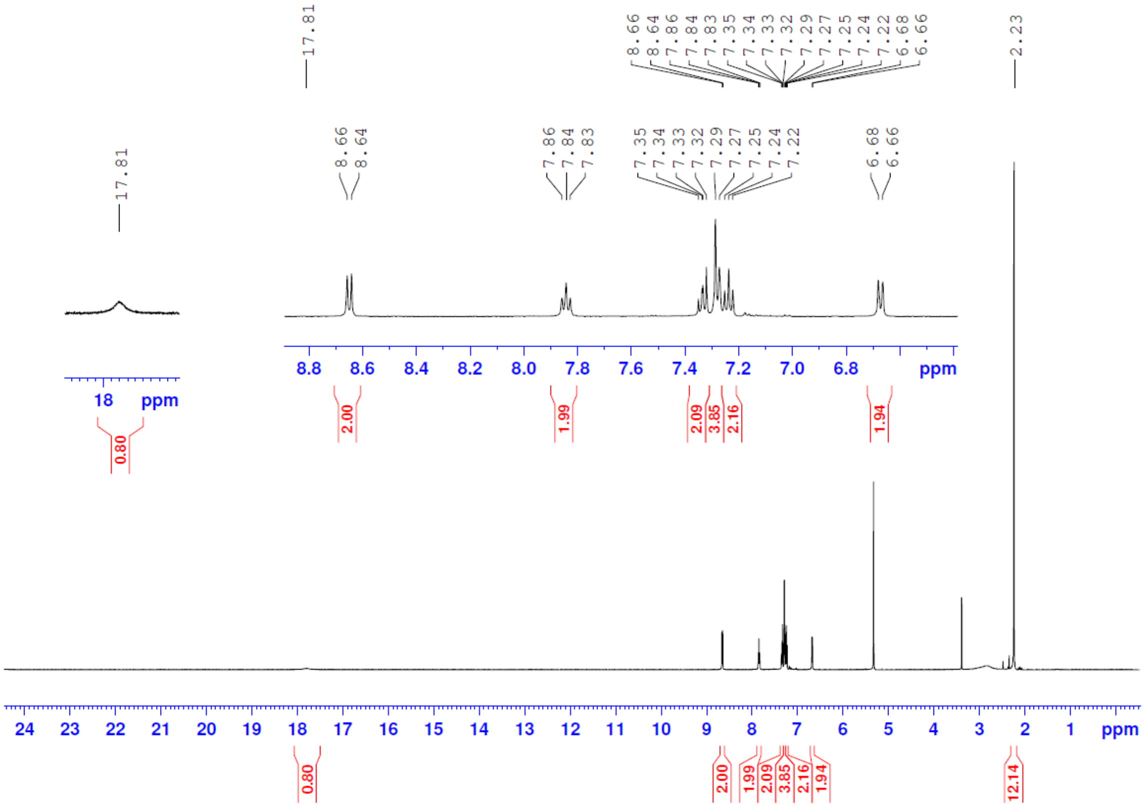

Appendix B-36 ^{1}H NMR spectrum of **4.6aH**$^+$Cl$^-$ in CD_2Cl_2 at 500 MHz.

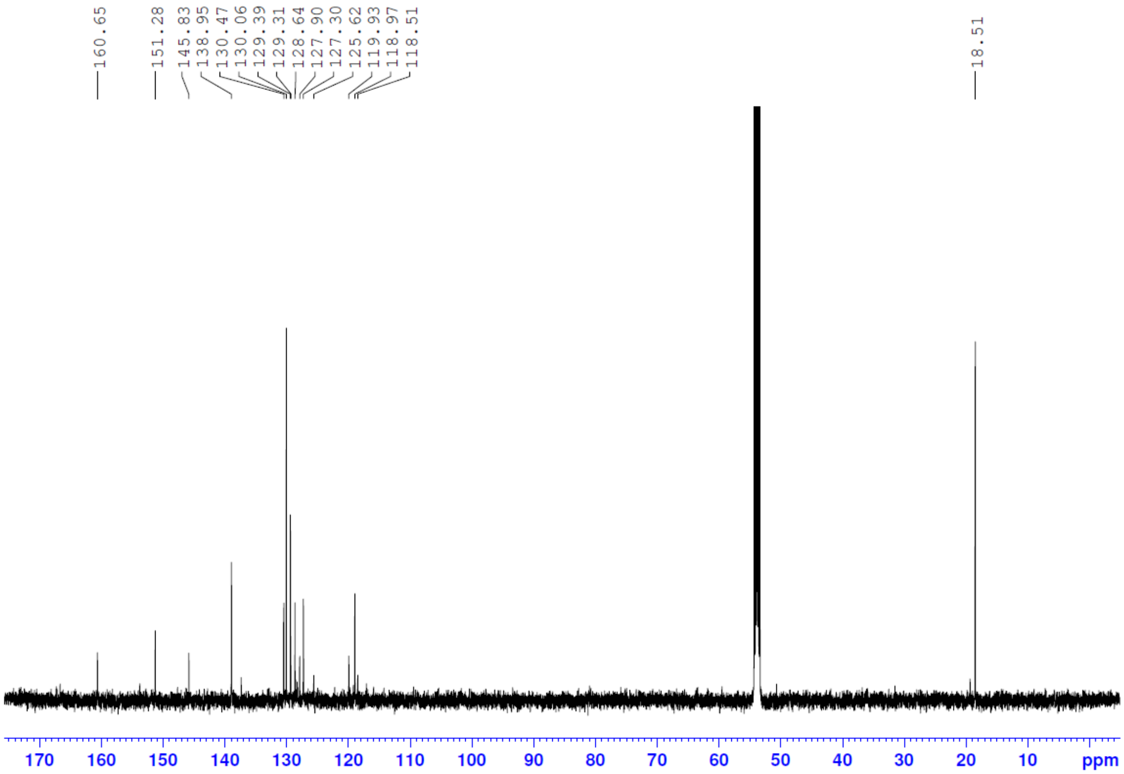

Appendix B-37 ^{13}C NMR spectrum of **4.6aH$^+$**Cl$^-$ in CD_2Cl_2 at 126 MHz.

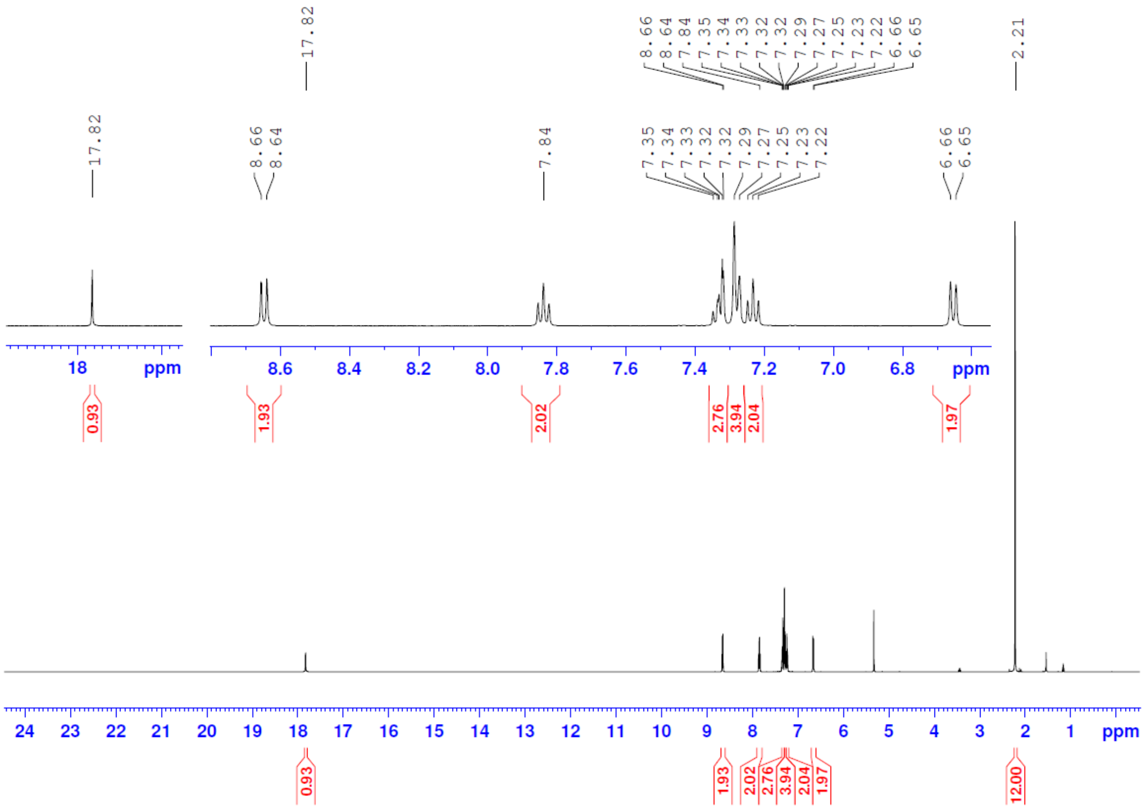

Appendix B-38 ^{1}H NMR spectrum of **4.6aH**$^+$BF$_4^-$ in CD$_2$Cl$_2$ at 500 MH.

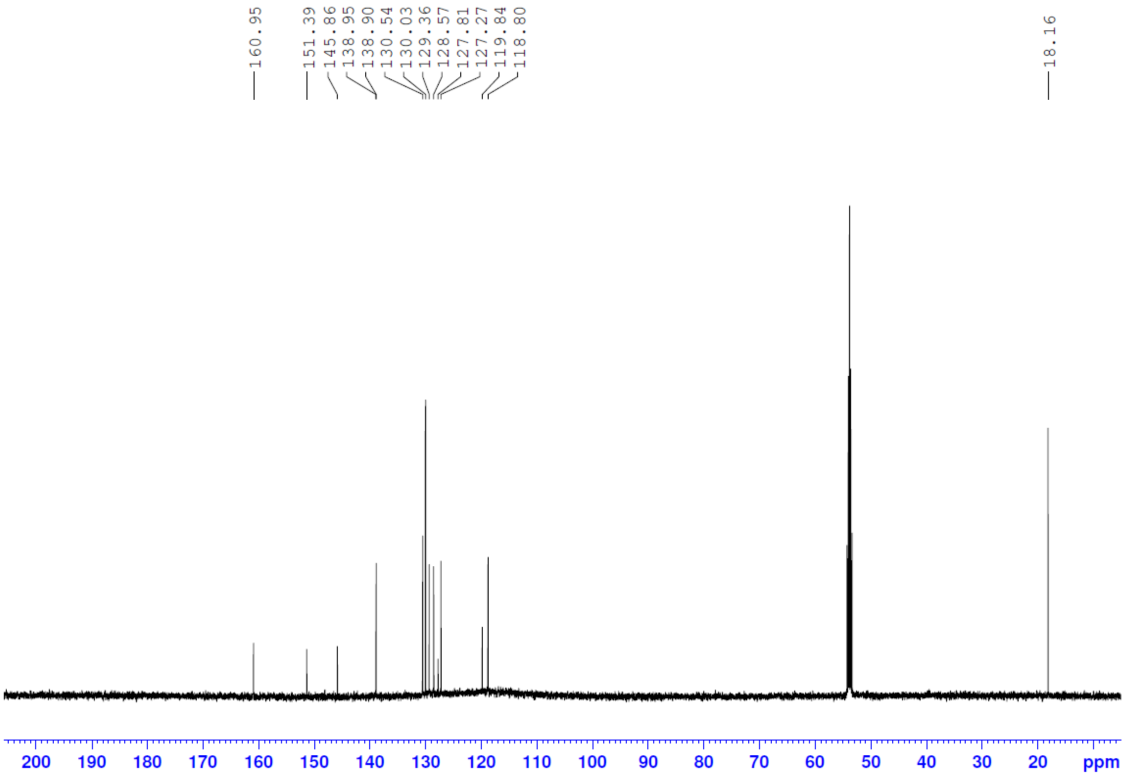

Appendix B-39 ^{13}C NMR spectrum of **4.6aH**$^{+}$BF$_4^-$ in CD$_2$Cl$_2$ at 126 MHz.

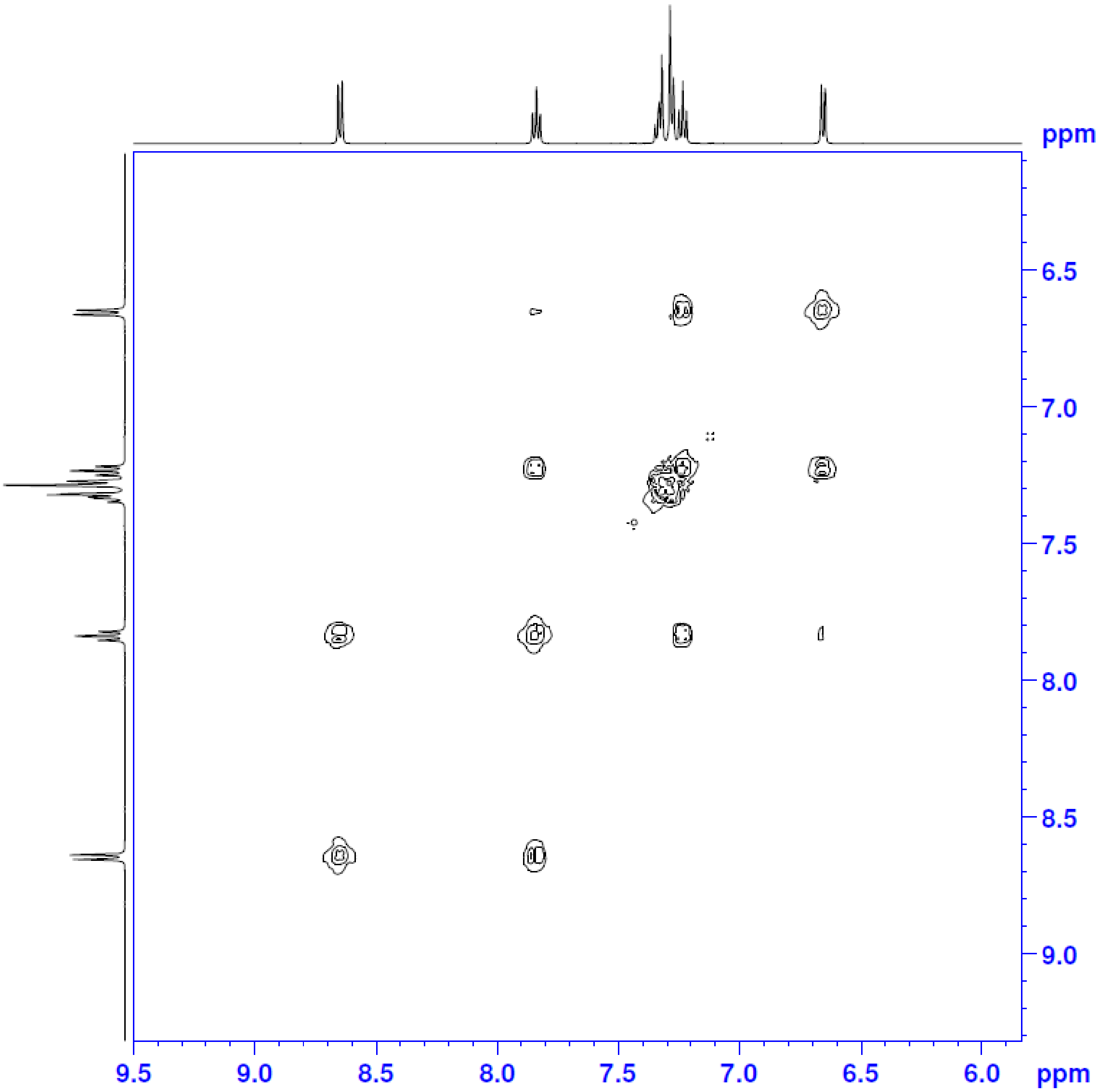

Appendix B-40 2D ^1H-^1H COSY spectrum of **4.6aH**$^+$BF$_4^-$ in CD_2Cl_2 at 500 MHz.

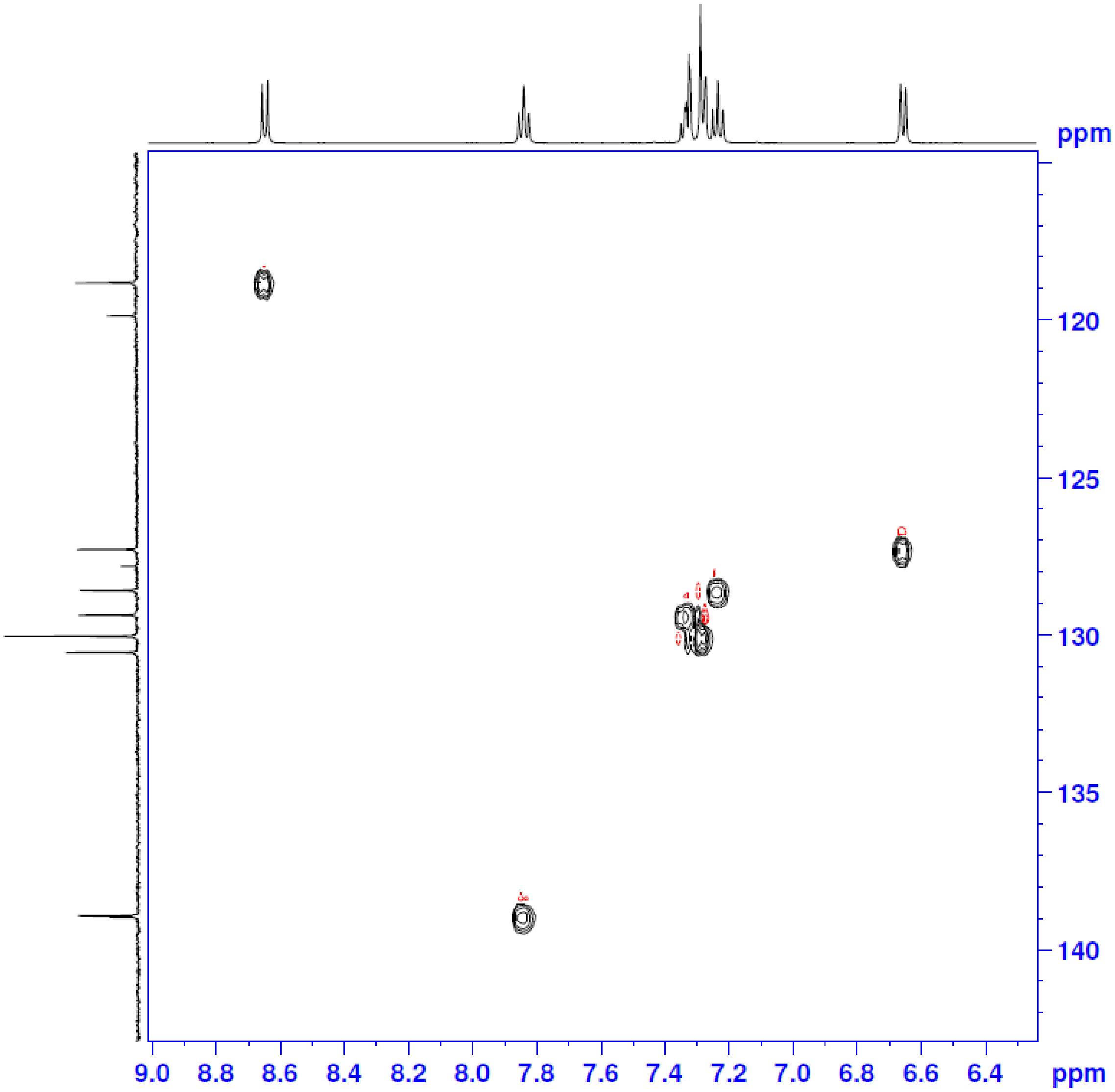

Appendix B-41 2D ^{1}H-^{13}C HSQC spectrum of **4.6aH**$^{+}$BF$_4^-$ in CD$_2$Cl$_2$.

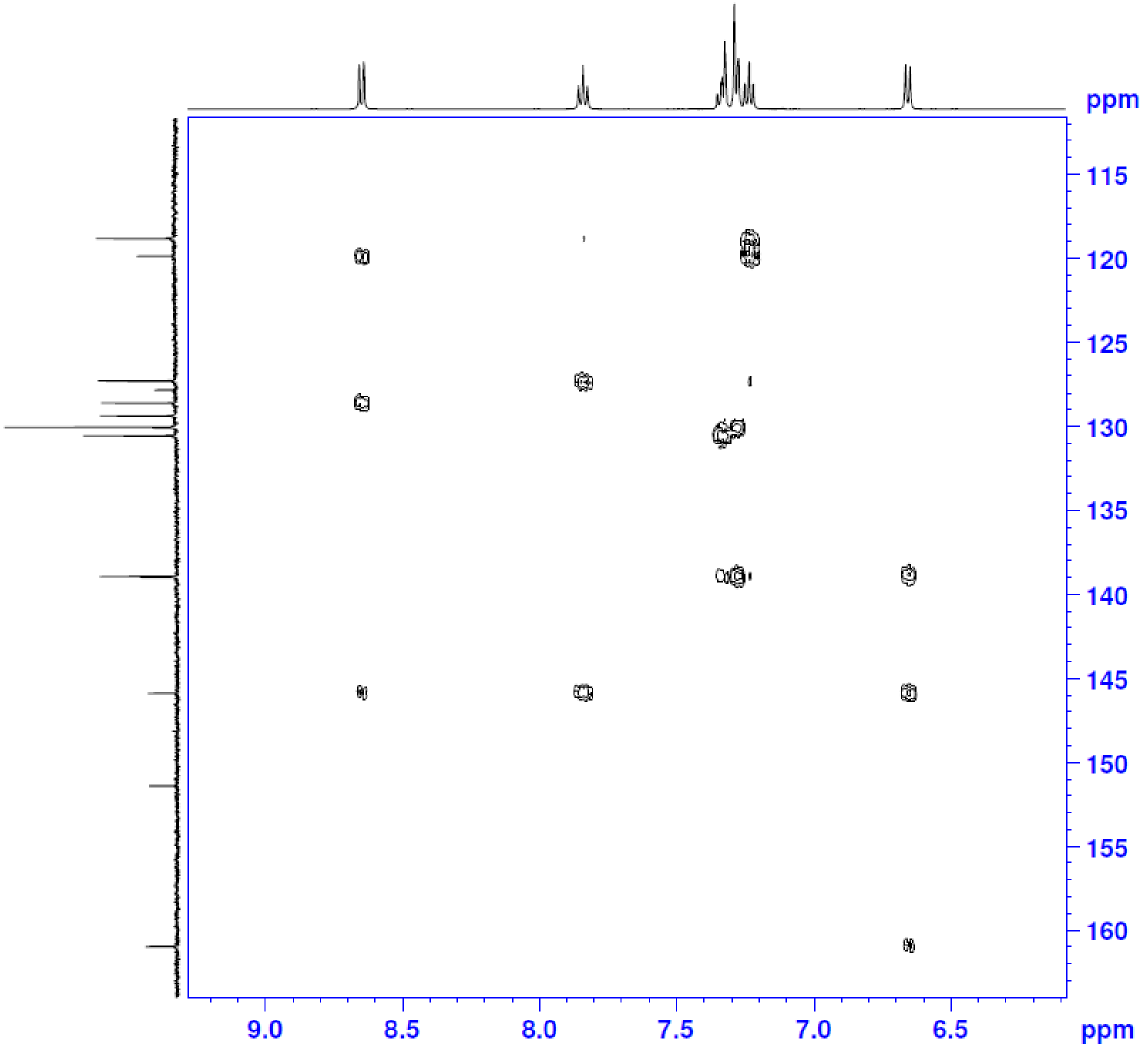

Appendix B-42 2D ^{1}H-^{13}C HMBC spectrum of **4.6aH**$^{+}$$BF_4^{-}$ in CD_2Cl_2.

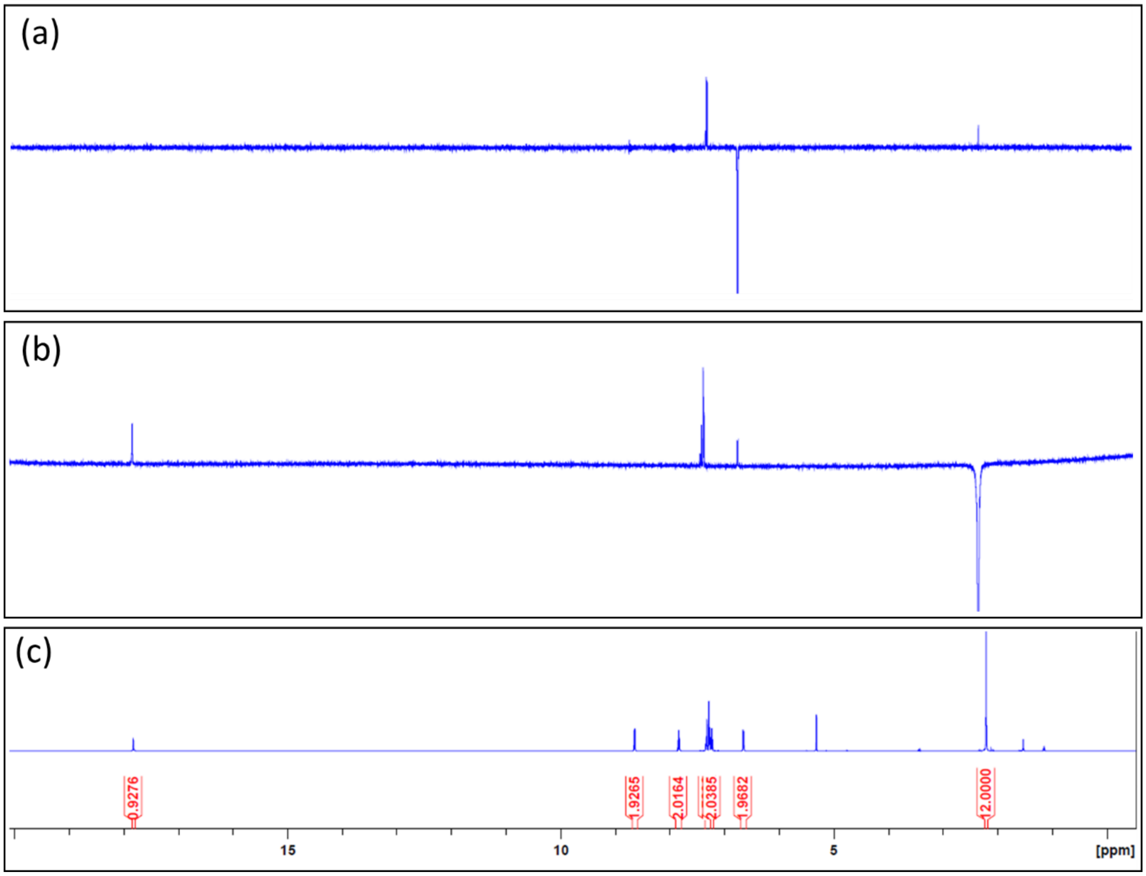

Appendix B-43 Selective Gradient NOESY spectrum of **4.6aH**$^+$BF$_4^-$ in CD$_2$Cl$_2$. (a) after irradiation at frequency of 6.65 ppm. (b) after irradiation at frequency of 2.21 ppm. (c) a reference ^{1}H NMR spectrum. A doublet at 6.65 ppm (H4 proton) shows a NOE correlation with the methyl group at 2.21 ppm. Multiplet between 7.26 – 7.36 ppm are hydrogen signals on the DmP group.

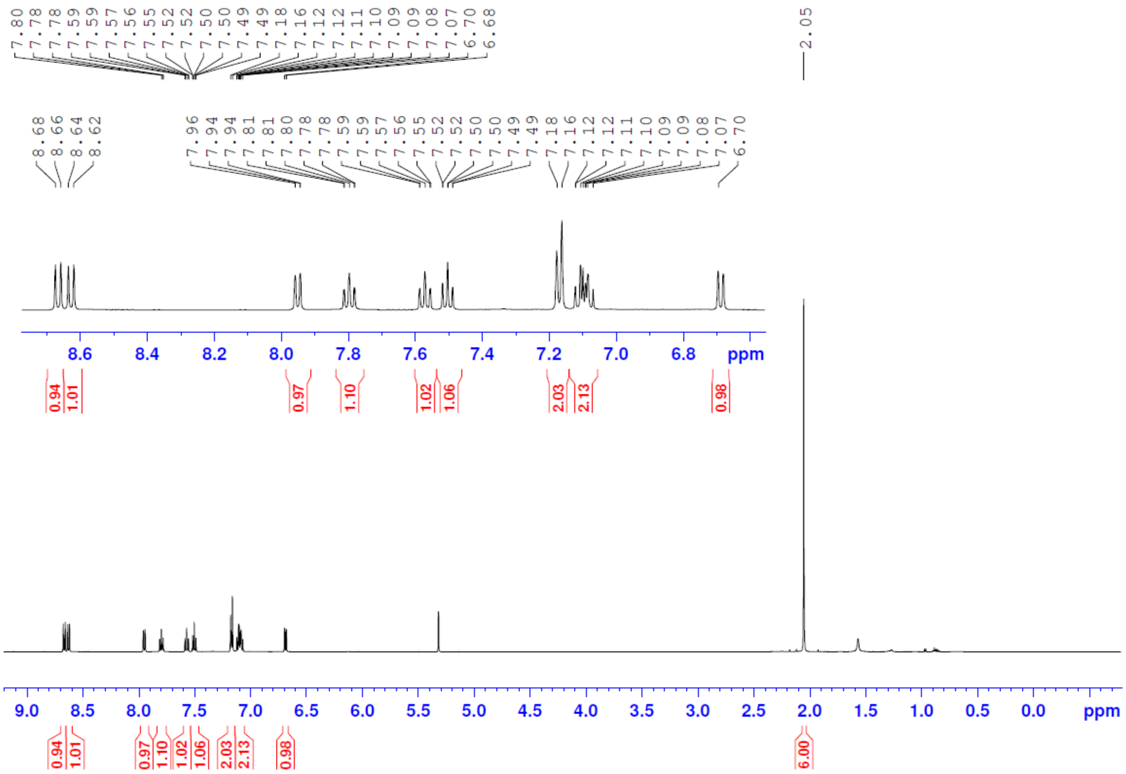

Appendix B-44 ^{1}H NMR spectrum of **4.7a** in CD_2Cl_2 at 500 MHz.

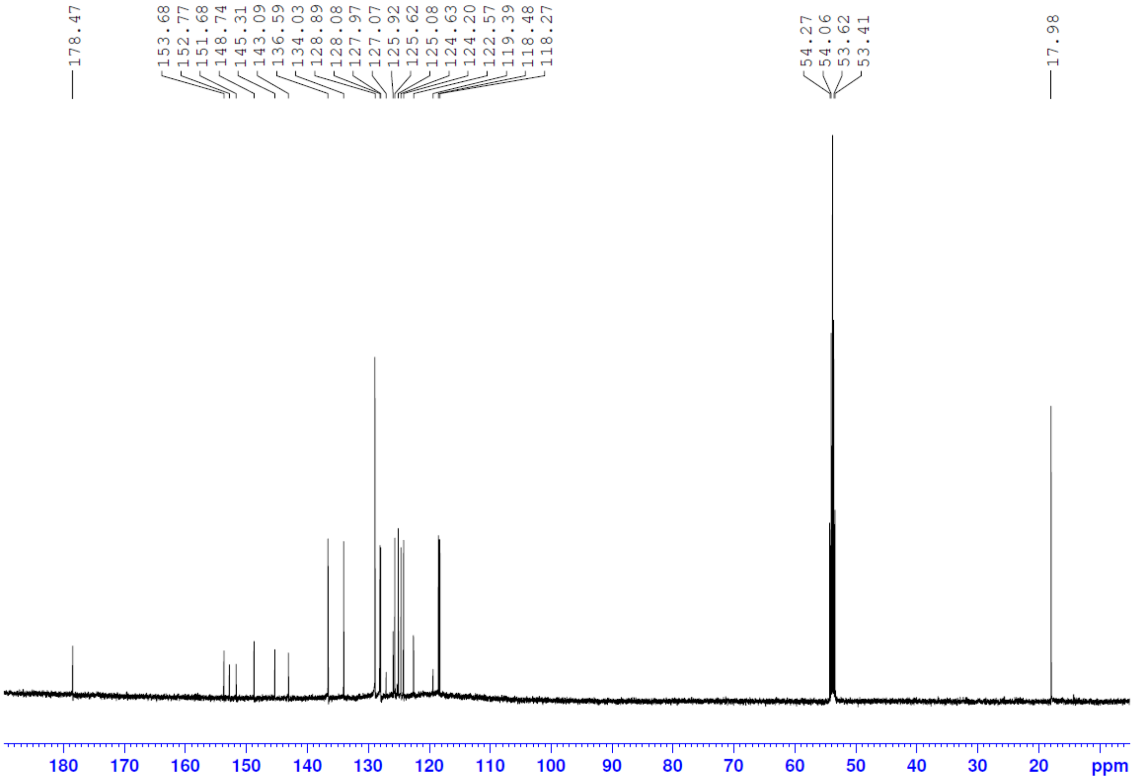

Appendix B-45 ^{13}C NMR spectrum of **4.7a** in CD_2Cl_2 at 126 MHz.

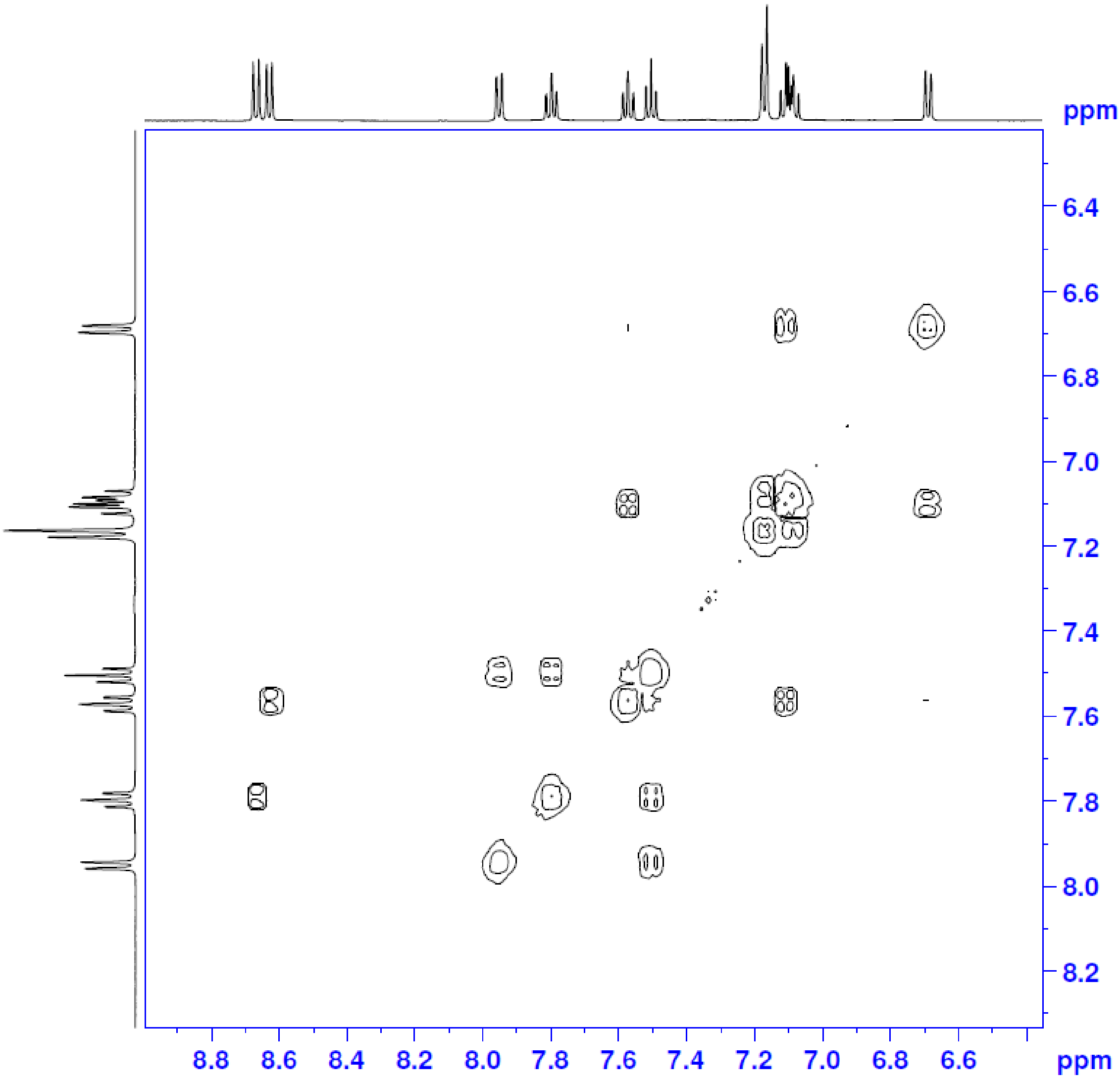

Appendix B-46 2D ^{1}H-^{1}H COSY spectrum of **4.7a** in CD_2Cl_2 at 500 MHz.

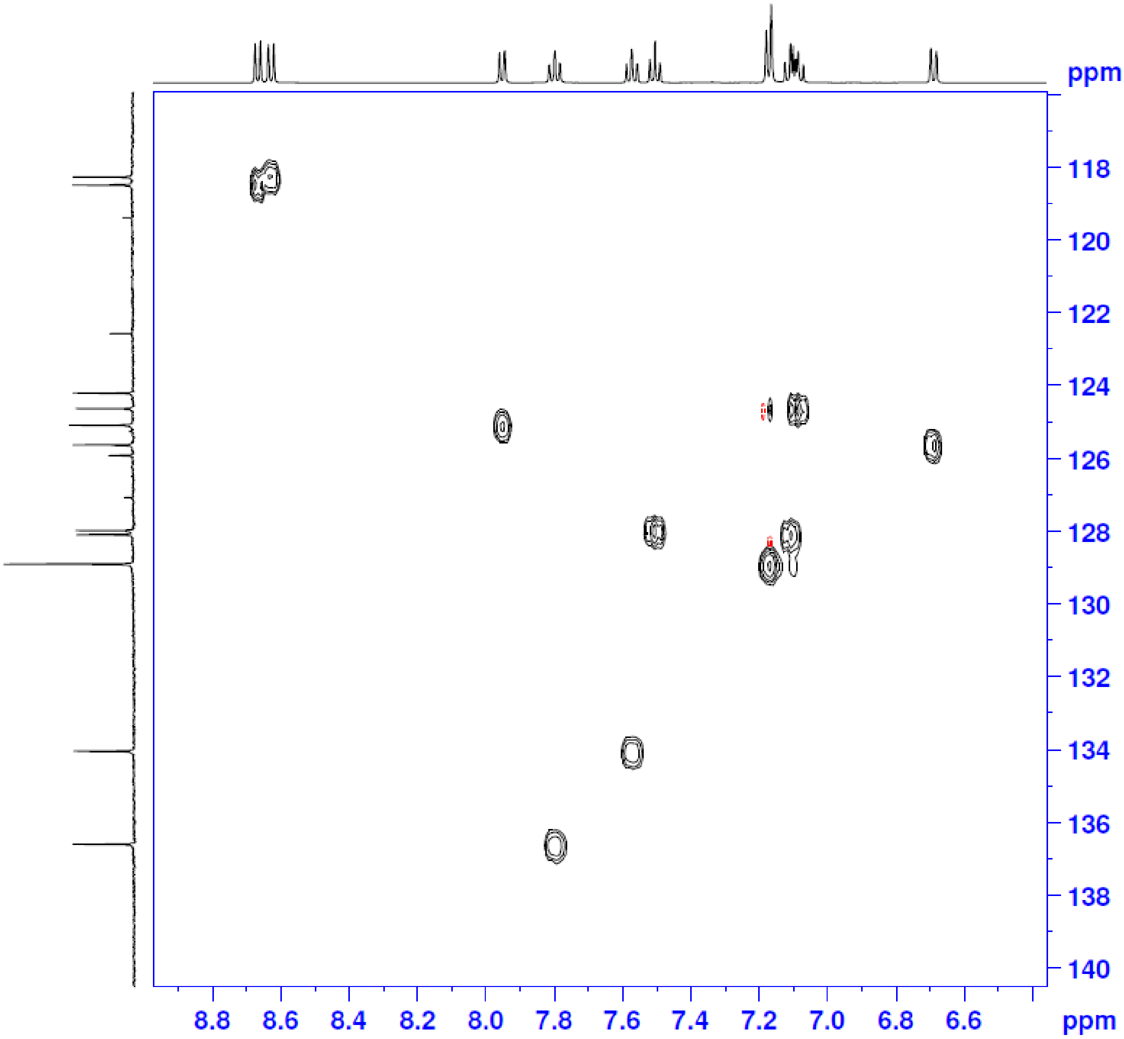

Appendix B-47 2D ^{1}H-^{13}C HSQC spectrum of **4.7a** in CD_2Cl_2.

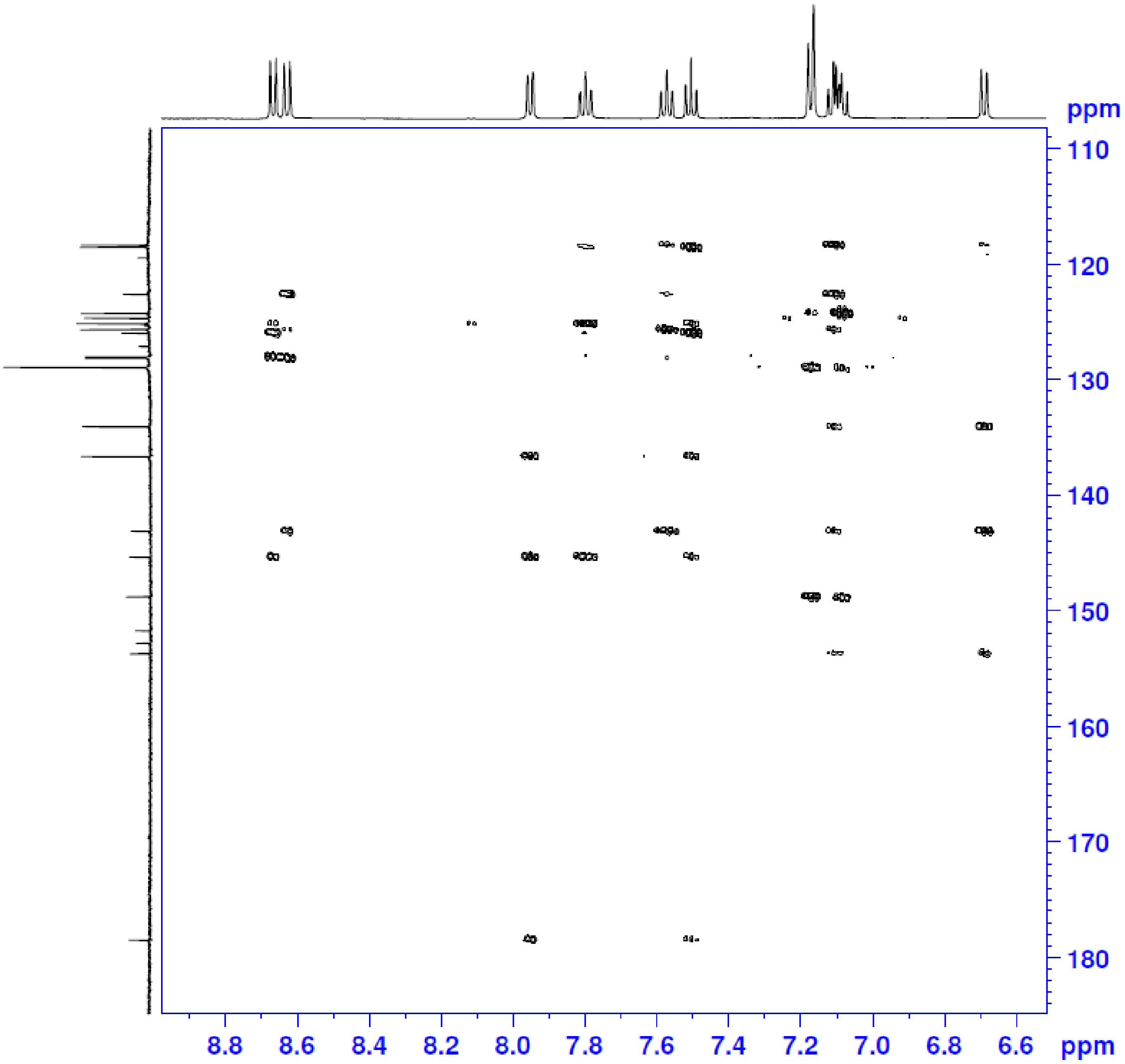

Appendix B-48 2D ^{1}H-^{13}C HMBC spectrum of **4.7a** in CD_2Cl_2.

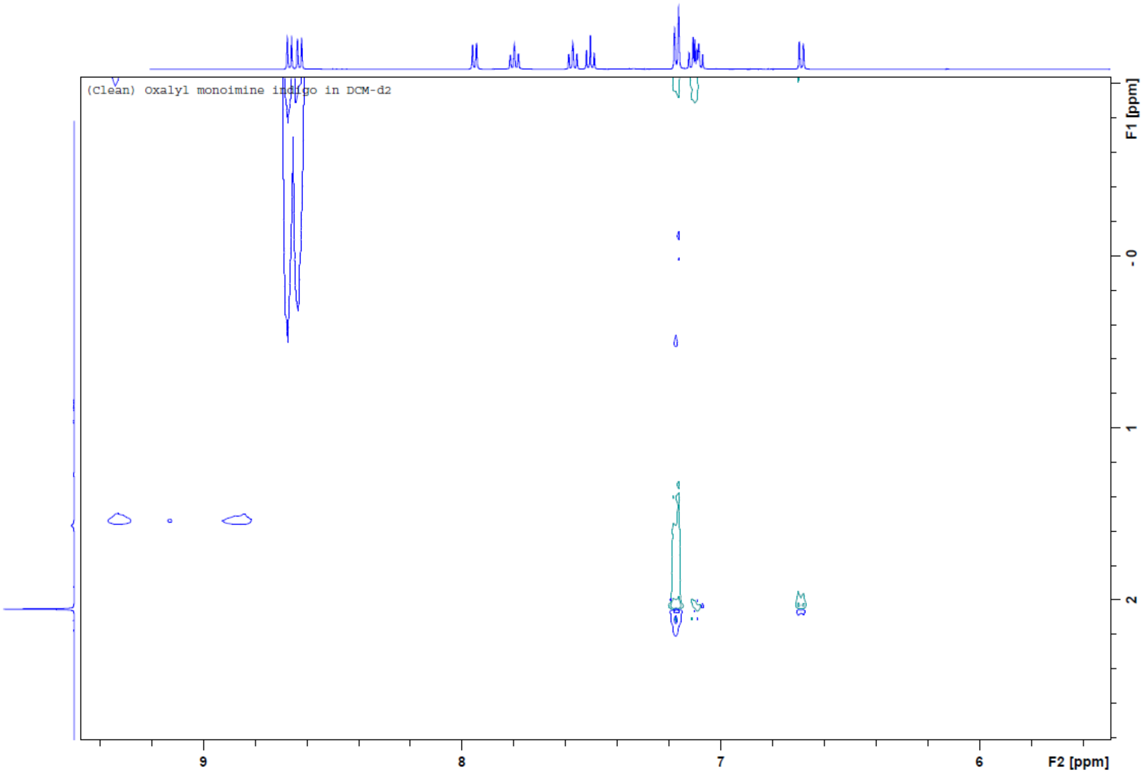

Appendix B-49 2D ^{1}H-^{1}H NOESY spectrum of **4.7a** in CD_2Cl_2 at 500 MHz.

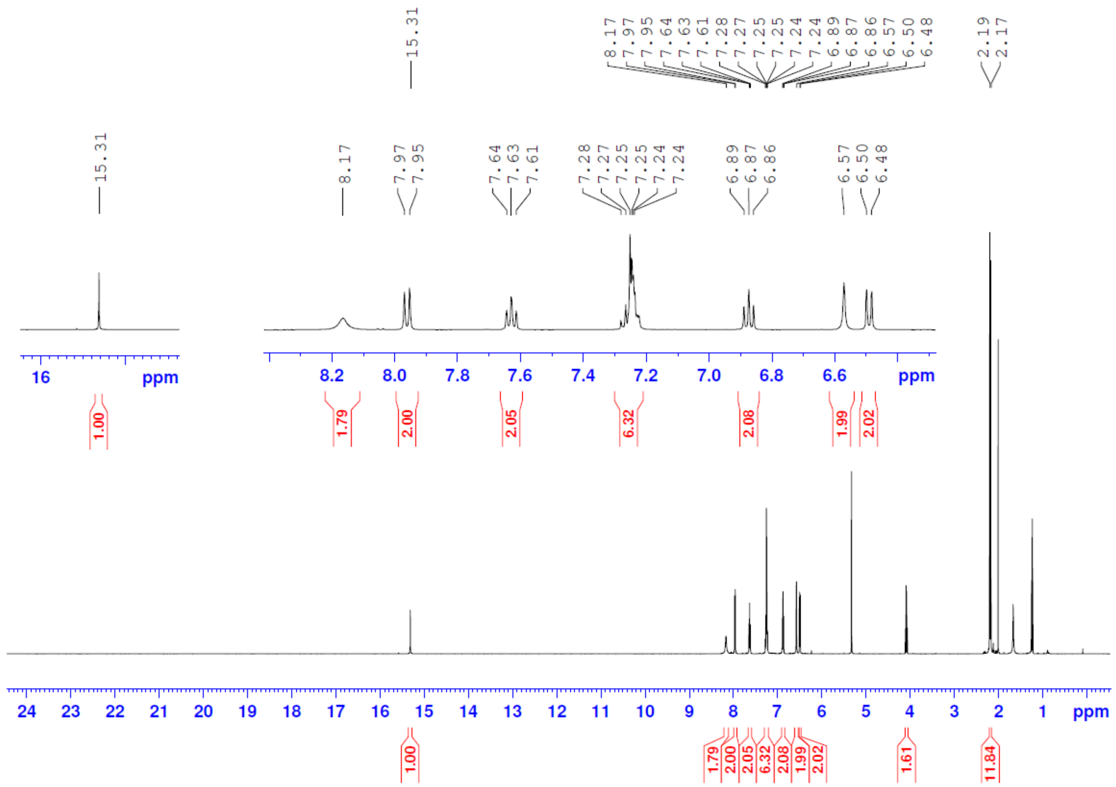

Appendix B-50 ^{1}H NMR spectrum of **4.9aH**$^{+}$Cl^{-} in CD_2Cl_2 at 500 MHz. The ethyl acetate peak at 4.08 ppm has been integrated in order to calculate the effective molecular weight for the compound. In this incident, this batch contains 1 : 0.58 ratio between the product and ethyl acetate.

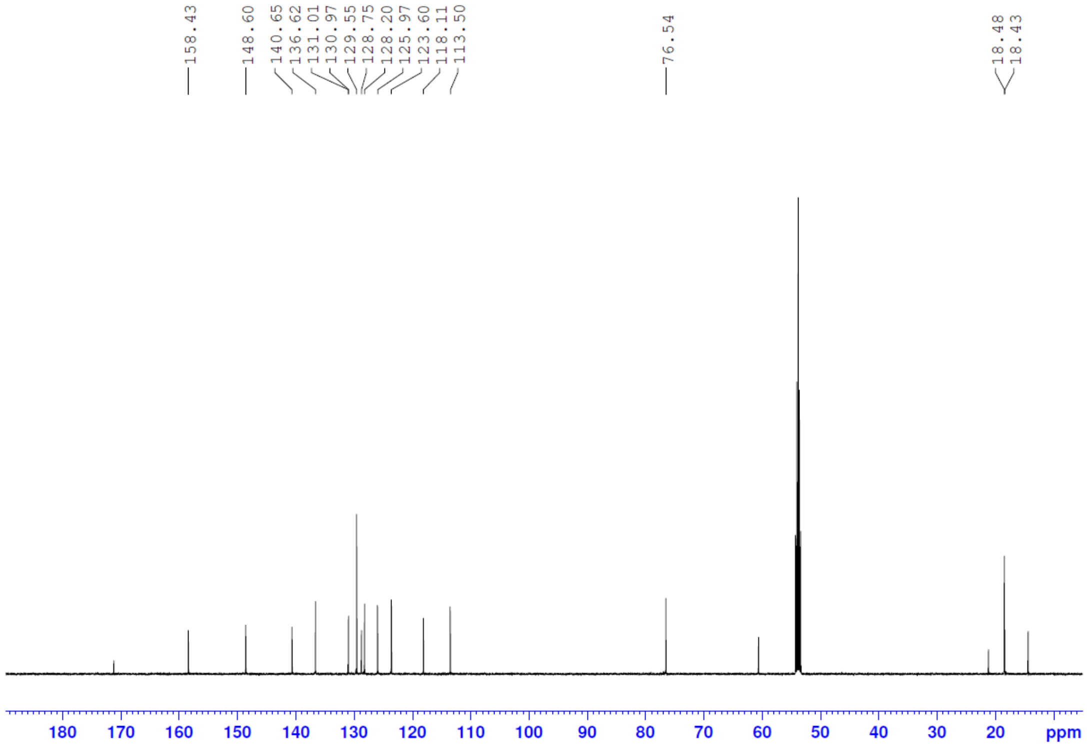

Appendix B-51 ^{13}C NMR spectrum of **4.9aH**$^{+}$Cl^{-} in CD_2Cl_2 at 126 MHz.

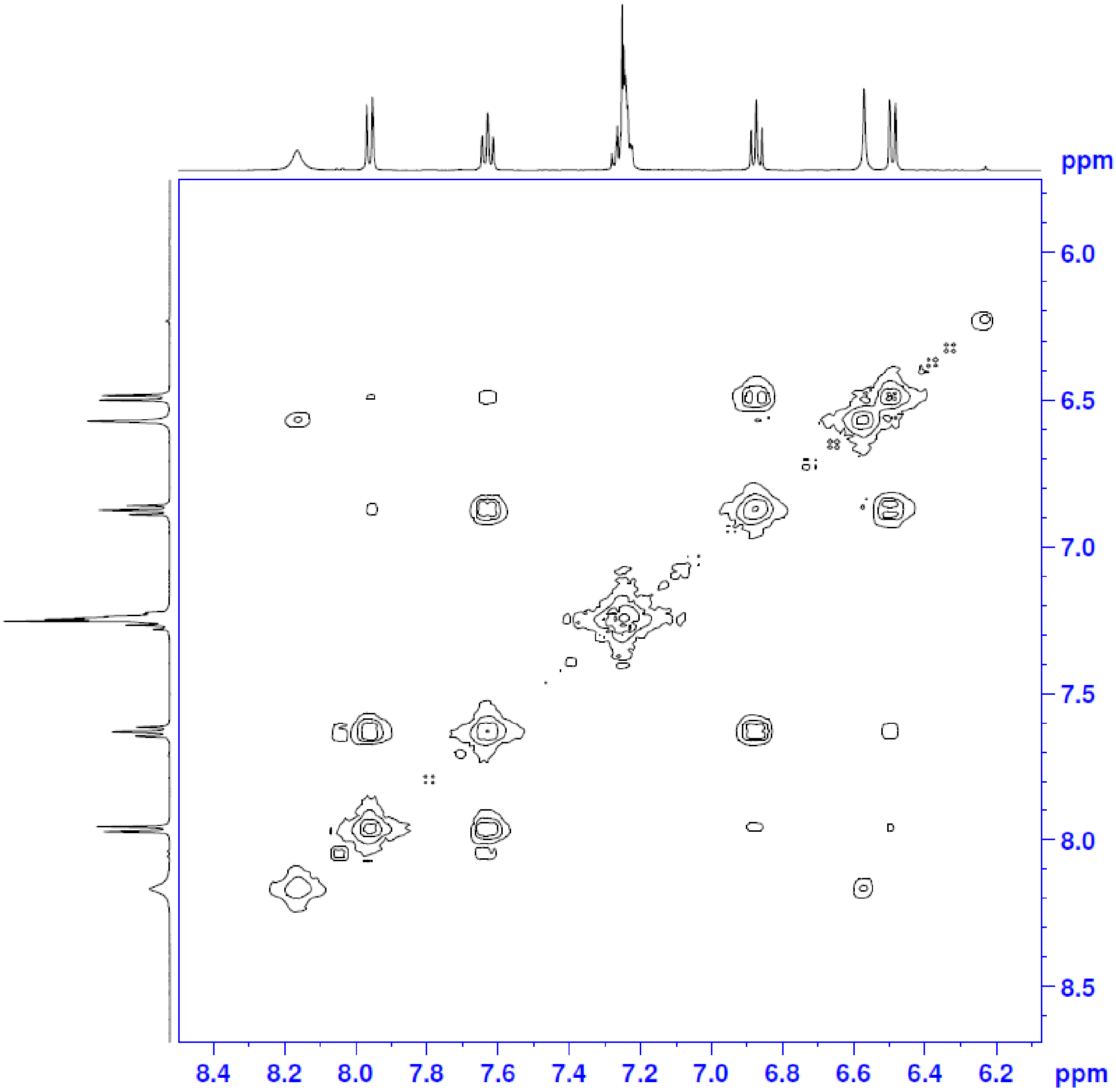

Appendix B-52 2D ^{1}H-^{1}H COSY spectrum of **4.9aH$^+$**Cl$^-$ in CD$_2$Cl$_2$ at 500 MHz.

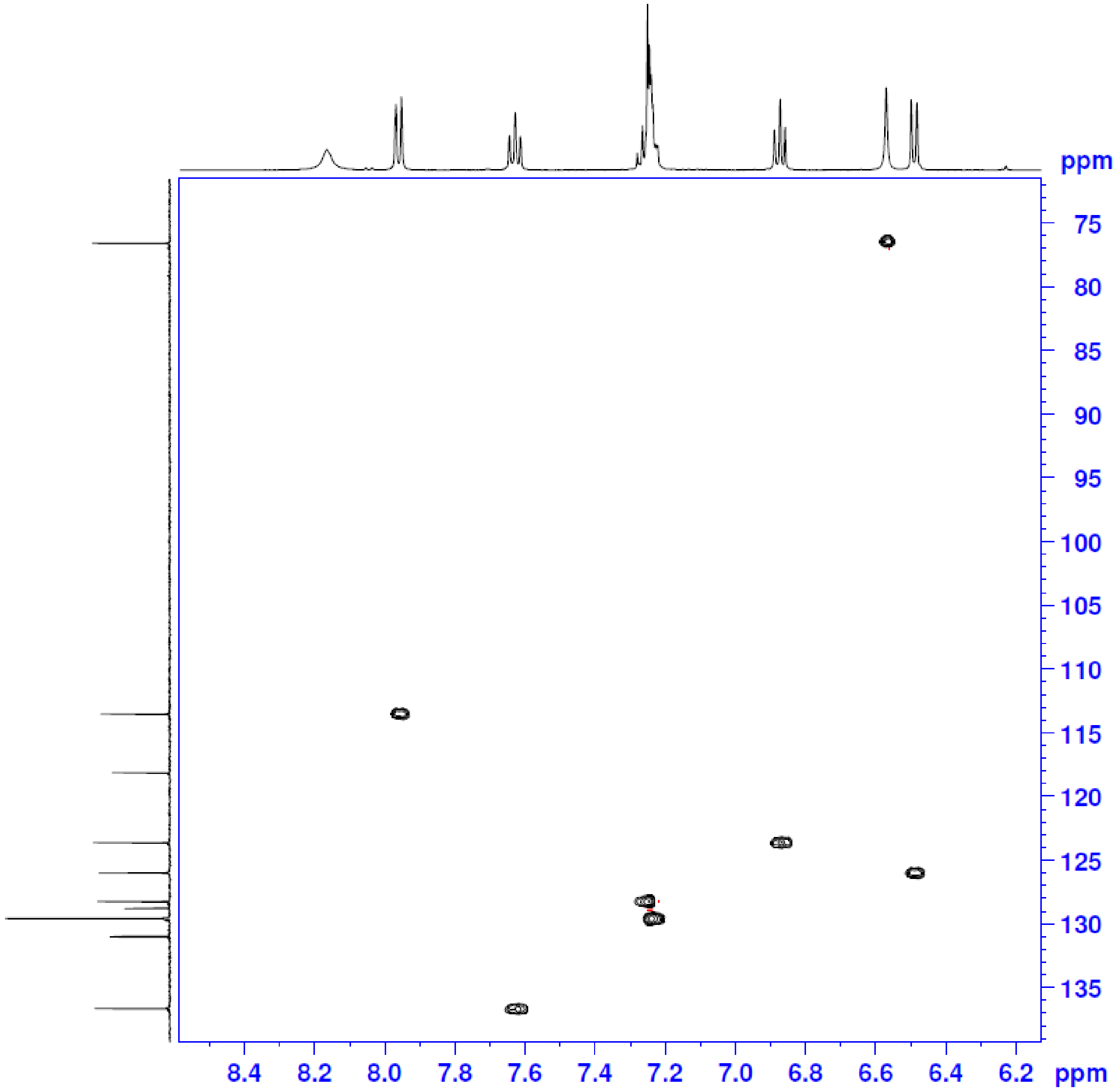

Appendix B-53 2D ^{1}H-^{13}C HSQC spectrum of **4.9aH$^+$**Cl$^-$ in CD_2Cl_2.

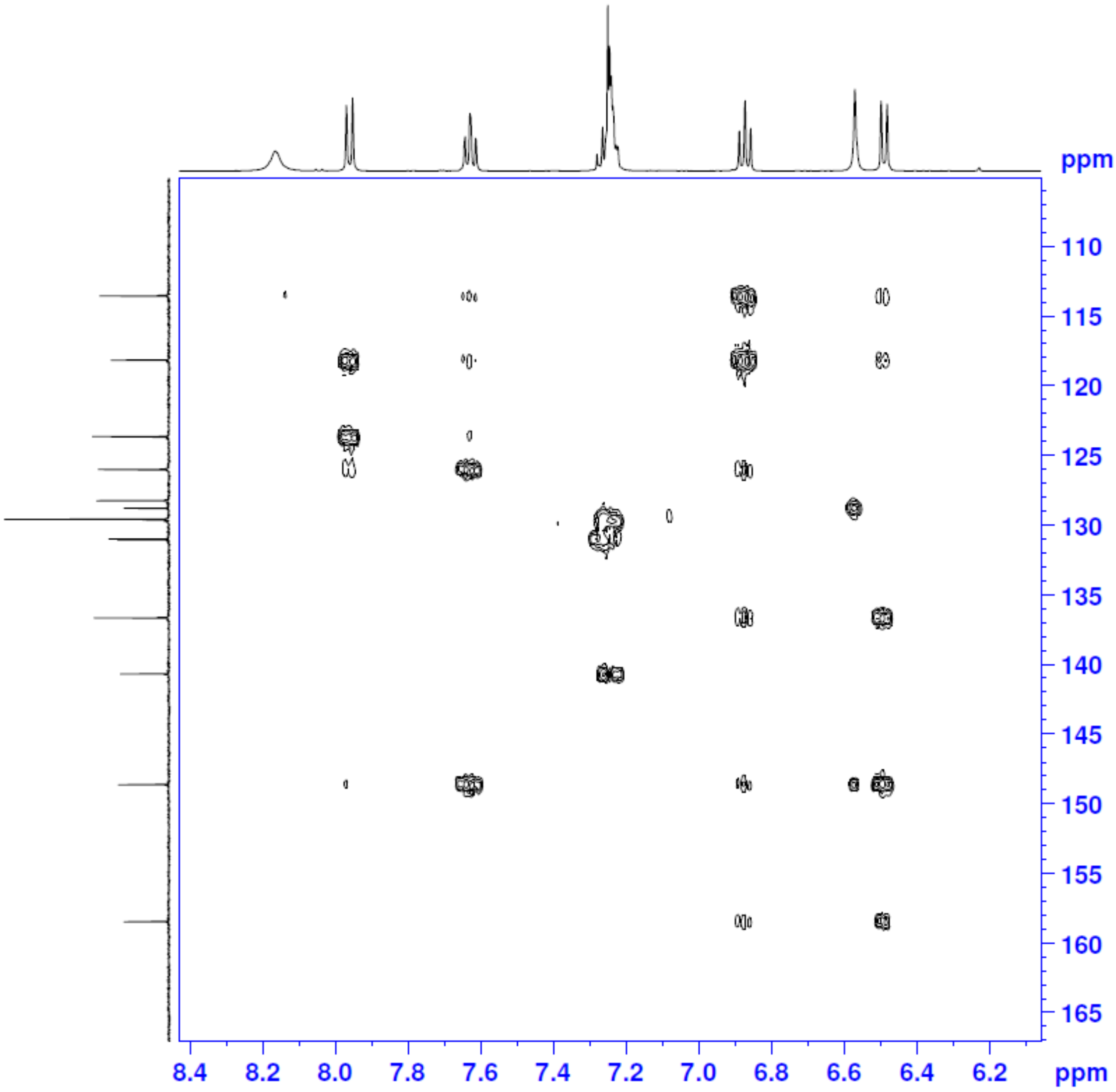

Appendix B-54 2D ^{1}H-^{13}C HMBC spectrum of **4.9aH**$^{+}Cl^{-}$ in CD_2Cl_2.

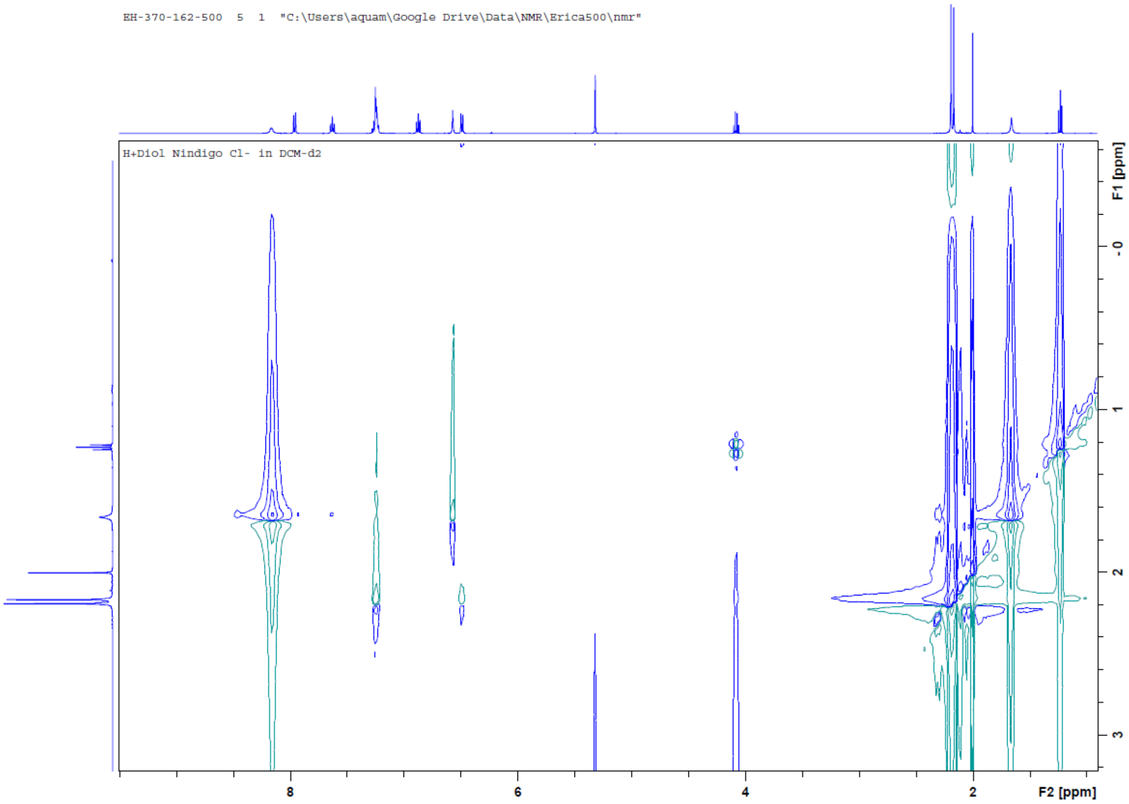

Appendix B-55 2D ^{1}H-^{1}H NOESY spectrum of **4.9aH**$^+$Cl$^-$ in CD_2Cl_2 at 500 MHz.

Appendix C: UV-Vis Spectra

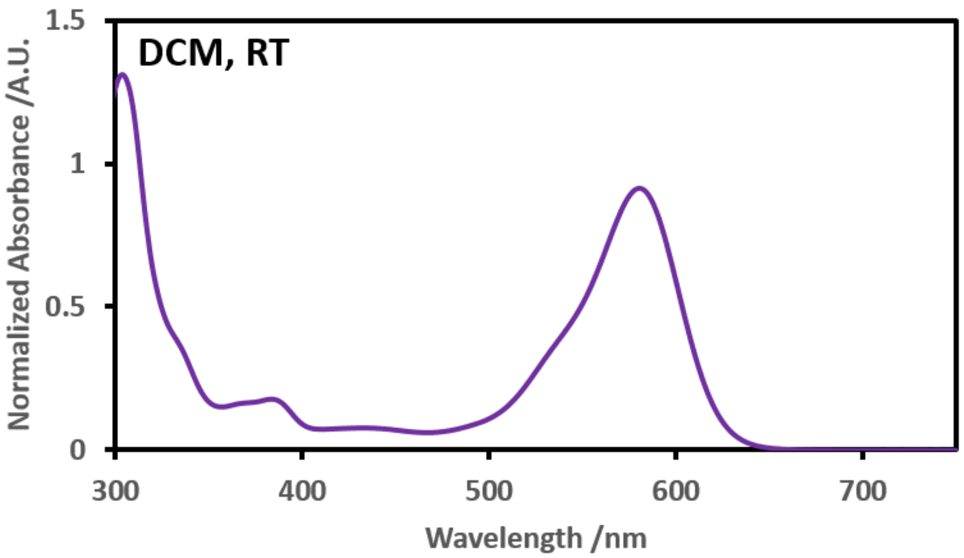

Appendix C-1 UV-Vis spectrum of **2.5** in DCM. (ca. 50 μM)

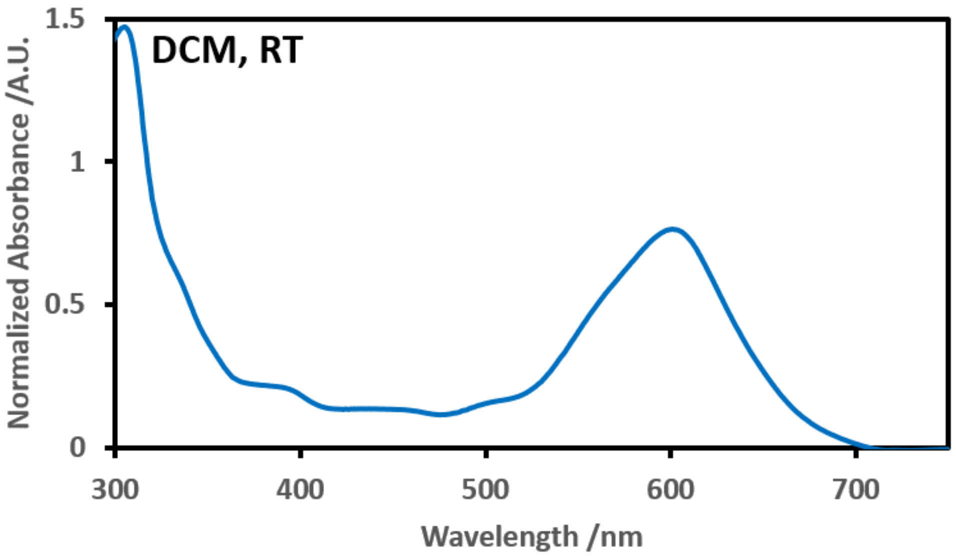

Appendix C-2 UV-Vis spectrum of **2.6** in DCM. (ca. 50 μM)

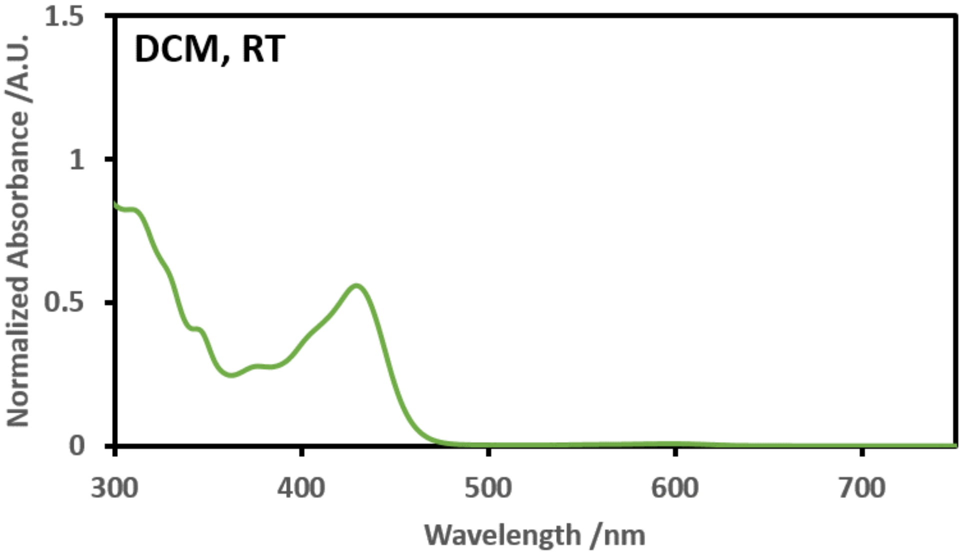

Appendix C-3 UV-Vis spectrum of **2.7** in DCM. (ca. 50 μM)

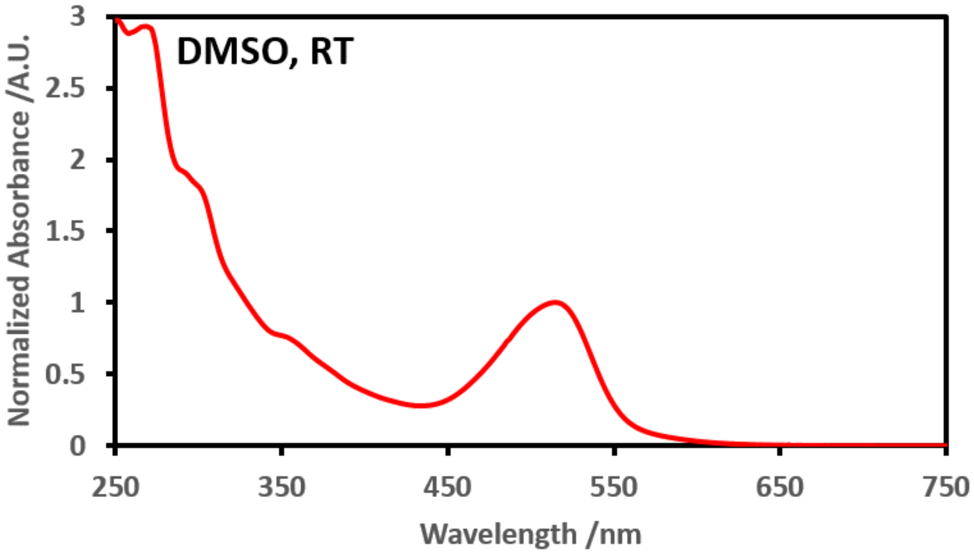

Appendix C-4 UV-Vis spectrum of **3.2** in DMSO.

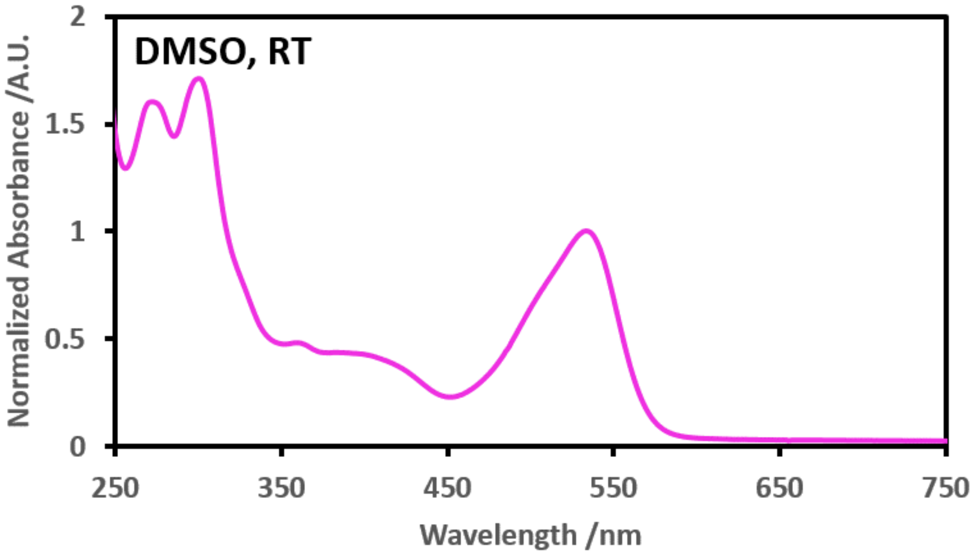

Appendix C-5 UV-Vis spectrum of **3.3** in DMSO.

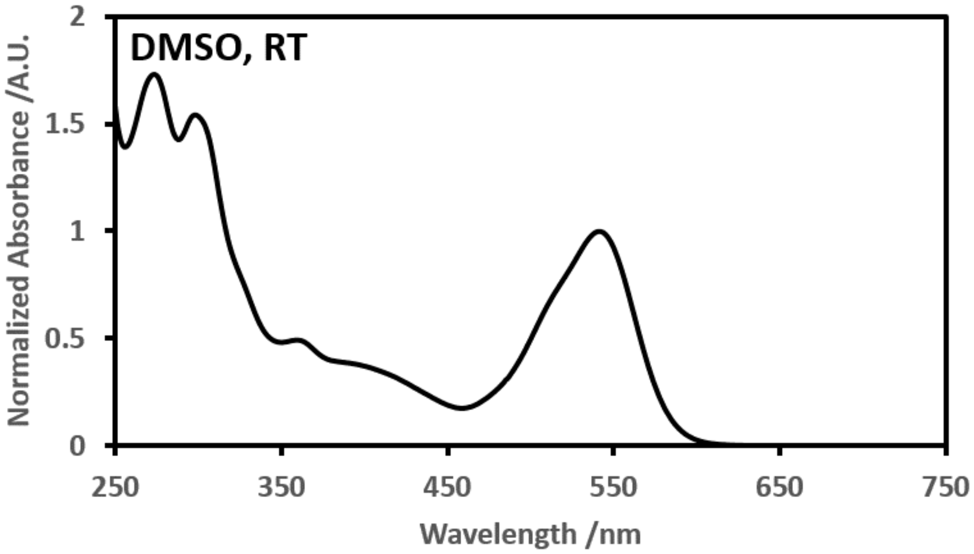

Appendix C-6 UV-Vis spectrum of **3.4** in DMSO.

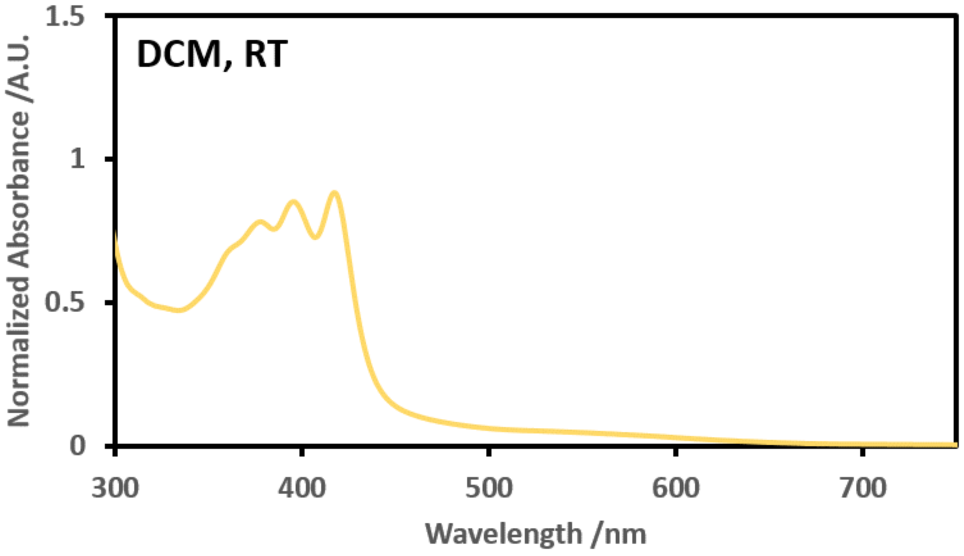

Appendix C-7 UV-Vis spectrum of **4.6a** in DCM. (ca. 50 μM)

Appendix D: FT-IR Spectra

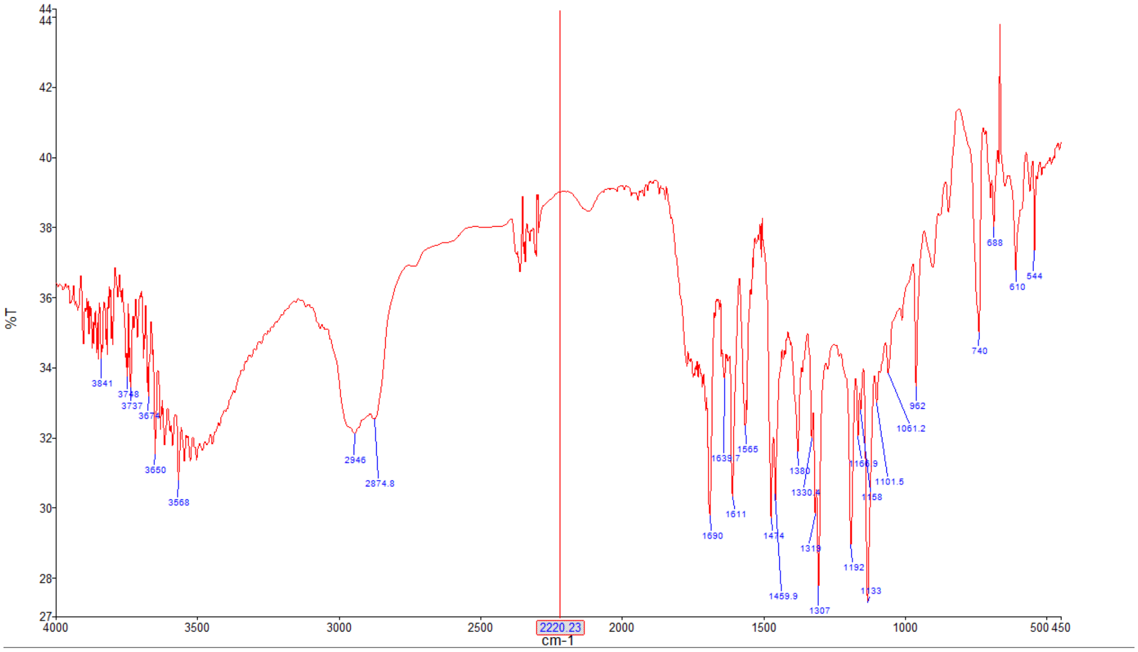

Appendix D-1 FT-IR spectrum of **2.5** in KBr pellet. Air background.

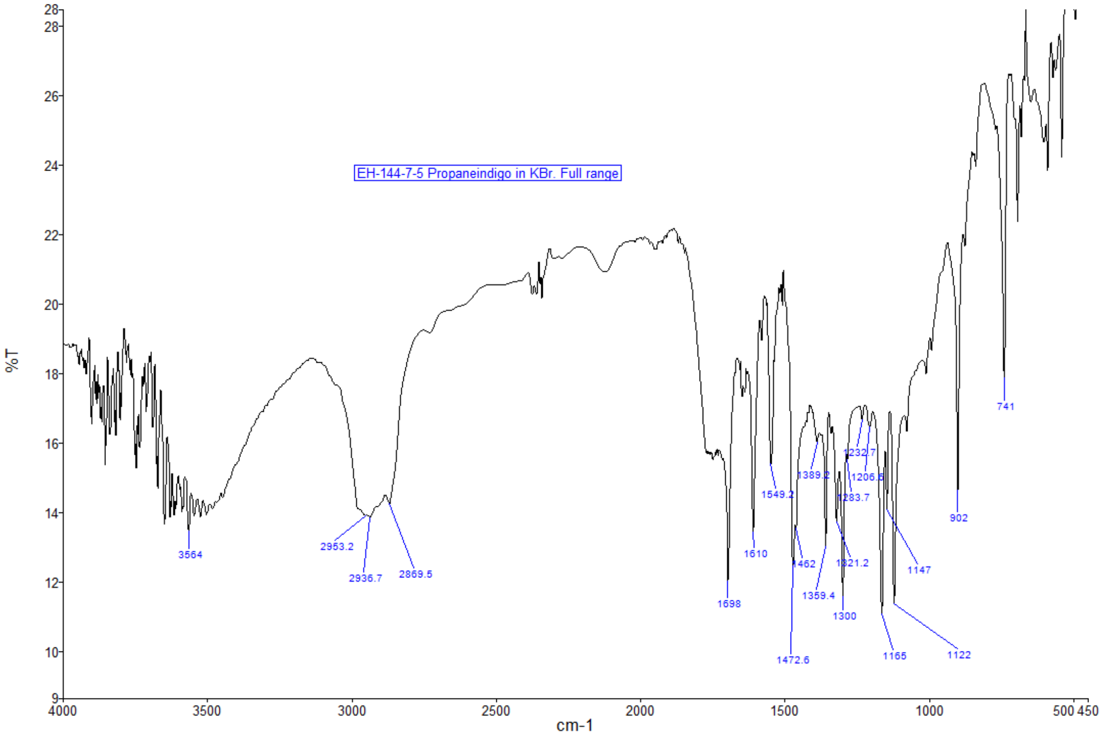

Appendix D-2 FT-IR spectrum of **2.6** in KBr pellet. Air background.

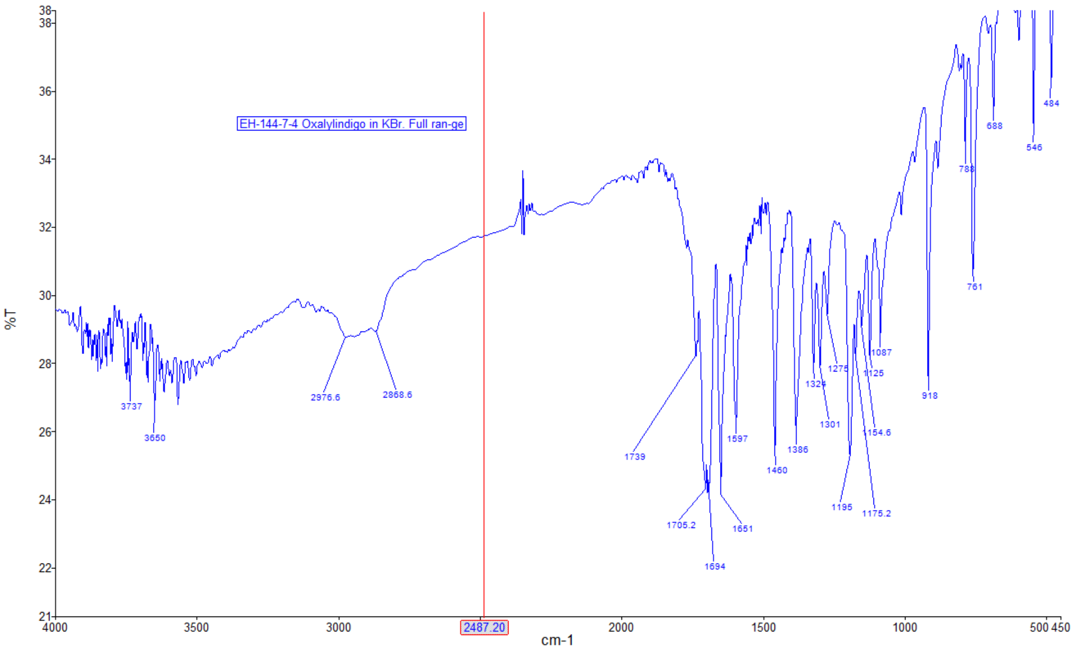

Appendix D-3 FT-IR spectrum of **2.7** in KBr pellet. Air background.

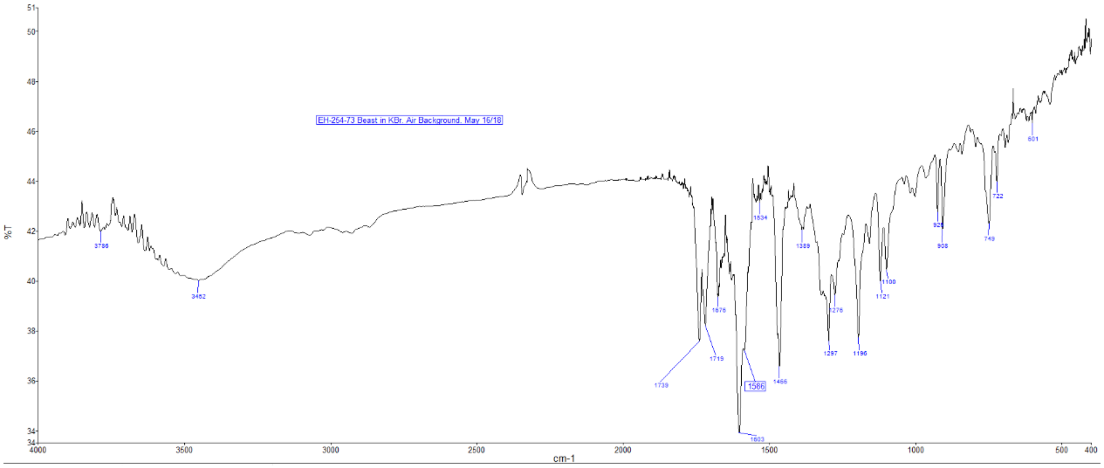

Appendix D-4 FT-IR spectrum of **3.2** in KBr pellet. Air background.

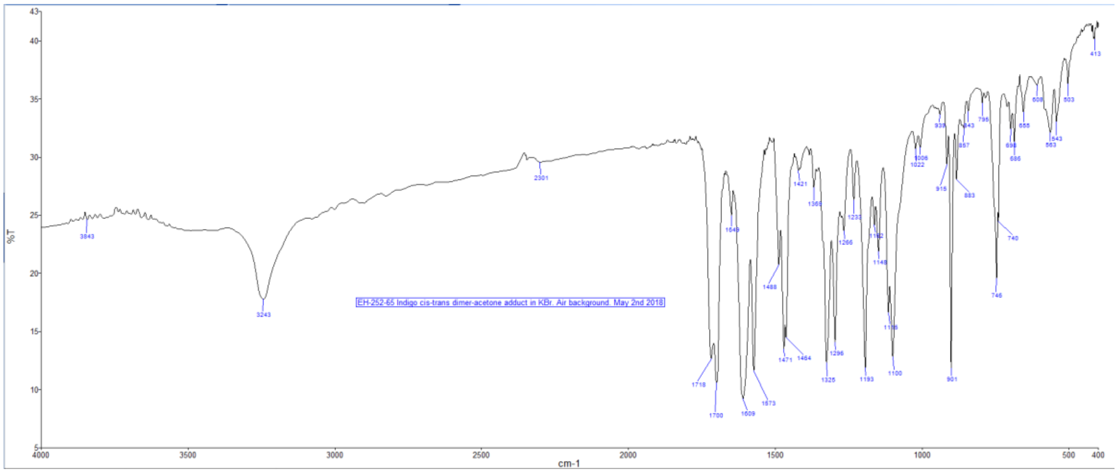

Appendix D-5 FT-IR spectrum of **3.3** in KBr pellet. Air background.

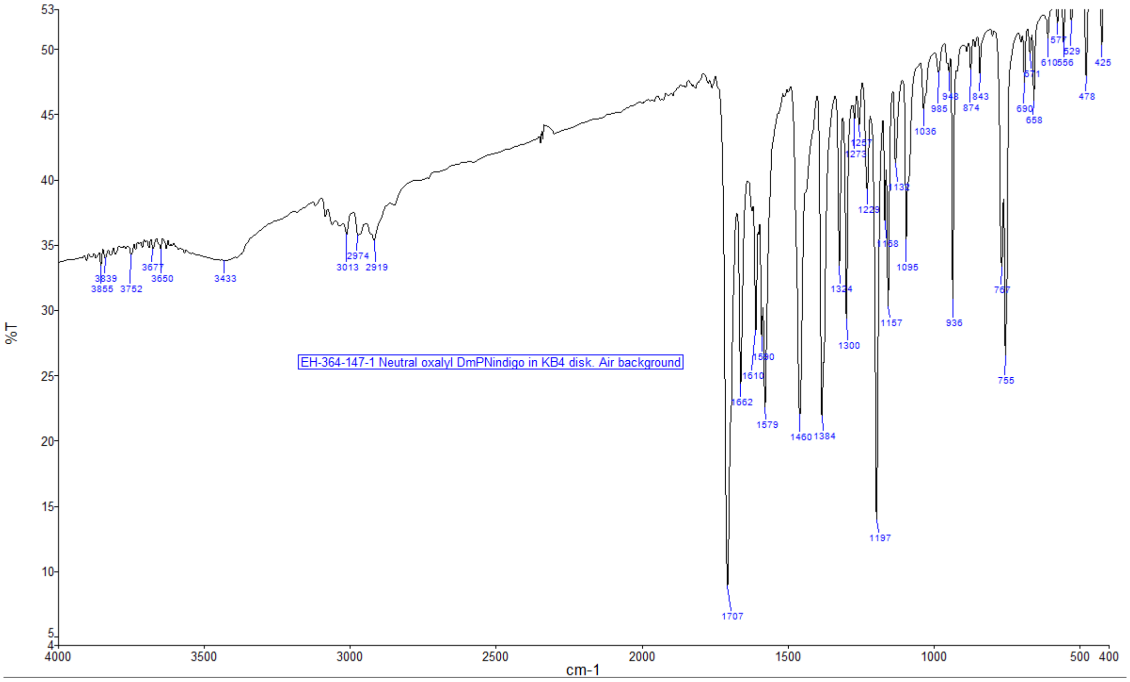

Appendix D-6 FT-IR spectrum of **4.6a** in KBr pellet. Air background.

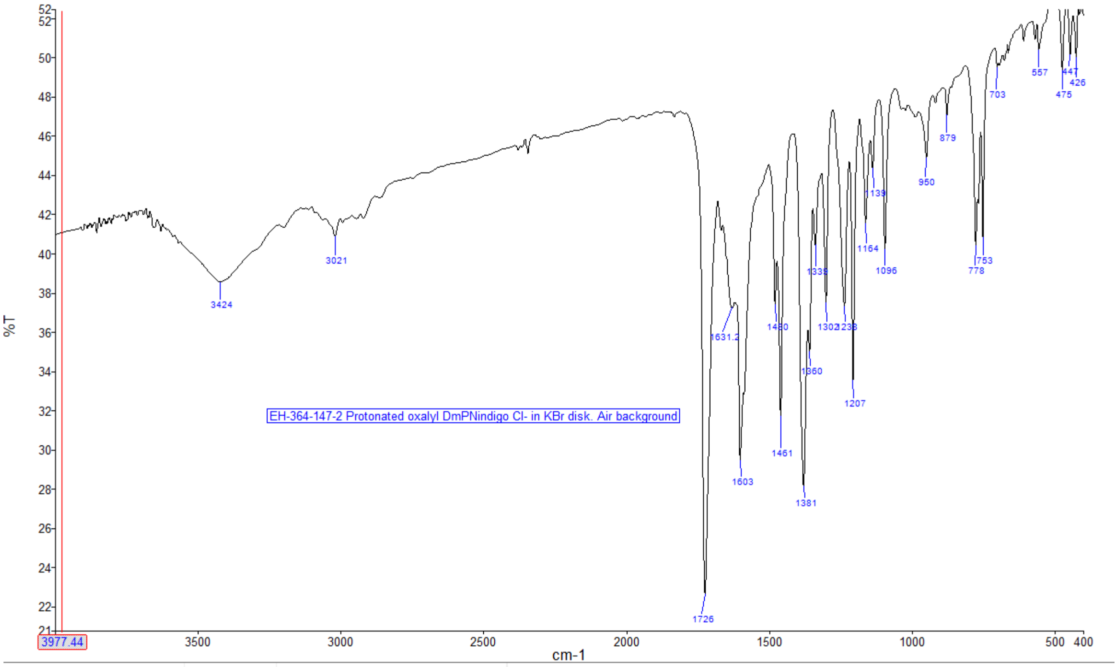

Appendix D-7 FT-IR spectrum of **4.6aH**$^+$Cl$^-$ in KBr pellet. Air background.

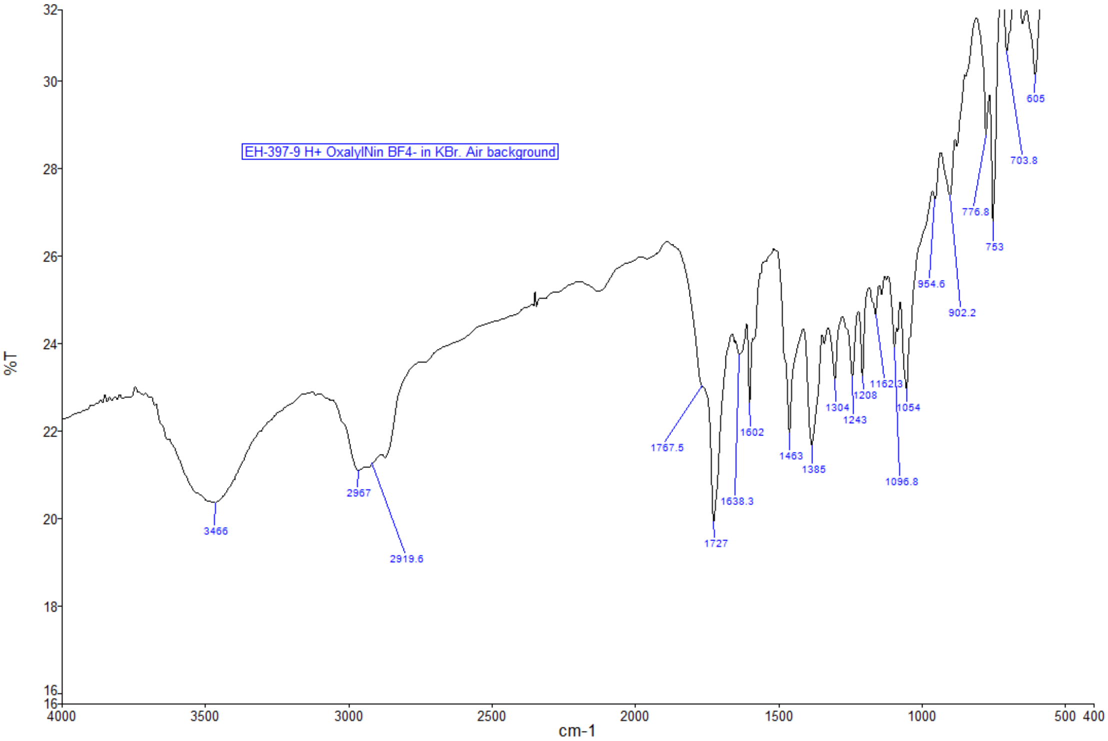

Appendix D-8 FT-IR spectrum of **4.6aH**$^+$BF$_4^-$ in KBr pellet. Air background.

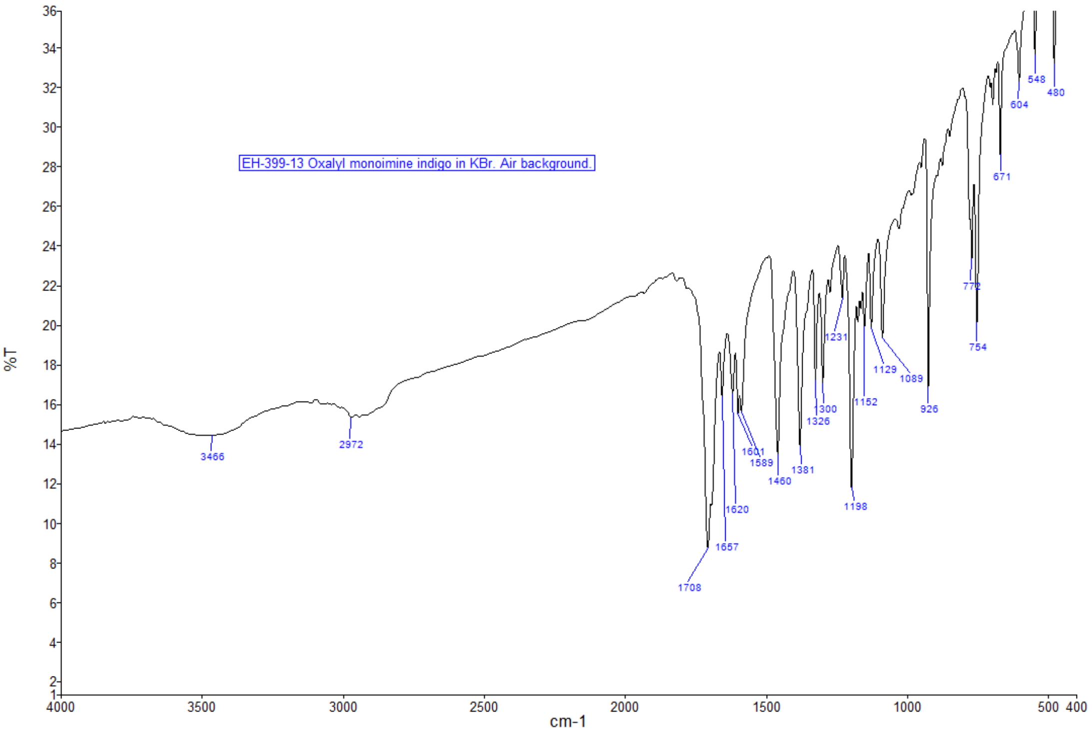

Appendix D-9 FT-IR spectrum of **4.7a** in KBr pellet. Air background.

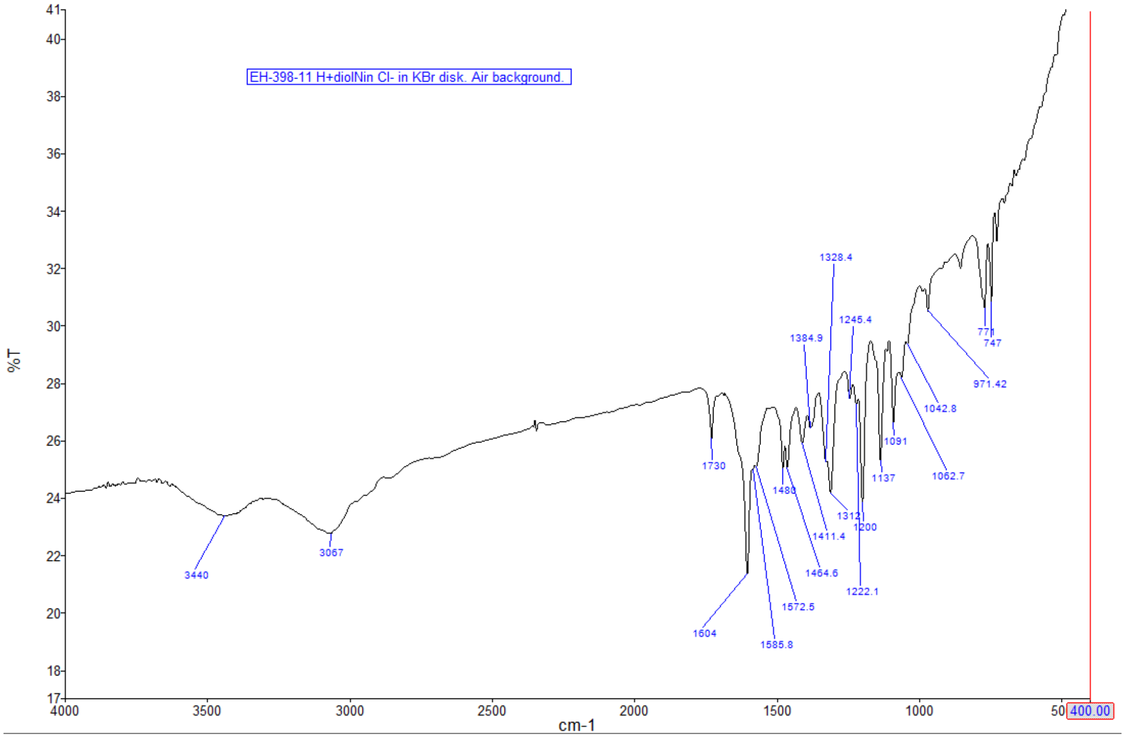

Appendix D-10 FT-IR spectrum of **4.9aH**$^+$Cl$^-$ in KBr pellet. Air background.

Appendix E: Mass Spectra

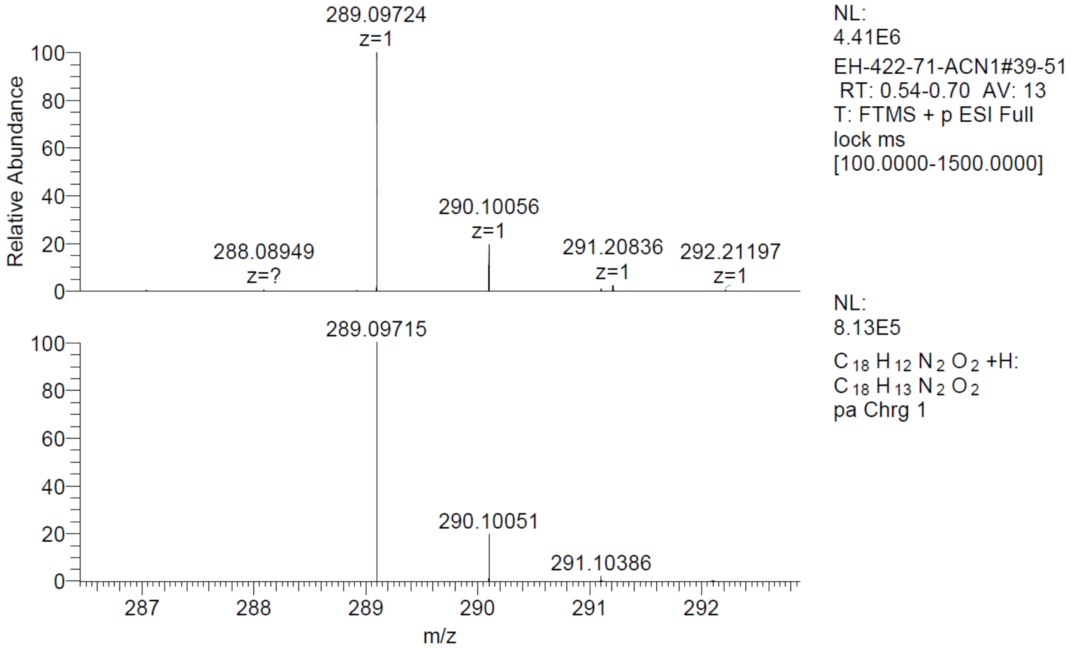

Appendix E-1 HR-MS spectrum of **2.5** and a simulation.

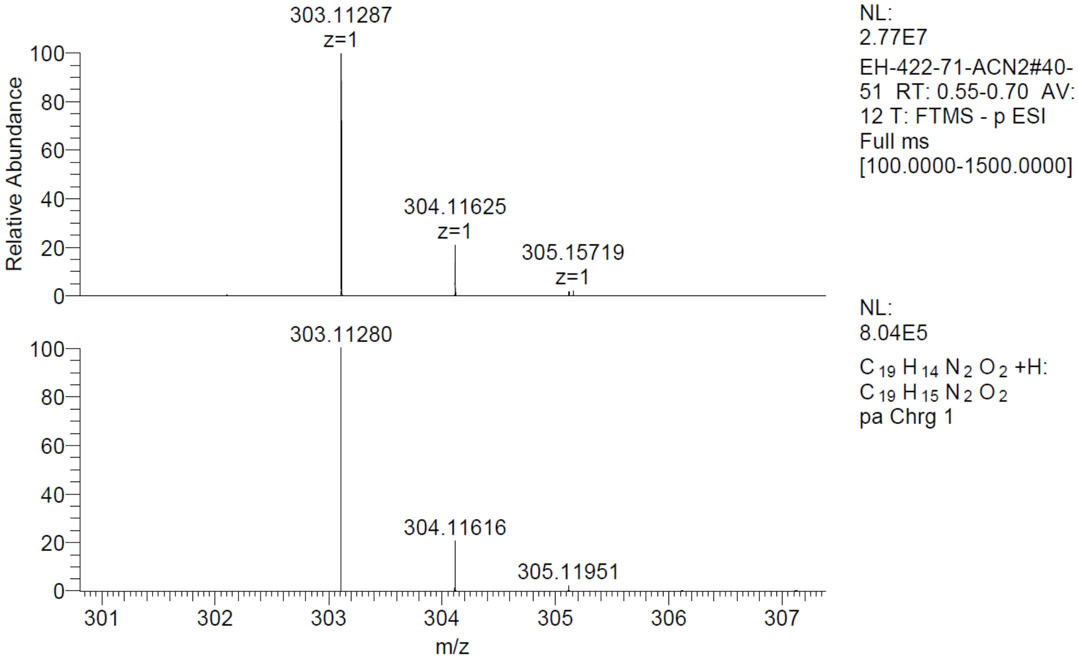

Appendix E-2 HR-MS spectrum of **2.6** and a simulation.

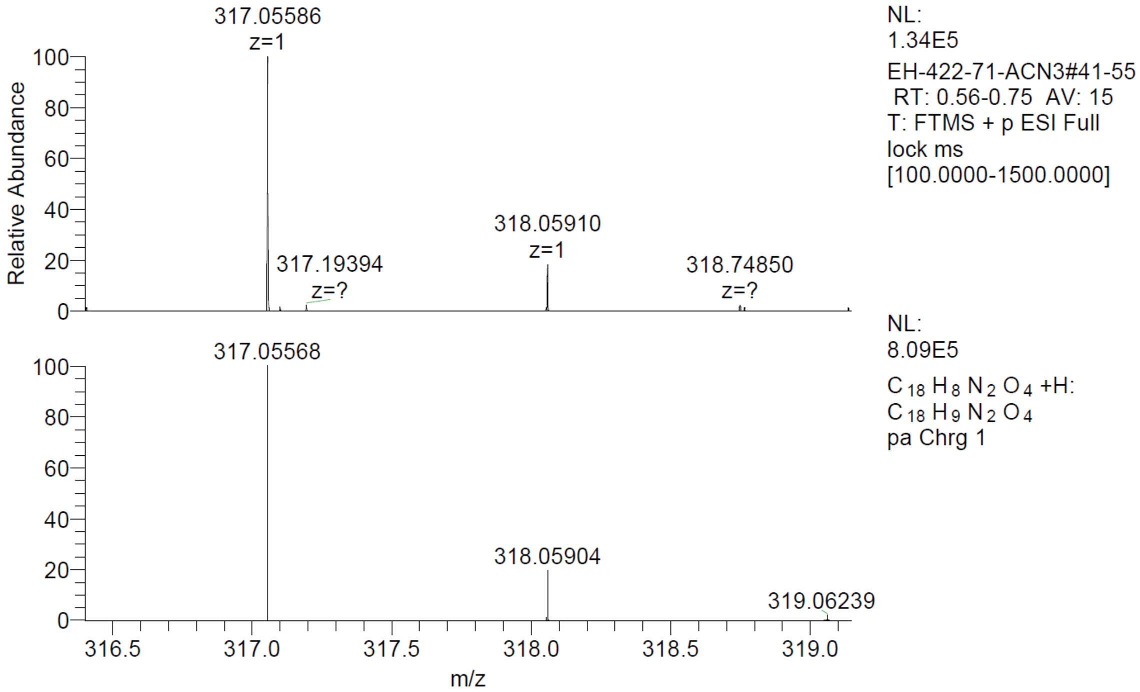

Appendix E-3 HR-MS spectrum of **2.7** and a simulation.

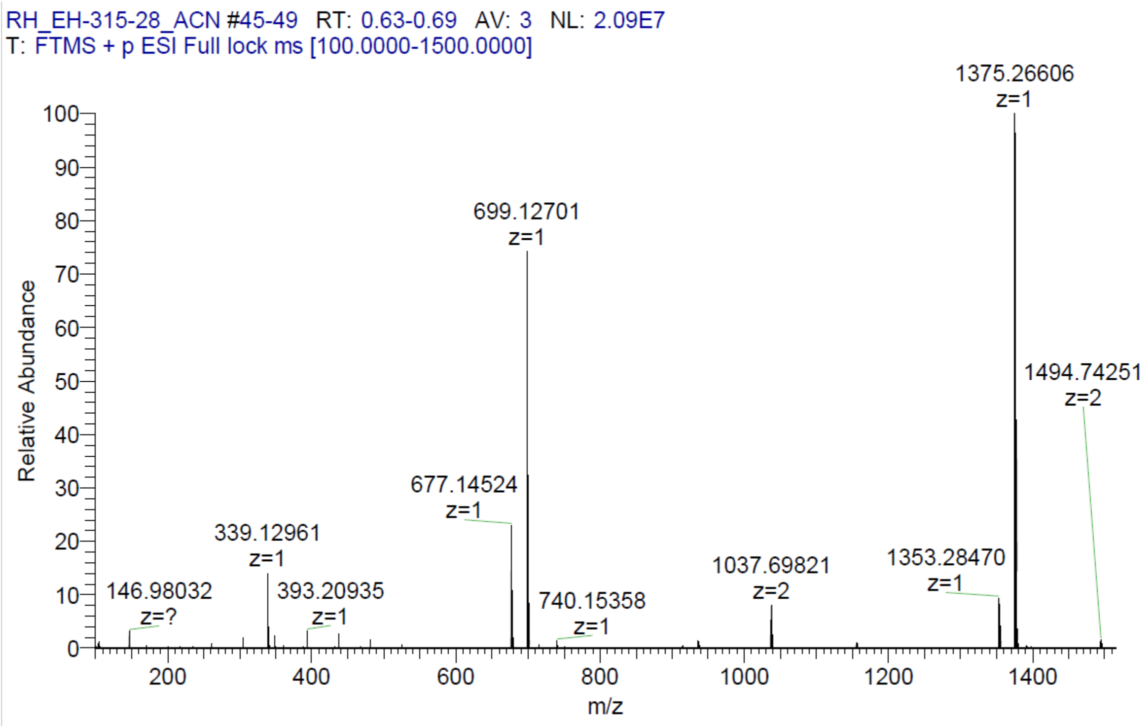

Appendix E-4 HR-MS spectrum of **3.2**.

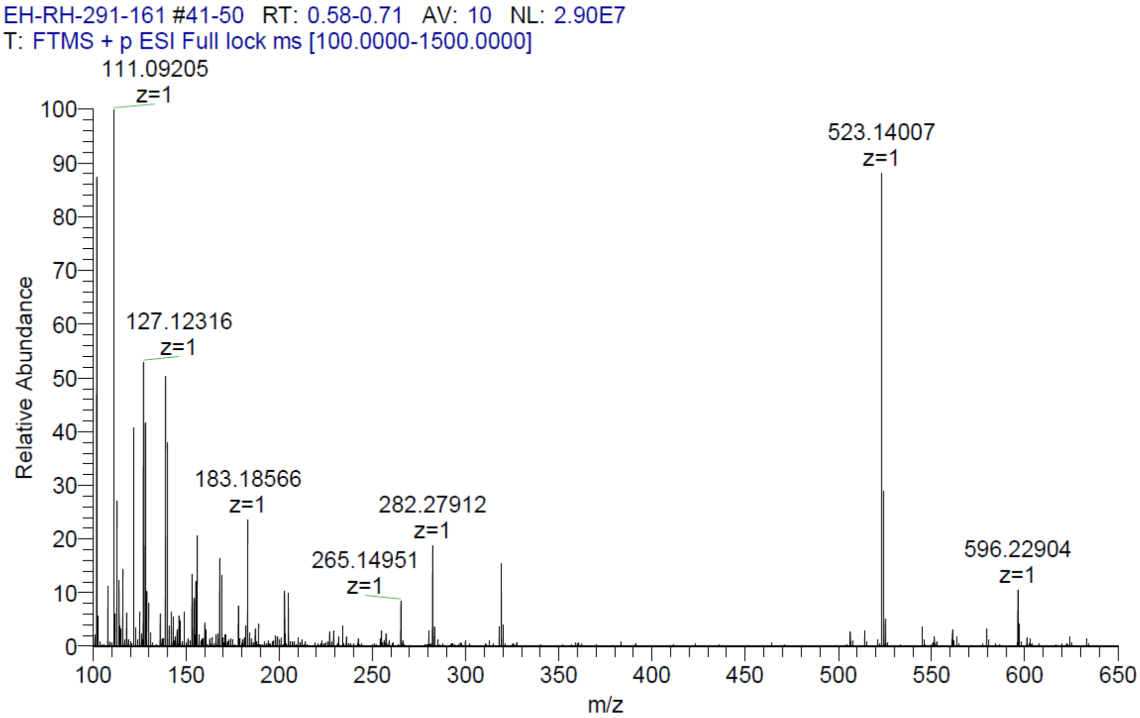

Appendix E-5 HR-MS spectrum of **3.3**.

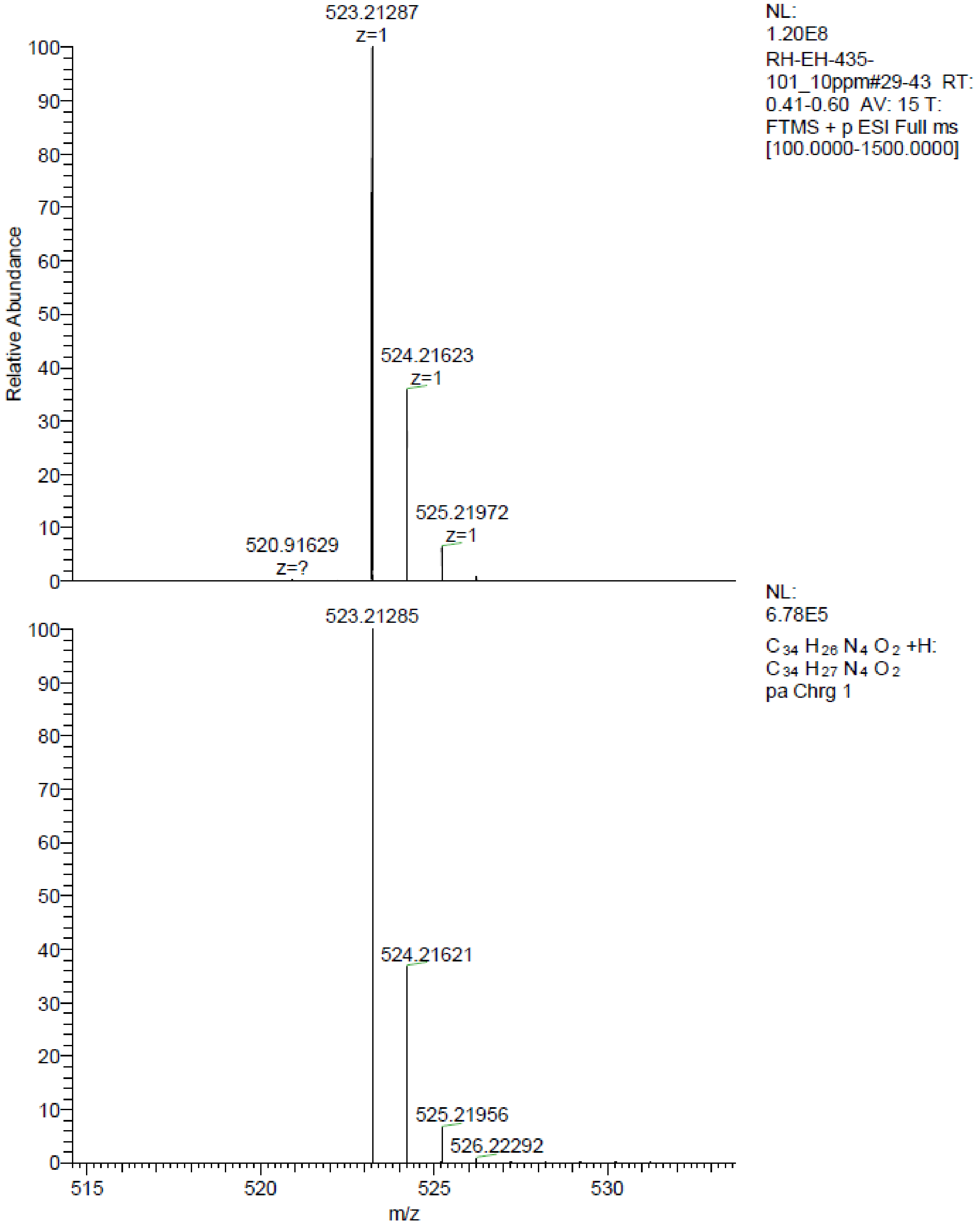

Appendix E-6 HR-MS spectrum of **4.6a** and a simulation.

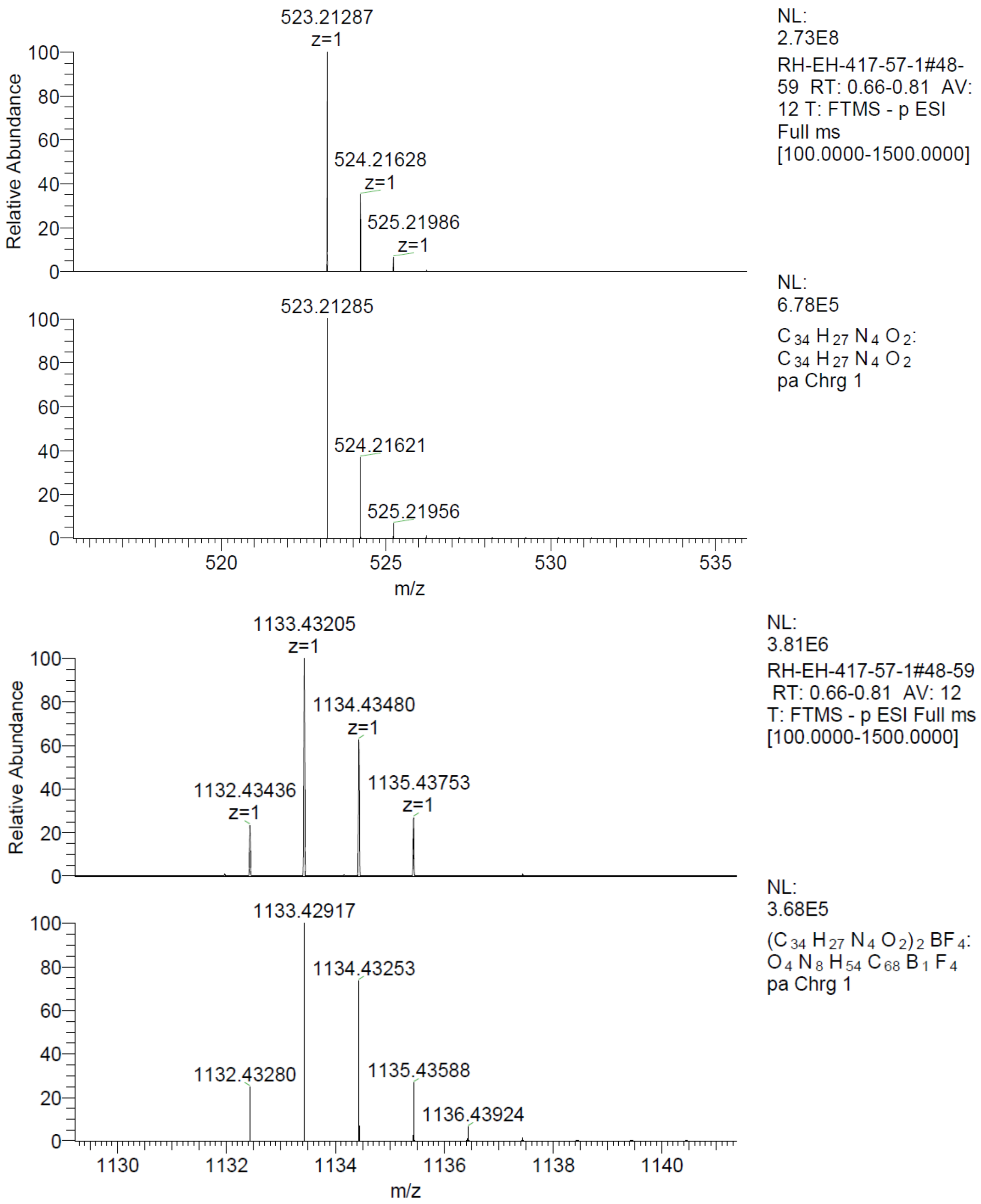

Appendix E-7 HR-MS spectrum of **4.6aH**$^+$BF$_4^-$ and a simulation.

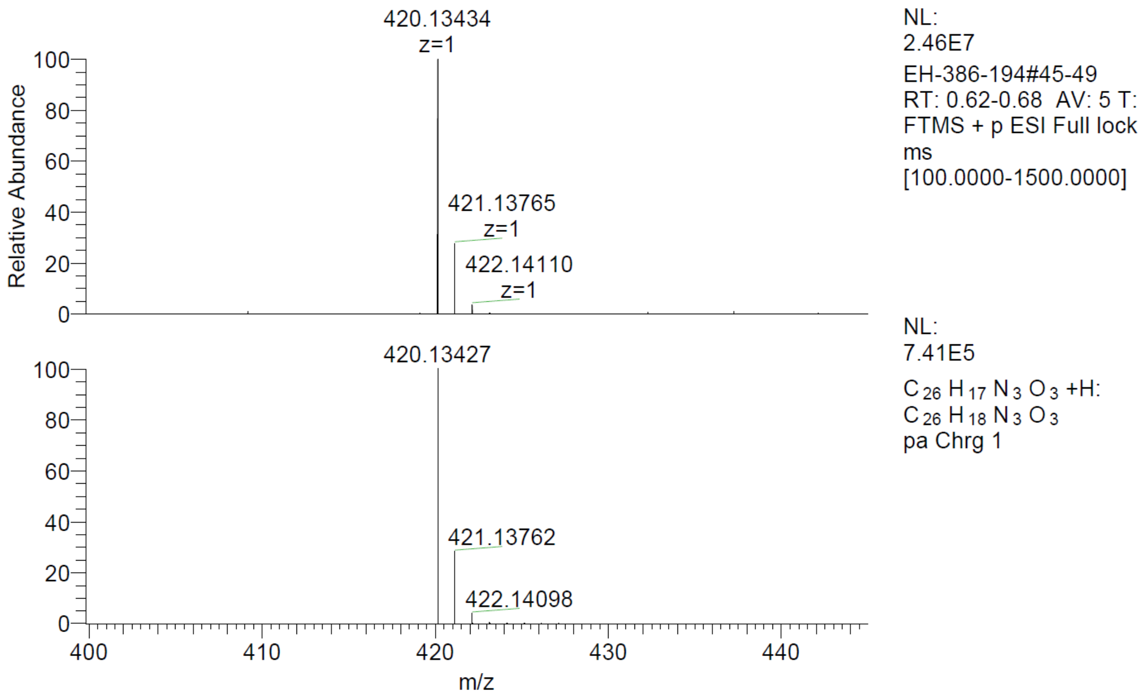

Appendix E-8 HR-MS spectrum of **4.7a** and a simulation.

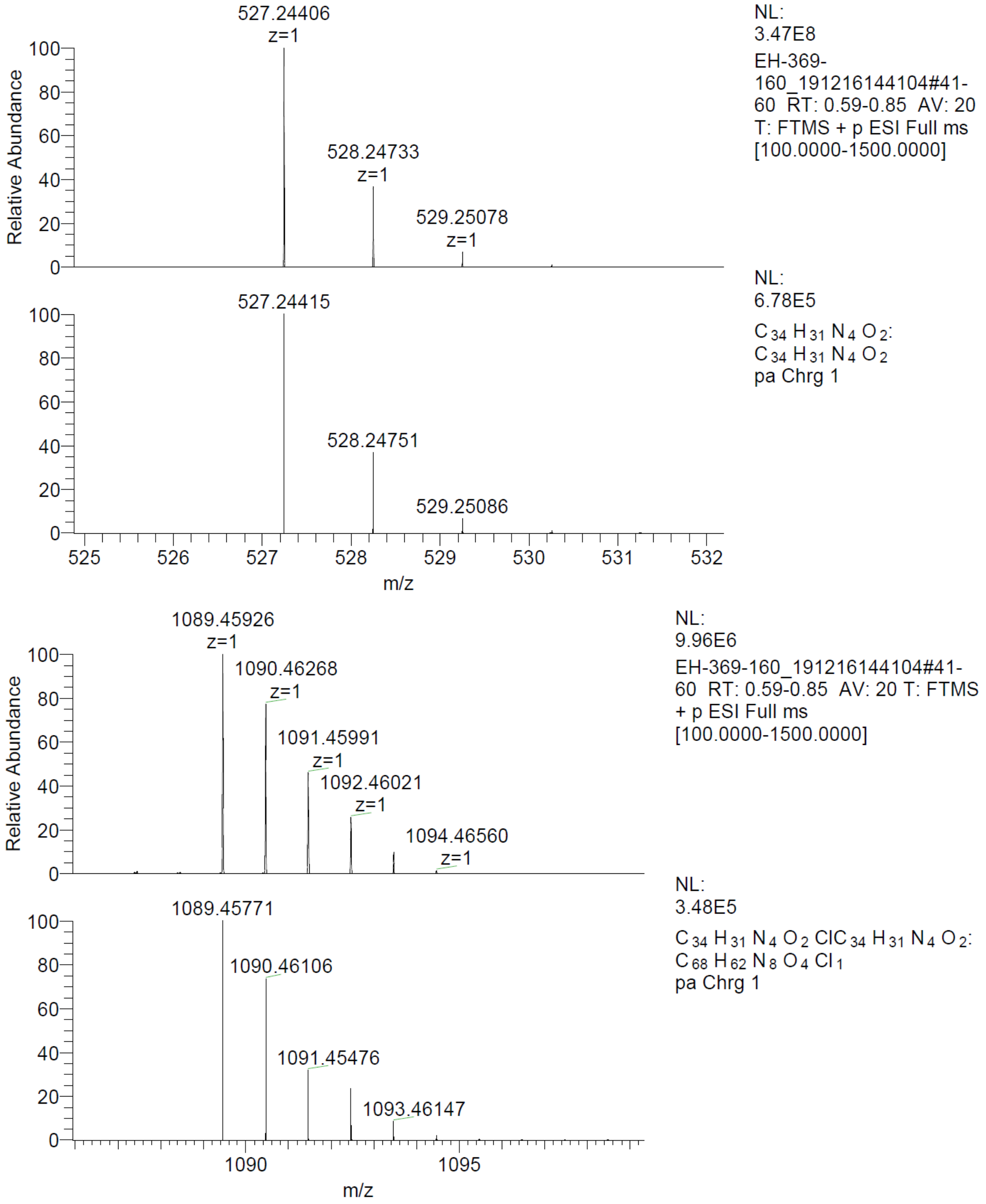

Appendix E-9 HR-MS spectrum of **4.9aH**$^+$Cl$^-$ and a simulation.

Appendix F: Crystallographic Data

Appendix F-1 Table of crystallographic parameters for **2.5**, **2.6** and **2.7**

Compound number	**2.5**	**2.6**	**2.7**
Empirical formula	$C_{18}H_{12}N_2O_2$	$C_{19}H_{14}N_2O_2$	$C_{18}H_8N_2O_4$
Formula weight	288.30	302.32	316.26
Temperature/K	90	90.15	90
Crystal system	triclinic	monoclinic	triclinic
Space group	P-1	$P2_1/c$	P-1
a/Å	6.9945(11)	9.8858(8)	5.8137(16)
b/Å	8.5021(13)	6.8961(6)	7.145(2)
c/Å	11.5307(17)	19.9066(17)	8.240(3)
α/°	90.714(5)	90	105.127(17)
β/°	107.584(5)	92.783(2)	91.52(2)
γ/°	97.407(5)	90	100.683(16)
Volume/Å^3	647.25(17)	1355.5(2)	323.64(16)
Z	2	4	1
ρ_{calc}g/cm^3	1.479	1.481	1.623
μ/mm^{-1}	0.098	0.098	0.118
F(000)	300.0	632.0	162.0
Crystal size/mm^3	0.45 × 0.18 × 0.03	0.29 × 0.19 × 0.09	0.31 × 0.19 × 0.08
Radiation	MoKα (λ = 0.71073)	MoKα (λ = 0.71073)	MoKα (λ = 0.71073)
2Θ range for data collection/°	3.71 to 52.884	4.096 to 60.068	5.138 to 50.992
Index ranges	-8 ≤ h ≤ 8, -8 ≤ k ≤ 10, -14 ≤ l ≤ 14	-13 ≤ h ≤ 13, -8 ≤ k ≤ 9, -28 ≤ l ≤ 28	-6 ≤ h ≤ 6, -8 ≤ k ≤ 8, -9 ≤ l ≤ 9
Reflections collected	10109	16334	2741
Independent reflections	2640 [R_{int} = 0.0353, R_{sigma} = 0.0382]	3960 [R_{int} = 0.0258, R_{sigma} = 0.0219]	1159 [R_{int} = 0.0339, R_{sigma} = 0.0434]
Data/restraints/parameters	2640/0/199	3960/0/208	1159/216/193
Goodness-of-fit on F^2	1.095	1.033	1.199
Final R indexes [I>=2σ (I)]	R_1 = 0.0615, wR_2 = 0.1849	R_1 = 0.0397, wR_2 = 0.1096	R_1 = 0.0466, wR_2 = 0.1140
Final R indexes [all data]	R_1 = 0.0732, wR_2 = 0.1946	R_1 = 0.0477, wR_2 = 0.1172	R_1 = 0.0541, wR_2 = 0.1171
Largest diff. peak/hole / e Å^{-3}	0.48/-0.37	0.51/-0.22	0.20/-0.20

Appendix F-2 Table of crystallographic parameters for **2.8** and **2.9**

Compound number	**2.8**	**2.9**
Empirical formula	$C_{19}H_{14}N_2O_2$	$C_{19}H_{14}N_2O_2$
Formula weight	302.32	302.32
Temperature/K	90	90
Crystal system	orthorhombic	monoclinic
Space group	$Pna2_1$	$P2_1/c$
a/Å	9.9608(17)	9.5907(16)
b/Å	23.908(4)	16.981(3)
c/Å	5.8445(9)	17.274(3)
α/°	90	90
β/°	90	97.164(9)
γ/°	90	90
Volume/Å^3	1391.8(4)	2791.3(8)
Z	4	8
ρ_{calc}g/cm^3	1.443	1.439
μ/mm^{-1}	0.095	0.095
F(000)	632.0	1264.0
Crystal size/mm^3	0.57 × 0.07 × 0.05	0.55 × 0.17 × 0.03
Radiation	MoKα (λ = 0.71073)	MoKα (λ = 0.71073)
2Θ range for data collection/°	4.43 to 52.874	3.376 to 50.016
Index ranges	$-12 \leq h \leq 12, -29 \leq k \leq 29, -6 \leq l \leq 7$	$-11 \leq h \leq 11, -19 \leq k \leq 20, -19 \leq l \leq 20$
Reflections collected	10837	16059
Independent reflections	2847 [R_{int} = 0.0433, R_{sigma} = 0.0393]	4883 [R_{int} = 0.0613, R_{sigma} = 0.0824]
Data/restraints/parameters	2847/1/248	4883/0/431
Goodness-of-fit on F^2	1.020	1.010
Final R indexes [I>=2σ (I)]	R_1 = 0.0367, wR_2 = 0.0812	R_1 = 0.0669, wR_2 = 0.1547
Final R indexes [all data]	R_1 = 0.0478, wR_2 = 0.0863	R_1 = 0.1142, wR_2 = 0.1791
Largest diff. peak/hole / e Å^{-3}	0.14/-0.16	0.30/-0.29
Flack parameter	-0.6(8)	

Appendix F-3 Table of crystallographic parameters for **3.2** and **3.3**

Compound number	**3.2**	**3.3**
Empirical formula	$C_{28}H_{17.07}N_{2.13}O_{3.2}$	$C_{128}H_{72}N_{16}O_{16}$
Formula weight	434.57	2090.01
Temperature/K	90	90
Crystal system	monoclinic	monoclinic
Space group	C2/c	$P2_1/n$
a/Å	39.337(3)	15.8835(3)
b/Å	13.8936(10)	7.9818(2)
c/Å	28.683(2)	18.7804(4)
α/°	90	90
β/°	93.498(4)	98.4500(10)
γ/°	90	90
Volume/Å^3	15647.3(19)	2355.11(9)
Z	30	1
ρ_{calc}g/cm^3	1.384	1.474
μ/mm^{-1}	0.092	0.100
F(000)	6768.0	1080.0
Crystal size/mm^3	0.23 × 0.19 × 0.12	0.2 × 0.11 × 0.07
Radiation	MoKα (λ = 0.71073)	MoKα (λ = 0.71073)
2Θ range for data collection/°	2.846 to 55.864	3.632 to 56.518
Index ranges	$-51 \le h \le 51$, $-18 \le k \le 17$, $-31 \le l \le 37$	$-21 \le h \le 20$, $-10 \le k \le 7$, $-25 \le l \le 24$
Reflections collected	79517	28111
Independent reflections	18680 [R_{int} = 0.0512, R_{sigma} = 0.0486]	5833 [R_{int} = 0.0383, R_{sigma} = 0.0344]
Data/restraints/parameters	18680/0/1213	5833/0/369
Goodness-of-fit on F^2	0.988	1.048
Final R indexes [I>=2σ (I)]	R_1 = 0.0522, wR_2 = 0.1395	R_1 = 0.0474, wR_2 = 0.1199
Final R indexes [all data]	R_1 = 0.0763, wR_2 = 0.1575	R_1 = 0.0630, wR_2 = 0.1297
Largest diff. peak/hole / e Å^{-3}	0.39/-0.27	0.38/-0.24
CCDC number	1950571	1950567

Appendix F-4 Table of crystallographic parameters for **3.4** and **3.5**

Compound number	**3.4**	**3.5**
Empirical formula	$C_{256}H_{152}N_{32}O_{36}$	$C_{124}H_{64}N_{16}O_{12}$
Formula weight	4252.09	1969.91
Temperature/K	90	296.15
Crystal system	monoclinic	monoclinic
Space group	C2/c	$P2_1/n$
a/Å	27.7629(15)	12.0211(3)
b/Å	10.8917(6)	11.7866(3)
c/Å	17.5795(9)	16.5760(5)
α/°	90	90
β/°	113.574(4)	109.3940(10)
γ/°	90	90
Volume/Å^3	4872.1(5)	2215.35(10)
Z	1	1
ρ_{calc}g/cm^3	1.449	1.477
μ/mm^{-1}	0.813	0.098
F(000)	2200.0	1016.0
Crystal size/mm^3	0.11 × 0.04 × 0.03	0.46 × 0.31 × 0.22
Radiation	CuKα (λ = 1.54184)	MoKα (λ = 0.71073)
2Θ range for data collection/°	6.948 to 112.06	3.67 to 61.088
Index ranges	$-29 \le h \le 29$, $-11 \le k \le 11$, $-18 \le l \le 18$	$-15 \le h \le 17$, $-13 \le k \le 16$, $-23 \le l \le 23$
Reflections collected	15242	28699
Independent reflections	3176 [R_{int} = 0.0697, R_{sigma} = 0.0549]	6767 [R_{int} = 0.0311, R_{sigma} = 0.0295]
Data/restraints/parameters	3176/0/383	6767/0/343
Goodness-of-fit on F^2	1.016	1.022
Final R indexes [I>=2σ (I)]	R_1 = 0.0382, wR_2 = 0.0836	R_1 = 0.0446, wR_2 = 0.1131
Final R indexes [all data]	R_1 = 0.0552, wR_2 = 0.0914	R_1 = 0.0593, wR_2 = 0.1235
Largest diff. peak/hole / e Å^{-3}	0.18/-0.19	0.49/-0.26
CCDC number	1950568	1950569

Appendix F-5 Table of crystallographic parameters for **4.6**, **4.6aH**$^+$TFA$^-$ and **4.7a**

Compound number	**4.6a**	**4.6aH**$^+$TFA$^-$	**4.7a**
Empirical formula	$C_{136}H_{104}N_{16}O_8$	$C_{152}H_{112}F_{24}N_{16}O_{24}$	$C_{26}H_{17}N_3O_3$
Formula weight	2090.35	3002.57	419.42
Temperature/K	90	90	90
Crystal system	monoclinic	monoclinic	triclinic
Space group	$P2_1/c$	$P2_1/c$	P-1
a/Å	8.7367(4)	14.5163(16)	7.3242(8)
b/Å	16.8819(8)	10.6820(14)	10.5403(12)
c/Å	17.7764(9)	22.178(2)	13.3297(15)
α/°	90	90	97.394(3)
β/°	97.911(2)	94.725(5)	102.379(3)
γ/°	90	90	104.101(3)
Volume/Å^3	2596.9(2)	3427.2(7)	956.89(19)
Z	1	1	2
ρ_{calc}g/cm^3	1.337	1.455	1.456
μ/mm^{-1}	0.085	0.121	0.097
F(000)	1096.0	1544.0	436.0
Crystal size/mm^3	0.29 × 0.22 × 0.09	0.23 × 0.17 × 0.1	0.25 × 0.23 × 0.16
Radiation	MoKα (λ = 0.71073)	MoKα (λ = 0.71073)	MoKα (λ = 0.71073)
2Θ range for data collection/°	3.342 to 60.204	3.686 to 45.22	4.06 to 61.06
Index ranges	-11 ≤ h ≤ 12, -23 ≤ k ≤ 23, -24 ≤ l ≤ 24	-15 ≤ h ≤ 15, -11 ≤ k ≤ 11, -23 ≤ l ≤ 23	-10 ≤ h ≤ 10, -15 ≤ k ≤ 15, -19 ≤ l ≤ 19
Reflections collected	31988	25317	22665
Independent reflections	7582 [R_{int} = 0.0390, R_{sigma} = 0.0361]	4538 [R_{int} = 0.0489, R_{sigma} = 0.0414]	5832 [R_{int} = 0.0386, R_{sigma} = 0.0338]
Data/restraints/parameters	7582/0/365	4538/0/495	5832/0/291
Goodness-of-fit on F^2	1.055	1.032	1.016
Final R indexes [I>=2σ (I)]	R_1 = 0.0528, wR_2 = 0.1395	R_1 = 0.0462, wR_2 = 0.1078	R_1 = 0.0434, wR_2 = 0.1142
Final R indexes [all data]	R_1 = 0.0702, wR_2 = 0.1518	R_1 = 0.0728, wR_2 = 0.1203	R_1 = 0.0532, wR_2 = 0.1216
Largest diff. peak/hole / e Å^{-3}	0.40/-0.23	0.78/-0.37	0.58/-0.30

Appendix F-6 Table of crystallographic parameters for **4.8/4.8-Cl** and **4.9aH**$^+$Cl$^-$

Compound number	**4.8/4.8-Cl**	**4.9aH**$^+$Cl$^-$
Empirical formula	$C_{67}H_{45.51}Cl_{2.49}N_8O_6$	$C_{38}H_{37}ClN_6O_2$
Formula weight	1146.89	645.18
Temperature/K	90	90
Crystal system	monoclinic	triclinic
Space group	C2/c	P-1
a/Å	22.124(5)	7.8947(5)
b/Å	10.106(2)	11.8267(7)
c/Å	24.923(6)	18.6476(11)
α/°	90	92.083(3)
β/°	107.801(3)	99.558(3)
γ/°	90	102.969(3)
Volume/Å^3	5305(2)	1668.21(18)
Z	4	2
ρ_{calc}g/cm^3	1.436	1.284
μ/mm^{-1}	0.214	0.158
F(000)	2375.0	680.0
Crystal size/mm^3	0.22 × 0.22 × 0.096	0.42 × 0.2 × 0.03
Radiation	MoKα (λ = 0.71073)	MoKα (λ = 0.71073)
2Θ range for data collection/°	3.432 to 53.524	4.326 to 60.19
Index ranges	$-27 \leq h \leq 27, -12 \leq k \leq 12, -31 \leq l \leq 30$	$-11 \leq h \leq 11, -16 \leq k \leq 16, -26 \leq l \leq 26$
Reflections collected	20964	34606
Independent reflections	5610 [R_{int} = 0.0327, R_{sigma} = 0.0298]	9728 [R_{int} = 0.0385, R_{sigma} = 0.0459]
Data/restraints/parameters	5610/0/397	9728/0/442
Goodness-of-fit on F^2	0.983	1.030
Final R indexes [I>=2σ (I)]	R_1 = 0.0736, wR_2 = 0.1945	R_1 = 0.0553, wR_2 = 0.1413
Final R indexes [all data]	R_1 = 0.0922, wR_2 = 0.2096	R_1 = 0.0781, wR_2 = 0.1543
Largest diff. peak/hole / e Å^{-3}	1.02/-0.76	0.63/-0.30

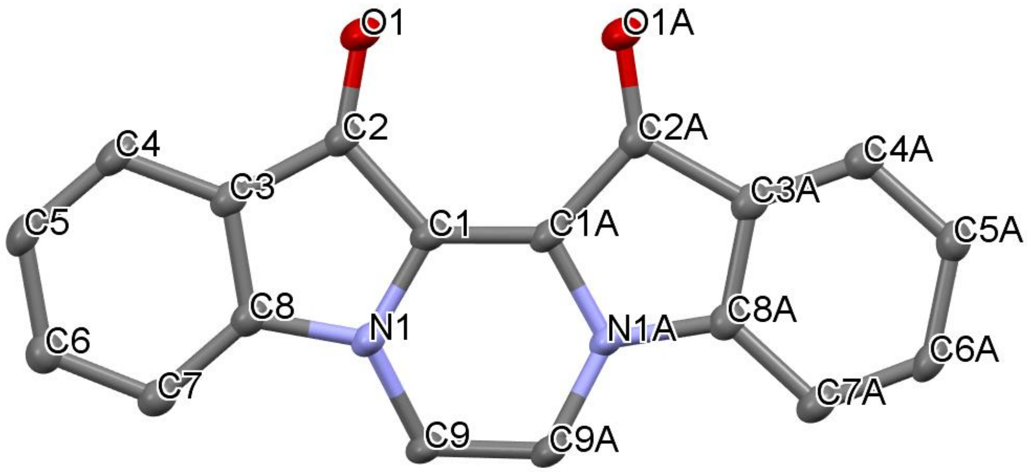

Appendix F-7 X-ray structure of **2.5**. Hydrogen atoms are omitted for clarity. Thermal ellipsoids represented at 50%.

Appendix F-8 Table of bond lengths (Å) for **2.5**

Atom	Atom	Length/Å	Atom	Atom	Length/Å
C1	C2	1.489(3)	C9	C9A	1.529(3)
C1	N1	1.386(3)	C1A	C2A	1.505(3)
C1	C1A	1.374(3)	C1A	N1A	1.384(3)
C2	C3	1.468(3)	C2A	C3A	1.483(3)
C2	O1	1.225(3)	C2A	O1A	1.217(3)
C3	C4	1.395(3)	C3A	C4A	1.389(3)
C3	C8	1.392(3)	C3A	C8A	1.391(3)
C4	C5	1.388(3)	C4A	C5A	1.385(3)
C5	C6	1.387(3)	C5A	C6A	1.398(3)
C6	C7	1.392(3)	C6A	C7A	1.387(3)
C7	C8	1.395(3)	C7A	C8A	1.399(3)
C8	N1	1.392(3)	C8A	N1A	1.396(3)
C9	N1	1.454(3)	C9A	N1A	1.456(3)

Appendix F-9 Table of bond angles (°) for **2.5**

Atom	Atom	Atom	Angle/˚	Atom	Atom	Atom	Angle/˚
N1	C1	C2	107.90(17)	C1	C1A	C2A	132.6(2)
C1A	C1	C2	132.4(2)	C1	C1A	N1A	119.21(19)
C1A	C1	N1	119.69(19)	N1A	C1A	C2A	108.20(18)

C3	C2	C1	104.13(17)	C3A	C2A	C1A	103.34(17)
O1	C2	C1	127.8(2)	O1A	C2A	C1A	128.6(2)
O1	C2	C3	128.02(19)	O1A	C2A	C3A	128.0(2)
C4	C3	C2	131.2(2)	C4A	C3A	C2A	130.6(2)
C8	C3	C2	108.39(18)	C4A	C3A	C8A	120.89(19)
C8	C3	C4	120.4(2)	C8A	C3A	C2A	108.48(18)
C5	C4	C3	118.5(2)	C5A	C4A	C3A	118.2(2)
C6	C5	C4	120.4(2)	C4A	C5A	C6A	120.4(2)
C5	C6	C7	122.0(2)	C7A	C6A	C5A	122.3(2)
C6	C7	C8	117.1(2)	C6A	C7A	C8A	116.5(2)
C3	C8	C7	121.5(2)	C3A	C8A	C7A	121.7(2)
N1	C8	C3	109.64(19)	C3A	C8A	N1A	110.01(18)
N1	C8	C7	128.9(2)	N1A	C8A	C7A	128.3(2)
N1	C9	C9A	109.55(17)	N1A	C9A	C9	109.55(16)
C1	N1	C8	109.84(17)	C1A	N1A	C8A	109.89(17)
C1	N1	C9	121.76(17)	C1A	N1A	C9A	121.62(17)
C8	N1	C9	125.98(18)	C8A	N1A	C9A	125.73(17)

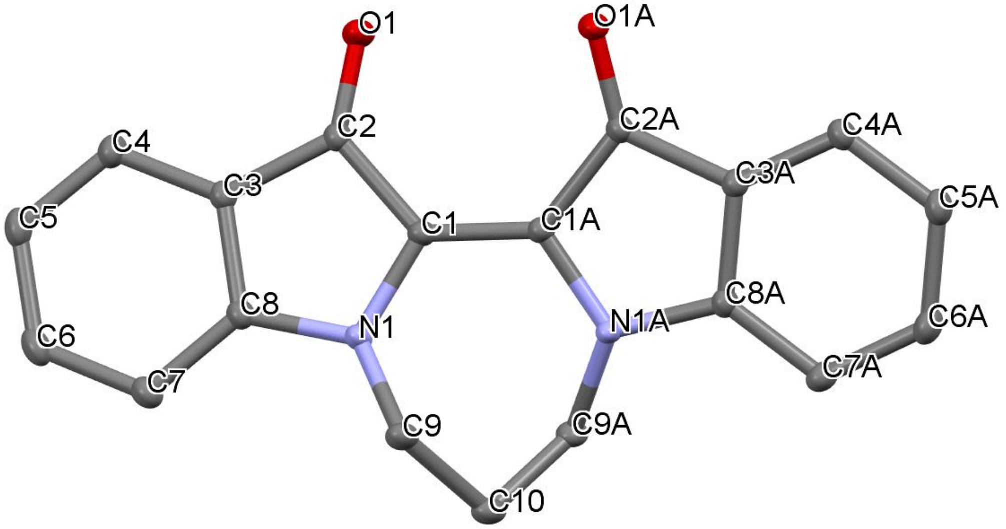

Appendix F-10 X-ray structure of **2.6**. Hydrogen atoms are omitted for clarity. Thermal ellipsoids represented at 50%.

Appendix F-11 Table of bond lengths (Å) for **2.6**

Atom	**Atom**	**Length/Å**	**Atom**	**Atom**	**Length/Å**
C1	C2	1.5033(13)	C10	C9A	1.5270(14)
C1	N1	1.3967(12)	C1A	C2A	1.5045(13)
C1	C1A	1.3719(13)	C1A	N1A	1.3960(12)
C2	C3	1.4699(13)	C2A	C3A	1.4704(13)
C2	O1	1.2273(12)	C2A	O1A	1.2259(12)
C3	C4	1.3923(13)	C3A	C4A	1.3905(13)
C3	C8	1.3995(13)	C3A	C8A	1.4007(13)
C4	C5	1.3879(14)	C4A	C5A	1.3885(13)
C5	C6	1.3976(15)	C5A	C6A	1.3993(15)
C6	C7	1.3945(14)	C6A	C7A	1.3928(14)
C7	C8	1.3967(13)	C7A	C8A	1.3970(13)
C8	N1	1.3931(12)	C8A	N1A	1.3917(12)
C9	C10	1.5275(14)	C9A	N1A	1.4668(12)
C9	N1	1.4683(12)			

Appendix F-12 Table of bond angles (°) for **2.6**

Atom	**Atom**	**Atom**	**Angle/°**	**Atom**	**Atom**	**Atom**	**Angle/°**
N1	C1	C2	107.91(8)	C1	C1A	C2A	129.45(9)
C1A	C1	C2	129.52(9)	C1	C1A	N1A	122.26(9)
C1A	C1	N1	122.37(9)	N1A	C1A	C2A	107.86(8)
C3	C2	C1	104.06(8)	C3A	C2A	C1A	103.97(8)
O1	C2	C1	128.30(9)	O1A	C2A	C1A	128.45(9)
O1	C2	C3	127.56(9)	O1A	C2A	C3A	127.50(9)
C4	C3	C2	130.71(9)	C4A	C3A	C2A	130.56(9)
C4	C3	C8	121.05(9)	C4A	C3A	C8A	121.10(9)
C8	C3	C2	108.25(8)	C8A	C3A	C2A	108.34(8)
C5	C4	C3	118.45(9)	C5A	C4A	C3A	118.43(9)
C4	C5	C6	120.14(9)	C4A	C5A	C6A	120.15(9)
C7	C6	C5	122.24(10)	C7A	C6A	C5A	122.18(9)
C6	C7	C8	117.03(9)	C6A	C7A	C8A	117.10(9)
C7	C8	C3	121.08(9)	C7A	C8A	C3A	121.01(9)
N1	C8	C3	110.34(8)	N1A	C8A	C3A	110.17(8)
N1	C8	C7	128.57(9)	N1A	C8A	C7A	128.81(9)
N1	C9	C10	112.22(9)	N1A	C9A	C10	112.16(9)
C9A	C10	C9	110.54(8)	C1A	N1A	C9A	121.39(8)
C1	N1	C9	121.06(8)	C8A	N1A	C1A	109.63(8)
C8	N1	C1	109.42(8)	C8A	N1A	C9A	124.63(8)
C8	N1	C9	123.76(8)				

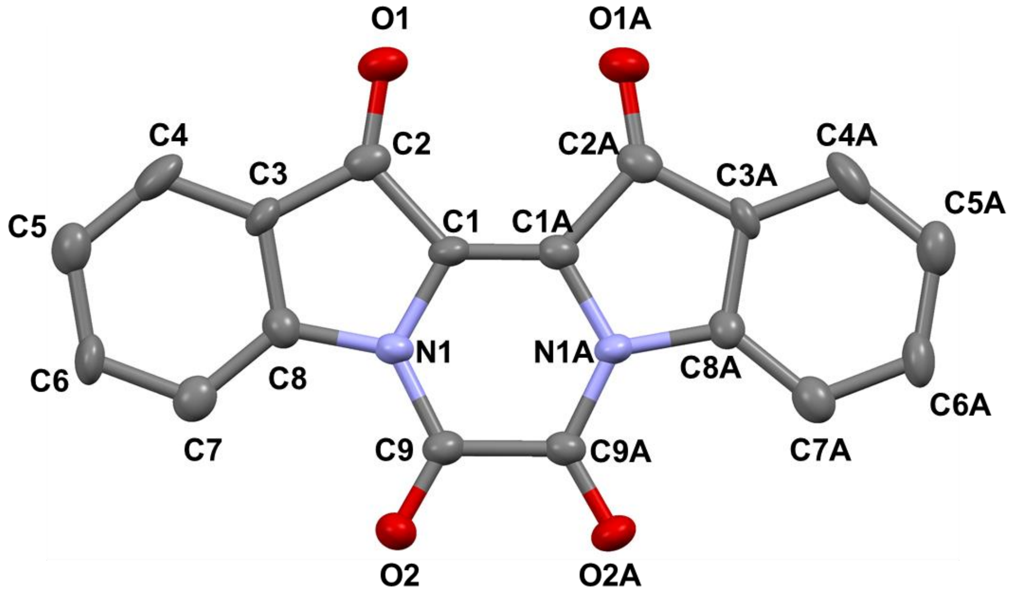

Appendix F-13 X-ray structure of **2.7**. Hydrogen atoms are omitted for clarity. Thermal ellipsoids represented at 50%.

Appendix F-14 Table of bond lengths (Å) for **2.7**

Atom	Atom	Length/Å	Atom	Atom	Length/Å
C1	C2	1.501(6)	C9	C9A	1.510(6)
C1	N1	1.383(7)	C1A	C2A	1.501(6)
C1	C1A	1.351(7)	C1A	N1A	1.392(6)
C2	C3	1.465(6)	C2A	C3A	1.458(6)
C2	O1	1.231(12)	C2A	O1A	1.224(13)
C8	C7	1.3900	C4A	C5A	1.3900
C8	C3	1.3900	C4A	C3A	1.3900
C8	N1	1.419(6)	C5A	C6A	1.3900
C7	C6	1.3900	C6A	C7A	1.3900
C6	C5	1.3900	C7A	C8A	1.3900
C5	C4	1.3900	C8A	C3A	1.3900
C4	C3	1.3900	C8A	N1A	1.417(6)
C9	N1	1.377(6)	C9A	N1A	1.376(6)
C9	O2	1.210(16)	C9A	O2A	1.200(15)

Appendix F-15 Table of bond angles (°) for **2.7**

Atom	Atom	Atom	Angle/°	Atom	Atom	Atom	Angle/°
N1	C1	C2	107.7(4)	C1	C1A	C2A	133.0(6)
C1A	C1	C2	132.1(6)	C1	C1A	N1A	119.2(7)
C1A	C1	N1	120.2(7)	N1A	C1A	C2A	107.8(4)
C3	C2	C1	104.3(4)	C3A	C2A	C1A	104.9(4)
O1	C2	C1	128.6(9)	O1A	C2A	C1A	128.2(11)
O1	C2	C3	127.1(9)	O1A	C2A	C3A	126.9(11)
C7	C8	C3	120.0	C5A	C4A	C3A	120.0
C7	C8	N1	131.0(5)	C6A	C5A	C4A	120.0
C3	C8	N1	109.0(5)	C5A	C6A	C7A	120.0
C8	C7	C6	120.0	C8A	C7A	C6A	120.0
C5	C6	C7	120.0	C7A	C8A	C3A	120.0
C6	C5	C4	120.0	C7A	C8A	N1A	129.7(5)
C3	C4	C5	120.0	C3A	C8A	N1A	110.3(5)
C8	C3	C2	109.0(5)	C4A	C3A	C2A	131.7(5)
C4	C3	C2	131.0(5)	C8A	C3A	C2A	108.2(5)
C4	C3	C8	120.0	C8A	C3A	C4A	120.0
N1	C9	C9A	115.9(4)	N1A	C9A	C9	116.5(4)
O2	C9	N1	124.0(9)	O2A	C9A	C9	119.8(7)
O2	C9	C9A	120.1(8)	O2A	C9A	N1A	123.7(7)
C1	N1	C8	109.9(4)	C1A	N1A	C8A	108.7(4)
C9	N1	C1	124.1(5)	C9A	N1A	C1A	124.0(5)
C9	N1	C8	126.0(5)	C9A	N1A	C8A	127.3(5)

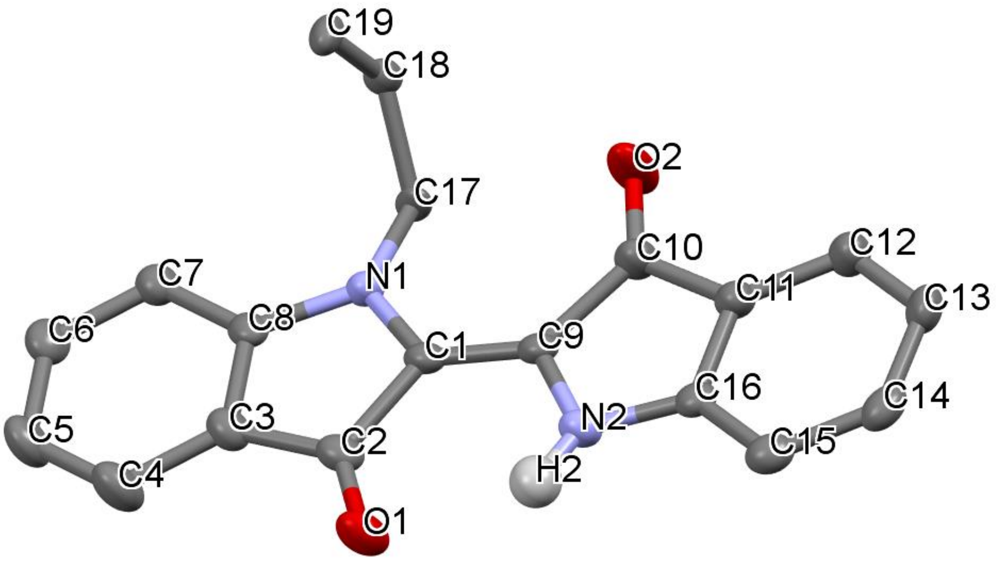

Appendix F-16 X-ray structure of **2.8**. Hydrogen atoms except -N<u>H</u> are omitted for clarity. Thermal ellipsoids represented at 50%.

Appendix F-17 Table of bond lengths (Å) for **2.8**

Atom	**Atom**	**Length/Å**	**Atom**	**Atom**	**Length/Å**
C1	C2	1.491(4)	C10	O2	1.214(3)
C1	C9	1.369(4)	C11	C12	1.381(4)
C1	N1	1.380(3)	C11	C16	1.393(3)
C2	C3	1.451(4)	C12	C13	1.376(4)
C2	O1	1.230(3)	C13	C14	1.395(4)
C3	C4	1.387(4)	C14	C15	1.375(4)
C3	C8	1.393(4)	C15	C16	1.389(4)
C4	C5	1.374(4)	C16	N2	1.377(3)
C5	C6	1.389(4)	C17	C18	1.475(12)
C6	C7	1.375(4)	C17	N1	1.484(9)
C7	C8	1.385(4)	C18	C19	1.309(8)
C8	N1	1.385(3)	N1	C17A	1.38(4)
C9	C10	1.496(4)	C17A	C18A	1.52(4)
C9	N2	1.378(3)	C18A	C19A	1.29(2)
C10	C11	1.457(4)			

Appendix F-18 Table of bond angles (°) for **2.8**

Atom	**Atom**	**Atom**	**Angle/°**	**Atom**	**Atom**	**Atom**	**Angle/°**
C9	C1	C2	121.1(2)	O2	C10	C11	127.1(3)
C9	C1	N1	131.3(2)	C12	C11	C10	131.0(2)
N1	C1	C2	107.5(2)	C12	C11	C16	121.1(3)
C3	C2	C1	105.1(2)	C16	C11	C10	107.9(2)
O1	C2	C1	126.2(3)	C13	C12	C11	118.7(3)
O1	C2	C3	128.7(2)	C12	C13	C14	119.9(3)
C4	C3	C2	131.8(3)	C15	C14	C13	122.1(3)
C4	C3	C8	121.0(3)	C14	C15	C16	117.6(2)
C8	C3	C2	107.2(2)	C15	C16	C11	120.5(2)
C5	C4	C3	118.2(3)	N2	C16	C11	109.5(2)
C4	C5	C6	120.4(3)	N2	C16	C15	129.9(2)
C7	C6	C5	122.2(3)	C18	C17	N1	114.5(9)
C6	C7	C8	117.4(2)	C19	C18	C17	125.4(6)
C7	C8	C3	120.8(2)	C1	N1	C8	109.3(2)
C7	C8	N1	128.4(2)	C1	N1	C17	129.6(5)
N1	C8	C3	110.8(2)	C8	N1	C17	119.4(5)
C1	C9	C10	131.6(2)	C17A	N1	C1	130.2(18)
C1	C9	N2	121.8(2)	C17A	N1	C8	120.5(18)
N2	C9	C10	106.6(2)	C16	N2	C9	111.1(2)
C11	C10	C9	104.8(2)	N1	C17A	C18A	114(2)
O2	C10	C9	128.0(3)	C19A	C18A	C17A	124(2)

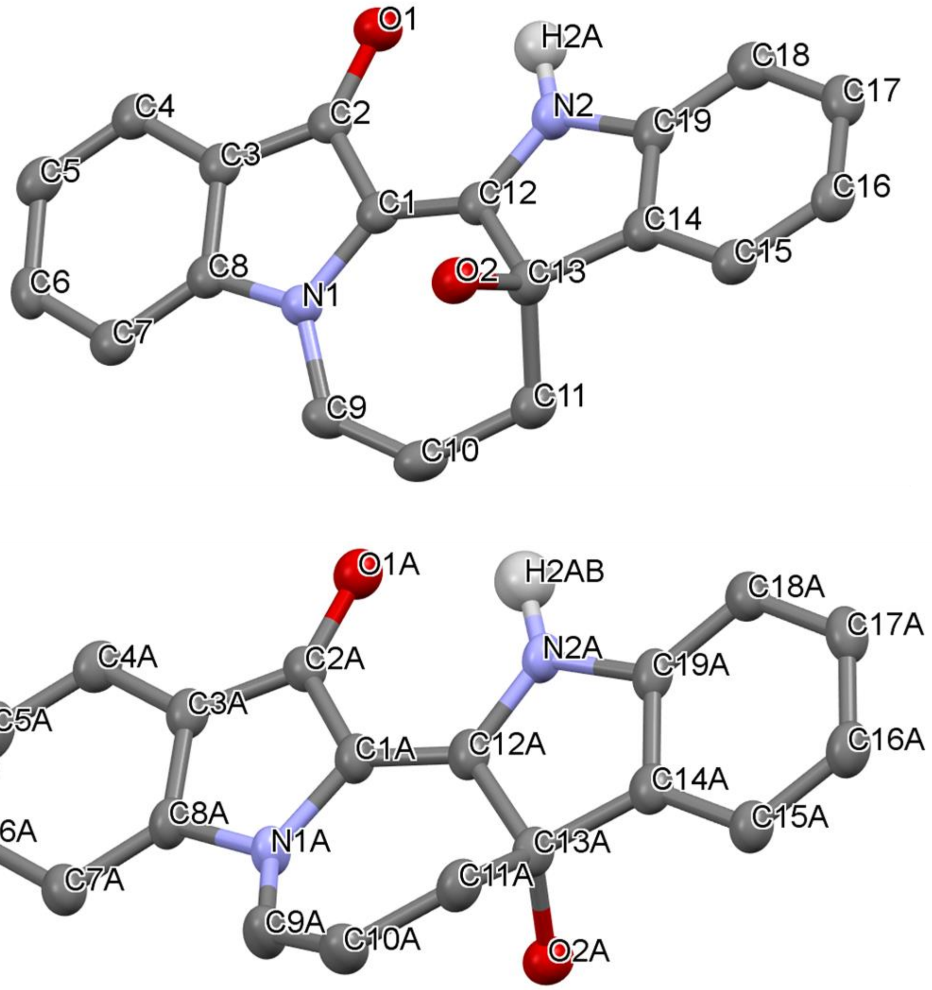

Appendix F-19 X-ray structure of **2.9**. A single crystal consists of two enantiomeric forms and both structures are shown here. Hydrogen atoms except -N<u>H</u> are omitted for clarity. Thermal ellipsoids represented at 50%.

Appendix F-20 Table of bond lengths (Å) for **2.9**

Atom	**Atom**	**Length/Å**	**Atom**	**Atom**	**Length/Å**
O1	C2	1.261(4)	O1A	C2A	1.260(4)
O2	C13	1.447(4)	O2A	C13A	1.435(4)
N1	C1	1.414(4)	N1A	C1A	1.406(4)
N1	C8	1.403(4)	N1A	C8A	1.410(4)
N1	C9	1.406(4)	N1A	C9A	1.407(4)
N2	C12	1.360(4)	N2A	C12A	1.355(4)
N2	C19	1.406(4)	N2A	C19A	1.420(4)

C1	C2	1.452(4)	C1A	C2A	1.451(4)
C1	C12	1.369(4)	C1A	C12A	1.367(4)
C2	C3	1.448(5)	C2A	C3A	1.448(5)
C3	C4	1.407(4)	C3A	C4A	1.406(4)
C3	C8	1.404(4)	C3A	C8A	1.406(4)
C4	C5	1.385(5)	C4A	C5A	1.381(5)
C5	C6	1.396(5)	C5A	C6A	1.393(5)
C6	C7	1.397(4)	C6A	C7A	1.399(4)
C7	C8	1.399(5)	C7A	C8A	1.394(5)
C9	C10	1.335(4)	C9A	C10A	1.343(4)
C10	C11	1.515(5)	C10A	C11A	1.500(5)
C11	C13	1.516(4)	C11A	C13A	1.530(4)
C12	C13	1.543(4)	C12A	C13A	1.541(4)
C13	C14	1.515(5)	C13A	C14A	1.518(5)
C14	C15	1.386(4)	C14A	C15A	1.388(4)
C14	C19	1.391(4)	C14A	C19A	1.397(4)
C15	C16	1.389(5)	C15A	C16A	1.384(5)
C16	C17	1.394(5)	C16A	C17A	1.394(5)
C17	C18	1.399(4)	C17A	C18A	1.400(4)
C18	C19	1.392(5)	C18A	C19A	1.379(5)

Appendix F-21 Table of bond angles (°) for **2.9**

Atom	**Atom**	**Atom**	**Angle/°**	**Atom**	**Atom**	**Atom**	**Angle/°**
C8	N1	C1	107.3(2)	C1A	N1A	C8A	107.6(2)
C8	N1	C9	123.0(3)	C1A	N1A	C9A	126.7(3)
C9	N1	C1	127.0(3)	C9A	N1A	C8A	122.0(3)
C12	N2	C19	111.3(3)	C12A	N2A	C19A	111.2(2)
N1	C1	C2	109.0(3)	N1A	C1A	C2A	109.1(3)
C12	C1	N1	126.5(3)	C12A	C1A	N1A	126.4(3)
C12	C1	C2	124.3(3)	C12A	C1A	C2A	124.4(3)
O1	C2	C1	124.6(3)	O1A	C2A	C1A	124.4(3)
O1	C2	C3	129.9(3)	O1A	C2A	C3A	129.9(3)
C3	C2	C1	105.5(3)	C3A	C2A	C1A	105.7(3)
C4	C3	C2	131.5(3)	C4A	C3A	C2A	131.9(3)
C8	C3	C2	107.9(3)	C8A	C3A	C2A	107.9(3)
C8	C3	C4	120.5(3)	C8A	C3A	C4A	120.2(3)
C5	C4	C3	118.4(3)	C5A	C4A	C3A	118.5(3)
C4	C5	C6	120.7(3)	C4A	C5A	C6A	120.8(3)
C5	C6	C7	121.9(3)	C5A	C6A	C7A	121.9(3)
C6	C7	C8	117.4(3)	C8A	C7A	C6A	117.2(3)

N1	C8	C3	110.1(3)	C3A	C8A	N1A	109.7(3)
C7	C8	N1	128.7(3)	C7A	C8A	N1A	128.8(3)
C7	C8	C3	121.1(3)	C7A	C8A	C3A	121.4(3)
C10	C9	N1	129.6(3)	C10A	C9A	N1A	129.2(3)
C9	C10	C11	131.3(3)	C9A	C10A	C11A	130.4(3)
C10	C11	C13	116.0(3)	C10A	C11A	C13A	114.1(3)
N2	C12	C1	122.5(3)	N2A	C12A	C1A	122.8(3)
N2	C12	C13	108.7(3)	N2A	C12A	C13A	109.7(3)
C1	C12	C13	128.8(3)	C1A	C12A	C13A	127.4(3)
O2	C13	C11	106.3(3)	O2A	C13A	C11A	106.2(3)
O2	C13	C12	109.6(2)	O2A	C13A	C12A	111.6(2)
O2	C13	C14	113.8(3)	O2A	C13A	C14A	113.2(2)
C11	C13	C12	112.5(2)	C11A	C13A	C12A	110.8(2)
C14	C13	C11	113.6(3)	C14A	C13A	C11A	114.7(3)
C14	C13	C12	101.1(3)	C14A	C13A	C12A	100.5(3)
C15	C14	C13	131.2(3)	C15A	C14A	C13A	131.0(3)
C15	C14	C19	119.4(3)	C15A	C14A	C19A	118.8(3)
C19	C14	C13	109.4(3)	C19A	C14A	C13A	110.2(3)
C14	C15	C16	118.8(3)	C16A	C15A	C14A	118.9(3)
C15	C16	C17	121.4(3)	C15A	C16A	C17A	121.6(3)
C16	C17	C18	120.5(3)	C16A	C17A	C18A	120.1(3)
C19	C18	C17	116.9(3)	C19A	C18A	C17A	117.3(3)
C14	C19	N2	109.3(3)	C14A	C19A	N2A	108.4(3)
C14	C19	C18	122.9(3)	C18A	C19A	N2A	128.4(3)
C18	C19	N2	127.7(3)	C18A	C19A	C14A	123.2(3)

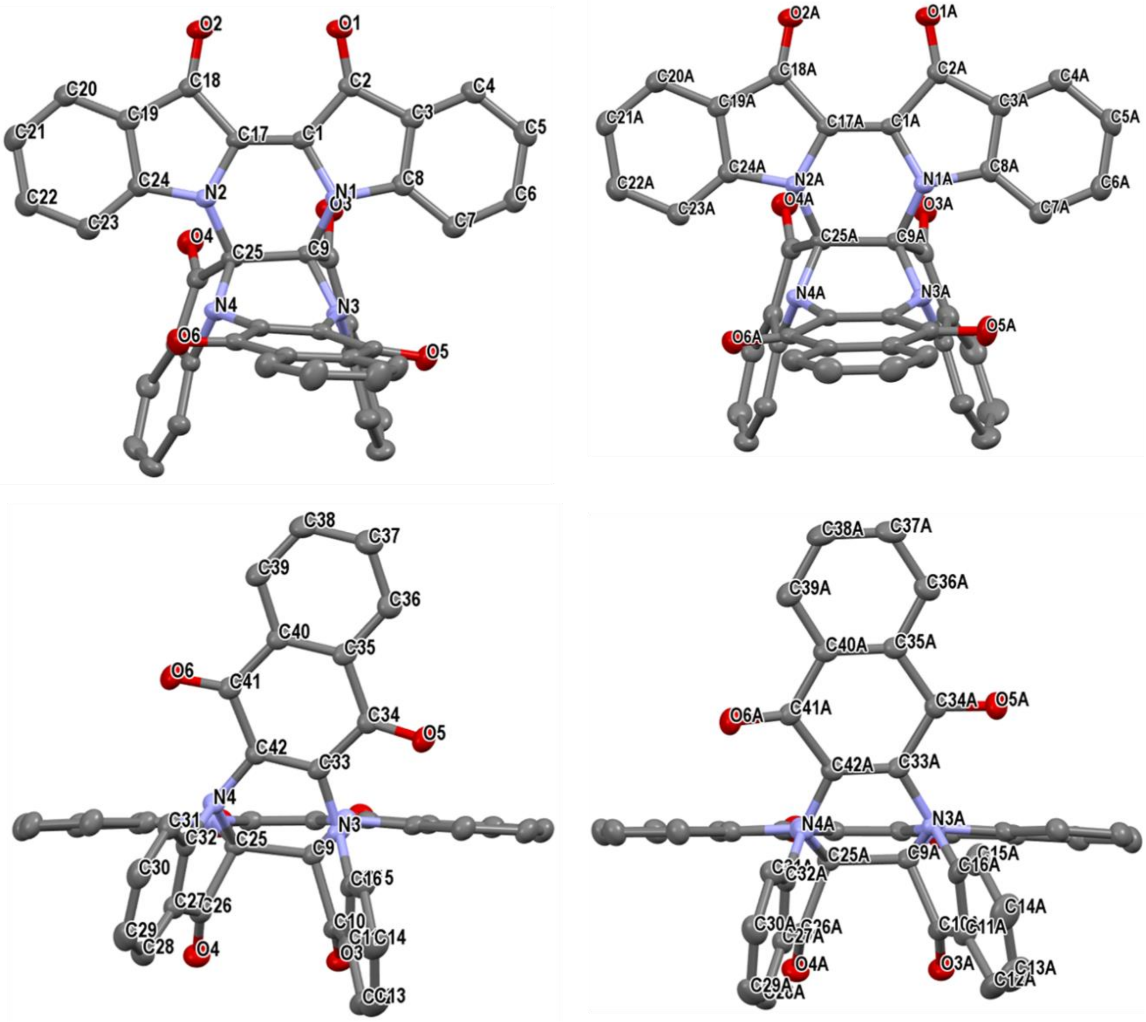

Appendix F-22 X-ray structure of **3.2(A)** (left) and **3.2(B)** (right). Top: front view. Bottom: rotated view. A single crystal consists of two crystallographically different molecules **(A)** and **(B)** and both geometries are shown here. Hydrogen atoms except -N<u>H</u> are omitted for clarity. Thermal ellipsoids represented at 50%.

Appendix F-23 Table of bond lengths (Å) for **3.2**

Atom	**Atom**	**Length/Å**	**Atom**	**Atom**	**Length/Å**
C1	C2	1.490(2)	C10A	O3A	1.2128(18)
C1	C17	1.351(2)	C11A	C12A	1.397(2)
C1	N1	1.4067(18)	C11A	C16A	1.395(2)
C2	C3	1.467(2)	C12A	C13A	1.383(3)
C2	O1	1.2219(17)	C13A	C14A	1.395(3)

C3	C4	1.396(2)	C14A	C15A	1.388(3)
C3	C8	1.399(2)	C15A	C16A	1.395(2)
C4	C5	1.389(2)	C16A	N3A	1.4080(19)
C5	C6	1.404(2)	C17A	C18A	1.492(2)
C6	C7	1.393(2)	C17A	N2A	1.4019(18)
C7	C8	1.394(2)	C18A	C19A	1.465(2)
C8	N1	1.428(2)	C18A	O2A	1.2224(17)
C9	C10	1.576(2)	C19A	C20A	1.395(2)
C9	C25	1.595(2)	C19A	C24A	1.403(2)
C9	N1	1.4653(19)	C20A	C21A	1.389(2)
C9	N3	1.4676(18)	C21A	C22A	1.400(2)
C10	C11	1.459(2)	C22A	C23A	1.392(2)
C10	O3	1.2119(18)	C23A	C24A	1.393(2)
C11	C12	1.399(2)	C24A	N2A	1.426(2)
C11	C16	1.403(2)	C25A	C26A	1.576(2)
C12	C13	1.382(2)	C25A	N2A	1.4626(18)
C13	C14	1.399(3)	C25A	N4A	1.4697(18)
C14	C15	1.388(2)	C26A	C27A	1.463(2)
C15	C16	1.386(2)	C26A	O4A	1.2149(18)
C16	N3	1.4066(19)	C27A	C28A	1.393(2)
C17	C18	1.501(2)	C27A	C32A	1.400(2)
C17	N2	1.4008(18)	C28A	C29A	1.386(2)
C18	C19	1.473(2)	C29A	C30A	1.398(2)
C18	O2	1.2196(18)	C30A	C31A	1.390(2)
C19	C20	1.389(2)	C31A	C32A	1.389(2)
C19	C24	1.401(2)	C32A	N4A	1.4148(19)
C20	C21	1.393(2)	C33A	C34A	1.486(2)
C21	C22	1.397(2)	C33A	C42A	1.338(2)
C22	C23	1.389(2)	C33A	N3A	1.4130(18)
C23	C24	1.392(2)	C34A	C35A	1.483(2)
C24	N2	1.416(2)	C34A	O5A	1.222(2)
C25	C26	1.584(2)	C35A	C36A	1.393(2)
C25	N2	1.4569(19)	C35A	C40A	1.400(2)
C25	N4	1.4897(18)	C36A	C37A	1.388(2)
C26	C27	1.457(2)	C37A	C38A	1.378(3)
C26	O4	1.2112(18)	C38A	C39A	1.393(2)
C27	C28	1.395(2)	C39A	C40A	1.395(2)
C27	C32	1.396(2)	C40A	C41A	1.493(2)
C28	C29	1.378(2)	C41A	C42A	1.487(2)
C29	C30	1.401(3)	C41A	O6A	1.2185(19)
C30	C31	1.393(2)	C42A	N4A	1.4127(18)
C31	C32	1.398(2)	C62	C63	1.404(11)

C32	N4	1.4203(19)	C62	C67	1.416(11)
C33	C34	1.491(2)	C63	C64	1.358(18)
C33	C42	1.335(2)	C64	C65	1.39(2)
C33	N3	1.4135(18)	C65	C66	1.413(18)
C34	C35	1.485(2)	C66	C67	1.409(10)
C34	O5	1.2202(19)	C67	C68	1.470(13)
C35	C36	1.392(2)	C43	C44	1.371(3)
C35	C40	1.405(2)	C43	C48	1.372(3)
C36	C37	1.390(2)	C44	C45	1.380(3)
C37	C38	1.382(3)	C45	C46	1.400(3)
C38	C39	1.392(2)	C46	C47	1.402(3)
C39	C40	1.396(2)	C46	C49	1.503(3)
C40	C41	1.492(2)	C47	C48	1.375(3)
C41	C42	1.492(2)	C61	C60	1.5070
C41	O6	1.221(2)	C55	C56	1.3961
C42	N4	1.4173(19)	C55	C60	1.4025
C1A	C2A	1.504(2)	C56	C57	1.3968
C1A	C17A	1.349(2)	C57	C58	1.3965
C1A	N1A	1.4025(18)	C58	C59	1.3962
C2A	C3A	1.471(2)	C59	C60	1.4023
C2A	O1A	1.2204(18)	C69	C70	1.377(13)
C3A	C4A	1.395(2)	C69	C74	1.359(12)
C3A	C8A	1.396(2)	C70	C71	1.385(18)
C4A	C5A	1.389(2)	C71	C72	1.35(3)
C5A	C6A	1.399(2)	C72	C73	1.35(2)
C6A	C7A	1.394(2)	C73	C74	1.385(11)
C7A	C8A	1.390(2)	C74	C75	1.537(15)
C8A	N1A	1.426(2)	C50	C51	1.386(3)
C9A	C10A	1.577(2)	C50	C51^1	1.386(3)
C9A	C25A	1.603(2)	C51	C52	1.377(3)
C9A	N1A	1.4638(18)	C52	C53	1.400(2)
C9A	N3A	1.4721(18)	C53	C52^1	1.400(2)
C10A	C11A	1.460(2)	C53	C54	1.506(4)

Appendix F-24 Table of bond angles (°) for **3.2**

Atom	**Atom**	**Atom**	**Angle/°**	**Atom**	**Atom**	**Atom**	**Angle/°**
C17	C1	C2	131.78(14)	N1A	C9A	N3A	109.84(12)
C17	C1	N1	119.51(13)	N3A	C9A	C10A	102.17(12)
N1	C1	C2	108.70(13)	N3A	C9A	C25A	110.61(12)
C3	C2	C1	104.38(12)	C11A	C10A	C9A	106.49(12)

O1	C2	C1	127.88(15)	O3A	C10A	C9A	122.36(14)
O1	C2	C3	127.74(14)	O3A	C10A	C11A	131.04(15)
C4	C3	C2	129.53(14)	C12A	C11A	C10A	130.85(16)
C4	C3	C8	121.52(15)	C16A	C11A	C10A	108.09(13)
C8	C3	C2	108.95(14)	C16A	C11A	C12A	121.05(16)
C5	C4	C3	118.34(14)	C13A	C12A	C11A	117.97(17)
C4	C5	C6	119.56(16)	C12A	C13A	C14A	120.39(17)
C7	C6	C5	122.75(16)	C15A	C14A	C13A	122.51(18)
C6	C7	C8	117.04(15)	C14A	C15A	C16A	116.72(17)
C3	C8	N1	109.55(13)	C11A	C16A	C15A	121.28(15)
C7	C8	C3	120.79(15)	C11A	C16A	N3A	111.78(13)
C7	C8	N1	129.59(14)	C15A	C16A	N3A	126.93(15)
C10	C9	C25	112.78(12)	C1A	C17A	C18A	131.67(14)
N1	C9	C10	109.90(12)	C1A	C17A	N2A	119.77(13)
N1	C9	C25	112.56(12)	N2A	C17A	C18A	108.51(13)
N1	C9	N3	109.83(12)	C19A	C18A	C17A	104.61(12)
N3	C9	C10	101.81(12)	O2A	C18A	C17A	127.17(15)
N3	C9	C25	109.41(11)	O2A	C18A	C19A	128.21(15)
C11	C10	C9	105.67(12)	C20A	C19A	C18A	129.82(14)
O3	C10	C9	122.96(14)	C20A	C19A	C24A	121.44(15)
O3	C10	C11	131.18(15)	C24A	C19A	C18A	108.73(14)
C12	C11	C10	131.23(15)	C21A	C20A	C19A	117.93(15)
C12	C11	C16	120.50(15)	C20A	C21A	C22A	120.26(16)
C16	C11	C10	108.26(13)	C23A	C22A	C21A	122.32(16)
C13	C12	C11	118.27(16)	C22A	C23A	C24A	117.19(15)
C12	C13	C14	120.28(16)	C19A	C24A	N2A	109.46(13)
C15	C14	C13	122.37(16)	C23A	C24A	C19A	120.86(15)
C16	C15	C14	116.98(16)	C23A	C24A	N2A	129.64(14)
C11	C16	N3	110.90(13)	C26A	C25A	C9A	111.88(12)
C15	C16	C11	121.57(15)	N2A	C25A	C9A	112.40(12)
C15	C16	N3	127.53(14)	N2A	C25A	C26A	109.71(12)
C1	C17	C18	131.89(14)	N2A	C25A	N4A	110.09(12)
C1	C17	N2	119.64(13)	N4A	C25A	C9A	110.34(11)
N2	C17	C18	108.47(13)	N4A	C25A	C26A	101.94(11)
C19	C18	C17	104.16(13)	C27A	C26A	C25A	105.90(12)
O2	C18	C17	128.18(15)	O4A	C26A	C25A	122.94(14)
O2	C18	C19	127.66(15)	O4A	C26A	C27A	131.05(15)
C20	C19	C18	130.11(14)	C28A	C27A	C26A	131.16(15)
C20	C19	C24	121.32(15)	C28A	C27A	C32A	120.73(15)
C24	C19	C18	108.57(14)	C32A	C27A	C26A	108.11(13)
C19	C20	C21	118.21(15)	C29A	C28A	C27A	118.34(15)
C20	C21	C22	120.14(16)	C28A	C29A	C30A	120.19(15)

C23	C22	C21	121.98(16)	C31A	C30A	C29A	122.28(15)
C22	C23	C24	117.71(15)	C32A	C31A	C30A	116.97(15)
C19	C24	N2	110.00(13)	C27A	C32A	N4A	111.14(13)
C23	C24	C19	120.60(15)	C31A	C32A	C27A	121.45(14)
C23	C24	N2	129.37(14)	C31A	C32A	N4A	127.40(14)
C26	C25	C9	111.03(12)	C42A	C33A	C34A	122.55(14)
N2	C25	C9	112.44(12)	C42A	C33A	N3A	117.47(13)
N2	C25	C26	108.67(12)	N3A	C33A	C34A	119.87(14)
N2	C25	N4	110.51(12)	C35A	C34A	C33A	115.90(14)
N4	C25	C9	111.16(12)	O5A	C34A	C33A	120.89(14)
N4	C25	C26	102.58(11)	O5A	C34A	C35A	123.20(14)
C27	C26	C25	106.44(12)	C36A	C35A	C34A	118.39(15)
O4	C26	C25	122.67(14)	C36A	C35A	C40A	119.92(15)
O4	C26	C27	130.85(15)	C40A	C35A	C34A	121.66(14)
C28	C27	C26	130.24(15)	C37A	C36A	C35A	120.10(16)
C28	C27	C32	121.41(15)	C38A	C37A	C36A	120.15(16)
C32	C27	C26	108.35(13)	C37A	C38A	C39A	120.40(16)
C29	C28	C27	118.02(16)	C38A	C39A	C40A	119.96(17)
C28	C29	C30	120.55(16)	C35A	C40A	C41A	121.14(14)
C31	C30	C29	122.18(15)	C39A	C40A	C35A	119.46(15)
C30	C31	C32	116.83(15)	C39A	C40A	C41A	119.39(15)
C27	C32	C31	120.93(14)	C42A	C41A	C40A	115.42(14)
C27	C32	N4	112.38(13)	O6A	C41A	C40A	124.02(14)
C31	C32	N4	126.68(14)	O6A	C41A	C42A	120.53(14)
C42	C33	C34	123.07(14)	C33A	C42A	C41A	123.09(14)
C42	C33	N3	117.09(14)	C33A	C42A	N4A	117.09(13)
N3	C33	C34	119.69(14)	N4A	C42A	C41A	119.80(14)
C35	C34	C33	115.75(14)	C1A	N1A	C8A	108.30(12)
O5	C34	C33	120.69(14)	C1A	N1A	C9A	120.44(12)
O5	C34	C35	123.53(15)	C8A	N1A	C9A	120.43(12)
C36	C35	C34	118.86(15)	C17A	N2A	C24A	108.51(12)
C36	C35	C40	119.90(15)	C17A	N2A	C25A	119.87(12)
C40	C35	C34	121.24(14)	C24A	N2A	C25A	120.85(12)
C37	C36	C35	120.10(17)	C16A	N3A	C9A	109.47(12)
C38	C37	C36	120.23(17)	C16A	N3A	C33A	121.47(12)
C37	C38	C39	120.28(16)	C33A	N3A	C9A	118.06(12)
C38	C39	C40	120.12(17)	C32A	N4A	C25A	109.10(12)
C35	C40	C41	121.29(14)	C42A	N4A	C25A	117.74(12)
C39	C40	C35	119.36(15)	C42A	N4A	C32A	120.96(12)
C39	C40	C41	119.30(15)	C63	C62	C67	121.0(10)
C40	C41	C42	115.76(14)	C64	C63	C62	120.9(13)
O6	C41	C40	123.44(14)	C63	C64	C65	120.4(15)

O6	C41	C42	120.79(14)	C64	C65	C66	119.6(18)
C33	C42	C41	122.53(14)	C67	C66	C65	121.2(14)
C33	C42	N4	117.64(14)	C62	C67	C68	122.3(7)
N4	C42	C41	119.80(13)	C66	C67	C62	116.8(10)
C1	N1	C8	108.10(12)	C66	C67	C68	120.9(10)
C1	N1	C9	118.42(12)	C44	C43	C48	119.29(18)
C8	N1	C9	120.23(12)	C43	C44	C45	120.99(18)
C17	N2	C24	108.77(12)	C44	C45	C46	120.45(18)
C17	N2	C25	122.58(13)	C45	C46	C47	117.66(17)
C24	N2	C25	121.94(12)	C45	C46	C49	122.1(2)
C16	N3	C9	109.44(12)	C47	C46	C49	120.3(2)
C16	N3	C33	125.38(12)	C48	C47	C46	120.63(18)
C33	N3	C9	116.99(12)	C43	C48	C47	120.97(19)
C32	N4	C25	108.10(12)	C56	C55	C60	121.1
C42	N4	C25	118.19(12)	C55	C56	C57	120.1
C42	N4	C32	116.64(12)	C58	C57	C56	119.4
C17A	C1A	C2A	132.12(14)	C59	C58	C57	120.1
C17A	C1A	N1A	119.07(13)	C58	C59	C60	121.1
N1A	C1A	C2A	108.80(13)	C55	C60	C61	121.0
C3A	C2A	C1A	103.79(13)	C59	C60	C61	120.9
O1A	C2A	C1A	128.05(15)	C59	C60	C55	118.1
O1A	C2A	C3A	128.16(15)	C74	C69	C70	121.1(12)
C4A	C3A	C2A	129.29(14)	C69	C70	C71	119.4(12)
C4A	C3A	C8A	121.57(15)	C72	C71	C70	119.6(17)
C8A	C3A	C2A	109.14(14)	C71	C72	C73	120(2)
C5A	C4A	C3A	117.67(15)	C72	C73	C74	121.7(19)
C4A	C5A	C6A	120.66(16)	C69	C74	C73	117.7(13)
C7A	C6A	C5A	121.65(16)	C69	C74	C75	122.2(12)
C8A	C7A	C6A	117.57(14)	C73	C74	C75	120.1(12)
C3A	C8A	N1A	109.86(13)	C51	C50	C51^{1}	119.7(3)
C7A	C8A	C3A	120.79(15)	C52	C51	C50	120.2(2)
C7A	C8A	N1A	129.29(14)	C51	C52	C53	121.09(19)
C10A	C9A	C25A	112.12(12)	C52	C53	C52^{1}	117.8(3)
N1A	C9A	C10A	108.87(12)	C52^{1}	C53	C54	121.11(13)
N1A	C9A	C25A	112.71(11)	C52	C53	C54	121.11(13)

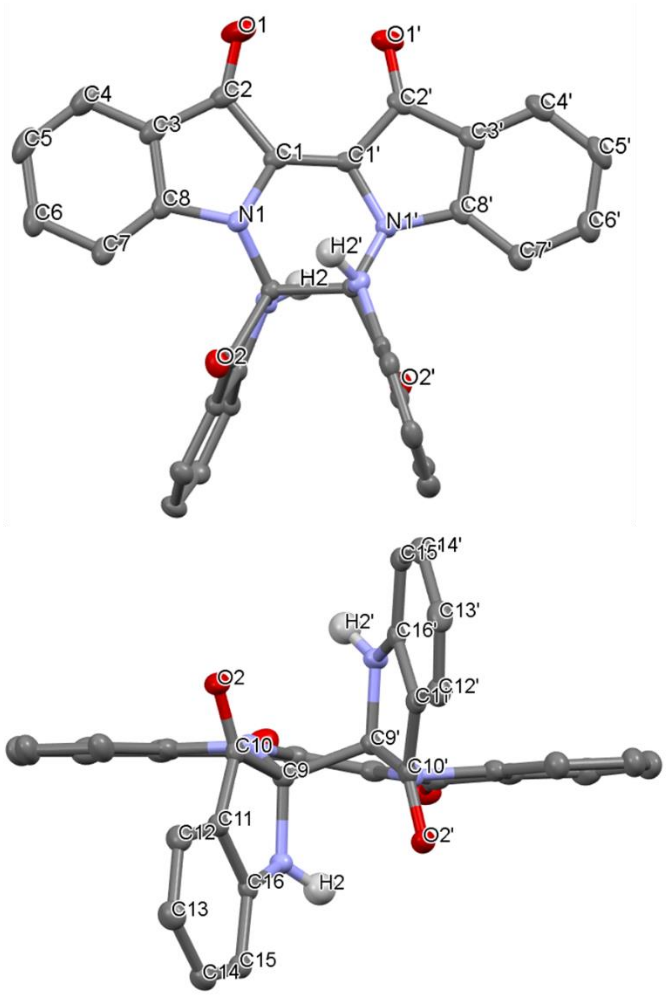

Appendix F-25 X-ray structure of **3.3**. Hydrogen atoms except -N<u>H</u> are omitted for clarity. Thermal ellipsoids represented at 50%.

Appendix F-26 Table of bond lengths (Å) for **3.3**

Atom	Atom	Length/Å	Atom	Atom	Length/Å
O2'	C10'	1.2110(17)	C1	C1'	1.354(2)
O2	C10	1.2140(17)	C1	C2	1.495(2)
O1'	C2'	1.2245(19)	C15	C14	1.376(2)
O1	C2	1.222(2)	C1'	C2'	1.491(2)
N1'	C1'	1.4008(19)	C9	C9'	1.5837(19)
N1'	C9'	1.4521(18)	C8'	C3'	1.398(2)
N1'	C8'	1.4124(18)	C8'	C7'	1.385(2)
N2	C16	1.3881(18)	C14	C13	1.404(2)

N2	C9	1.4520(18)	C3'	C2'	1.456(2)
N1	C1	1.3992(19)	C3'	C4'	1.387(2)
N1	C9	1.4543(18)	C12	C13	1.377(2)
N1	C8	1.4186(18)	C12'	C13'	1.379(2)
N2'	C16'	1.3788(19)	C8	C3	1.396(2)
N2'	C9'	1.4412(18)	C8	C7	1.389(2)
C16	C11	1.398(2)	C15'	C14'	1.379(2)
C16	C15	1.395(2)	C3	C2	1.471(2)
C10'	C11'	1.454(2)	C3	C4	1.389(2)
C10'	C9'	1.573(2)	C13'	C14'	1.409(2)
C11	C10	1.451(2)	C7'	C6'	1.393(2)
C11	C12	1.398(2)	C7	C6	1.397(2)
C16'	C11'	1.402(2)	C6'	C5'	1.394(2)
C16'	C15'	1.395(2)	C4'	C5'	1.379(3)
C10	C9	1.572(2)	C4	C5	1.382(3)
C11'	C12'	1.393(2)	C6	C5	1.389(3)

Appendix F-27 Table of bond angles (°) for **3.3**

Atom	**Atom**	**Atom**	**Angle/°**	**Atom**	**Atom**	**Atom**	**Angle/°**
C1'	N1'	C9'	117.89(11)	N1'	C9'	C10'	113.30(11)
C1'	N1'	C8'	108.35(12)	N1'	C9'	C9	105.78(11)
C8'	N1'	C9'	125.20(12)	N2'	C9'	N1'	112.67(11)
C16	N2	C9	109.48(12)	N2'	C9'	C10'	103.52(11)
C1	N1	C9	116.39(12)	N2'	C9'	C9	113.70(11)
C1	N1	C8	108.33(12)	C10'	C9'	C9	107.97(11)
C8	N1	C9	125.31(12)	C3'	C8'	N1'	109.42(13)
C16'	N2'	C9'	110.31(12)	C7'	C8'	N1'	130.19(14)
N2	C16	C11	112.21(12)	C7'	C8'	C3'	120.38(14)
N2	C16	C15	126.87(13)	C15	C14	C13	122.51(14)
C15	C16	C11	120.89(13)	C8'	C3'	C2'	108.89(13)
O2'	C10'	C11'	130.74(14)	C4'	C3'	C8'	121.49(15)
O2'	C10'	C9'	124.06(13)	C4'	C3'	C2'	129.61(15)
C11'	C10'	C9'	105.20(11)	C13	C12	C11	118.33(14)
C16	C11	C10	108.38(12)	C13'	C12'	C11'	118.42(14)
C12	C11	C16	120.95(13)	C3	C8	N1	109.47(14)
C12	C11	C10	130.66(13)	C7	C8	N1	129.96(15)
N2'	C16'	C11'	111.79(13)	C7	C8	C3	120.53(14)
N2'	C16'	C15'	127.62(13)	O1'	C2'	C1'	127.60(15)
C15'	C16'	C11'	120.57(14)	O1'	C2'	C3'	128.21(14)
O2	C10	C11	130.61(14)	C3'	C2'	C1'	104.17(12)

O2	C10	C9	123.94(13)	C14'	C15'	C16'	117.36(14)
C11	C10	C9	105.44(11)	C8	C3	C2	109.09(13)
C16'	C11'	C10'	108.14(13)	C4	C3	C8	121.39(16)
C12'	C11'	C10'	130.57(14)	C4	C3	C2	129.50(16)
C12'	C11'	C16'	121.29(13)	C12'	C13'	C14'	119.76(14)
N1	C1	C2	108.57(13)	C15'	C14'	C13'	122.50(14)
C1'	C1	N1	120.53(13)	O1	C2	C1	127.75(16)
C1'	C1	C2	130.84(14)	O1	C2	C3	128.69(15)
C14	C15	C16	117.26(13)	C3	C2	C1	103.55(13)
N1'	C1'	C2'	107.95(12)	C12	C13	C14	120.05(14)
C1	C1'	N1'	121.22(13)	C8'	C7'	C6'	117.50(15)
C1	C1'	C2'	130.68(14)	C8	C7	C6	117.26(16)
N2	C9	N1	111.67(11)	C7'	C6'	C5'	122.23(16)
N2	C9	C10	103.92(11)	C5'	C4'	C3'	118.53(16)
N2	C9	C9'	111.90(11)	C5	C4	C3	118.57(17)
N1	C9	C10	112.93(11)	C4'	C5'	C6'	119.85(15)
N1	C9	C9'	106.75(11)	C5	C6	C7	122.37(17)
C10	C9	C9'	109.76(11)	C4	C5	C6	119.85(15)

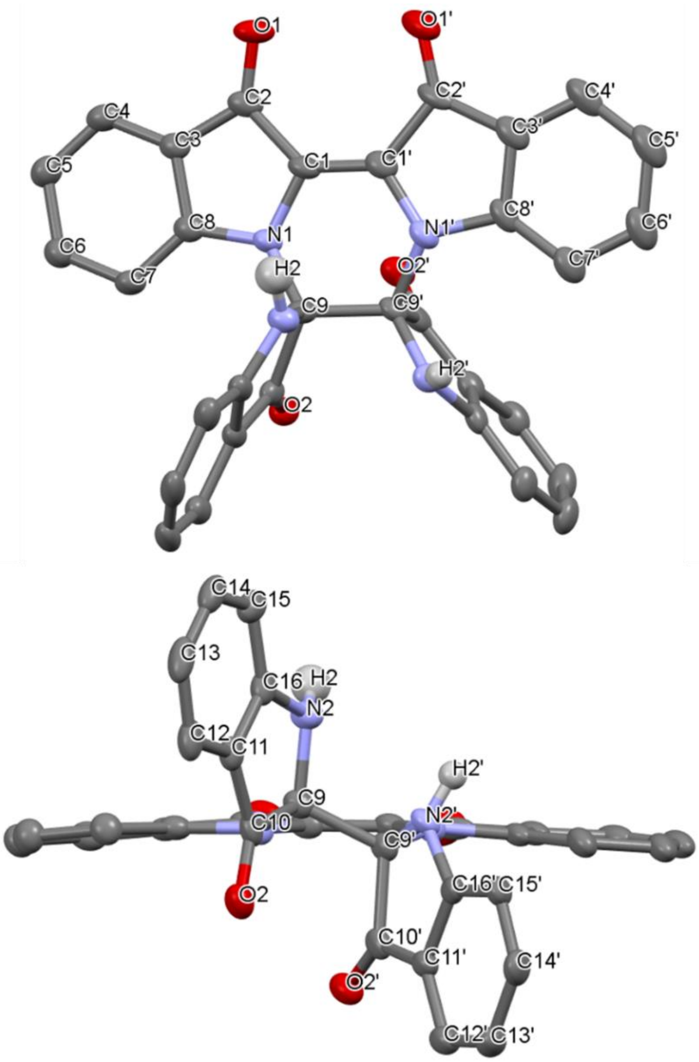

Appendix F-28 X-ray structure of **3.4**. Hydrogen atoms except -N<u>H</u> are omitted for clarity. Thermal ellipsoids represented at 50%.

Appendix F-29 Table of bond lengths (Å) for **3.4**

Atom	**Atom**	**Length/Å**	**Atom**	**Atom**	**Length/Å**
O2	C10	1.216(3)	C11'	C12'	1.390(3)
O2'	C10'	1.216(3)	C3	C2	1.464(3)
O1	C2	1.233(3)	C3	C4	1.371(3)
O1'	C2'	1.224(3)	C16	C15	1.396(3)
N1	C8	1.400(3)	C8'	C3'	1.394(3)
N1	C9	1.446(3)	C8'	C7'	1.388(3)
N1	C1	1.407(3)	C1	C2	1.482(3)

N2	C9	1.452(3)	C1	C1'	1.357(3)
N2	C16	1.383(3)	C16'	C15'	1.386(3)
N2'	C9'	1.433(3)	C7	C6	1.388(3)
N2'	C16'	1.389(3)	C1'	C2'	1.494(3)
N1'	C9'	1.460(3)	C2'	C3'	1.458(4)
N1'	C8'	1.422(3)	C3'	C4'	1.396(3)
N1'	C1'	1.387(3)	C12	C13	1.375(3)
C9'	C9	1.550(3)	C4	C5	1.383(3)
C9'	C10'	1.569(3)	C15'	C14'	1.381(3)
C8	C3	1.407(3)	C12'	C13'	1.374(3)
C8	C7	1.384(3)	C6	C5	1.390(3)
C11	C16	1.393(3)	C15	C14	1.375(3)
C11	C10	1.444(3)	C14'	C13'	1.395(3)
C11	C12	1.397(3)	C14	C13	1.396(4)
C9	C10	1.563(3)	C7'	C6'	1.391(3)
C11'	C16'	1.398(3)	C4'	C5'	1.380(4)
C11'	C10'	1.454(3)	C6'	C5'	1.387(4)

Appendix F-30 Table of bond angles (°) for **3.4**

Atom	**Atom**	**Atom**	**Angle/°**	**Atom**	**Atom**	**Atom**	**Angle/°**
C8	N1	C9	128.39(18)	C1'	C1	N1	119.9(2)
C8	N1	C1	109.48(18)	C1'	C1	C2	132.4(2)
C1	N1	C9	118.43(18)	O1	C2	C3	128.0(2)
C16	N2	C9	109.99(19)	O1	C2	C1	127.0(2)
C16'	N2'	C9'	110.33(18)	C3	C2	C1	104.98(19)
C8'	N1'	C9'	127.53(19)	O2	C10	C11	131.0(2)
C1'	N1'	C9'	119.42(18)	O2	C10	C9	122.5(2)
C1'	N1'	C8'	109.73(18)	C11	C10	C9	106.4(2)
N2'	C9'	N1'	113.20(18)	N2'	C16'	C11'	111.7(2)
N2'	C9'	C9	108.87(17)	C15'	C16'	N2'	127.8(2)
N2'	C9'	C10'	103.83(18)	C15'	C16'	C11'	120.4(2)
N1'	C9'	C9	108.69(18)	C8	C7	C6	117.7(2)
N1'	C9'	C10'	108.85(17)	N1'	C1'	C2'	107.6(2)
C9	C9'	C10'	113.43(17)	C1	C1'	N1'	120.9(2)
N1	C8	C3	109.38(19)	C1	C1'	C2'	131.5(2)
C7	C8	N1	130.2(2)	O1'	C2'	C1'	127.7(2)
C7	C8	C3	120.3(2)	O1'	C2'	C3'	127.5(2)
C16	C11	C10	107.99(19)	C3'	C2'	C1'	104.8(2)
C16	C11	C12	121.2(2)	O2'	C10'	C9'	124.1(2)
C12	C11	C10	130.8(2)	O2'	C10'	C11'	130.2(2)

N1	C9	N2	112.97(18)	C11'	C10'	C9'	105.54(18)
N1	C9	C9'	108.16(17)	C8'	C3'	C2'	109.0(2)
N1	C9	C10	115.31(18)	C8'	C3'	C4'	121.4(2)
N2	C9	C9'	110.85(18)	C4'	C3'	C2'	129.6(2)
N2	C9	C10	103.10(17)	C13	C12	C11	118.4(2)
C9'	C9	C10	106.22(18)	C3	C4	C5	118.7(2)
C16'	C11'	C10'	108.1(2)	C14'	C15'	C16'	117.5(2)
C12'	C11'	C16'	121.0(2)	C13'	C12'	C11'	119.0(2)
C12'	C11'	C10'	131.0(2)	C7	C6	C5	121.8(2)
C8	C3	C2	108.2(2)	C4	C5	C6	120.1(2)
C4	C3	C8	121.2(2)	C14	C15	C16	117.6(2)
C4	C3	C2	130.6(2)	C15'	C14'	C13'	122.6(2)
N2	C16	C11	112.1(2)	C15	C14	C13	122.5(2)
N2	C16	C15	127.6(2)	C12'	C13'	C14'	119.5(2)
C11	C16	C15	120.3(2)	C8'	C7'	C6'	117.2(2)
C3'	C8'	N1'	108.7(2)	C5'	C4'	C3'	117.6(3)
C7'	C8'	N1'	130.4(2)	C5'	C6'	C7'	122.1(3)
C7'	C8'	C3'	120.9(2)	C12	C13	C14	120.0(2)
N1	C1	C2	107.69(19)	C4'	C5'	C6'	120.8(2)

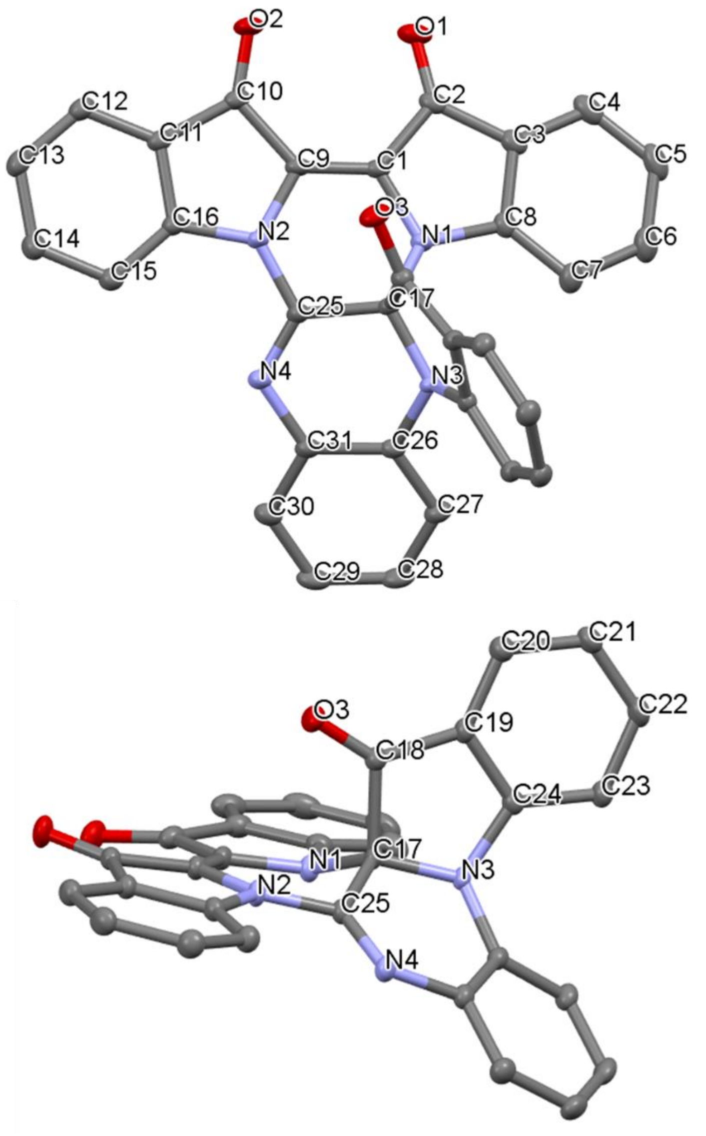

Appendix F-31 X-ray structure of **3.5**. Hydrogen atoms except -N<u>H</u> are omitted for clarity. Thermal ellipsoids represented at 50%.

Appendix F-32 Table of bond lengths (Å) for **3.5**

Atom	**Atom**	**Length/Å**	**Atom**	**Atom**	**Length/Å**
O3	C18	1.2103(14)	C19	C18	1.4574(15)
O2	C10	1.2224(14)	C19	C20	1.3957(17)
O1	C2	1.2199(14)	C25	C17	1.5250(17)
N3	C24	1.4244(15)	C18	C17	1.5740(16)
N3	C26	1.4298(14)	C26	C31	1.4026(17)

N3	C17	1.4542(13)	C26	C27	1.3908(15)
N2	C9	1.4064(14)	C8	C3	1.4044(16)
N2	C16	1.4121(15)	C8	C7	1.3914(17)
N2	C25	1.3843(14)	C31	C30	1.3948(16)
N1	C1	1.4041(14)	C22	C21	1.4017(18)
N1	C8	1.4187(15)	C22	C23	1.3951(18)
N1	C17	1.4811(14)	C15	C14	1.3934(17)
N4	C25	1.2822(15)	C21	C20	1.3884(16)
N4	C31	1.4115(14)	C27	C28	1.3962(17)
C9	C1	1.3519(17)	C2	C3	1.4703(18)
C9	C10	1.4963(16)	C3	C4	1.3918(18)
C24	C19	1.3991(16)	C12	C13	1.3912(19)
C24	C23	1.3963(15)	C14	C13	1.3997(17)
C11	C16	1.4016(15)	C30	C29	1.3901(18)
C11	C10	1.4704(17)	C4	C5	1.390(2)
C11	C12	1.3926(17)	C29	C28	1.383(2)
C16	C15	1.3838(17)	C7	C6	1.3974(19)
C1	C2	1.4980(16)	C5	C6	1.397(2)

Appendix F-33 Table of bond angles (°) for **3.5**

Atom	**Atom**	**Atom**	**Angle/°**	**Atom**	**Atom**	**Atom**	**Angle/°**
C24	N3	C26	117.82(9)	O2	C10	C9	127.79(12)
C24	N3	C17	108.61(9)	O2	C10	C11	127.80(11)
C26	N3	C17	118.39(9)	C11	C10	C9	104.39(9)
C9	N2	C16	109.86(9)	C3	C8	N1	109.30(10)
C25	N2	C9	120.55(10)	C7	C8	N1	129.53(11)
C25	N2	C16	128.75(10)	C7	C8	C3	120.92(12)
C1	N1	C8	108.88(9)	C26	C31	N4	122.30(10)
C1	N1	C17	116.01(9)	C30	C31	N4	117.78(11)
C8	N1	C17	127.00(9)	C30	C31	C26	119.54(11)
C25	N4	C31	117.43(10)	C23	C22	C21	122.45(11)
N2	C9	C10	107.46(10)	C16	C15	C14	116.92(11)
C1	C9	N2	119.79(10)	N3	C17	N1	113.96(9)
C1	C9	C10	132.73(10)	N3	C17	C25	112.61(9)
C19	C24	N3	112.36(9)	N3	C17	C18	104.68(9)
C23	C24	N3	127.75(10)	N1	C17	C25	106.99(9)
C23	C24	C19	119.90(11)	N1	C17	C18	107.90(9)
C16	C11	C10	109.21(10)	C25	C17	C18	110.63(9)
C12	C11	C16	120.38(11)	C20	C21	C22	119.76(11)
C12	C11	C10	130.41(11)	C26	C27	C28	119.59(12)

C11	C16	N2	108.76(10)	C21	C20	C19	118.03(11)
C15	C16	N2	129.13(10)	O1	C2	C1	127.48(12)
C15	C16	C11	122.07(11)	O1	C2	C3	128.32(12)
N1	C1	C2	108.24(10)	C3	C2	C1	104.05(9)
C9	C1	N1	120.69(10)	C22	C23	C24	117.60(11)
C9	C1	C2	131.07(10)	C8	C3	C2	108.98(11)
C24	C19	C18	108.22(10)	C4	C3	C8	121.47(12)
C20	C19	C24	122.24(10)	C4	C3	C2	129.38(11)
C20	C19	C18	129.47(11)	C13	C12	C11	118.26(11)
N2	C25	C17	112.69(9)	C15	C14	C13	121.91(12)
N4	C25	N2	121.28(11)	C29	C30	C31	120.05(12)
N4	C25	C17	126.03(10)	C5	C4	C3	118.14(12)
O3	C18	C19	130.42(11)	C28	C29	C30	120.21(11)
O3	C18	C17	123.52(10)	C12	C13	C14	120.44(12)
C19	C18	C17	106.04(9)	C29	C28	C27	120.37(11)
C31	C26	N3	118.63(10)	C8	C7	C6	116.84(12)
C27	C26	N3	121.26(11)	C4	C5	C6	119.95(12)
C27	C26	C31	120.10(11)	C5	C6	C7	122.67(13)

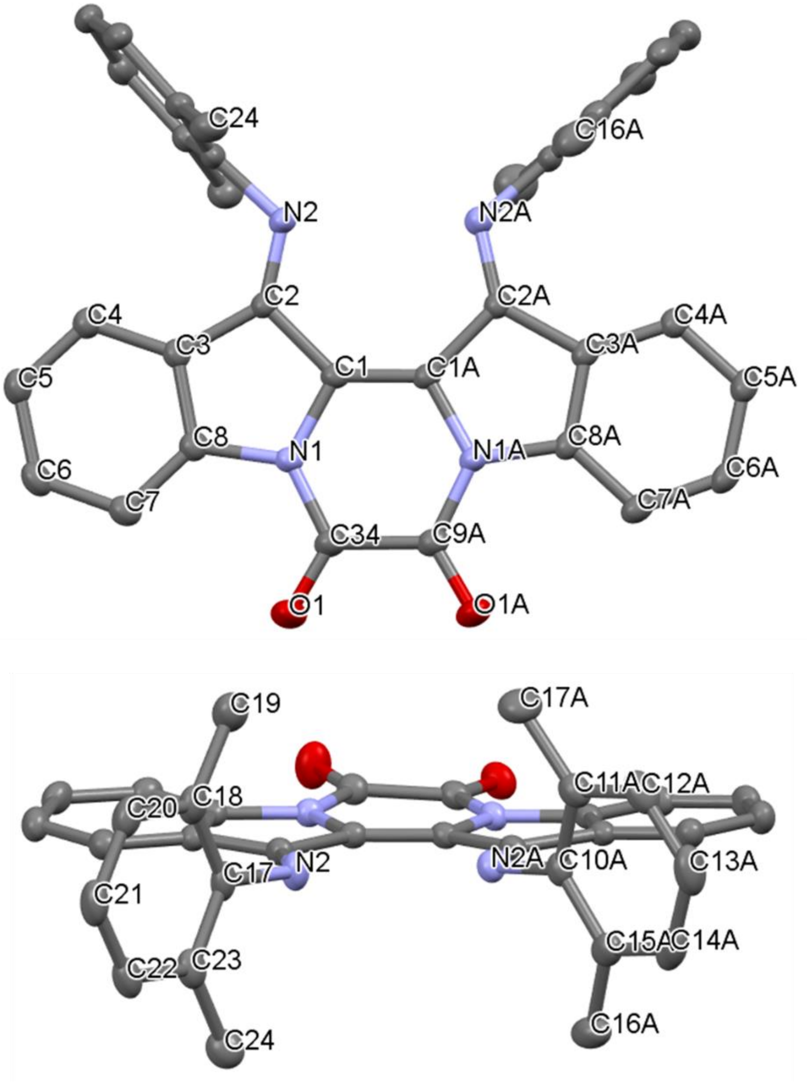

Appendix F-34 X-ray structure of **4.6a**. Hydrogen atoms except -N<u>H</u> are omitted for clarity. Thermal ellipsoids represented at 50%.

Appendix F-35 Table of bond lengths (Å) for **4.6a**

Atom	Atom	Length/Å	Atom	Atom	Length/Å
O(1A)	C(9A)	1.2166(15)	C(8)	C(7)	1.3941(18)
O(1)	C(34)	1.2185(15)	C(3)	C(4)	1.3975(18)
N(1)	C(1)	1.4209(15)	C(7)	C(6)	1.395(2)
N(1)	C(8)	1.4305(16)	C(34)	C(9A)	1.5210(19)
N(1)	C(34)	1.3787(16)	C(4A)	C(5A)	1.3928(18)
N(1A)	C(1A)	1.4141(15)	C(7A)	C(6A)	1.3918(19)

N(1A)	C(8A)	1.4256(16)	C(17)	C(23)	1.4079(19)
N(1A)	C(9A)	1.3792(16)	C(17)	C(18)	1.408(2)
N(2A)	C(2A)	1.2826(16)	C(4)	C(5)	1.3966(19)
N(2A)	C(10A)	1.4236(16)	C(23)	C(22)	1.3996(19)
N(2)	C(2)	1.2818(16)	C(23)	C(24)	1.502(2)
N(2)	C(17)	1.4248(17)	C(15A)	C(14A)	1.406(2)
C(2A)	C(3A)	1.4845(17)	C(15A)	C(16A)	1.505(2)
C(2A)	C(1A)	1.4936(17)	C(22)	C(21)	1.388(2)
C(3A)	C(8A)	1.4004(17)	C(11A)	C(12A)	1.391(2)
C(3A)	C(4A)	1.3982(18)	C(11A)	C(17A)	1.511(2)
C(1)	C(2)	1.4917(17)	C(5A)	C(6A)	1.395(2)
C(1)	C(1A)	1.3605(17)	C(5)	C(6)	1.395(2)
C(2)	C(3)	1.4876(17)	C(20)	C(18)	1.3983(19)
C(8A)	C(7A)	1.3953(17)	C(20)	C(21)	1.392(2)
C(10A)	C(15A)	1.4040(18)	C(18)	C(19)	1.508(2)
C(10A)	C(11A)	1.4060(19)	C(14A)	C(13A)	1.388(2)
C(8)	C(3)	1.3977(17)	C(12A)	C(13A)	1.379(2)

Appendix F-36 Table of bond angles (°) for **4.6a**

Atom	**Atom**	**Atom**	**Angle/°**	**Atom**	**Atom**	**Atom**	**Angle/°**
C(1)	N(1)	C(8)	110.09(10)	C(8)	C(7)	C(6)	116.71(12)
C(34)	N(1)	C(1)	125.15(11)	O(1)	C(34)	N(1)	123.23(12)
C(34)	N(1)	C(8)	124.68(10)	O(1)	C(34)	C(9A)	120.50(12)
C(1A)	N(1A)	C(8A)	110.24(10)	N(1)	C(34)	C(9A)	116.27(11)
C(9A)	N(1A)	C(1A)	125.35(11)	C(5A)	C(4A)	C(3A)	118.36(12)
C(9A)	N(1A)	C(8A)	124.32(11)	C(6A)	C(7A)	C(8A)	116.54(12)
C(2A)	N(2A)	C(10A)	119.55(11)	O(1A)	C(9A)	N(1A)	124.33(12)
C(2)	N(2)	C(17)	121.12(11)	O(1A)	C(9A)	C(34)	120.23(12)
N(2A)	C(2A)	C(3A)	131.41(12)	N(1A)	C(9A)	C(34)	115.43(11)
N(2A)	C(2A)	C(1A)	123.18(11)	C(23)	C(17)	N(2)	118.84(13)
C(3A)	C(2A)	C(1A)	105.40(10)	C(23)	C(17)	C(18)	121.94(12)
C(8A)	C(3A)	C(2A)	108.54(11)	C(18)	C(17)	N(2)	118.87(12)
C(4A)	C(3A)	C(2A)	132.01(12)	C(5)	C(4)	C(3)	118.39(12)
C(4A)	C(3A)	C(8A)	119.45(12)	C(17)	C(23)	C(24)	120.60(13)
N(1)	C(1)	C(2)	106.81(10)	C(22)	C(23)	C(17)	117.54(14)
C(1A)	C(1)	N(1)	118.25(11)	C(22)	C(23)	C(24)	121.85(13)
C(1A)	C(1)	C(2)	134.92(11)	C(10A)	C(15A)	C(14A)	117.56(13)
N(2)	C(2)	C(1)	123.38(12)	C(10A)	C(15A)	C(16A)	120.77(13)
N(2)	C(2)	C(3)	131.10(12)	C(14A)	C(15A)	C(16A)	121.61(13)
C(3)	C(2)	C(1)	105.50(10)	C(21)	C(22)	C(23)	121.62(13)

N(1A)	C(1A)	C(2A)	106.87(10)	C(10A)	C(11A)	C(17A)	120.30(13)
C(1)	C(1A)	N(1A)	119.32(11)	C(12A)	C(11A)	C(10A)	118.56(13)
C(1)	C(1A)	C(2A)	133.74(11)	C(12A)	C(11A)	C(17A)	121.14(13)
C(3A)	C(8A)	N(1A)	108.92(11)	C(4A)	C(5A)	C(6A)	121.11(13)
C(7A)	C(8A)	N(1A)	128.22(12)	C(6)	C(5)	C(4)	120.91(13)
C(7A)	C(8A)	C(3A)	122.85(12)	C(7A)	C(6A)	C(5A)	121.67(13)
C(15A)	C(10A)	N(2A)	120.53(12)	C(5)	C(6)	C(7)	121.59(13)
C(15A)	C(10A)	C(11A)	121.52(12)	C(21)	C(20)	C(18)	120.98(14)
C(11A)	C(10A)	N(2A)	117.86(12)	C(17)	C(18)	C(19)	120.42(13)
C(3)	C(8)	N(1)	108.90(11)	C(20)	C(18)	C(17)	118.13(13)
C(7)	C(8)	N(1)	128.38(12)	C(20)	C(18)	C(19)	121.45(14)
C(7)	C(8)	C(3)	122.72(12)	C(22)	C(21)	C(20)	119.75(13)
C(8)	C(3)	C(2)	108.69(11)	C(13A)	C(14A)	C(15A)	121.25(14)
C(4)	C(3)	C(2)	131.66(12)	C(13A)	C(12A)	C(11A)	121.07(14)
C(4)	C(3)	C(8)	119.65(12)	C(12A)	C(13A)	C(14A)	119.94(14)

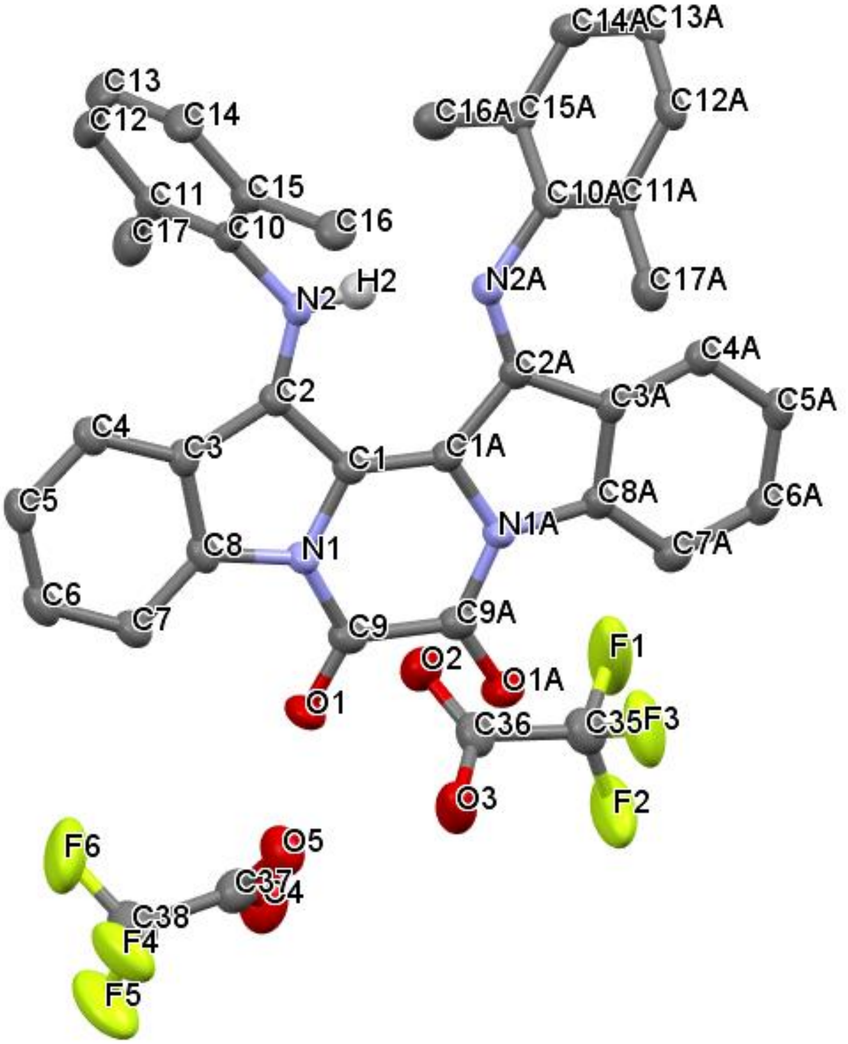

Appendix F-37 X-ray structure of **4.6aH**$^{+}$TFA^{-}. Hydrogen atoms except -N<u>H</u> are omitted for clarity. Thermal ellipsoids represented at 50%.

Appendix F-38 Table of bond lengths (Å) for **4.6aH**$^{+}$TFA^{-}

Atom	**Atom**	**Length/Å**	**Atom**	**Atom**	**Length/Å**
O1A	C9A	1.213(3)	C3	C4	1.391(4)
O1	C9	1.206(3)	C2	C1	1.465(4)
F3	C35	1.313(4)	C11A	C10A	1.394(4)
F4	C38	1.330(4)	C11A	C12A	1.392(4)
O5	C37	1.291(4)	C11A	C17A	1.505(4)
O2	C36	1.216(4)	C10	C15	1.398(4)
O3	C36	1.260(4)	C10	C11	1.398(4)

N1A	C1A	1.394(3)
N1A	C8A	1.419(3)
N1A	C9A	1.379(4)
N1	C1	1.396(3)
N1	C8	1.423(3)
N1	C9	1.385(4)
N2	C2	1.286(3)
N2	C10	1.432(3)
N2A	C2A	1.296(3)
N2A	C10A	1.438(3)
F5	C38	1.319(4)
F1	C35	1.301(4)
F6	C38	1.342(4)
O4	C37	1.200(4)
F2	C35	1.331(4)
C3A	C2A	1.462(4)
C3A	C8A	1.398(4)
C3A	C4A	1.392(4)
C2A	C1A	1.467(4)
C1A	C1	1.355(4)
C3	C2	1.464(4)
C3	C8	1.400(4)
C8A	C7A	1.377(4)
C4A	C5A	1.386(4)
C10A	C15A	1.397(4)
C8	C7	1.379(4)
C15A	C14A	1.389(4)
C15A	C16A	1.508(4)
C15	C14	1.388(4)
C15	C16	1.503(4)
C4	C5	1.388(4)
C9A	C9	1.524(4)
C11	C12	1.390(4)
C11	C17	1.504(4)
C12A	C13A	1.371(4)
C14A	C13A	1.375(4)
C5A	C6A	1.387(4)
C7	C6	1.383(4)
C5	C6	1.387(4)
C36	C35	1.535(4)
C6A	C7A	1.384(4)
C12	C13	1.381(5)
C37	C38	1.522(5)
C14	C13	1.380(5)

Appendix F-39 Table of bond angles (°) for **4.6aH**$^+$TFA$^-$

Atom	**Atom**	**Atom**	**Angle/°**
C1A	N1A	C8A	109.4(2)
C9A	N1A	C1A	124.0(2)
C9A	N1A	C8A	126.6(2)
C1	N1	C8	109.1(2)
C9	N1	C1	123.9(2)
C9	N1	C8	126.9(2)
C2	N2	C10	124.7(2)
C2A	N2A	C10A	127.1(2)
C8A	C3A	C2A	107.7(2)
C4A	C3A	C2A	132.2(3)
C4A	C3A	C8A	120.0(3)
N2A	C2A	C3A	132.0(3)
N2A	C2A	C1A	121.8(2)
C3A	C2A	C1A	106.2(2)
N1A	C1A	C2A	107.6(2)
C14A	C15A	C16A	120.9(3)
C10	C15	C16	120.7(3)
C14	C15	C10	117.8(3)
C14	C15	C16	121.5(3)
C5	C4	C3	118.4(3)
O1A	C9A	N1A	123.7(3)
O1A	C9A	C9	119.9(3)
N1A	C9A	C9	116.3(3)
C10	C11	C17	123.4(3)
C12	C11	C10	116.7(3)
C12	C11	C17	119.9(3)
C13A	C12A	C11A	121.3(3)
O1	C9	N1	123.4(3)
O1	C9	C9A	120.6(3)
N1	C9	C9A	115.9(3)

C1	C1A	N1A	119.8(2)	C13A	C14A	C15A	121.0(3)
C1	C1A	C2A	132.6(3)	C4A	C5A	C6A	120.6(3)
C8	C3	C2	108.1(2)	C8	C7	C6	116.7(3)
C4	C3	C2	132.3(3)	C6	C5	C4	120.6(3)
C4	C3	C8	119.5(3)	C12A	C13A	C14A	120.4(3)
N2	C2	C3	133.0(3)	O2	C36	O3	130.5(3)
N2	C2	C1	121.3(2)	O2	C36	C35	118.0(3)
C3	C2	C1	105.7(2)	O3	C36	C35	111.6(3)
N1	C1	C2	108.0(2)	C7	C6	C5	122.2(3)
C1A	C1	N1	119.8(2)	C7A	C6A	C5A	122.2(3)
C1A	C1	C2	132.2(3)	C13	C12	C11	121.8(3)
C10A	C11A	C17A	122.7(3)	C8A	C7A	C6A	116.7(3)
C12A	C11A	C10A	117.1(3)	O5	C37	C38	113.1(3)
C12A	C11A	C17A	120.2(3)	O4	C37	O5	128.3(3)
C15	C10	N2	116.1(2)	O4	C37	C38	118.6(3)
C15	C10	C11	122.8(3)	C13	C14	C15	120.8(3)
C11	C10	N2	120.8(3)	F3	C35	F2	104.8(3)
C3A	C8A	N1A	109.2(2)	F3	C35	C36	112.6(3)
C7A	C8A	N1A	128.4(3)	F1	C35	F3	106.0(3)
C7A	C8A	C3A	122.3(3)	F1	C35	F2	105.9(3)
C5A	C4A	C3A	118.1(3)	F1	C35	C36	114.4(3)
C11A	C10A	N2A	121.0(2)	F2	C35	C36	112.5(3)
C11A	C10A	C15A	122.7(3)	C14	C13	C12	120.0(3)
C15A	C10A	N2A	115.9(2)	F4	C38	F6	106.6(3)
C3	C8	N1	108.8(2)	F4	C38	C37	113.6(3)
C7	C8	N1	128.6(3)	F5	C38	F4	108.2(3)
C7	C8	C3	122.6(3)	F5	C38	F6	106.7(3)
C10A	C15A	C16A	121.7(3)	F5	C38	C37	111.7(3)
C14A	C15A	C10A	117.4(3)	F6	C38	C37	109.7(3)

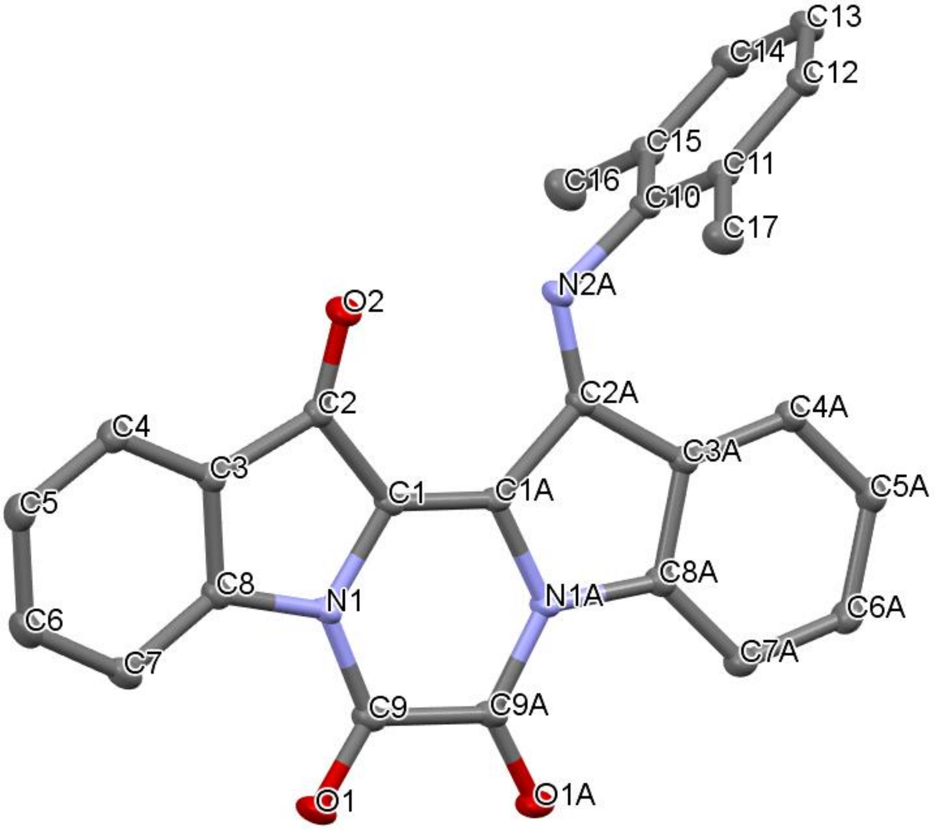

Appendix F-40 X-ray structure of **4.7a**. Hydrogen atoms are omitted for clarity. Thermal ellipsoids represented at 50%.

Appendix F-41 Table of bond lengths (Å) for **4.7a**

Atom	Atom	Length/Å	Atom	Atom	Length/Å
O1	C9	1.2135(13)	C11	C17	1.5062(16)
O2	C2	1.2116(13)	C12	C13	1.3879(17)
N1	C1	1.4124(13)	C13	C14	1.3904(18)
N1	C8	1.4255(14)	C14	C15	1.4006(15)
N1	C9	1.3779(14)	C15	C16	1.5054(17)
C1	C2	1.5011(14)	O1A	C9A	1.2142(13)
C1	C1A	1.3518(14)	N1A	C1A	1.4061(13)
C2	C3	1.4765(15)	N1A	C8A	1.4273(14)
C3	C4	1.3907(15)	N1A	C9A	1.3831(13)
C3	C8	1.3915(14)	N2A	C2A	1.2776(13)
C4	C5	1.3831(16)	C1A	C2A	1.4896(14)
C5	C6	1.4007(17)	C2A	C3A	1.4786(15)

C6	C7	1.3979(16)	C3A	C4A	1.3982(15)
C7	C8	1.3949(14)	C3A	C8A	1.3999(14)
C9	C9A	1.5243(15)	C4A	C5A	1.3930(15)
C10	C11	1.4046(16)	C5A	C6A	1.3978(16)
C10	C15	1.4037(16)	C6A	C7A	1.3952(16)
C10	N2A	1.4281(13)	C7A	C8A	1.3840(15)
C11	C12	1.3957(15)			

Appendix F-42 Table of bond angles (°) for **4.7a**

Atom	Atom	Atom	Angle/°	Atom	Atom	Atom	Angle/°
C1	N1	C8	109.91(8)	C12	C13	C14	119.80(10)
C9	N1	C1	124.74(9)	C13	C14	C15	121.15(11)
C9	N1	C8	125.24(9)	C10	C15	C16	121.39(10)
N1	C1	C2	107.41(9)	C14	C15	C10	117.84(10)
C1A	C1	N1	119.27(9)	C14	C15	C16	120.76(10)
C1A	C1	C2	133.21(9)	C1A	N1A	C8A	109.52(8)
O2	C2	C1	128.72(10)	C9A	N1A	C1A	124.70(9)
O2	C2	C3	127.19(10)	C9A	N1A	C8A	125.77(9)
C3	C2	C1	104.06(8)	C2A	N2A	C10	119.29(9)
C4	C3	C2	128.84(10)	C1	C1A	N1A	119.28(9)
C4	C3	C8	121.10(10)	C1	C1A	C2A	133.20(9)
C8	C3	C2	110.06(9)	N1A	C1A	C2A	107.52(9)
C5	C4	C3	118.52(10)	N2A	C2A	C1A	122.72(10)
C4	C5	C6	119.92(11)	N2A	C2A	C3A	131.96(10)
C7	C6	C5	122.46(10)	C3A	C2A	C1A	105.31(8)
C8	C7	C6	116.38(10)	C4A	C3A	C2A	132.39(10)
C3	C8	N1	108.42(9)	C4A	C3A	C8A	119.29(10)
C3	C8	C7	121.60(10)	C8A	C3A	C2A	108.30(9)
C7	C8	N1	129.97(10)	C5A	C4A	C3A	118.64(10)
O1	C9	N1	123.93(10)	C4A	C5A	C6A	120.90(10)
O1	C9	C9A	120.22(10)	C7A	C6A	C5A	121.12(10)
N1	C9	C9A	115.85(9)	C8A	C7A	C6A	117.20(10)
C11	C10	N2A	118.31(10)	C3A	C8A	N1A	109.27(9)
C15	C10	C11	121.92(10)	C7A	C8A	N1A	127.94(10)
C15	C10	N2A	119.68(10)	C7A	C8A	C3A	122.79(10)
C10	C11	C17	121.03(10)	O1A	C9A	C9	120.56(10)
C12	C11	C10	118.11(10)	O1A	C9A	N1A	123.43(10)
C12	C11	C17	120.83(10)	N1A	C9A	C9	116.01(9)
C13	C12	C11	121.14(11)				

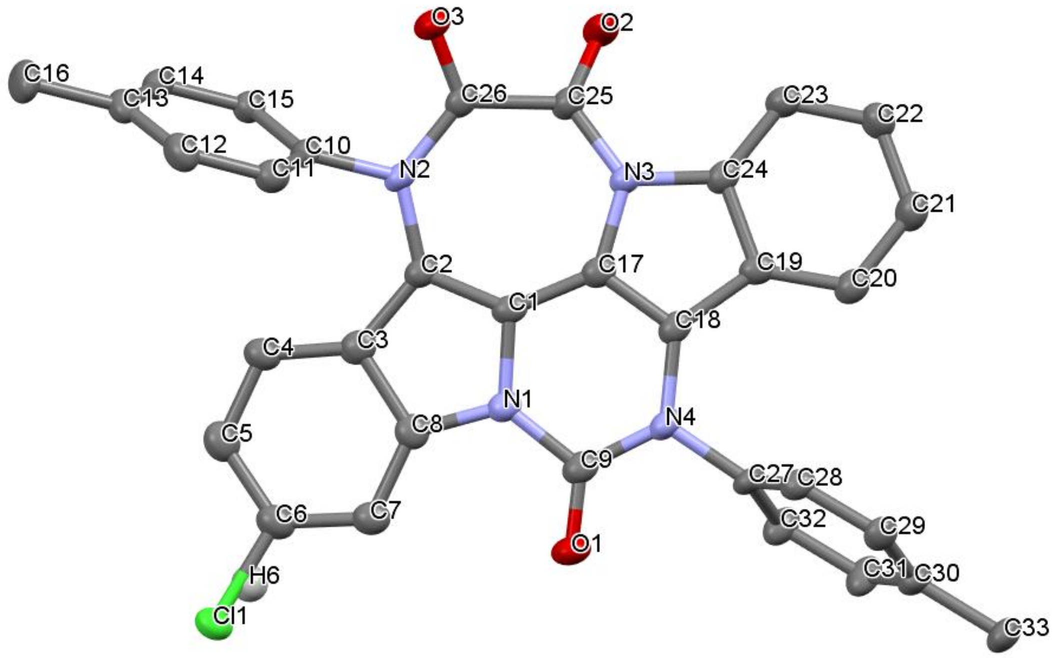

Appendix F-43 X-ray structure of **4.8/4.8-Cl**. A single crystal consists of 75% of **4.8** and 25% of **4.8-Cl**. Hydrogen atoms except H6 are omitted for clarity. Thermal ellipsoids represented at 50%.

Appendix F-44 Table of bond lengths (Å) for **4.8/4.8-Cl**

Atom	**Atom**	**Length/Å**	**Atom**	**Atom**	**Length/Å**
Cl1	C6	1.717(4)	C10	C11	1.387(4)
O1	C9	1.206(4)	C10	C15	1.388(4)
O2	C25	1.201(4)	C11	C12	1.397(5)
O3	C26	1.206(4)	C12	C13	1.397(5)
N1	C1	1.403(4)	C13	C14	1.396(5)
N1	C8	1.394(4)	C13	C16	1.515(5)
N1	C9	1.411(4)	C14	C15	1.395(4)
N2	C2	1.411(4)	C17	C18	1.362(4)
N2	C10	1.461(4)	C18	C19	1.450(5)
N2	C26	1.397(4)	C19	C20	1.388(5)
N3	C17	1.394(4)	C19	C24	1.429(4)
N3	C24	1.413(4)	C20	C21	1.385(5)
N3	C25	1.391(4)	C21	C22	1.395(5)
N4	C9	1.381(4)	C22	C23	1.390(5)

N4	C18	1.404(4)	C23	C24	1.392(5)
N4	C27	1.452(4)	C25	C26	1.568(4)
C1	C2	1.383(4)	C27	C28	1.384(4)
C1	C17	1.395(5)	C27	C32	1.378(5)
C2	C3	1.434(5)	C28	C29	1.391(4)
C3	C4	1.400(5)	C29	C30	1.393(5)
C3	C8	1.441(4)	C30	C31	1.386(5)
C4	C5	1.394(5)	C30	C33	1.509(4)
C5	C6	1.398(5)	C31	C32	1.394(5)
C6	C7	1.394(5)	Cl2	C34	1.763(3)
C7	C8	1.388(5)	C34	Cl2^1	1.763(3)

Appendix F-45 Table of bond angles (°) for **4.8/4.8-Cl**

Atom	**Atom**	**Atom**	**Angle/°**	**Atom**	**Atom**	**Atom**	**Angle/°**
C1	N1	C9	124.9(3)	C12	C13	C16	121.0(3)
C8	N1	C1	108.7(3)	C14	C13	C12	118.2(3)
C8	N1	C9	126.4(3)	C14	C13	C16	120.8(3)
C2	N2	C10	116.4(3)	C15	C14	C13	121.5(3)
C26	N2	C2	128.6(3)	C10	C15	C14	119.1(3)
C26	N2	C10	114.1(2)	N3	C17	C1	127.9(3)
C17	N3	C24	107.7(2)	C18	C17	N3	109.8(3)
C25	N3	C17	127.6(3)	C18	C17	C1	121.4(3)
C25	N3	C24	124.1(3)	N4	C18	C19	130.5(3)
C9	N4	C18	122.0(3)	C17	C18	N4	120.3(3)
C9	N4	C27	119.2(3)	C17	C18	C19	109.0(3)
C18	N4	C27	118.6(3)	C20	C19	C18	135.0(3)
C2	C1	N1	109.3(3)	C20	C19	C24	119.9(3)
C2	C1	C17	134.5(3)	C24	C19	C18	105.1(3)
C17	C1	N1	116.0(3)	C21	C20	C19	118.6(3)
N2	C2	C3	127.7(3)	C20	C21	C22	121.3(3)
C1	C2	N2	124.5(3)	C23	C22	C21	121.5(3)
C1	C2	C3	107.8(3)	C22	C23	C24	117.6(3)
C2	C3	C8	106.7(3)	N3	C24	C19	108.4(3)
C4	C3	C2	135.0(3)	C23	C24	N3	130.5(3)
C4	C3	C8	118.3(3)	C23	C24	C19	121.1(3)
C5	C4	C3	119.9(3)	O2	C25	N3	120.5(3)
C4	C5	C6	120.4(3)	O2	C25	C26	115.1(3)
C5	C6	Cl1	115.0(3)	N3	C25	C26	124.1(3)
C7	C6	Cl1	122.7(3)	O3	C26	N2	119.7(3)
C7	C6	C5	121.6(3)	O3	C26	C25	113.5(3)

C8	C7	C6	118.0(3)	N2	C26	C25	126.8(3)
N1	C8	C3	107.4(3)	C28	C27	N4	119.5(3)
C7	C8	N1	130.8(3)	C32	C27	N4	119.6(3)
C7	C8	C3	121.8(3)	C32	C27	C28	120.8(3)
O1	C9	N1	121.7(3)	C27	C28	C29	119.1(3)
O1	C9	N4	123.3(3)	C28	C29	C30	121.4(3)
N4	C9	N1	114.9(3)	C29	C30	C33	120.7(3)
C11	C10	N2	119.5(3)	C31	C30	C29	118.1(3)
C11	C10	C15	120.7(3)	C31	C30	C33	121.2(3)
C15	C10	N2	119.8(3)	C30	C31	C32	121.4(3)
C10	C11	C12	119.5(3)	C27	C32	C31	119.3(3)
C11	C12	C13	120.9(3)	Cl2	C34	Cl2^1	115.4(3)

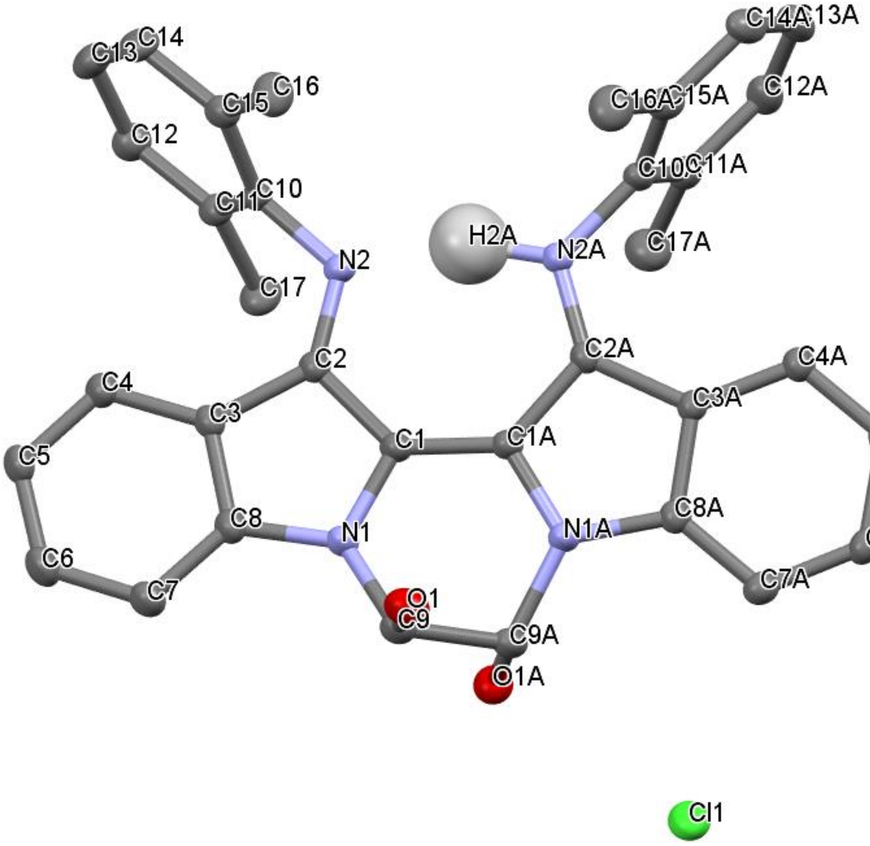

Appendix F-46 X-ray structure of **4.9aH**$^+$Cl$^-$. Hydrogen atoms except -N<u>H</u> are omitted for clarity. Thermal ellipsoids represented at 50%.

Appendix F-47 Table of bond lengths (Å) for **4.9aH**$^{+}$Cl^{-}

Atom	**Atom**	**Length/Å**	**Atom**	**Atom**	**Length/Å**
O1	C9	1.405(2)	N1A	C1A	1.3854(19)
N1	C1	1.3813(18)	N1A	C8A	1.3932(19)
N1	C8	1.397(2)	N1A	C9A	1.4648(19)
N1	C9	1.458(2)	N2A	C2A	1.306(2)
N2	C2	1.3115(19)	N2A	C10A	1.4384(18)
N2	C10	1.434(2)	C1A	C2A	1.4604(19)
C1	C2	1.470(2)	C2A	C3A	1.462(2)
C1	C1A	1.372(2)	C3A	C4A	1.405(2)
C2	C3	1.4663(19)	C3A	C8A	1.414(2)
C3	C4	1.406(2)	C4A	C5A	1.387(2)
C3	C8	1.412(2)	C5A	C6A	1.405(2)
C4	C5	1.390(2)	C6A	C7A	1.388(2)
C5	C6	1.400(2)	C7A	C8A	1.392(2)
C6	C7	1.384(2)	C10A	C11A	1.399(2)
C7	C8	1.394(2)	C10A	C15A	1.397(2)
C9	C9A	1.537(2)	C11A	C12A	1.394(2)
C10	C11	1.400(2)	C11A	C17A	1.512(2)
C10	C15	1.407(2)	C12A	C13A	1.380(3)
C11	C12	1.395(2)	C13A	C14A	1.386(3)
C11	C17	1.510(2)	C14A	C15A	1.402(2)
C12	C13	1.394(2)	C15A	C16A	1.506(2)
C13	C14	1.383(2)	N4	C21	1.148(3)
C14	C15	1.397(2)	C20	C21	1.456(3)
C15	C16	1.504(2)	N3	C19	1.143(2)
O1A	C9A	1.4084(19)	C18	C19	1.457(3)

Appendix F-48 Table of bond angles (°) for **4.9aH**$^{+}$Cl^{-}

Atom	**Atom**	**Atom**	**Angle/˚**	**Atom**	**Atom**	**Atom**	**Angle/˚**
C1	N1	C8	109.47(13)	C1A	N1A	C9A	120.76(12)
C1	N1	C9	121.43(12)	C8A	N1A	C9A	127.65(13)
C8	N1	C9	127.46(12)	C2A	N2A	C10A	120.80(13)
C2	N2	C10	120.37(13)	C1	C1A	N1A	119.49(13)
N1	C1	C2	108.37(12)	C1	C1A	C2A	132.20(14)
C1A	C1	N1	119.17(14)	N1A	C1A	C2A	108.28(12)
C1A	C1	C2	132.45(13)	N2A	C2A	C1A	123.49(14)
N2	C2	C1	123.07(13)	N2A	C2A	C3A	130.95(13)
N2	C2	C3	131.48(14)	C1A	C2A	C3A	105.56(12)

C3	C2	C1	105.45(12)	C4A	C3A	C2A	133.12(14)
C4	C3	C2	133.48(14)	C4A	C3A	C8A	119.77(14)
C4	C3	C8	119.69(13)	C8A	C3A	C2A	107.11(12)
C8	C3	C2	106.83(13)	C5A	C4A	C3A	118.24(14)
C5	C4	C3	118.30(15)	C4A	C5A	C6A	120.98(14)
C4	C5	C6	120.63(15)	C7A	C6A	C5A	121.80(15)
C7	C6	C5	122.40(14)	C6A	C7A	C8A	117.13(14)
C6	C7	C8	116.86(15)	N1A	C8A	C3A	109.31(13)
N1	C8	C3	109.81(13)	C7A	C8A	N1A	128.66(14)
C7	C8	N1	128.12(15)	C7A	C8A	C3A	122.03(14)
C7	C8	C3	122.07(15)	O1A	C9A	C9	107.82(13)
O1	C9	N1	112.77(13)	O1A	C9A	N1A	111.83(12)
O1	C9	C9A	111.96(13)	N1A	C9A	C9	107.86(13)
N1	C9	C9A	107.49(12)	C11A	C10A	N2A	117.98(13)
C11	C10	N2	119.74(14)	C15A	C10A	N2A	118.94(14)
C11	C10	C15	121.92(14)	C15A	C10A	C11A	123.06(14)
C15	C10	N2	118.32(14)	C10A	C11A	C17A	120.82(14)
C10	C11	C17	120.95(15)	C12A	C11A	C10A	117.69(15)
C12	C11	C10	118.35(14)	C12A	C11A	C17A	121.48(15)
C12	C11	C17	120.70(15)	C13A	C12A	C11A	120.78(16)
C13	C12	C11	120.68(15)	C12A	C13A	C14A	120.38(15)
C14	C13	C12	119.74(16)	C13A	C14A	C15A	121.15(16)
C13	C14	C15	121.69(15)	C10A	C15A	C14A	116.87(15)
C10	C15	C16	121.04(15)	C10A	C15A	C16A	121.21(15)
C14	C15	C10	117.41(15)	C14A	C15A	C16A	121.92(15)
C14	C15	C16	121.55(15)	N4	C21	C20	178.9(2)
C1A	N1A	C8A	109.63(12)	N3	C19	C18	179.1(2)

Appendix G: Miscellaneous spectra

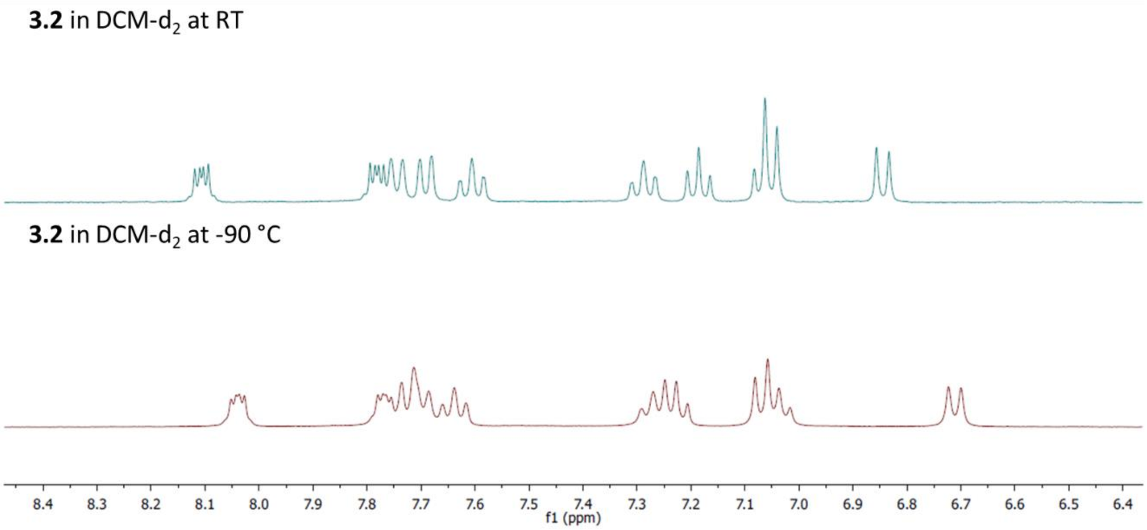

Appendix G-1 ^{1}H NMR spectrum of **3.2** collected at two different temperatures in CD_2Cl_2 at 360 MHz. A single species was observed.

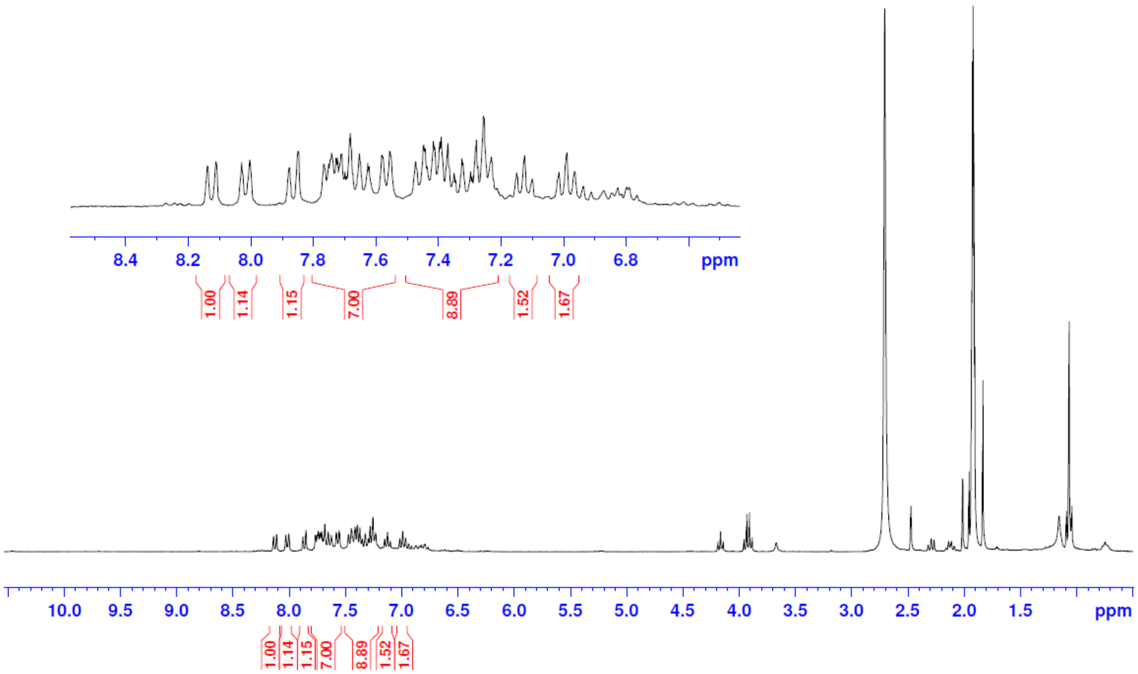

Appendix G-2 ^{1}H NMR spectrum of the red fraction in acetone-d_6 that is used to grow a single X-ray crystal of **3.5**

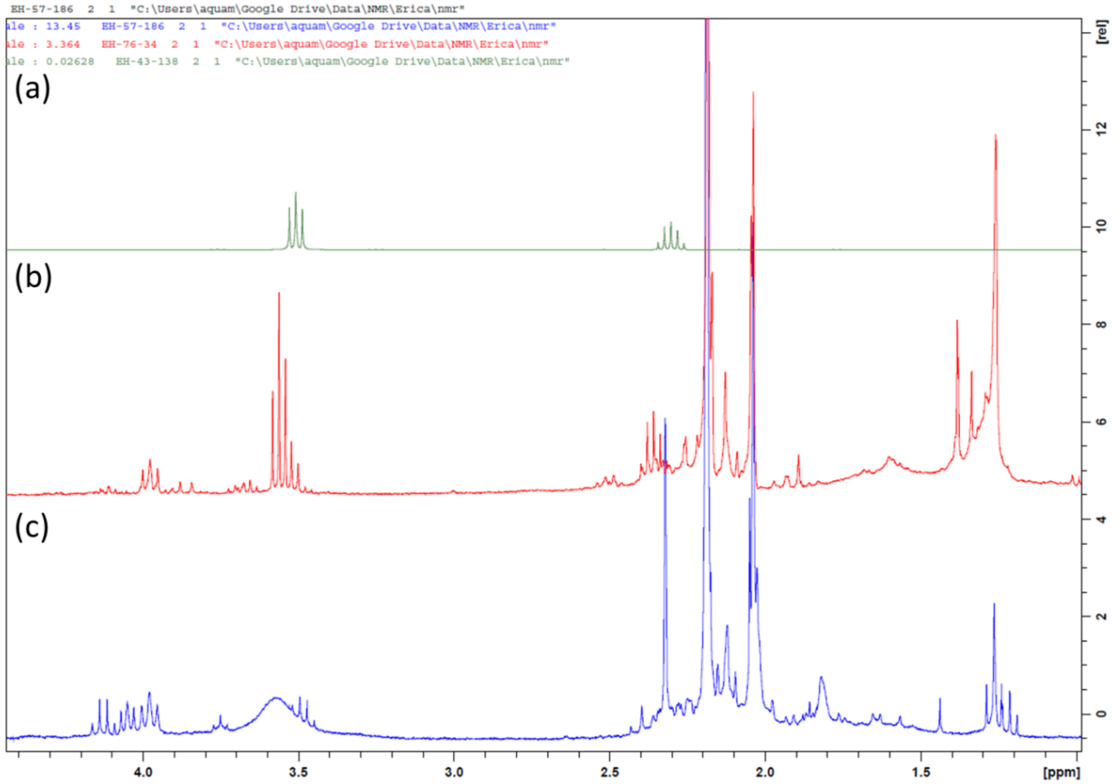

Appendix G-3 ^{1}H NMR spectrum in $CDCl_3$ of (a) a reference of 1,3-dibromopropane (b) reaction crude after alkylation attempt using a base on Nindigo **1.16a** (c) reaction crude after attempted Nindigo procedure on indigo **2.6**. A new triplet signal at 3.98 ppm is observed in both (b) and (c).

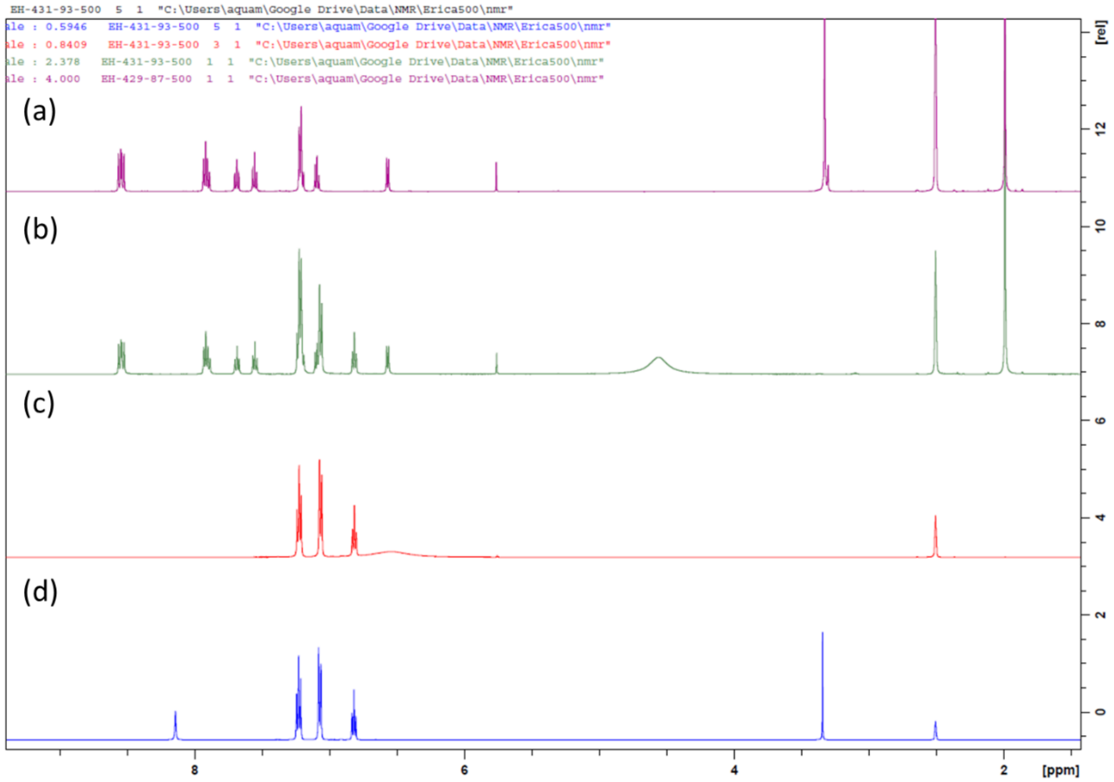

Appendix G-4 ^{1}H NMR spectra of (a) neutral monoimine indigo **4.7a** in DMSO-d_6 (b) after addition of 1.05 *eq*. diphenylammonium triflate (c) reference diphenylammonium triflate in DMSO-d_6 (d) reference diphenylamine in DMSO-d_6.

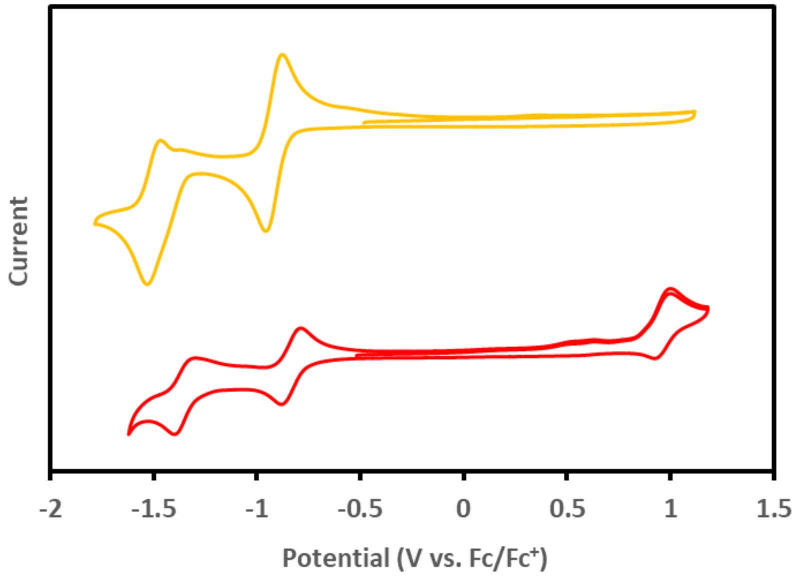

Appendix G-5 Cyclic voltammograms of 2,3-dibromo-1,4-naphthoquinone (top, yellow line, scan rate = 100 mV s^{-1}) and **3.2** (bottom, red line, scan rate = 50 mV s^{-1}) in DCM. 0.1 M NBu_4PF_6 electrolyte. Reproduced from Reference[112] with permission from the Royal Society of Chemistry.

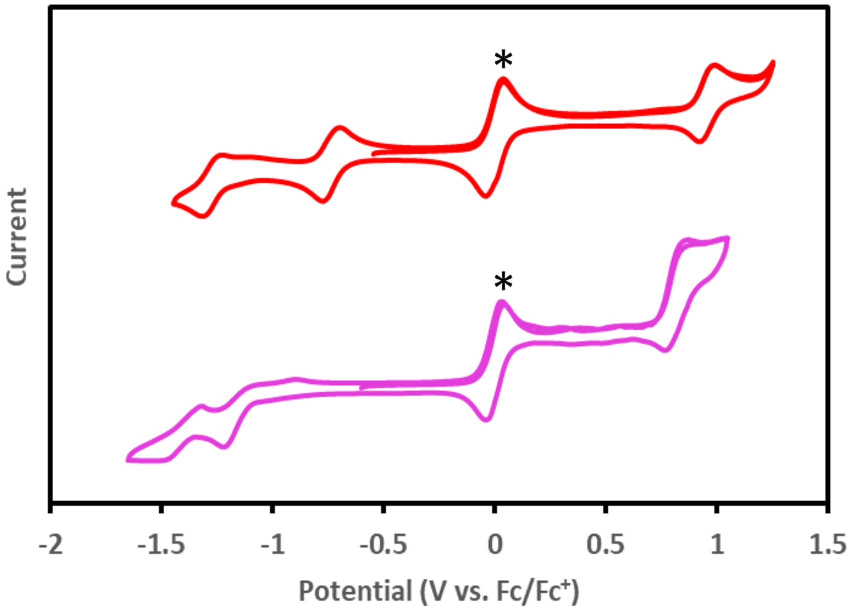

Appendix G-6 Cyclic voltammogram of **3.2** (top, red line) and **3.3** (bottom, pink line) in ACN in the light, 0.1 M NBu4PF_6 electrolyte, scan rate 100 mV s^{-1}. Ferrocene (Fc)/

ferrocenium (Fc^+) peaks are denoted with (*). Reproduced from Reference[112] with permission from the Royal Society of Chemistry.

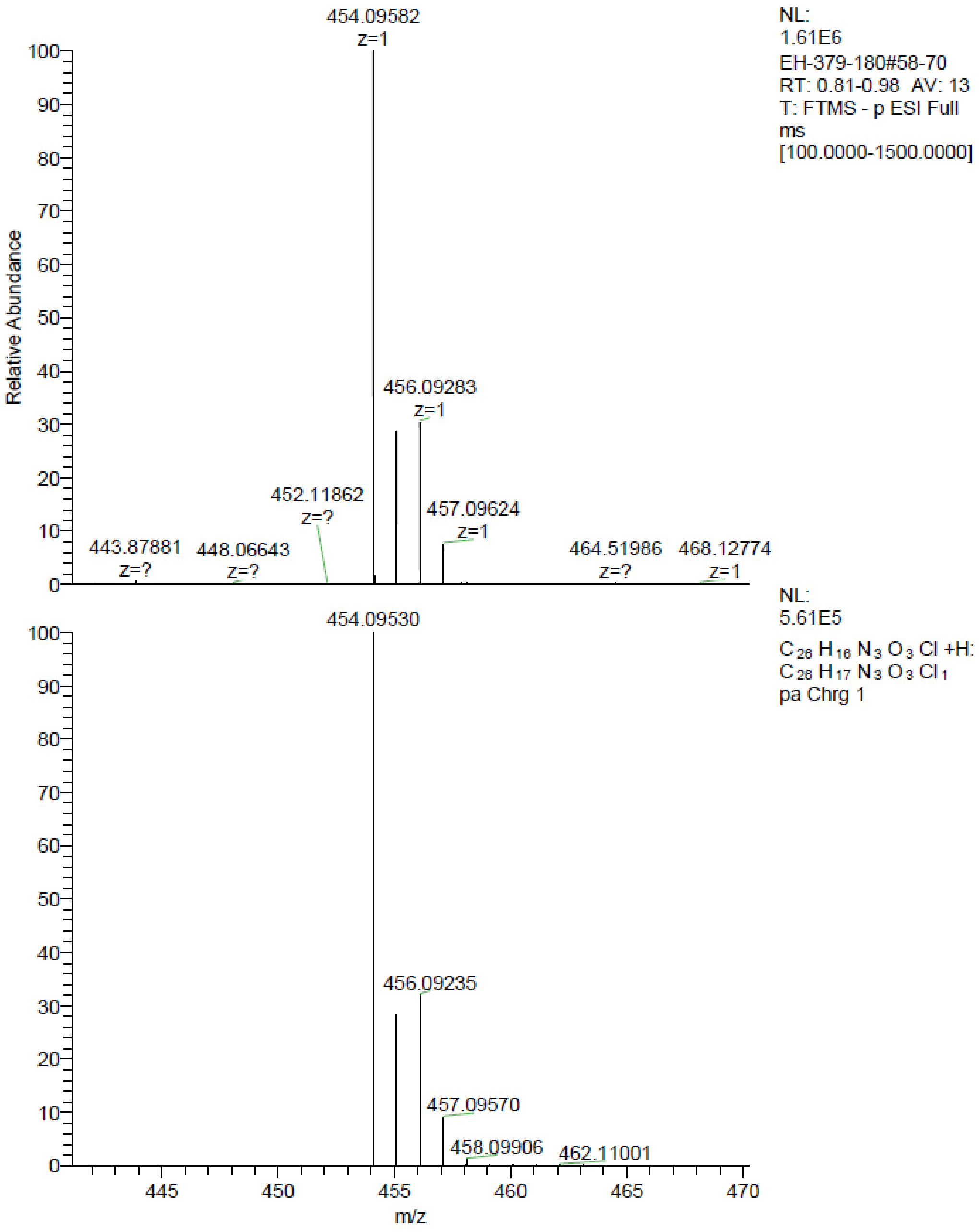

Appendix G-7 HR-MS spectrum of a mono-chlorinated byproduct (suspected structure: **4.7a-Cl**) from the synthesis of **4.7a.** The spectrum matches with a simulation.